APJS MS 54422: REVISED APRIL 16, 2002 / ACCEPTED APRIL 18, 2002
Preprint typeset using LaTeX style emulateapj v.5 (11/12/01)

AN *HST* SURVEY OF THE MID-UV MORPHOLOGY OF NEARBY GALAXIES[1,2]

ROGIER A. WINDHORST[3], VIOLET A. TAYLOR[3,13], ROLF A. JANSEN[3], STEPHEN C. ODEWAHN[3],
CLAUDIA A. T. CHIARENZA[3], CHRISTOPHER J. CONSELICE[4,14], RICHARD DE GRIJS[5],
ROELOF S. DE JONG[6,15], JOHN W. MACKENTY[6], PAUL B. ESKRIDGE[7,13], JAY A. FROGEL[8,13],
JOHN S. GALLAGHER, III[9,14], JOHN E. HIBBARD[10,14], LYNN D. MATTHEWS[11,14],
AND ROBERT W. O'CONNELL[12]
Email: Rogier.Windhorst@asu.edu

ApJS MS 54422: Revised April 16, 2002 / Accepted April 18, 2002

ABSTRACT

We present a systematic imaging survey of 37 nearby galaxies observed with the *Hubble Space Telescope* (*HST*) Wide Field and Planetary Camera 2 (WFPC2) in the mid-UV F300W filter, centered at 2930Å, as well as in the *I*-band (F814W) filter at 8230Å. Eleven of these galaxies were also imaged in the F255W filter, centered at 2550Å. Our sample is carefully selected to include galaxies of sufficiently small radius and high predicted mid-UV surface brightness to be detectable with WFPC2 in one orbit, and covers a wide range of Hubble types and inclinations. The mid-UV (2000–3200Å) spans the gap between ground-based $UBVR(IJHK)$ images, which are available or were acquired for the current study, and far-UV images available from the *Astro*/*UIT* missions for 15 galaxies in our sample. The first qualitative results from our study are:

(1) Early-type galaxies show a significant decrease in surface brightness going from the red to the mid-UV, reflecting the absence of a dominant young stellar population, and in some cases the presence of significant (central) dust lanes. Galaxies that are early-types in the optical show a variety of morphologies in the mid-UV that can lead to a different morphological classification, although not necessarily as later–type. Some early-type galaxies become dominated by a blue nuclear feature or a point source in the mid-UV, e.g., due to the presence of a Seyfert nucleus or a LINER. This is in part due to our mid-UV surface brightness selection, but it also suggests that part of the strong apparent evolution of weak AGN in early-type galaxies may be due to surface brightness dimming of their UV-faint stellar population, which renders the early-type host galaxies invisible at intermediate to higher redshifts.

(2) About half of the mid-type spiral and star-forming galaxies appear as a later morphological type in the mid-UV, as *Astro*/*UIT* also found primarily in the far-UV. Sometimes these differences are dramatic (e.g., NGC 6782 shows a spectacular ring of hot stars in the mid-UV). However, not all mid-type spiral galaxies look significantly different in the mid-UV. Their mid-UV images show a considerable range in the scale and surface brightness of individual star-forming regions. Almost without exception, the mid-type spirals in our sample have their small bulges bisected by a dust-lane, which often appears to be connected to the inner spiral arm structure.

(3) The majority of the heterogeneous subset of late-type, irregular, peculiar and merging galaxies display F300W morphologies that are similar to those seen in F814W, but with important differences due to recognizable dust-features absorbing the bluer light, and due to hot stars, star-clusters, and star-formation "ridges" that are bright in the mid-UV. Less than one third of the galaxies classified as late-type in the optical appears sufficiently different in the mid-UV to result in a different classification.

Our *HST* mid-UV survey of nearby galaxies shows that —when observed in the rest-frame mid-UV— early- to mid-type galaxies are more likely to be misclassified as later types than late-type galaxies are to be misclassified as earlier types. This is because the later type galaxies are dominated by the same young and hot stars in all filters from the mid-UV to the red, and so have a smaller "morphological K-correction" than true earlier type galaxies. The morphological K-correction can thus explain part, but certainly not all of the excess faint blue late-type galaxies seen in deep *HST* fields.

Subject headings: galaxies: elliptical and lenticular — galaxies: spiral — galaxies: irregular — galaxies: interactions — galaxies: peculiar — ultraviolet: galaxies

1. INTRODUCTION

1.1. *The Need for Reliable Classification of Faint Optical Galaxy Samples*

Since the mid 1990's, faint galaxies have been observed with the *Hubble Space Telescope* (*HST*). The best statistics, spatial sampling, and areal coverage are currently achieved in the *I*-band (F814W). Good *HST* morphological information is available today for $\sim 10^5$ galaxies with $I \lesssim 26$ mag. These galaxies come from the two Hubble Deep Fields ("HDF"s; Williams et al. 1996, 1998), their flanking fields, the *HST* Medium-Deep Survey, and other *HST* parallel surveys (e.g., Griffiths et al. 1994; Driver et al. 1995a, 1995b; Odewahn et al. 1996; Abraham et al. 1996, 1999; Roche et al. 1997; Cohen et al. 2002).

[1] Based on observations made with the NASA/ESA *Hubble Space Telescope*, obtained at the Space Telescope Science Institute (STScI), which is operated by the Association of Universities for Research in Astronomy (AURA), Inc., under NASA contract NAS 5-26555

[2] Based in part on observations made with the Vatican Advanced Technology Telescope: the Alice P. Lennon Telescope and the Thomas J. Bannan Astrophysics Facility.

The median half-light radius of faint field galaxies with $I \sim 26$ mag is $r_e \simeq 0.''2$–$0.''3$ (Odewahn et al. 1996). Because of the high spatial resolution required for proper morphological classifications (e.g., using artificial neural networks), *HST*'s 2.4 m aperture limits the useful wavelength for quantitative galaxy classification to $4000 \lesssim \lambda \lesssim 8000$Å. NICMOS H-band images ($\sim 0.''16$ FWHM) do not necessarily sufficiently resolve these faint galaxies to accurately measure their half-light radii and other important parameters.

For $I \lesssim 23$ mag, a few hundred galaxies have their morphology measured at *HST* resolution *and* have measured spectroscopic redshifts plus velocity dispersion or rotation curves (e.g., Cohen et al. 2000; Lilly et al. 1998, Simard et al. 1999; Vogt et al. 1997), leading to more quantitative studies of their physical properties such as mass and M/L ratios. However, because morphology can be determined with relative ease with *HST* for a very large number of galaxies, this ability allows us to explore a part of parameter space that constrains galaxy formation and evolution, and that is not yet accessible to satisfactory spectroscopic study and thus lacks kinematic data for mass measurements.

The most dramatic result from these *HST* morphological studies in the mid–late 1990's was that at faint fluxes, late-type/irregular galaxies completely dominate the faint blue galaxy counts (see Driver et al. 1995a, 1995b, 1998; Glazebrook et al. 1995; Odewahn et al. 1996; Windhorst et al. 1996, 1998b, 2000). A number of authors interpreted this result as evidence for the existence of a population of star-forming galaxies that underwent substantial evolution since $z \lesssim 3$ (Ellis et al. 1996; Pascarelle et al. 1996; Driver et al. 1998; Abraham et al. 1999). Ellipticals and early-type spirals, on the other hand, have evolved much less since $z \lesssim 1$ (see Driver et al. 1995a; Lilly et al. 1998; Cohen et al. 2002). The photometric redshift distribution as a function of observed I-band morphological type — N(z_{phot}, type) — suggests a differential evolution of galaxies as a function of type (Driver et al. 1998), implying a gradual formation of the Hubble sequence with cosmic time.

In the deepest *HST* fields, where morphological classifications are achievable to $I \lesssim 26$ mag (e.g., Odewahn et al. 1996; Driver et al. 1998), the sampled redshift range is $z \simeq 1-3$, while the bulk of the galaxies is at $z \lesssim 2$. Faint high redshift galaxies observed in the I-band are therefore primarily seen in the rest-frame mid-ultraviolet (mid-UV) wavelength range, or 2000–3200Å. The reliability of results derived from the faint *HST* galaxy morphologies is therefore fundamentally limited by the uncertain rest-frame mid-UV morphology of nearby galaxies. For instance, although these faint, late-type/irregular objects resemble some classes of nearby late-type and peculiar galaxies (e.g., Hibbard & Vacca 1997), they need not be physically late-type objects; instead, they may be earlier-type galaxies that look dramatically different in the rest-frame UV. Because of the wavelength dependence of nearby galaxy morphology (especially toward the UV), the outcome of faint galaxy classifications will depend on the rest-frame wavelength sampled. This "morphological K-correction" can be quite significant, even between the B and near-IR bands (e.g., Knapen & Beckman 1996), and must be quantified in order to distinguish genuine evolutionary effects from simple band-pass shifting.

The mid-UV is the optimal wavelength region for comparing the galaxies seen with *HST* in the I-band at $z \gtrsim 2$ to nearby samples, and to address the question of whether the numerous late-type objects that dominate the faint blue galaxy counts are truly new classes of objects, or just reflect the redshifted UV morphology of ordinary galaxies as seen nearby. In the mid-UV, one currently attains the highest resolution *plus* largest field-of-view ("FOV") with the *HST* Wide Field and Planetary Camera 2 ("WFPC2").

In this paper, we therefore present a systematic WFPC2 mid-UV imaging survey for a representative sample of 37 nearby galaxies. Having observations for both nearby and distant objects at the *same* rest-frame wavelength will allow us to calibrate the dependence of morphology on rest-frame wavelength and, thus, to improve our ability to interpret the morphology of distant galaxies. Such a survey will also help us better understand the *physical* drivers of the rest-frame mid-UV emission, i.e., the relation between star formation (SF) and the global physical characteristics of galaxies, their recent star-formation history, and the role of dust absorption and scattering.

1.2. *UV Morphology of Nearby Galaxies as Benchmark for High Redshift Classifications*

Observations of high redshift galaxies in the optical spectral region detect light that was emitted as UV luminosity in these galaxies' rest-frames. They therefore primarily trace high surface brightness ("SB") regions populated by high densities of young ($\lesssim 1$ Gyr) hot stellar populations. The dominance of young stellar complexes in producing UV light from star-forming galaxies was recognized from early satellite UV photometric observations (e.g., Code & Welch 1982; Israel et al. 1986), *IUE* far-UV spectra (e.g., Kinney et al. 1993, and references therein), as well as imaging of a few key objects from sounding rockets (e.g., Carruthers et al. 1978; Stecher et al. 1982). These results were confirmed when UV images became available from the FOCA balloon observations (Millard et al. 1992) and the *Astro/UIT* flights. The latter imaged $\sim$100 nearby galaxies in the far-UV (1500Å) and $\sim$40 in the mid-UV (2500Å) at a resolution of $\sim 3''$ FWHM (Bohlin et al. 1991; Hill et al. 1992; Kuchinski et al. 2000; Marcum et al. 2001). Morphological K-corrections derived from these *UIT* images (and from earlier sounding rocket data) were first investigated by Bohlin et al. (1991) and Giavalisco et al. (1996). This, as well as the FOCA data, showed that galaxy morphology changes quite dramatically below 3600–4000Å, where the hot (young) stellar population — located mainly in spiral arms and H II-regions — dominates the spectral energy distribution (SED) and where

[3]Department of Physics and Astronomy, Arizona State University, Box 871504, Tempe, AZ 85287-1504
[4]Department of Astronomy, Caltech, MS 105-24 Pasadena, CA 91125
[5]Institute of Astronomy, Madingley Road, University of Cambridge, Cambridge, CB3 0HA, UK
[6]Space Telescope Science Institute, 3700 San Martin Drive, Baltimore, MD 21218
[7]Department of Physics and Astronomy, Minnesota State University, Mankato, MN 56003
[8]Code S, NASA Headquarters, 300 D Street SW, Washington, DC 20546
[9]Department of Astronomy, University of Wisconsin, 475 N. Charter St., Madison, WI 53706-1582
[10]National Radio Astronomy Observatory, 520 Edgemont Road, Charlottesville, VA 22903-2475
[11]Center for Astrophysics, 60 Garden Street, Cambridge, MA 02138
[12]Department of Astronomy, University of Virginia, P.O. Box 3818, Charlottesville, VA 22903-0818
[13]Visiting Astronomer, Cerro Tololo International Observatory, National Optical Astronomy Observatory, which is operated by AURA, Inc., under cooperative agreement with the National Science Foundation (NSF).
[14]Visiting Astronomer, Kitt Peak National Observatory, National Optical Astronomy Observatory, which is operated by AURA, Inc., under cooperative agreement with the NSF.
[15]Hubble Fellow.

bulges essentially disappear (see also Burgarella et al. 2001; Kuchinski et al. 2001). Galaxies therefore often appear to be of later Hubble type the further one looks into the rest-frame UV. Qualitatively, this is easy to understand: in the optical/near-IR, we see the accumulated luminous phases of long-lived (>1 Gyr) stars, which emit most of their energy at longer wavelengths, whereas the mid-UV samples the star-formation rate (SFR) averaged over the past Gyr or less. The mid-UV includes the longest wavelengths where young stars can dominate the integrated galaxy light and traces primarily presently active star forming regions, or those regions where star-formation has only recently shut down.

Far-UV images of nearby *early-type* galaxies are not always appropriate for high redshift comparisons; they may be affected by the "UV upturn", a spectral feature that is likely caused by hot, *low-mass, old* stars (O'Connell et al. 1992; O'Connell 1999), and that only appears at relatively recent epochs ($z \lesssim 0.3$; Burstein et al. 1988; Greggio & Renzini 1990; Brown et al. 2000). However, middle-aged stellar systems can be very dim in the UV compared to either older or younger objects, as in the case in, e.g., M32. In galaxies of all types the far–mid-UV emission can also be modulated by dust.

1.3. *Other Ways of Addressing the Morphological K-correction*

A number of authors have explored the effects of band-pass shifting using multicolor optical images to extrapolate to the rest-frame UV on a pixel-by-pixel basis. This has been done both using ground-based data (e.g., Hibbard & Vacca, 1997; Brinchmann et al. 1998), FOCA mid-UV images (Burgarella et al. 2001), *UIT* far-UV images (Kuchinski et al. 2000), and *HST* images of galaxies at moderate redshifts (Abraham et al. 1999; Bouwens, Broadhurst, & Silk 1998). The peculiarities in shape and size distributions measured in deep *HST* surveys are found to considerably exceed the effects of band-pass shifting. While this is a robust result, these methods may not capture the full range of rest-frame UV galaxy SEDs, and are less suitable for making detailed comparisons with the local universe.

For instance, there is considerable scatter in the mid-UV for galaxies of a given optical color. Donas, Milliard & Laget (1995) find a 3 magnitude range in $(\mathrm{UV}-B)$ colors at a given $(B-R)$ color in a faint space-based galaxy sample, where a 2000Å filter was used to measure the UV flux. This UV/optical decoupling is confirmed by the spectroscopy of Treyer et al. (1998) and implies that the true evolutionary history of galaxies can be very different from that inferred from optical data alone, and that mid-UV observations are necessary for a better understanding.

Recent observations of the HDF-North with *HST*/NICMOS show that some galaxies out to $z \sim 2.5$ appear 'regular' and fit into the Hubble sequence in the near-IR, but look more patchy and irregular at shorter wavelengths (Dickinson et al. 2001). Galaxies that look disturbed in the optical, on the other hand, in general also look very similar in the rest-frame UV. These distorted high-z galaxies also tend to be high SB objects in the UV, forming stars at a high rate. Nearby galaxies whose structure is dominated by star-formation also have similar morphologies in the rest-frame optical and mid-UV (e.g., Conselice et al. 2000), which suggests that some nearby star-bursts galaxies may be analogs to these 'peculiar' high-z objects.

1.4. *Goals of our* HST *Mid-UV Imaging Survey*

In this section we briefly summarize the main science goals of our project, which determine the size and properties of our WFPC2 mid-UV sample. We aim to:
(1) provide local benchmark images that we can artificially redshift to $z \simeq 1$–3 for quantitative comparison to the morphology and photometric properties of high redshift galaxies;
(2) consistently classify polychromatic structures within galaxies from 0.2–2μm with artificial neural networks.
(3) map the spatial distribution, luminosities, and sizes of star-forming regions dominating the UV morphology, and relate these to global galaxy properties;
(4) map the effects of dust at mid-UV wavelengths in galaxies as a function of type, inclination, and galactocentric radius;
In the present paper, we present the benchmark mid-UV images and a qualitative discussion of our results in the context of these science goals. More quantitative studies will be presented in subsequent papers by members of our mid-UV team.

This paper is organized as follows. In section 2, we outline our survey strategy, describe the sample selection and discuss the WFPC2 observations. We also discuss the data processing and calibration. Our WFPC2 mid-UV and ground-based optical images are presented in § 3, where we also discuss individual objects. We describe the general trends in galaxy morphology as observed from the mid-UV through the optical in § 4. And in § 5, we present our main conclusions from this data set.

2. STRATEGY, SAMPLE SELECTION AND OBSERVATIONS

2.1. *WFPC2 Mid-UV Survey Strategy*

2.1.1. *Mid-UV Filters*

With the *HST* Wide Field and Planetary Camera 2 ("WFPC2"), we have obtained images of 37 nearby galaxies through one or, whenever possible, two wide-band mid-UV filters below the atmospheric cutoff. These filters are F300W ($\lambda_{cent} \simeq 2930$Å; $\Delta\lambda \simeq 740$Å FWHM) and F255W ($\lambda_{cent} \simeq 2550$Å; $\Delta\lambda \simeq 395$Å FWHM), which provide reasonable red-leak suppression. The F255W, F300W, and the Johnson U and B filters are approximately equally spaced in energy (i.e., in the logarithm of the wavelength), and so add significantly to the existing ground-based optical–near-IR color baseline.

Since the *HST*/WFPC2 system throughput is ∼2.0% in F300W and ∼0.5% in F255W (Biretta et al. 2001; Appendix 1), we can only detect the highest SB, bluest objects in F255W in a single *HST* orbit and so have selected our sample accordingly. The mid-UV is the longest wavelength where younger stars can dominate the integrated galaxy light, and therefore the regime of choice to measure the SFR averaged over $\lesssim 1$ Gyr. We have observed *all* selected galaxies through the F300W filter, spending no more than one full orbit per galaxy. In that same orbit a short exposure through a red filter (F814W) is taken for adequate red-leak correction (see §2.4.3). For galaxies in the *HST* Continuous Viewing Zone (CVZ), we also took exposures in the F255W filter (see §2.1.4).

2.1.2. *Predicted Mid-UV Surface Brightness*

We predict the average mid-UV SB, μ_{F300W}, for a given galaxy from its total B magnitude, B_T, its $(U-B)$ color, its half-light radius, r_e, and its ellipticity, b/a, (as tabulated in or derived from the RC3 catalogue [de Vaucouleurs et al. 1991], or the NASA/IPAC Extragalactic Database, NED) as following:

$$\mu_{F300W} = F300W_T + 0.75 + 2.5\log(\pi\, r_e^2 \times b/a)\,, \qquad (1)$$

i.e., half the total predicted F300W magnitude, $F300W_T$, within the effective area. We used the updated Bruzual & Charlot (1993) models to transform the $(U-B)$ color for each galaxy type to a predicted ($F300W$–B) color, from which $F300W_T$ follows. To a reasonable approximation we find $(F300W-B) \simeq 2 \times (U-B)$. In the absence of a $(U-B)$ color, a prediction for $(U-B)$ was made from the measured $(B-V)$ color and the known $(U-B)$ vs. $(B-V)$ relation for RC3 galaxies as a function of galaxy type (de Vaucouleurs et al. 1991). Our sample was selected to have $18 \lesssim \mu_{F300W} \lesssim 22.5$–$23.0$ mag arcsec^{-2}. For this range in SB, a galaxy can be detected out to $r \simeq 2$–$3\,r_e$ with WFPC2 in one orbit with sufficiently high S/N to allow morphological features to be recognized.

The bias toward selecting higher SB galaxies can be addressed as in Driver et al. (1995b). In short, selecting high SB galaxies as the nearby template objects is not an overriding concern, since the high-redshift samples are similarly biased (or more so) in favor of high SB galaxies due to the severe cosmological SB dimming. For monochromatic light, SB-dimming is proportional to $(1+z)^{(4+\alpha)}$, with α the spectral index if the object spectrum were to be represented by a power-law SED.

The resolution of *HST*'s Optical Telescope Assembly (OTA) in F300W is $\sim$0.″04. This is somewhat larger than *HST*'s formal diffraction limit at 2930Å ($1.22 \cdot \lambda/\mathrm{D} \simeq 0.''03$), which doesn't set in until longward of 4000Å due to mirror micro-roughness. The WFPC2 WFC pixel size is $\simeq 0.''0996$/pixel. Hence, because the UV images are already severely undersampled, on-chip rebinning to gain SB-sensitivity is not an option. Instead, where needed, we can rebin the images in the post-processing stage to measure the outskirts to fainter SB-levels. This improves the SB-sensitivity (see § 2.4.2) in the outskirts to $\sim$25.8–26.3 mag arcsec^{-2} in F300W and to $\sim$23.8–24.2 mag arcsec^{-2} in F255W, sufficient to get good light-profiles for $r \lesssim 2$–$3\,r_e$.

2.1.3. *Target Size and Placement Inside WFPC2*

The WFPC2 FOV measures $\sim$2.5′ (along the WFC CCDs). We selected the sample to fit within the FOV, and preferably within a single $75'' \times 75''$ WFC CCD, allowing us to derive reliable SB-profiles without having to mosaic multiple WFPC2 fields. For galaxies with a B-band half-light radius in the range $0.'1 \lesssim r_e \lesssim 1.'0$ (as derived from the RC3 catalogue, de Vaucouleurs et al. 1991), about $\sim$3–5 scale-lengths fit in a single WFPC2 field.

For most of our sample galaxies, the nucleus has been placed on WFPC2's WF3 CCD, near pixel $(X,Y) = (300, 300)$, so that both the WF2 and WF4 CCDs maximally sample the galaxies' outskirts, allowing optimal subtraction of any sky-background when mosaicing the four WFPC2 CCDs. For some of the larger galaxies and for galaxies in pairs or small groups, we center the object(s) in another part of the WFPC2 FOV, or constrain the *HST* roll angle ("ORIENT") to assure that the largest possible portion of the galaxy or galaxy group is observed.

2.1.4. *The* HST *Continuous Viewing Zone*

Part of the galaxy sample is located in the *HST* Continuous Viewing Zone (CVZ), i.e., at $53^\circ \leq |\mathrm{DEC}| \leq 72^\circ$, where objects are observable for an entire *HST* orbit, typically doubling the available integration time. For any such galaxies, we were able to obtain F255W as well as F300W images without the cost of an extra *HST* orbit. We select the sample to maximize the fraction of galaxies in the CVZ.

Since the Zodiacal background reflects the color of the Sun, the sky-background will be darker in the F255W filter ($\sim$24.5–25.0 mag arcsec^{-2}) than in the F300W filter ($\sim$24.0 mag arcsec^{-2}), partly compensating for the lower sensitivity in F255W. Observations in the CVZ may suffer from higher sky-background levels due to the Earth's limb (Williams et al. 1996). We minimize the probability of excessive sky-levels by interspersing the exposures in the different filters using the sequence: F814W, F255W, F300W, F255W, F300W, F814W, F255W, and F300W. This sequence ensures that never more than one F255W or F300W exposure is taken close to the Earth's limb in a full CVZ orbit, and also minimizes the number of Fine Guidance Sensor (FGS) motions needed to create a pointing dither-pattern. For non-CVZ targets we use the sequence: F814W, F300W, F300W, and F814W, to push the F300W exposures farthest from the Earth's limb.

2.2. *Sample Selection*

2.2.1. *Available Ground- and Space-based Observations*

In selecting our galaxy sample we aimed to take advantage of as much pre-existing ground- and space-based UV, optical and near-IR images as possible. In particular, high priority was given to galaxies that have been observed with *UIT* in the far-UV (1500Å) and obeyed the SB and size criteria (§ 2.1.2 and § 2.1.3). Some of these galaxies are close to the *UIT* detection limit, as they are minor members in galaxy groups targeted by *UIT*.

Also, nearby galaxies already observed with *HST*/WFPC2 in the mid-UV F300W and/or F255W filter that match our criteria will be included in our final sample. When the final Cycle 9 target list was compiled in early 2000, the *HST* Archive contained 15 such galaxies with F300W images obtained and two more imaged in F255W. These Archival observations came primarily from Cycle 4 program GO 5381 (PI: Koratkar) and Cycle 6 program GO 6355 (PI: Giavalisco). We will analyze these 17 Archival mid-UV images in a separate paper (Taylor et al. 2002, in preparation). The current Cycle 9 sample is designed and must be understood to be complementary to this existing Archival sample.

Over the last decade, several of us have systematically imaged from the ground a total of about 750 nearby galaxies covering all Hubble types and inclinations. The majority of these galaxies — which includes most of the galaxies imaged in the far-UV with *UIT* (primarily at 1500Å) — were observed in *UBVRI*, but a good fraction was observed in the near-IR *JHK* filters as well (Eskridge et al. 2002b). The data base thus compiled consists of seven individual galaxy samples:

(1) 86 face-on spiral galaxies of de Jong & van der Kruit (1994);
(2) 220 galaxies with Hubble types later than S0 from the OSU *BVRJHK* survey (Frogel et al. 1996; Eskridge et al. 2000, 2002b) (all inclinations);
(3) 113 galaxies from the Frei et al. (1996) survey in B and R, to which we added U and V-band images (good number of early-type galaxies; all inclinations; Taylor et al. 2002; in prep.);
(4) 100 galaxies with 1500Å and 40 with 2500Å images from the *Astro*/*UIT* mission (Kuchinski et al. 2000; Marcum et al. 2001) (all inclinations);
(5) 48 edge-on galaxies (de Grijs & Peletier 1997; de Grijs, Peletier, & van der Kruit, 1997);
(6) 150 late-type UGC galaxies selected to be morphologically irregular, peculiar, or merging (Hibbard & Vacca 1997; Hibbard et al. 2002). These have a range of impact parameters (i.e., the

distance between the two interacting or colliding objects); and
(7) 49 late-type dwarf spiral galaxies (Matthews & Gallagher 1997) and compact, high-SB luminous blue galaxies (Gallagher et al. 1989, 2001) (all inclinations).
with some overlap among the samples. The last two sets were specifically added to provide a good number of likely local counterparts of the peculiar and irregular galaxies seen with *HST* in large numbers at high redshifts. The *UBVRI* + *JHK* images from these ground-based surveys, where available, are included in the data presented in § 3 (Fig. 4).

2.2.2. *Required Statistics*

To date, the *HST* Archive contains over 10,000 orbits of data on a multitude of distant galaxy projects (including parallels). To match these numerous observations of distant galaxies, we need a statistically significant and representative comparison sample of nearby galaxies that includes all morphological types. To cover a broad range of nearby galaxies, we will use three broad bins of Hubble types: (1) early-type galaxies (E–S0), (2) early-mid type spiral galaxies (Sa–Sc), and (3) late-type galaxies, irregulars (Sd–Irr), plus peculiars and mergers. For statistical studies as a function of photometric parameters, we will cover a range in inclination angles in three bins of $\sin i$: edge-on, face-on, and intermediate angles. Thus, we need about 54 galaxies in total, to populate each of the nine type–inclination bins with 6 galaxies to begin to average over galaxy properties.

Of the 20 galaxies with WFPC2 F300W images in the Archive as of early 2000 (mostly E/S0/Sabc's), about 17 are small enough to be contained within the WFPC2 FOV. To this available mid-UV sample we add here a complementary set of 37 galaxies, which we selected from the ground-based samples of about 750 galaxies described in section 2.2.1. These objects comprise 24 new irregulars, peculiars, and merging/interacting galaxies, and 13 new E/S0/Sabc's to complement the 17 usable galaxies available in the *HST* Archive.

2.2.3. *Selection of the* HST*/WFPC2 Mid-UV Sample*

The selection criteria for inclusion in the *HST*/WFPC2 sample of 37 galaxies are:
(a) the *B*-band half-light radius should fall within the range $0\farcs1 \lesssim r_e \lesssim 1\farcs0$;
(b) the predicted average SB in F300W out to $r \simeq r_e$ should be in the range $18 \lesssim \mu_{F300W} \lesssim 22.5$–$23.0$ mag arcsec^{-2};
(c) the distribution of Hubble types should be representative for nearby galaxy samples when combined with the set of archival galaxies;
(d) the distribution over apparent axis ratio (and hence inclination) should resemble that of nearby galaxy samples;
(e) priority should be given, first, to the 15 galaxies with available *UIT* 1500Å images that obey the other selection criteria above, and then to galaxies with multi-band ground-based images available;
(f) as much as possible, select galaxies that are schedulable in the *HST* CVZ, while satisfying **(a)** – **(e)**. Replace candidates that are difficult to schedule by alternates.

In Table 1 we list the properties of the selected sample. Most of the table entries are taken or derived from values listed in the RC3 catalogue (de Vaucouleurs et al. 1991). Cols. 2 and 3 list the coordinates of the galaxy centers as measured on the Digital Sky Survey (DSS). In a few cases of complex galaxies, merging/interacting galaxies, or galaxies in small groups, the listed coordinates refer to a "center of mass" position, allowing optimal centering inside the WFPC2 FOV. Col. 4 shows the apparent axis ratio of the minor and major axis isophotal diameter measured at the $\mu_B = 25.0$ mag arcsec^{-2} isophote. The half-light radius, r_e and the radius at the $\mu_B = 25.0$ mag arcsec^{-2} isophote, r_{25}, are listed in Cols. 5 and 6, respectively; the predicted average SB in F300W out to r_e and r_{25}, and the predicted total *F300W* magnitude (see section 2.2) are tabulated in Cols. 7, 8, and 12. Col. 13 lists the revised T-type (numeric morphological type on the 16-step de Vaucouleurs scale). The redshifts in Col. 14 are given with respect to the Galactic Standard of Rest. Col. 15 lists for each galaxy the physical image scale in pc/($''$) at the distance of the galaxy, assuming a Hubble constant $H_0 = 67$ km s^{-1} Mpc^{-1}. And Col. 16 gives the physical size of a single WFC CCD-frame at that redshift. For the typical redshift range, $z \simeq 0.004$—0.02 (i.e., Virgo–Coma cluster like distances), a single WFPC2 CCD covers 6.8–34 kpc.

The SB-selection of the sample is illustrated in Fig. 1, which shows the normalized distributions of the predicted average μ_{F300W} out to r_e for the full (54 galaxy) sample and for the 37 galaxies in the Cycle 9 WFPC2 mid-UV sample, and compares these with the distribution over SB derived for the 3009 galaxies in the RC3 with measured B_T, $(U-B)$ and r_e. Clearly, we sample predominantly galaxies with higher SB than the median SB-value in the RC3, which is $\mu_{F300W} \simeq 22.3$ mag arcsec^{-2}.

As nearby galaxy samples like the RC3 are also limited by significant SB-selection (Disney 1976, Driver 1999), this thus means that our Cycle 9 *HST* sample represents only the tip of the local galaxy SB-distribution. Fig. 1 shows that our sample covers only about the brightest 50% SB-percentile seen in the RC3, while it over-represents the highest SB galaxies seen in the RC3. If one wanted to use our sample to represent all galaxies in the RC3 with $\mu_{F300W} \leq 23$ mag arcsec^{-2}, one would have to apply weights to each of our galaxies in a given observed SB-bin that could be derived from dividing the two distributions over SB in Fig. 1. This will obviously not work for galaxies with $\mu_{F300W} \geq 23$ mag arcsec^{-2}, since almost no galaxies at average SB-levels that faint were observed with *HST*.

As aforementioned, this SB-selection is justified when the primary goal is to construct a sample for comparison of nearby and high-redshift galaxies, since the strong cosmological SB-dimming limits our view of the high-redshift universe in a similar way (or worse). For example, simulations by Windhorst et al. (2002), who investigate how the galaxies in the present sample would appear to NGST under realistic observing conditions, show that at very high redshifts ($z \sim 7$–15) only the highest SB mid-UV structures (with average rest-frame μ_{F300W} out to r_e brighter than 20–21 mag arcsec^{-2}) will be visible to NGST.

Figures 2*a*–*d* show the distributions of morphological type, of apparent axis ratio b/a, of the estimated average $(U-B)$ color within the effective radius, and of the effective radius r_e, within the selected sample. These figures will help the reader to evaluate the usefulness or the weight to apply to individual galaxies in the present sample when using these data for his or her particular purpose. We stress that the present sample is *not formally complete* and, therefore is not suitable for studies that rely on complete statistics (i.e., studies that cover the complete local galaxy luminosity function or the complete range in local galaxy SB). Nonetheless, important trends are visible in Figs. 2*a*–2*d* that will help the reader to make our sample useful for high-redshift comparisons. These trends are:
• Fig. 2*a* shows that our selected mid-UV galaxies overemphasize late-types a bit more than the RC3. This was done on pur-

pose, since late-types are the dominant galaxy population at high redshifts (see Driver et al. 1995a).

• Fig. 2*b* shows that our selected mid-UV galaxies sample the b/a distribution of the RC3 fairly, given the small number statistics. Since Odewahn, Burstein, & Windhorst (1997) found no significant trend in the galaxy b/a distribution from the RC3 level ($B \lesssim 15$ mag) all the way down to the HDF limit ($B \lesssim 28$ mag), our nearby comparison sample is thus a fair one in terms of galaxy ellipticities at all redshifts.

• Fig. 2*c* shows that our selected mid-UV galaxies overemphasize the bluest object in $(U-B)$ a bit more than the RC3. Like Fig. 2*a*, this was done on purpose, since faint blue galaxies are the dominant population at faint magnitudes.

• Fig. 2*d* shows that our selected mid-UV galaxies overemphasize the intrinsically smaller galaxies in r_e more than the RC3, which was again done on purpose, since faint blue galaxies are on average significantly smaller than the ones seen nearby (see Odewahn et al. 1996, Pascarelle et al. 1996, Cohen et al. 2002).

Again, any non-representativeness of our galaxy sample compared to the RC3, or to any other galaxy catalog for that matter, can be addressed by applying the appropriate weights to individual galaxies in our sample when comparing it to any other samples. These weights can be determined from the ratios between the observed distributions in Fig. 2*a*–2*d*, or between our sample and any other sample than the RC3.

2.3. *Observations*

2.3.1. HST/*WFPC2 Observations*

All 37 selected galaxies were observed with WFPC2 during Cycle 9. Typically, we exposed 2×800–1000 s in F300W and 2×100–160 s in F814W. Exposures times were made flexible to optimally use the full *HST* orbit allocated per galaxy. Of the 24 galaxies located in the CVZ, 11 could indeed be scheduled there during Cycle 9. For these, exposure times were 3×400–500 s in both the F255W and F300W filters, and 2×100–160 s in F814W. In none of the 37 Cycle 9 targets did we see evidence for elevated sky-levels in F300W (see § 2.1.4).

We adopted a linear dither pattern such that exposures in the same filter are offset by $n+0.34$ WFC pixels in the case of two (non-CVZ), and $n+0.33$ and $n+0.66$ WFC pixels in the case of three exposures per filter (CVZ). Here, n is a multiple of 5 pixels (ideally 10–30 pixels in both directions to fill in the vignetted regions between the WFPC2 CCD's), and the pixel fractions assure optimal drizzling in a later stage. The actual shifts may slightly deviate from the listed values depending on the quality of the FGS lock achieved for a particular galaxy.

2.3.2. *Ground-based Observations*

Most of the ground-based *UBVRI* CCD images for the 37 galaxies in the present sample were obtained with the 1.8 m Vatican Advanced Technology Telescope (VATT) on Mt. Graham, with additional images taken with the 0.9 m telescope at Cerro Tololo (CTIO), the Danish 1.5 m telescope at the European Southern Observatory (ESO), the 2.1 m telescope at Kitt Peak (KPNO), the 2.2 m University of Hawaii telescope at Mauna Kea (UH), or the 1.0 m Jacobus Kapteyn Telescope (JKT) at La Palma. The optical data were obtained mostly with $2k\times2k$ CCD's. Further details are given in Matthews & Gallagher (1997), Eskridge et al. (2002b), and Taylor et al. (2002, in prep.).

Ground-based near-IR imaging was done using the 1.5 m telescope at Cerro Tololo, the ESO 2.2 m telescope, the Carnegie 2.5 m du Pont telescope at Las Campanas (LCO), or the 3.8 m United Kingdom InfraRed Telescope (UKIRT) at Mauna Kea, mostly with 256^2 HgCdTe-arrays (and 1024^2 in the case of the du Pont telescope). Images were obtained in *JHK*, or a subset of these filters. For further details on these near-IR data we refer to de Grijs et al. (1997), de Jong & van der Kruit (1994), and Eskridge et al. (2002b).

The *JHK* filters sample the underlying cooler (and usually older) stellar population, which in general also dominates the *R* and *I*-bands, so that the *RIJHK* filters in general reveal similar galaxy morphology. Morphological contrast is added through the younger stellar populations in the bluer and UV filters. Since the older stellar population dominates the *RIJHK* fluxes of earlier type galaxies, a comparison of these filters can in principle provide a measure of the dust content, whose effects are strongly wavelength dependent — noting the usual caveat that effects from dust and metallicity are hard to separate, and require spatially resolved spectroscopy in addition to broad-band photometry to address this quantitatively.

We aimed for a photometric zero-point accuracy better than 0.03–0.05 mag, in the optical as well as the near-IR. The ground-based CCD images were reduced following standard procedures, as described in Matthews & Gallagher (1997), and Neuschaefer & Windhorst (1995).

In Table 2 we summarize our Cycle 9 *HST* observations together with the *UIT* and ground-based images available to date. For WFPC2 observations, we list the *HST* roll-angle (`PA_V3`) and the nominal FWHM of the *HST* PSF; for ground-based observation, we list the airmass and the median FWHM in each image stack. These FWHM values were measured from unsaturated stellar images using `SExtractor` (Bertin & Arnouts, 1996). We clipped the FWHM distribution at $0\farcs3$ to filter out cosmic rays and bad pixels, and at $5''$ to filter out misclassified extended objects (e.g., H II or star-forming regions inside the galaxies of interest). These values, and the FWHM values of Moffat (1969) profiles as fitted using the task `imexamine` within IRAF, are consistent to within 2.5% with a dispersion of 9%. FWHM values could be measured for 124 (out of 131) ground-based images. For the remaining images that did not contain any unsaturated stars, the FWHM was estimated from the images taken closest in time that did. The mean (median) seeing over all ground-based images is $2\farcs04 \pm 0\farcs52$ ($2\farcs00 \pm 0\farcs52$) (1-σ). This rather large average image-FWHM is due to the majority of VATT images having a focus component in their PSF as a result of the rapid change of focus with temperature in this f/1 telescope (for details, see Taylor et al. 2002). Even with FWHM $\sim 2\farcs0$, these ground-based images are quite suitable for our current purpose of galaxy surface photometry in *UBVR*.

2.3.3. *Archival* HST *Images in Additional Filters*

Several of the galaxies in the present sample have been observed with *HST* in filters other than F300W and F255W, or with instruments other than WFPC2. Maoz et al. (1996), for example, imaged the central $22'' \times 22''$ in 110 nearby galaxies in the mid-UV (2300Å) using the Faint Object Camera (FOC). The red-leak in the FOC mid-UV filters, however, is more severe ($\sim$24%; Keel & Windhorst 1993) than that in the WFPC2 filters ($\simeq$ 5–7%; see §2.4.3), and the FOV is much smaller. Sixteen of our objects have been observed in other WFPC2 filters before — generally in a heterogeneous mixture of filters: F170W (far-UV), F336W, F439W, F555W, F606W, F702W, and/or some additional F814W images. These data are summarized in Table 3. In the archival WFPC2 exposures, the galaxy nucleus was often placed in the

Planetary Camera (PC), which due to its smaller pixel size is less suited for accurate surface-photometry. Also, for galaxies $\sim 1'$ in extent, more of a galaxy tends to be lost outside WFPC2's FOV when its nucleus is placed in the PC. We will study these Archival WFPC2 images in the other filters, where appropriate, in future papers.

Where Archival NICMOS images in the F110M/F110W, F160W or F222M filters are available (GTO 7218, PI: Rieke, see e.g., Alonso-Herrero et al. 2000; GTO 7219, PI: Scoville, see Scoville et al. 2000; GO 7268, PI: van der Marel, see Ravindranath et al. 2001; SNAP 7328, PI: Malkan, see Quillen et al. 2001; SNAP 7330, PI: Mulchaey, see Regan & Mulchaey 1999) we use them in lieu of ground-based *JHK* data in Table 2 and Fig. 4.

2.4. *Calibration and Processing of the* HST *Observations*

2.4.1. *Standard Processing*

Standard WFPC2 CCD processing following Windhorst et al. (1994b, 1994c, 1998a), Driver et al. (1995a), Neuschaefer & Windhorst (1995), and Odewahn et al. (1996) included bias and dark-subtraction, and flat-fielding. Photometric calibration was done using the STSDAS On-The-Fly-Reduction (OTFR) routines as available since summer 2000. Custom calibration, in general, does not significantly improve upon the STScI WFPC2 pipeline, owing to the significant work that went into building and improving that pipeline. The OTFR takes into account the latest improvements in knowledge of the instrument every time one retrieves data from the *HST* Archive.

Because the mid-UV images have extremely low sky-background levels, the background subtraction is limited by the quality of the bias and dark current removal. It is therefore important that the very best possible biases and latest dark-current and hot-pixel maps are used. We paid close attention to whether the correct dark-frames were used when observations were taken near the monthly warm-up of WFPC2 (to decontaminate the optics and anneal many of the new hot-pixels). The OTFR uses the best available super-dark taken after the relevant science images, but before the next decontamination. Hence, it is conservative in nature — repairing more pixels than needed, but never too few. We re-ran the OTFR on all data one month after the last images for this project were taken (in April 2001) to incorporate the latest knowledge on the WFPC2 data. The difference between this second run and the first was very small, but went in the direction of removing a more appropriate (smaller) number of pixels deemed "hot".

We co-added all images in the same filter after registration using integer pixel shifts. Our in-house IDL routine `STCombine` (Pascarelle et al. 1998; Cohen et al. 2002) was used to optimally remove the signal induced by the many Cosmic-Ray (CR) hits. This routine, optimized for the low signal domain, applies a one-sided 2-σ rejection in creating the final stacked image (following Windhorst et al. 1994a).

2.4.2. *Achieved S/N in the WFPC2 Images*

The Zodiacal sky-background at the North Ecliptic Pole is $\sim$24.0 mag arcsec^{-2} in F300W (Windhorst et al. 1994b, 1998a) and $\sim$24.7 mag arcsec^{-2} in F255W (Cornett et al. 1994), and is as low in the sunlit part of the orbit as it is in the occulted part (unless the angle to the Earth's limb becomes small). Since our WFPC2 mid-UV images are read-noise limited, the resulting 1-orbit 1-σ SB-sensitivity is 25.1 ± 0.15 mag arcsec^{-2} in F300W and 23.0 ± 0.15 mag arcsec^{-2} in F255W on a per pixel basis. The relation between the detected SB-level and the S/N in a pixel is given by: S/N = $10^{-0.4\,(\mu_{F300W}-25.1)}$ and S/N = $10^{-0.4\,(\mu_{F255W}-23.0)}$ for F300W and F255W, respectively. These mid-UV SB-limits are consistent with the values expected from the Cycle 5–6 images in F410M and F450W (Pascarelle et al. 1996, Odewahn et al. 1996, Windhorst et al. 1998a) and the relatively red color of the zodiacal sky-background. Taking into the account the $(1+z)^4$ SB-dimming and the typical $(U-I)$ color of galaxies at $z \simeq 1$–2, the SB-sensitivity reached in the present data matches that achieved for typical faint $I \lesssim 26$ galaxies seen in deep *HST* images.

The 1-orbit 3-σ point source sensitivity is 26.4 ± 0.15 mag in F300W and $\sim$24.5 mag in F255W. Hence, many of the galaxies in our sample are resolved into their brightest star-forming regions and — most likely — into their OB associations and young star clusters. This is not true, however, for most of the merging/interacting galaxies that were selected into our sample from the sample of Hibbard et al. (2002). Because these systems are relatively rare, they tend to be 2–3 times more distant than the bulk of our sample (see Table 1, Col. 14), and so are not resolved into stars.

2.4.3. *Red-leak*

The F300W filter has a significant red-leak, causing a fraction of an object's flux longward of 4000Å to be detected in this mid-UV filter. Fig. 3.10 of the WFPC2 Handbook (Biretta et al. 2001) shows that red-leak portion of the $QE \times T$ curve of the F300W filter resembles the throughput curve of the F814W filter which transmits mostly photons in the 7000–9000Å range. Table 3.13 of the WFPC2 handbook suggests that the red-leak is generally no more than 5% of the total F300W flux for stellar populations dominated by stars of spectral type K3V or earlier, although it can be as much as 10–50% of the total F300W flux for stellar populations dominated by M0–M8V stars. Hence, even for elliptical galaxies with K-star spectra, the red-leak is expected to be relatively small, and for late-type galaxies dominated by young hot stellar populations it should be almost negligible.

For realistic galaxy SEDs, Eskridge et al. (2002a) find that the red-leak is typically 5–7% of the total F300W flux, and never exceeds 10% of the F300W flux, not even in the reddest galaxy bulges. We verified this for several red galaxies in our sample by subtracting a fraction of the F814W images from the F300W images, after appropriately rescaling with the relative exposure time, and making sure both images were registered the same way. This fraction of the subtracted F814W image amounted to 7% of the total F300W flux in the brightest region of the galaxy bulge that is presumed to be dominated by G8-K3 stars (following the red-leak as modeled by Eskridge et al. 2002a).

We found that for the redder stellar populations in those images no noticeable additional structure was introduced in our F300W images at the locations of the brightest F814W flux. To illustrate this, a very red star is seen just above the center of both edge-on galaxies ESO033-G22 and IC 4394 in the F814W images of Fig. 3.19 and 3.20. For IC 4394, Fig. 4.20 shows how red this star is, where it is seen just South of the galaxy center. These stars are saturated in the F814W images of both galaxies, and at the corresponding locations in the (non-red-leak corrected) F300W images of Fig. 3.19–3.20, only a very faint red-leak flux is seen. These worst case examples show that the apparent F300W morphology of any of our galaxies would not be significantly affected by the red-leak in a few of the very reddest and brightest galaxy areas in the F814W images. Such areas would have to be significantly saturated in our F814W exposures

to generate significant red-leak in the F300W images, and none of our targeted galaxies were saturated anywhere in the F814W images. Hence, for the current qualitative presentation of the mid-UV images, and given that our sample is biased toward the bluer galaxies, we have thus not corrected the images presented in the mid-UV atlas of § 3 for the small contamination by red-leak in the brightest and reddest areas.

For accurate quantitative measurements of galaxy properties we will subtract the red-leak in future papers where necessary (e.g., Eskridge et al. 2002a). This will be done together with the determination of pixel-to-pixel SEDs for each galaxy, in case there are subtle dependencies of the red-leak on the red SED. However, to first order there should be no such dependency, since galaxies of all spectral types show remarkably little change in their relative SED's between 7000-9000Å.

2.4.4. *Data Archiving*

As we expect these data to be of use beyond the scope of our immediate science goals, we will make all images available to the community in digital form when this paper goes to press. We do this, even though the photometric zero-points for part of the ground-based images are not yet established. We will update the FITS headers as new photometry becomes available (see also Taylor et al. 2002). Hence, the FITS headers in the public data base will override any values currently listed in Table 2. The images will be made public via ADS and also at the following public Web-Site at ASU:

www.public.asu.edu/∼caburg/hstuband/newhstuband/

Both the *HST* and ground-based data will be made publicly available at this site. The raw WFPC2 data can be obtained from the *HST* Archive. Additional information regarding this survey and its planning, the observations, and reduction procedures can be found at:

www.public.asu.edu/∼asusco/research/uband/red1/

and at:

presto.stsci.edu/apsb/doc/pep/public-proposals/8645.prop

3. PRESENTATION OF THE WFPC2 MID-UV IMAGES

In this section, we describe the *HST*/WFPC2 images and discuss each individual object in the sample. In view of the large volume of the combined ground- plus space-based data set, we opted to only present the Cycle 9 *HST*/WFPC2 images in the printed version of the present paper (Figs. 3). The electronic version contains the full "pan-chromatic atlas of nearby galaxies", that include *UIT* and ground-based $UBVR(I)$ and JHK images, wherever available. Of these, we show in the printed version a few example pages (Figs. 4) to clarify the adopted format.

The galaxies are presented roughly in order of their observed morphological type. We start with the regular early-type galaxies in § 3.01–3.03 (and correspondingly numbered figures Figs. 3.01–3.03 and 4.01–4.03). Subsequent sections present early-type galaxies with significant AGN in the mid-UV (§ 3.04–3.06), and merger products which are likely to evolve into early-type remnants (§ 3.07–3.09). Next, we discuss early- through mid-type spiral galaxies showing spiral structure in the mid-UV (§ 3.10), grand design spirals (§ 3.11–3.14), a spiral with an inner ring (§ 3.15), and edge-on spiral galaxies (§ 3.16–3.20). We discuss the late-type- and dwarf spiral galaxies in § 3.21–3.27, and the Magellanic Irregulars in § 3.27–3.33. We finish with the peculiar galaxies and merging/interacting systems (§ 3.34–3.38).

Although they are not part of the selected sample, other galaxies that appear within the WFPC2 FOV will be discussed below (including their types), in context with the targeted galaxies of similar morphological type. In a few cases, our *HST* and ground-based images show the type listed in the RC3 to be incorrect, for various reasons explained below.

Most of our Cycle 9 mid-UV galaxies, except for some of their outskirts, fit inside a single WFPC2 CCD, and so the current paper shows only a single WFPC2 CCD in most Figures 3.nn–4.nn. However, a few edge-on galaxies are too large to fit on a single WFPC2 CCD. For these galaxies, the relevant parts of a full WFPC2 CCD *mosaic* are therefore shown instead in the current paper (see UGC 10043 in Fig. 3.16). Since the number of pixels we can display in this manner on one ApJ page does not do full justice to the high quality of the WFPC2 data, we will display in a sequel paper (Odewahn et al. 2002b) the multi-color WFPC2 mosaics in full-page size for the two remaining large edge-on galaxies (i.e., ESO 033−G022 in Fig. 3.19 and IC 4394 in Fig. 3.20) and possibly for a few other large objects, as needed. This sequel paper will dither all WFPC2 mosaics for our sample of 37 objects, and do a detailed sky-subtraction across the CCD's, which is needed for reliable determination of the mosaic-wide multi-color light-profiles, as well as the subsequent quantitative analysis. This paper will thus show a few additional images not shown in the current paper.

The *HST* images, in general, have a very high dynamic range. This makes it difficult to properly display the full range of structures within a galaxy. Each of the grey-scale renditions in the atlas is displayed using an inverse logarithmic stretch with lower and upper display limits approximately equal to the sky-background (*displayed as white*) and the 3 times the maximum data value in the galaxies' brightest parts (*black*). This compromise allows one to discern individual high-SB structures within a galaxy while still being able to see much of the faint outer parts within a galaxy. The two unexposed edges of each WFPC2 image allow one to trace the total $80'' \times 80''$ ($75'' \times 75''$ useful) FOV of a WFC CCD. When a galaxy is much smaller than the WFC FOV, or when there is too much morphological information contained within a single WFPC2 CCD, we (also) present the relevant portion of that CCD-frame, but enlarged by a factor of 2 or 4 (i.e., a $37'' \times 37''$ or $19'' \times 19''$ FOV).

The ground-based images (in Figs. 4) tend to have a much smaller dynamic range (because of the much higher sky-background and lower resolution). Nonetheless, we use a similarly defined stretch and display limits. Often, the extent of a galaxy becomes more obvious in these ground-based images than in the mid-UV images. In Figs. 4.01–4.38 all images are displayed on the same angular scale and at the same orientation, with North up and East to the left.

MID-UV–FAINT EARLY-TYPE GALAXIES:

3.01 CGCG 097–094 (T=−5; E) An early-type galaxy in Abell 1367 that is faint in the mid-UV compared to F814W. CGCG 097−094 was observed in the field of primary target MCG+03−30−071. Other cluster members are also visible (Figs. 3.01 and 4.01): the edge-on galaxy is still visible in F300W, suggesting that, despite its dust content, it still transmits some light at 2930Å. Most of this UV light may come just from the near edge of the disk (the side facing us). MCG+03−30−071 itself is discussed in § 3.21, and edge-on galaxies are discussed further in § 3.16–3.20 below.

The vertical image flaws (faint streaks) in the F300W image are due to WFPC2 Charge Transfer Efficiency (CTE) effects, the severity of which has significantly increased over the past years.

They are visible in the high contrast stretches that were needed to show the fainter features of this and other objects in the atlas.

3.02 NGC 1396 (T=–3; S0–) A lenticular galaxy that is faint in the mid-UV compared to F814W, indicative of an old stellar population. It has a weak nuclear point source. NGC 1396 is not detected at 150 nm in the *UIT* far-UV image of its bright neighbor NGC 1399, and is at best barely visible in the 250 nm *UIT* image. We do not have ground-based images as yet for this galaxy, and so substitute SERC IIIaJ and POSS-II IIIaF plate scans for the *B* and *R* images, respectively.

3.03 NGC 4478 (T=–5; E) An elliptical galaxy that is faint in the mid-UV compared to F814W, although comparatively not as faint in F300W as some of the other early-type galaxies discussed. NGC 4478 is one of the giant ellipticals in the Virgo cluster, many of which have a UV-upturn in their far-UV spectrum (Burstein et al. 1988). This UV-upturn population is expected to be mostly visible below 2000Å and contributes less than 3–30%, and in most cases less than 10% of the total light at 2930Å (see Figs. 6–7 of Burstein et al. 1988). Another point source is seen just below the nucleus. It is very bright at F300W and in the *UIT* 250 nm image, and is likely a blue foreground star.

EARLY-TYPE GALAXIES WITH SIGNIFICANT AGN EMISSION IN THE MID-UV:

3.04 NGC 3516 (T=–2; S0) NGC 3516 is a well known classical Seyfert 1 galaxy (Seyfert 1943; Khachikian 1974; Keel & Weedman 1978; Kent 1985; Filippenko, 1985) that becomes essentially a point source in the *HST* mid-UV images. The AGN-dominated F300W image shows a strong central point source exhibiting diffraction spikes. A faint extension is seen in this filter, but not in F255W. The faint fuzz seen around the central point-source in the 150 nm UIT image is likely due in a significant part to the PSF caused by the far-UV optics plus photographic film of the *UIT* camera. The ground-based and F814W images show a faint bar with a position angle PA $\simeq -17°$. NGC 3516 has a companion galaxy with a small velocity difference (Keel 1996). It is also a well-known radio- and X-ray source (e.g., Taylor et al. 1996; White & Becker 1992; Laurent-Muehleisen 1997; Perlman et al. 1998; Radecke 1997), and is a low-luminosity AGN with the jet pointing close to the line-of-sight to the observer. Quantitative PSF-fits of all these AGN dominated objects will be given by Odewahn et al. (2002, in prep.), in conjunction with the *HST*+ground-based light-profiles for all our Cycle 9 sample.

3.05 UGC 03426 (a.k.a. Mrk 3; T=–2; S0) An early-type Seyfert 2 galaxy with a blue, nuclear "disk-like" feature that may be associated with a bipolar outflow (Ruiz et al. 2001) rather than a nuclear star-forming disk. The feature is oriented roughly perpendicular to the galaxy major axis in F814W and is visible in both F300W and F255W. Note the apparent change in galaxy position angle blueward of the B filter in Fig. 4.05.

3.06 UGC 08823 (a.k.a. Mrk 279; T=–2; S0) An early-type galaxy that becomes essentially a point source in the mid-UV. Note that almost no extended light is seen in F300W compared to F814W. It appears to be interacting with its neighbor MCG+12–13–024, with which it forms a physical pair (Keel 1996). It is a well known Seyfert 1 galaxy (Khachikian 1974; Osterbrock, 1977). For a high-resolution optical study of this object we refer the reader to Knapen, Shlosman, & Peletier (2000).

EARLY-TYPE GALAXIES WITH EVIDENCE FOR RECENT MERGING OR STRONG INTERACTION:

The next three systems (sections 3.07–3.09) include morphologically peculiar objects with single stellar systems. We discuss these objects here, at the end of the sequence of early-types, because they will likely evolve into early-types on relatively short time scales ($\lesssim$ 1 Gyr; see Barnes & Hernquist 1992), and likely already have developed $r^{1/4}$ profiles in their inner parts (e.g., van Albada 1982, Windhorst et al. 1994b, 1998). Earlier stage interactions — in which the two galaxies are still separated — are discussed at the end of the sequence (sections 3.33–4.38), after the Spirals and Irregulars, since at high redshift such objects are more likely seen as interacting galaxies or peculiars.

3.07 NGC 3921 (a.k.a. Arp 224, Mrk 430, UGC 08823; T=0; S0a) NGC 3921 is a disturbed early-type galaxy with a blue nuclear region which is visible in F300W. This object is a well-studied merger remnant (Schweizer 1996, Yun & Hibbard 2001a), and was probably produced by the merger of a gas-rich and gas-poor progenitor (Hibbard & van Gorkom 1996, Schweizer et al. 1996). It lies near the end of the Toomre Sequence of on-going mergers (Toomre 1977), and represents the final stage of merging, where there is a single nucleus but multiple tidal features. It will likely evolve into an elliptical galaxy (Schweizer 1996, Hibbard & Yun 1999a). The ground-based images in Fig. 4.07 show the fainter debris beyond the nuclear regions, including remaining tidal features. The near-IR images show a "wake" to the North of the bulge — possibly also a tidal feature from the same merger.

3.08 UGC 05101 (T=11; Pec) This object is very faint in F300W and is not detected in F255W. The F814W images show that it has an inclined dusty disk. This object is an Ultra-Luminous Infrared Galaxy (ULIG) with $L_{\rm IR} \gtrsim 10^{12} L_\odot$ (Sanders et al. 1988). Like NGC 3921, it appears to be a late stage merger remnant, with a single nucleus (Scoville et al. 2000) and multiple extended tidal features seen at larger scales in the ground-based images, including a tidal tail and a loop or polar ring-like structure (Sanders et al. 1988; Surace, Sanders & Evans 2000). The latter authors explain the large scale morphology as resulting from a "plunging" collision at non-zero impact parameter of two highly inclined disks.

Structures like these are typical for a merger in progress. The tails are thought to evolve on time-scales of >1 Gyr while, once the halos overlap, the galaxy nuclei evolve on much shorter time-scales (of order 100 Myr). This results in one visible tidal tail per progenitor disk, while the other side of the disk gets pulled into a "bridge" before it disperses. A dusty disk, such as seen in UGC 05101, is a common feature of gas-rich merger remnants, e.g., NGC 2623 (Bryant & Scoville 1999), NGC 3256 (Zepf et al. 1999), NGC 7252 (Wang, Schweizer & Scoville 1992; Whitmore et al. 1993), and Mrk 273 and NGC 3310 (this paper). Disks have recently been reproduced in numerical simulations of merging galaxies (Naab & Burkert 2001; Barnes 2002), and hence their presence does not rule out a major merger origin, as was once thought.

3.09 UGC 08696 (a.k.a. Mrk 273, VV 851; T=11; Pec) This object is faint in F300W and barely detected in F255W. The F300W morphology is very similar to the U' morphology presented in Surace & Sanders (2000). It appears to have a dusty disk, visible on one side of the nucleus in F814W. It is a merger product, as attested to by the tidal tail evident in F814W and in the ground-based images (Fig. 4.09). The horizontal streak in the ground-based R-band image is due to a bright star outside the FOV. Like UGC 05101, this system is a well known and well studied ULIG. But unlike the previous two systems, radio and near-IR imaging

reveal two distinct nuclei separated by 1″ (Majewski et al. 1993; Knapen et al. 1997; Scoville et al. 2000). One of the near-IR and radio nuclei coincides with the brightest peak in the F300W image, but the second near-IR nucleus is obscured, even at F814W. The southern peak in the F300W image has no optical or near-IR counterpart, and is probably a very young star cluster (Surace & Sanders 2000). CO-line mapping reveals the presence of two orthogonal kinematic components (Yun & Scoville 1995; Downes & Solomon 1998), suggesting a highly inclined encounter between two gas-rich system.

EARLY-TYPE GALAXIES DISPLAYING SPIRAL STRUCTURE IN THE MID-UV:

3.10 NGC 2551 (T=0.2; S0a) An early-type spiral galaxy, whose spiral structure is much more pronounced in F300W than in F814W. In the optical/red, the galaxy would be classified as an S0a, in the mid-UV as an Scd, so its morphological K-correction is significant. NGC 2551's bulge is faint in the mid-UV compared to F814W, although it seems bluer than that of other early-type spirals. The background galaxy seen in F814W does not appear in F300W, but this does not necessarily mean that the disk of NGC 2551 is very dusty at this location — the background galaxy may just be as red as some of the other field galaxies seen in the background of our other images (we chose the exposure times in F300W and F814W to provide relatively high S/N for nearby galaxies, not for higher redshift ones). Fig. 4.10 shows that NGC 2551 was also detected with *UIT* at 250 nm, but probably not at 150 nm. The *UIT* resolution (FWHM $\sim 3''$) is much lower than *HST*'s, but on large scales, the *UIT* 250 nm morphology is comparable to our *HST* F300W image.

GRAND-DESIGN SPIRAL GALAXIES:

3.11 NGC 6753 (T=3; Sb) Grand-design spiral galaxy with very pronounced spiral structure in both F814W and F300W. Dust-lanes are visible crossing the spiral arms in F814W, corresponding to regions of reduced or no light in F300W. A detailed discussion of the *HST* images of this object is given by Eskridge et al. (2002a). An enlargement of Fig. 3.11*a* is shown in Fig. 3.11*b*. In addition to dust lanes crossing the spiral arms in a regular pattern and with a fairly constant pitch angle, there is a large dust-lane crossing the inner spiral arms under a significantly different pitch angle, best seen in the F814W image. This is likely a foreground trail of dust (see also § 3.38). Fig. 4.11 shows that the morphological K-correction is modest from F300W through the *I*-band, although in the near-IR the object appears to be of earlier type in ground-based seeing.

3.12 NGC 7769 (a.k.a. Mrk 9005; T=3; Sb) Grand-design spiral galaxy with very significant spiral structure in F300W, which is more pronounced than that seen in F814W, suggesting active star-formation. In the optical/red, the galaxy would be classified as an Sb, in the mid-UV as an Scd, so its morphological K-correction is significant. The enlargement in Fig. 3.12*b* shows dust-lanes crossing the spiral arms in F814W, corresponding to regions of reduced or no light in F300W. The object also shows a faint nuclear dust-lane crossing its small bulge. NGC 7769 is interacting with SBa galaxy NGC 7771. H I mapping observations by Nordgren et al. (1997) show NGC 7771 to have an extended gaseous tail, while NGC 7769 counter-rotates with respect to NGC 7771. Therefore, this is thought to be a prograde-retrograde encounter, with NGC 7769 having retrograde kinematics. Note the possible emergence of a bar in the ground-based near-IR *J* and *H*-band images.

3.13 NGC 3310 (a.k.a. Arp 217, VV 356; T=4; Sbc) This mid-type spiral galaxy is well-known to harbor a substantial global star-burst, likely either the remnant of a merger or a significant accretion event (Balick & Heckman 1981; Mulder, van Driel, & Braine 1995; Smith et al. 1996b; Kregel & Sancisi 2001; and references therein). Intense star formation is readily visible in the nuclear ring (Conselice et al. 2000), the spiral arms, and linear "arrow" feature (e.g., Mulder & van Driel 1996). H I mapping of this object shows extended H I tails (Kregel & Sancisi 2001), and it is likely that the spiral "arms" do not lie in a single plane. As a result of the global star-burst, the morphology of NGC 3310 remains similar in the F300W and F814W images. Some differences in structure between the red and mid-UV result from dust features, however. The enlargement in Fig. 3.13*b* shows that the galaxy nucleus appears displaced from the line of symmetry of the inner spiral arms. Fig. 3.13*b* also shows a small nuclear dust-lane crossing its small bulge, and dust-lanes crossing the spiral arms (some at significant pitch-angles) in F814W, corresponding to regions of reduced or no light in F300W.

The ground-based images in Fig. 4.13 show that the outer spiral arms are more complicated, and appear to dissolve in the southern part at all wavelengths. The far-UV morphology of NGC 3310 at *UIT* spatial resolution (Smith et al. 1996b) is also shown for comparison. This is an example of a galaxy that looks rather similar in all filters from the far-UV through the red.

3.14 NGC 7685 (T=5.3; Sc) Barred late-type spiral with significant spiral structure in F300W and F814W. A small bar and nuclear bulge are visible in F814W. The bulge appears to be bisected by a small nuclear dust lane. Fig. 4.14 shows that the morphological K-correction is modest from F300W through the *K*-band.

SPIRAL GALAXIES WITH INNER RINGS:

3.15 NGC 6782 (T=0.8; Sa) Early-type spiral galaxy with a spectacular ring structure in the mid-UV, visible in both F300W and F255W. An enlargement of Fig. 3.15*a* is shown in Fig. 3.15*b*. This ring is surrounded by two faint and apparently partially dusty spiral arms as visible in F814W, and an outer spiral structure and outer ring that is visible in F300W and in the optical pass-bands (Fig. 4.15). The inner ring appears to be driven by a small bar visible in F814W and F300W at PA $= -30°$. The ground-based images in Fig. 4.15 show that the outer ring encloses an outer bar, with a position angle (PA $\simeq 0°$) that differs from that of the inner bar visible in the *HST* images. A detailed discussion of the *HST* images of this object is given by Eskridge et al. (2002a). In depth studies of galaxies with such star-forming rings are given by Buta et al. (e.g., 1996, 1998ab, 2000, 2001). Fig. 4.15 suggests a significant morphological K-correction from F255W through the *K*-band, most of which is caused by the ring, but with the bars being more prevalent at the longer wavelengths, as noticed in the ground-based near-IR study of Eskridge et al. (2000).

EDGE-ON SPIRAL GALAXIES:

Here, we discuss edge-on galaxies as a single morphological class to allow easier comparison, despite the fact that their intrinsic T-types may span most of the Hubble sequence.

3.16 UGC 10043 (T=4.0; Sbc pec) An edge-on spiral galaxy that is faint in F300W, although it is still visible in this filter almost throughout the entire disk. The central bulge is relatively small in size and faint in the mid-UV, as for most of the other edge-on galaxies in our sample. The PA of the (major axis of the) bulge is approximately perpendicular to that of the disk,

which is most clearly seen in the *HST* observations when compared to the ground-based images (Fig. 4.16). This may indicate a polar ring, which interpretation we hope to confirm with spectroscopy in a future paper. The F814W images show significant dust lanes, mostly in the inner parts of the edge-on disk. Compared to F814W, the F300W flux shines through better in the outskirts than in the central part of the disk, and in particular, it shines through well in several bright knots. It is also possible that, instead, the knots visible in the mid-UV are in front of most of the dust.

Qualitatively, it appears that the dust extinction — if this relative dimming of the UV-light is indeed due to dust extinction — decreases from the inside outwards (see also Jansen et al. 1994). Examples of these edge-on objects have been studied in the optical by de Grijs (1999). In the mid-UV, edge-on disk galaxies have a large range in brightness. Some are particularly bright in the UV (e.g., UGC 06697, Marcum et al. 2001; NGC 4631, Smith et al. 2001), while others are much fainter, such as some of the edge-on galaxies shown in the current paper. As pointed out by Kuchinski et al. (2001), it is as yet unclear to which degree dust attenuation affects the appearance of highly inclined galaxies at UV wavelengths. This is due to a likely complex dependence on the distribution of dust and actively star-forming regions throughout a galactic disk (Kuchinski et al. 2001). Due to the lack of a statistically significant population of edge-on galaxies observed in mid-UV light, a detailed discussion of this effect is beyond the scope of the present paper, but will be addressed in a future paper when more edge-on objects have been observed in the mid-UV.

3.17 UGC 06697 (T=10; Im) Late-type edge-on galaxy with almost no bulge and with significant dust-lanes seen by comparing F300W to F814W. Although this galaxy is bright in the UV and was observed both at 2500Å and 1500Å by *UIT*, comparison of the F300W and F814W images shows that several regions seem to be completely obscured by dust. They appear to be dust pockets that bisect the disk. The ground-based images in Fig. 4.17 show a significant warp on larger scales, which is possibly related to the two or three companion galaxies visible within the FOV. On balance, though, the overall appearance of this object is very similar from the far-UV through F814W.

3.18 IC 3949 (T=–2; S0 pec) Edge-on spiral with a very faint bulge, if any, and significant dust-lanes (compare the F300W and F814W image), especially in the lower (western) part of the displayed image. The plane of the dust appears to be warped, and asymmetric in the western part of the image compared to the upper (eastern) part. The biggest dust pocket to the lower right of the center is also visible as a depression in the light in the ground-based *UBVR* images (Fig. 4.18).

Four faint edge-on galaxies are seen to the left of IC 3949 in F814W (Fig. 3.18*a*), two of which are barely visible in F300W. It is perhaps noteworthy that all four of these highly inclined galaxies point their major axis towards the central part of IC 3949. Although this is probably a chance alignment and the edge-on galaxies are probably background galaxies, it would be interesting to test this hypothesis with further kinematic data. If these systems turn out to be at a similar distance as IC 3949, they might be smaller dwarf-like objects falling into IC 3949, perhaps disturbing its disk as the irregularly distributed edge-on dust-lanes might suggest. Schwarzkopf & Dettmar (2000) found that edge-on galaxies have on average 60% thicker disks and are $\sim 2\times$ more likely to have warps when they have low mass companions, which will likely soon result in minor mergers.

Fig. 3.18*b* shows other early-type objects surrounding IC 3949, which, like other early-type galaxies in our *HST* sample, have dim light distributions in F300W. The RC3 incorrectly classifies IC 3949 as S0 pec, which may be due to confusion with the brighter of these early-type galaxies, although this object is fainter than the edge-on galaxy. These objects were selected as field ellipticals and do not show AGN in the UV (unlike the others in our sample), although the two brightest ones show a small central disk or boxy isophotal structure.

3.19 ESO 033–G022 (T=7; Sd) Edge-on late-type spiral galaxy that is faint in F300W, although it is still barely visible in this filter throughout most of the disk. There is almost no central bulge. The F814W images show a thin dust lane in the plane of the galaxy, mostly in the inner parts of the edge-on disk. Compared to F814W, the F300W flux shines through better in the outskirts than in the central part of the disk, and in particular shines through well in several bright knots. In the ground-based images for this low Galactic latitude object from de Grijs, Peletier & van der Kruit (1997) (see Fig. 4.19), the bright stars (which are apparent in the F814W *HST* image) have been removed to allow for more accurate surface photometry.

3.20 IC 4394 (a.k.a. ESO 446–G044; T=6; Scd) Edge-on spiral galaxy that shows a thick dust lane in the plane of the galaxy in F814W, mostly in the inner parts of the edge-on disk. This galaxy is fainter in F300W than F814W as well, but comparatively not nearly as much as most of the other edge-on galaxies. This could be because its inclination is not as close to 90° as some of the others, allowing a more unimpeded view of the bright star forming regions located on the near side of the galaxy plane. Hence, the relative bright appearance in F300W does not imply a smaller dust content than inferred in other edge-ons. Almost no central bulge is visible. Compared to F814W, the F300W flux shines through better in the outskirts than in the central parts of the disk, and in particular in several bright knots, more so than seen in the other galaxies.

LATE-TYPE SPIRALS AND SMALLER SPIRALS:

3.21 MCG+03–30–071 (T=10; Im) Small late-type spiral galaxy in Abell 1367, displaying a four-armed spiral pattern that dissolves into individual star forming knots in F300W. MCG+03–30–071 was detected by *UIT* both at 1500Å and at 2500Å. There are several galaxies at small projected distances to this galaxy, but the smallest difference in velocity is 715 km s^{-1} (for the early-type neighbor $\sim 40''$ to the SW, MCG+03–30–067, which is also visible in the FOV). Comparing these two galaxies from the far–UV to F814W gives the best example of the general trends observed in this work (see the discussion in § 4).

3.22 MCG+06–24–047 (T=4; SBc) Small spiral galaxy with well-developed spiral structure that is more pronounced in F300W, although still clearly visible in F814W. The classification in the RC3 as T=11/Pec probably resulted from the bright foreground star $\sim 7''$ south of the nucleus. In the mid-UV this galaxy would be classified as a Sd/Irr rather than SBc, so the morphological K-correction is non-zero. The ground-based *UBVR* images (Fig. 4.22) show a rather modest dependence of the amplitude of the spiral structure on rest-frame wavelength, so most of the morphological K-correction is caused by the stellar population below the Balmer break. A small bulge is visible in F814W. The bright star is blue (it is even marginally detected at 1500Å), so that the F300W appearance is not significantly affected by the filters' red-leak.

3.23 UGC 05028/29 (a.k.a. Arp 300, VV 106; T=3+9;

Sbc+SBdm/Pec) Fig. 3.23*a* shows the small late-type/peculiar spiral galaxy UGC 05028 (Mrk 111) of the pair Arp 300 (see Fig. 4.23). It has spiral structure that is more pronounced in F300W although still clearly visible in F814W. Ground-based seeing hides most of the irregular nature of this object. No bulge is visible in F814W, although a small central bar-like structure is visible in both filters. The brightest "knot" in F300W and particularly in F814W, south of the center, is well resolved. Although reddening by dust plays a significant role, this "knot" may be the remnant of another small late-type galaxy that is merging with UGC 05028, as its color is similar to that of the small bulge of UGC 05028's larger companion UGC 05029. If so, this knot and the bar will eventually merge and form a central bulge. As presently observed UGC 05028 is extremely asymmetric.

Fig. 3.23*b* shows the second member of the Arp 300 system, Sbc spiral galaxy UGC 05029, which is a physical companion to UGC 05028. The spiral structure in this galaxy is more pronounced in F300W, although it is clearly also visible in F814W, like for some of the other early–mid type spirals discussed above (e.g., NGC 2551). Most of the blue OB associations are located on the side facing UGC 05028. Another edge-on field galaxy is seen in Fig. 4.23, but is too faint to be resolved into star-forming regions. The five rather red objects between this edge-on galaxy and the bright mid-type spiral are likely a group of background galaxies — they are not seen in F300W at all (see the discussion of other background objects above).

3.24 NGC 3860B (a.k.a. CGCG 97−114; T=10; Im) Small late-type spiral galaxy with spiral structure that is more pronounced in F300W, although it is still visible in F814W. Its rather late classification probably resulted from the fact that the spiral structure is only barely visible in the ground-based images. The *UIT*, *HST* and ground-based images show only a modest dependence of morphology on rest-frame wavelength. A very small bulge is visible in F814W (Fig. 3.24).

3.25 ESO 418–G008 (T=8; Sdm) Small late-type spiral galaxy that is resolved in at least its brighter star-forming regions (Fig. 3.25), which are mostly distributed along its outer perimeter, and perhaps constitute the beginning of spiral structure. The F814W image also suggests a faint bar running along the minor axis that may be connected to this spiral structure. The *B* and *V* images of Matthews & Gallagher (1997) show that ESO 418−G008 has a bright, prominent bar (see also Fig. 4.25). A faint low-SB structure is visible in F814W that is spread more smoothly throughout the galaxy, presumably its unresolved older stellar population. A color map made from our *HST* data (oposite.stsci.edu/pubinfo/pr/2001/04/) reveals a very faint red nucleus. Such compact nuclei are common features of extreme late-type spirals (Matthews & Gallagher 1997; Matthews et al. 1999; Böker et al. 2002). The nucleus of ESO 418-G008 was not previously visible in ground-based images (Matthews & Gallagher 1997), but Böker et al. (2002) have recently imaged it in the $F814W$ filter with the WFPC2 PC. They measure $M_I = -10.24$ mag, assuming a distance of 14.1 Mpc.

The galaxy appears to have sharp "edges" in both filters, but this may be largely a visual impression caused by the single star-forming region to the lower left (north) in Fig. 3.25. The ground-based *UBVR* images show similarly an outer spiral-like structure that becomes less and an inner bar that becomes more pronounced at longer wavelengths. A late-type galaxy with a modest morphological K-correction.

3.26 NGC 1510 (T=-2.3; S0 pec) Small blue, amorphous galaxy (Eichendorf & Nieto 1984). NGC 1510 is a physical companion to the much larger SB galaxy NGC 1512, with which it is interacting (Hawarden et al. 1979). The early-type classification in the RC3 probably resulted from ground-based seeing hiding most of the irregular nature of this object. No clear bulge is visible. NGC 1510 has fairly similar appearance in F814W and F300W, but the F814W image shows more of a diffuse component, while the F300W resembles more a disk-like component seen edge-on, and shows some linear dust features. The object is resolved in at least its brighter star-forming regions. Scans of ground-based photographic plates in *B* (from Lauberts & Valentijn 1989, as obtained through NED) and in R_F (from the second generation Digital Sky Survey) are substituted for CCD images in Fig. 4.26.

MAGELLANIC IRREGULARS:

3.27 NGC 5253 (a.k.a. Haro 10; T=10; Im) NGC 5253 is a peculiar I0 galaxy or type II irregular. This object has a very similar appearance in F300W and F814W, and is clearly resolved into individual bright star-forming regions or stars. Table 1 shows that it is one of the closest galaxies in our sample. The dust lane that appears to emerge from one side of the center outwards is visible at all wavelengths, including in the lower-resolution ground-based *UBVR* images (Fig. 4.27). Overall, this object has a largely similar appearance from *UIT* 150 nm through the ground-based *K*-band, with some mild wavelength dependence modulations due to dust patches.

This object was first described after discovery of a nearby nova (Hubble & Lundmark, 1923; Payne-Gaposchkin, 1936). NGC 5253 is a a well studied nearby star-bursting galaxy at a distance of 4.1 Mpc (Sandage et al. 1994). It is typically classified as an amorphous or irregular galaxy, but has outer isophotes reminiscent of a dwarf elliptical (Sersic et al. 1972; Caldwell & Phillips 1989). It has a star-burst located at its center, with dozens of intense blue star forming clusters (Caldwell & Phillips 1989; Storchi-Bergmann et al. 1995; Calzetti et al. 1995). NGC 5253 also contains an unusual Hα morphology (Marlowe et al. 1995; Calzetti et al. 1995) with loops and filaments and a diffuse component that is at least partially produced from shocks (Calzetti et al. 1999).

Recent *HST* images in optical broad-band and line-emission show that this object is a small star-bursting galaxy (Beck et al. 1996; Calzetti et al. 1997, 1999; Gorjian, 1996). The galaxy was detected by IRAS (IRAS 13370-3123 in the IRAS Point Source Catalog; Beichman et al. 1988), and is a weak radio source in the Parkes-MIT-NRAO 4.85 GHz Survey (Wright et al. 1996), and also had a FAUST Far-UV point source 0.5′ from the galaxy (Bowyer et al. 1994). Other recent studies include a systematic H I study (Kobulnicky & Skillman 1995), radio observations of a star-bursting knot that has no optical counterpart (Turner et al. 1998, 2000), as well as a CO-map (Turner et al. 1997), ROSAT X-ray studies of multiple super-bubbles in its star-burst nucleus (Strickland 1999), and ISO observations of its hot stars and Wolf-Rayet like outflow (Crowther et al. 1999), amongst others.

Only 130 kpc away is the larger spiral galaxy NGC 5236 (M 83) which also experiences a star-burst in its nuclear regions. NGC 5253 has a large outer distribution of H I gas that could be feeding the central star-burst in M 83 (Kobulnicky & Skillman 1995). Also, the bar in M 83 might be triggering its central star-burst. However, there is evidence that the star-bursting properties in this system are produced in part by a dynamical interaction between the two objects (Caldwell & Phillips 1989).

3.28 NGC 1140 (a.k.a. Mrk 1063, VV 482; T=10; Im) Irregu-

lar galaxy. This object has a fairly similar appearance from the mid-UV through the *I*-band (Fig. 4.28). In F300W and F814W (Fig. 3.28) the object is resolved in at least its brighter star-forming regions. The "super star clusters" visible here were studied using *HST* optical-band imaging by Hunter, O'Connell, & Gallagher (1994). The larger field-of-view in the ground-based images also shows a trail of knots to the south-west, possibly an infalling dwarf companion.

3.29 UGC 05626 (T=10; Im) Irregular galaxy. The object is resolved in at least its brighter star-forming regions which are mostly draped around its edges as seen in F300W. The bluest and brightest star-forming knots to the left (north) are also visible in F255W. In F814W, the object also shows a faint low-SB structure which is spread more smoothly throughout the galaxy, presumably its unresolved older stellar population. No central bulge is visible at any wavelength. The structure in the ground-based *UBVR* images (Fig. 4.29) is similarly independent of wavelength, and shows the outer rings of knots, resembling the beginning of spiral structure. It is curious that such spiral structure would start before even a small central bulge or bar has formed, and leads one to wonder about the dark matter content of (the central parts of) this galaxy.

3.30 UGC 09855 (T=10; Im) Magellanic type irregular. The object is resolved in at least its brighter star-forming regions. The brightest of these regions are also visible in F255W. The F814W shows a faint central bulge that is not quite aligned with the geometrical center of the object (see also the ground-based images in Fig. 4.30, and the disk of UGC 05626 in § 3.29).

3.31 NGC 6789 (T=10; Im) Magellanic type irregular. The object is resolved in at least its brighter star-forming regions. The brightest ones of these are also (but barely so) visible in F255W. The structure in the ground-based *UBVR* images (Fig. 4.31) is rather independent of wavelength, and no central bulge is visible at any wavelength.

3.32 Mrk 66 (T=11; Pec) This object shows a significant number of blue star-forming knots, the one to the left (west) of the center (Fig. 3.31, F814W) may be part of a faint small bulge. The knots to the right (east) are isolated from the main object in both filters, and may be separated from the main body by a dust-lane or pocket, as is also seen in the ground-based images (Fig. 4.32). It is not clear whether this galaxy is a small linear object or a late-type galaxy seen edge-on.

The ground-based images provide some additional clues, since in all *UBVR* filters, a low-SB disk or halo is seen surrounding the rather linear structure seen in F300W. If this rounder feature were a halo, then Mrk 66 could be a tri-axial amorphous galaxy, although the fact that this feature is also visible in the ground-based *U*-band filter below the 4000Å-break would imply a rather young halo age of $\lesssim$ 1–2 Gyrs. Alternatively, if this rounder feature is a face-on disk, then the linear feature that is primarily visible in F300W could be a star-forming bar. In that case, the rounder feature would have to be a rather old disk ($\sim$1 Gyr), since no spiral arm structure is visible at the same location in the F300W image. Spatially resolved spectroscopy and kinematics will be necessary to distinguish between these possibilities.

In combination with the *HST* F300W and F814W images, the ground-based *UBVR* images confirm that, to first order, this object has little morphological K-correction, i.e., its appearance is rather similar at most wavelengths. However, significant SB-dimming at high redshifts could change a roundish object like Mrk 66 as seen in visible light into a more linear object in the mid-UV, and so help explain the appearance of some of the "chain" galaxies seen at high redshifts (Cowie, Hu, & Songaila 1995; see also Dalcanton & Shectman 1996).

3.33 UGC 05189 (a.k.a. VV 547; T=10; Im) Like Mrk 66, the *HST* images of this object show a significant number of blue star-forming knots. The ground-based *UBVR* images (Fig. 4.33) show that the arc imaged with WFPC2 is in fact part of a much larger, low-SB structure. This is clearly a very dynamically disturbed system. There is no obvious central bulge. In combination with the *HST* F300W and F814W images, the ground-based *UBVR* images confirm that this object has almost no morphological K-correction, i.e., its appearance is about the same at all wavelengths. Its light must be dominated by young hot stars throughout.

INTERACTING, PECULIAR, AND MERGING GALAXIES:

3.34 NGC 3690/IC 0694 (a.k.a. Arp 299, VV 118; T=9; Sm) Merger of two late-type disk galaxies. The object has a very similar morphology in F814W, F300W, and F255W, although the sensitivity in F255W is much reduced. Comparison of the F300W and F814W images reveals significant dust patches, most of which are irregularly distributed, as shown in the enlargements in Fig. 3.34*b*. This figure also shows the numerous young super star clusters spread throughout the system (e.g., Meurer et al. 1995).

The objects somewhat resemble the Antennae Galaxies (NGC 4038/39), but the encounter geometry is more complicated and the merger is slightly more advanced in Arp 299. H I and CO kinematics suggest a prograde-retrograde or prograde-polar encounter (Hibbard & Yun 1999b, Casoli et al. 1999). There are no obvious bulges in the mid-UV–optical images, but NIR imaging reveals a bulge in at least the easternmost system (Smith et al. 1996a), which is quite hidden by dust in all filters blueward of $\sim$1μm. Several of the bluest star-forming knots shine through clearly in F300W and F255W, although most of the galaxy shows significantly dusty regions, where such star-bursting knots would be much more reddened.

3.35 UGC 06527 (a.k.a. Arp 322, Mrk 176, VV 150, HCG 056; T=11; Pec) Spiral galaxy in a Hickson compact group that is undergoing a merger with at least one of its companions (e.g., Fasano & Bettoni 1994, Allam et al. 1996). Its spiral disk and arms are distorted into tidal tails because of this encounter, as also implied by UV+photographic numerical simulations of such events (e.g., Barnes & Hernquist 1992). When comparing F814W to F300W, the inner bulge shows a dusty inner disk-like structure. The galaxy is not resolved into its brightest star-forming regions or stars, due to its larger distance. The ground-based images in Fig. 4.35 suggests a small morphological K-correction, if any.

3.36 UGC 08335 (a.k.a. Arp 238, VV 250; T=4; Sbc) Two strongly interacting disk galaxies of approximately equal luminosity. Both disks are distorted during this encounter and display tidal tails (Fig. 4.36), suggesting a prograde-prograde encounter (e.g., Barnes & Hernquist 1992). The RC3 morphological type probably results from confusing the tidal arms with spiral structure or the two nuclei with a central bar (Fig. 4.36) in ground-based images. When comparing F814W to F300W, the inner bulges of both systems show significant dust-lanes, possibly from gas-rich material raised during the encounter. The system is too distant to be resolved into its brightest star-forming regions or stars.

3.37 IC 2184 (a.k.a. Mrk 8, VV 644; T=9; Sm) The "flying

V" is probably a merger of two disk galaxies seen nearly edge-on, as indicated by the presence of pronounced tidal tails in deep ground-based images (Gallagher et al. 2000). Star formation is active in most of both of the disks, and in the F255W image only the brightest star-forming knots are seen due to the reduced sensitivity of WFPC2 in this filter. Dust patches are visible in F814W, corresponding to reduced or no light in F300W and F255W at those locations. The ground-based *UBVR* images (Figs. 4.37) similarly show a very modest dependence of the morphology on rest-frame wavelength.

3.38 NGC 5278/79 (a.k.a. Arp 239, Mrk 271, VV 19; T=3; Sb) This is one of the most curious objects in our sample. Like UGC 08335, this system consists of two strongly interacting spiral galaxies. The encounter clear distorts both galaxy disks, resulting in tidal tails and exciting a strong $m = 1$ mode in the larger of the two galaxies, similar to features seen in numerical simulations of such events (Zeltwanger, Comins, & Lovelace, 2000; see also Phookun et al. 1992). When comparing F814W to F300W, both the inner bulges show significant dust-lanes. Part of the dust appears to be pulled out along with one of the spiral arms in the tidal encounter, possibly due to a shock related to this encounter.

Most remarkable is the very curved thin dust-lane, best seen in *R* and $F814W$, that drapes across the bigger galaxy. This dust-lane starts somewhere in the southern spiral arm of the bigger galaxy (upper or southern part in the WFPC2 CCD as shown in Fig. 3.38), curves all the way across the small nuclear bulge of this galaxy, and makes it into the spiral arm to the lower left that appears to connect to the smaller galaxy. Careful comparison of the F300W and F814W images shows that the dust-lane starts in what appears to be at least two funnel-like regions from the southern arm of the bigger galaxy. The dust in the southern arm appears to be distributed non-uniformly along the arm in several (3–4) sizeable "dust pockets or patches", which appear to merge into the dust lane and tidal tail that wraps around the bigger galaxy's nuclear bulge. A somewhat similar but much thinner dust trail was seen in *HST* images of the colliding nearby galaxy pair NGC 1409/1420 (Keel 2000), with material being pulled out between the two galaxies.

These "dust pockets or patches" are clearly visible in the data of the F300W images, and at the same location, the F255W images are entirely devoid of flux, leading credence to the conjecture that dust pockets cause these depressions in the light distribution. The "patches" are best seen by blinking the F255W, F300W, and F814W images in rapid succession, each displayed at an appropriate logarithmic stretch. The bluer ground-based images (Fig. 4.38) show a similarly diminished surface brightness at the location of the dust patches.

4. DISCUSSION OF GENERAL TRENDS IN THE WFPC2 MID-UV IMAGES

Here we discuss the sub-samples of each of the Hubble types separately. The light-profiles of all types will be presented in a subsequent paper in conjunction with the ground-based *UBVR*-profiles, after all the ground-based zero-points have been secured (see Table 2).

4.1. *Early-type Galaxies*

The regular early-type galaxies (elliptical and S0's) in our sample show in general a significant change in SB from the mid-UV to the red, reflecting an overall lack of a young stellar population (CGCG 097–094, NGC 1396, NGC 4478; sections 3.01–3.03). Typically, the μ_{F300W} of E/S0's is 3–5 mag arcsec^{-2} fainter than μ_{F814W}. As was also seen in the far-UV *UIT* sample of Marcum et al. (2001) and Kuchinski et al. (2000), they are dominated by an older stellar population, and so are generally faint in F300W. Out of 7 early-type galaxies imaged, two have small blue nuclear features (UGC 03426, NGC 3921; § 3.05 and 3.07). UGC 03426 is a Seyfert 2, and so this feature could be associated with a bi-polar outflow. The other, NGC 3921, is a well studied merger-remnant from the Toomre sequence, and the blue nuclear feature could indicate a location of residual star-formation that is only partially obscured by dust. Three early-type galaxies (NGC 1396, NGC 3516, and UGC 08823; § 3.02, 3.04, and 3.06) become dominated by point sources in the mid-UV, indicating weak optical-UV AGN, Seyfert, or LINER nuclei. While these are small number statistics, their presence in our current small sample of early-type galaxies is due to our selection of galaxies with high predicted average SB in the mid-UV within their effective (i.e., half-light) area (§ 2.2.3). This resulted in including a number of objects in our sample that are dominated in the *U*-band and mid-UV by AGN.

If AGN generally reside in bulge-dominated galaxies (e.g., Magorrian et al. 1998), then the red and old stellar population of the underlying early-type galaxies will be generally faint in the UV, but the presence of a (weak) AGN will result in blue $(U-B)$ colors and therefore a high SB the mid–near UV, and so inclusion into UV-selected samples. Similarly, ground-based U-band selected surveys would result in significant numbers of AGN in unrecognized early-type galaxies at moderate redshifts ($z \simeq 0.3$). At redshifts of a few tenths, the ground-based U-band selection would similarly show these objects essentially as point sources, just like some of the nearby early-type galaxies selected in our *HST* mid-UV sample. However, had these objects been selected at $z \simeq 0.3$ from the ground at much longer wavelengths (i.e., in the *I*-band), then they would still have shown up as early-type galaxies in images with good ground-based seeing. This leads us to wonder to what extent the (strong) cosmological evolution of AGN selected optically or through their near-UV excess at modest redshifts (Koo & Kron 1988; Boyle & Terlevich 1998; Boyle et al. 2000) could in part be due to a "morphological K-correction" of early-type galaxies with weak AGN. A further discussion of the galaxy light underlying low redshift QSO's is given by Bahcall, Kirhakos & Schneider (1995, 1996, 1997), Kirhakos et al. (1999) and Maoz et al. (1996), who determine the AGN components seen with WFPC2 in early—mid type galaxies.

Two more galaxies, UGC 05101 (§ 3.08) and UGC 08696 (§ 3.09), are tentatively placed in this section of early-type galaxies. These objects are merger remnants and have significant dusty disks in the mid-UV at present, but we believe they will soon evolve into early-type galaxies.

4.2. *Mid-type Spirals*

In general, spiral arms are more pronounced in the mid-UV, as *UIT* has shown to be generally true in the far-UV (Bohlin et al. 1991, Hill et al. 1992, Kuchinski et al. 2001, Marcum et al. 2001), but mid-type spirals and star-forming galaxies (e.g., NGC 6753 [§ 3.11] and NGC 3310 [§ 3.13]) appear more similar from the mid-UV to the optical than the early-type galaxies discussed above. However, several appear as later types in the mid-UV (e.g., NGC 7769; § 3.12), and a few show drastic changes in type from the optical to the mid-UV, equivalent to an apparent change in morphological type $\Delta T \gtrsim 3$ (e.g., NGC 2551 [§ 3.10] and NGC 7685 [§ 3.14]). One galaxy shows

a spectacular resonance ring full of hot stars (NGC 6782; § 3.15), while the remainder of the disk becomes essentially invisible in the mid-UV. This object is discussed in detail by Eskridge et al. (2002a).

We see a variation in color of the galaxy bulges/centers in the spirals, and a considerable range in scale and SB of the individual star-forming forming regions. Dust features in mid-type spirals can be well traced by comparing the F300W to the F814W images. Dust is visible in lanes or patches (possibly trailing spiral density wave patterns?), in pockets, and/or bubbles. A curious feature is that almost without exception, the mid-type spirals in our sample have their small nuclear bulges bisected by a dust-lane, which is often connected to the inner spiral arm structure. This is interesting in the context of the recent finding that all bulge-dominated systems have a central black-hole with an average black hole mass $M_{bh} \simeq 0.005 \times M_{bulge}$ (Magorrian et al. 1998). The small nuclear dust-lane seen by comparing the F814W and mid-UV images of almost all mid–late-type spiral galaxies in our sample may then be involved in feeding the inner accretion disk (which is not visible in our *HST* images).

Some edge-on galaxies are very faint in F300W when compared to F814W (UGC 10043 [§ 3.16] and ESO 033–G22 [§ 3.19]), others emit/transmit significantly more in F300W (UGC 06697 [§ 3.17] and IC 3949 [§ 3.18]), while IC 4393 (§ 3.20) is an intermediate case. All show a F300W/F814W ratio increasing from the inside out, as expected for a decreasing dust content from the inside out, and/or a strong radial gradient in the stellar population, if we assume that the dust and light sources are well mixed (i.e., the light sources are not preferentially located in front of most of the dust; see, e.g., Jansen et al. 1994; Witt & Gordon 1996; Kuchinski et al. 1998).

4.3. *Late-type Galaxies and Irregulars*

The late-type and irregular galaxies imaged are a heterogeneous mixture. The majority of these galaxies show a F300W morphology that is similar to that in F814W. Important differences are seen, however, due to recognizable dust-lanes or pockets blocking out F300W light (e.g., UGC 06697 [§ 3.17]; NGC 5253 [§ 3.27]; UGC 09855 [§ 3.30]; Mrk 66 [§ 3.32]; Arp 299 [§ 3.34]; IC 2184 [§ 3.37]). Dust is visible in pockets, holes or bubbles, perhaps due to supernova-induced outflows or outflows fueled by bright star-forming regions, such as seen in M 82 at *HST* resolution (de Grijs et al. 2001).

Some late-type galaxies are physically smaller galaxies with what appears to be the beginning of spiral structure (MCG+03–30–071 and MCG+06–24–047 [§ 3.21–3.22], UGC 05028 [§ 3.23], NGC 3860B [§ 3.24], ESO 418–G008 [§ 3.25], UGC 05626 [§ 3.29]). Others are Magellanic Irregulars (NGC 5253, NGC 1140 and NGC 1510 [§ 3.26–3.28], UGC 09855, NGC 6789, Mrk 66, and UGC 05189 [§ 3.30–3.33]) with various regions of stochastic star-formation. Star-formation "ridges" are commonly seen in the late-type galaxies, as well as hot stars or star-clusters that are particularly conspicuous in the mid-UV (F300W and/or F255W).

A few late-type galaxies would be classified significantly different when observed in the mid-UV than in the F814W passband (MCG+06–24–047 [§ 3.22], UGC 05626 [§ 3.29], UGC 09855 [§ 3.30]), especially when observed under less than perfect atmospheric seeing conditions. A quantitative discussion of the classification changes as a function of rest-frame wavelength will be given by Odewahn et al. (2002b).

4.4. *Peculiars and Mergers*

The majority of the peculiars and interacting galaxies (UGC 05189, Arp 299, UGC 06527, UGC 08335, IC 2184, and Arp 239 [§ 3.33–3.38]) show a F300W morphology that is similar to that in F814W. Several mergers have spectacular dust-lanes that thread along with the spiral arms, which are tidally distorted during the interaction (UGC 08335; Arp 239), while most others have absorption in apparently random locations associated with a star-burst.

The *HST* images are in general not sufficiently deep nor do they sample a sufficiently large area on the sky to capture the lower SB features (e.g., low-SB tails and other large tidal features, faint extended disks or halos) that are well imaged on the ground-based photographic plates which were originally used to classify these objects. The inner regions of these objects reveal a wealth of structure in the *HST* images, but often are almost entirely burned out or blurred on these ground-based images. The *HST* images do thus not necessarily reflect the distribution of the extended (evolved) stellar population. This is particularly true of the interacting systems, where tidal forces first and most easily affect the outer regions of the participants. Because interacting galaxies have both a disturbed distribution of old stars in their outskirts *and* an irregular distribution of dust and young star-forming regions in their inner parts, their peculiar morphology is maintained over a range of spatial scales and surface brightnesses. As such, the morphological K-corrections derived from this sample mostly apply to the high-SB inner regions of these galaxies. However, these *are* the appropriate morphological K-corrections to be applied to studies of high-redshift galaxies, where cosmological SB-dimming similarly selects the high-SB regions as do our short *HST* exposures.

More statistics are needed to cover all late-types, and the major dynamical stages of peculiars and mergers, as these are likely the dominant population at high redshift. We will pursue such objects further through an *HST* SNAP-shot program of late-type/irregular and peculiar galaxies in Cycle 10.

5. SUMMARY AND CONCLUSIONS

In order to delineate the morphology of galaxies as observed in their rest-frame mid-ultraviolet, we have carried out a systematic imaging survey with *HST*/WFPC2 of 37 nearby galaxies the *mid-UV* filter F300W (centered at 2930Å), as well as in the *I*-band (filter F814W centered at 8230Å). These mid-UV images will be useful to more reliably classify the numerous faint galaxy images seen with *HST* in deep *I*-band surveys at high redshifts ($z \simeq 1$–2). Eleven galaxies located in the *HST* Continuous Viewing Zone were also imaged in the F255W filter (centered at 2550Å).

Our sample is carefully selected for size and surface brightness, and included galaxies of small enough radius and high enough predicted mid-UV SB to be observable with *HST*/WFPC2 in one orbit. Together with 17 galaxies imaged in F300W available in the *HST* Archive, our survey covers a wide range of Hubble types and inclinations. Complementary data at other wavelengths are available for our galaxy sample: most objects have ground-based *UBVR* images, some have *IJHK* images, and 15 have far-UV images from the *Astro*/*UIT* missions. Mid-UV images (2000–3200Å) have been the missing ingredient thus far.

In summary, our mid-UV imaging data base shows that in galaxies where star-formation is sufficiently pronounced, it can dominate the morphology from the mid-UV though the optical,

resulting in very little change in morphology from the UV to the red. However, when stellar populations older than about 1 Gyr produce most of the optical light, we see changes in morphology between the optical — where these stars tend to produce relatively regular structures due to the effects of orbital mixing within the galaxies — and the mid-UV — where younger stars whose locations still reflect the distribution of their birthplaces. An additional complication is introduced by the presence of dust obscuration. Dust lanes or clouds that are nearly transparent in the visible can be opaque in the mid-UV, thereby changing the apparent morphology.

As a function of intrinsic galaxy type, our first qualitative results from this Cycle 9 project can be summarized as following:

(1) Early-type galaxies (T=–6 to 0) show a significant change in SB in going from the mid-UV to the red, reflecting their relative paucity of a young stellar population. Some early types appear rather dim in the mid-UV due to significant central dust lanes, while others show mostly a small blue nuclear feature in the mid-UV. Three ellipticals become nearly point sources in the mid-UV (e.g., dominated by LINER's, Seyferts). This is in part due to our sample selection, which required the objects to have high (predicted) mid-UV SB. But it leads us to wonder to what extent the apparently strong cosmological evolution of weak AGN in early-type galaxies is due to the morphological K-correction plus SB-dimming, which causes the surrounding UV-faint early-type host to no longer be visible at higher redshifts. In summary, high SB early-type galaxies in the optical show a variety of morphologies in the mid-UV that *can* lead to a different morphological classification, although not necessarily always as later–type. The often rather peculiar mid-UV morphology of early-type galaxies is generally quite different than that of the real late-type galaxies as seen in the mid-UV, as discussed below.

(2) Mid-type spiral galaxies (T=1–5) and star-forming galaxies can appear as later morphological types in the mid-UV, as *Astro/UIT* has shown primarily in the far-UV. About half of the mid-type spirals in the optical appear as later morphological types in the mid-UV, but not all mid-type spiral galaxies do look dramatically different in the mid-UV. One mid-type spiral, NGC 6782 (§ 3.15), shows a spectacular resonance ring full of hot stars in the F255W and F300W filters. The mid-UV images show a considerable range in the scale and SB of individual star-forming regions. A comparison of F300W to F814W images yields good sensitivity to dust features. Almost without exception, the mid-type spirals in our sample have their small nuclear bulges bisected by a dust-lane, which is often connected to the inner spiral arm structure.

(3) The late-type, irregular, peculiar, and merging galaxies (T=6–11) in our sample show diverse properties in the mid-UV. The majority of these galaxies show a F300W morphology that is similar to that in F814W, but with important differences due to recognizable dust-features absorbing the F300W light, and hot stars, star-clusters, or star-formation "ridges" that are better visible in the mid-UV. Less than a third of galaxies classified as late-type in the optical show significantly different structures in the mid-UV to result in a different classification.

In conclusion, our *HST* mid-UV survey of nearby galaxies suggests that it is more likely to misclassify true early–mid type galaxies in the rest-frame mid-UV as later types, while known late-type galaxies are less likely to be misclassified (as earlier types) in the mid-UV. This is because *truly* late-type galaxies are dominated by young and hot stars in all filters from the mid-UV to the red, and so have to first order the same morphology and a very small morphological K-correction in general. However, early-type galaxies (ellipticals and early-type spirals) *can, although do not have to* look significantly different when one goes from the rest-frame mid-UV to the optical-red part of the spectrum.

Classification of faint galaxies in the rest-frame mid-UV will thus likely result in some fraction of early–mid type galaxies being misclassified as later-types, probably a larger fraction than vice versa. But it is unlikely that this morphological K-correction can explain all of the faint blue galaxy excess as misclassified earlier-type galaxies. And the morphological K-correction cannot explain the slight excess of early–mid type galaxies at faint magnitudes ($B \gtrsim 24$ mag) with respect to passively evolving models, as found by Odewahn et al. (1996) and Cohen et al. (2002), since the main misclassification error goes in the opposite direction. Instead, our mid-UV survey seems to support the conclusion of Cohen et al. (2002) that the number of faint galaxies is larger than the non-evolving predictions *for all galaxy types*, but more significantly so for the later types. Cohen et al. (2002) give a possible explanation of this finding in terms of hierarchical formation models in a Lambda-dominated Universe.

To address these issues further quantitatively, we will in a sequel paper use the Fourier decomposition method of Odewahn et al. (1995, 2002a), where we will quantify the morphological K-correction based on each galaxy's mid-UV photometric parameters as a function of rest-frame wavelength and observed type. Our goal is to use the current *HST* mid-UV sample to quantify the morphological K-correction, and apply it to a large complete sample of faint *HST* galaxies with know photometric redshifts to get reliable and consistent rest-frame classifications. These will then be used to compute the redshift distribution as a function of morphological type, which will help delineate the formation and evolution of galaxies along the Hubble sequence (see Driver et al. 1998).

The US authors acknowledge support from NASA grants GO-8645.* and AR-8765.*, and RSdJ acknowledges support from NASA through Hubble Fellowship grant HF-01106.01-A, awarded by STScI, which is operated by AURA for NASA under contract NAS 5-26555. RAW, CAC and SCO acknowledge support from NASA ADP grant NAG-6740. CAC and VAT acknowledge support from a NASA Space Grant Graduate Fellowship at ASU. This research has made use of the NASA/IPAC Extragalactic Database (NED), which is operated by the Jet Propulsion Laboratory, California Institute of Technology (Caltech) under contract with NASA, and has used NASA's Astrophysics Data System Bibliographic Services. The Second Palomar Observatory Sky Survey (POSS-II) was made by Caltech with funds from the NSF, NASA, the National Geographic Society, the Sloan Foundation, the Samuel Oschin Foundation, and the Eastman Kodak Corporation. The Oschin Schmidt Telescope is operated by Caltech and Palomar Observatory.
We thank Tony Roman and the STScI staff for their excellent help in getting these *HST* observations scheduled. We thank the staff of the Vatican Advanced Technology Telescope, in particular Richard Boyle, Chris Corbally, and Matt Nelson, for their excellent help in obtaining a large fraction of the ground-based images presented in this paper.
We thank Seth Cohen for advice in the data reduction, Dr. Arthur Code for a careful reading of the manuscript and for fruitful discussions, and Prof. Peter Strittmatter and the University of Ari-

zona for their hospitality during a working visit. We thank the referee, Dr. Rob Kennicutt, for a careful and helpful review of the manuscript, and for suggesting a new way to publish a paper like the current one.

REFERENCES

Abraham, R. G., Tanvir, N. R., Santiago, B. X., Ellis, R. S., Glazebrook, K., & van den Bergh, S. 1996, MNRAS, 279, L47
Abraham, R. G., et al. 1999, MNRAS, 308, 569
Allam, S., Assendorp, R., Longo, G., Braun, M., & Richter, G. 1996, A&AS, 117, 39
Alonso-Herrero, A., Rieke, G. H., Rieke, M. J., & Scoville, N. Z. 2000, ApJ, 532, 845
Arp, H. C. 1966, ApJS, 14, 1
Bahcall, J. N., Kirhakos, S., & Schneider, D. P. 1995, ApJ, 450, 486
Bahcall, J. N., Kirhakos, S., & Schneider, D. P. 1996, ApJ, 457, 557
Bahcall, J. N., Kirhakos, S., Saxe, D. H., & Schneider, D. P. 1997, ApJ, 479, 642
Balick, B., & Heckman, T. 1981, A&A, 96, 271
Barnes, J. E., & Hernquist, L. 1992, ARA&A, 30, 705
Barnes, J. E. 2002, MNRAS, in press (astro-ph/0201250)
Beck, S. C., Turner, J. L., Ho, P. T. P., Lacy, J. H., & Kelly, D. M. 1996 ,ApJ, 457, 610
Beichman, C., Neugebauer, G., Habing, H. J., Clegg, P. E., & Chester, T. J. 1988, "IRAS Catalogs and Atlases Explanatory Supplement", (Washington, DC: GPO), NASA RP-1190, Vol. 1
Bertin, E., & Arnouts, S. 1996, A&AS, 117, 393
Biretta, J., et al. 2001, WFPC2 Instrument Handbook, Version 6.0 (Baltimore: STScI)
Bohlin, R. C., et al. 1991, ApJ, 368, 12
Bouwens, R. J., Broadhurst, T., & Silk, J. 1998, ApJ, 506, 579
Bowyer S., Sasseen T. P., Wu X., Lampton M. 1995, ApJS, 96, 461
Boyle, B. J., & Terlevich, R. J. 1998, MNRAS, 293, 49
Boyle, B. J., Shanks, T., Croom, S. M., Smith, R. J., Miller, L., Loaring, N., & Heymans, C. 2000, MNRAS, 317, 1014
Brown, T. M., Bowers, C. W., Kimble, R. A., Ferguson, H. C. 2000, ApJ, 529, 89
Bruzual A. G. & Charlot, S. 1993, ApJ, 405, 538
Bryant, P. M., & Scoville, N. Z. 1999, AJ, 117, 2632
Burgarella, D., Buat, V., Donas, J., Milliard, B. & Chapelon, S. 2001, A&A, 369, 421
Burstein, D., Bertola, F., Buson, L. M., Faber, S. M., Lauer, T. R. 1988, ApJ, 328, 440
Buta, R., Purcell, G. B., & Crocker, D. A. 1996, AJ, 111, 983
Buta, R., Alpert, A. J., Cobb, M. L., Crocker, D. A., & Purcell, G. B. 1998, AJ, 116, 1142
Buta, R., & Purcell, G. B. 1998, AJ, 115, 484
Buta, R., Purcell, G. B., Cobb, M. L., Crocker, D. A., Rautiainen, P., & Salo, H. 1999, AJ, 117, 778
Buta, R., Treuthardt, P. M., Byrd, G. G., & Crocker, D. A. 2000, AJ, 120, 1289
Buta, R., Ryder, S. D., Madsen, G. J., Wesson, K., Crocker, D. A., & Combes, F. 2001, AJ, 121, 225
Boeker, T., Laine, S., van der Marel, R. P., Sarzi, M., Rix, H.-W., Ho, L. C., & Shields, J. C. 2001, BAAS199, Abstract 07.05
Caldwell, N., Phillips, M. M. 1989, ApJ, 338, 789
Calzetti, D., Bohlin, R. C., Kinney, A. L., Storchi-Bergmann, T., & Heckman, T. M. 1995, ApJ, 443, 136
Calzetti, D., Meurer, G. R., Bohlin, R. C., Garnett, D. R., Kinney, A. L., Leitherer, C., Storchi-Bergmann, T. 1997, AJ, 114, 1834
Calzetti, D., Conselice, C. J., Gallagher III, J. S., & Kinney, A. L. 1999, AJ, 118, 797
Carruthers, G. R., Opal, C. B. & Heckathorn, H. M. 1978, ApJ, 225, 346
Casoli, F., Willaime, M.-C., Viallefond, F., & Gerin, M. 1999, A&A, 346, 663
Code, A. D. & Welch, G. A. 1982, ApJ, 256, 1
Cohen, J. M., Hogg, D. W., Blandford, R., Cowie, L. L., Hu, E., Songaila, A., Shopbell, P., & Richberg, K. 2000, ApJ, 538, 29
Cohen, S. H., Windhorst, R. A., Chiarenza, C. A. T., Odewahn, S. C., & Driver, S. P. 2002, AJ, submitted
Conselice, C. J., Gallagher, J. S., Calzetti, D., Homeier, N., & Kinney, A. 2000, AJ, 119, 79
Cornett, R. H., et al. 1994, ApJ, 426, 553
Cowie, L. L., Hu, E. M., & Songaila, A. 1995, Nature, 377, 603
Crowther, P. A., Beck, S. C., Willis, A. J., Conti, P. S., Morris, P. W., & Sutherland, R. S. 1999, MNRAS, 304, 654
Dalcanton & Shectman, S. 1996, ApJ, 465, 9
Donas, J., Milliard, B., & Laget, M. 1995, A&A, 303, 661
de Grijs, R., & Peletier, R. F. 1997, A&A, 320, L21
de Grijs, R., Peletier, R. F., & van der Kruit, P. C. 1997, A&A, 327, 966
de Grijs R., O'Connell R. W., Gallagher J. S. 2001, AJ, 121, 768
de Jong, R. S., & van der Kruit, P. C. 1994, A&AS, 106, 451
de Vaucouleurs, G., de Vaucouleurs, A., Corwin, H., Buta, R., Paturel, G., & Fouqué, P. 1991, Third Reference Catalogue of Bright Galaxies (New York: Springer Verlag)
Dickinson, M. E. 2001, in: "Building Galaxies: From the Primordial Universe to the Present", eds. F. Hammer et al. , (Paris: Ed. Frontieres), 257 proceedings of the XIXth Moriond Astrophysics Meeting (March 1999), eds. F. Hammer, T.X. Thuan, V. Cayatte, B. Guiderdoni, & J. Tranh Than Van, (Paris: Ed. Frontieres), 257
Disney, M. J. 1976, Nature, 263, 573
Downes, D., & Solomon, P. M. 1998, ApJ, 507, 615
Driver, S. P. 1999, ApJ, 526, L69
Driver, S. P., Windhorst, R. A., Ostrander, E. J., Keel, W. C., Griffiths, R. E., & Ratnatunga, K. U. 1995a, ApJ, 449, L23
Driver, S. P., Windhorst, R. A., & Griffiths, R. E. 1995b, ApJ, 453, 48
Driver, S., Fernandez-Soto, A., Couch, W., Odewahn, S., Windhorst, R., Phillipps, S., Lanzetta, K., & Yahil, A. 1998, ApJ, 496, L93
Eichendorf, W. & Nieto, J.-L. 1984, A&A, 132, 342),
Ellis, R.S., Colless, M., Broadhurst, T., Heyl, J., & Glazebrook, K. 1996, MNRAS, 280, 235
Eskridge, P. B., Frogel, J. A., Pogge, R. W., Quillen, A. C., Davies, R. L., DePoy, D. L., Houdashelt, M. L., Kuchinski, L. E., et al. 2000, AJ, 119, 536
Eskridge, P. B., Taylor, V. A., Windhorst, R. A., Odewahn, S. C., Chiarenza, C. A., Conselice, C. J., de Grijs, R., Matthews, L. D., O'Connell, R.W., Frogel, J. A., & Gallagher, J. S., III, 2002a (in preparation)
Eskridge, P. B., Frogel, J. A., Pogge, R. W., Quillen, A. C., Berlind, A. A., Davies, R. L., DePoy, D. L., Gilbert, K. M., Houdashelt, M. L., Kuchinski, L. E., Ramírez, S. V., Sellgren, K., Stutz, A., Terndrup, D. M. & Tiede, G. P. 2002b, ApJS (submitted)
Fasano, G., & Bettoni, D. 1994, AJ, 107, 1649
Filippenko, A. V. 1985, ApJS, 57, 503
Frei, Z., Guhathakurta, P., Gunn, J. E., & Tyson, J. A. 1996, AJ, 111, 174
Frogel, J. A., Quillen, A. C., Pogge, R. W. 1996, in: "New Extragalactic Perspectives in the New South Africa" (Astrophysics and Space Science Library, Vol. 209), eds. D. L. Block & J. M. Greenberg, (Dordrecht: Kluwer), 65
Gallagher, J. S., Hunter, D. A., & Bushouse, H. 1989, AJ, 97, 700
Gallagher, J. S., Conselice, C. J., & Homeier, N. 2000, in Dynamical Galaxy Evolution from the Early Universe to the Present, ASP Conf. Ser. Vol. 197, eds. F. Combes, G. A. Mammon, & V. Charmandaris, p.309
Gallagher, J., et al. 2002, in preparation
Giavalisco, M., Livio, M., Bohlin, R. C., Macchetto, F. D., & Stecher, T. P. 1996, AJ, 112, 369
Glazebrook, K., Ellis, R. E. Santiago, B. & Griffiths, R. E. 1995, MNRAS, 275, L19
Gorjian, V. 1996, AJ, 112, 1886
Greggio, L., & Renzini, A. 1990, ApJ, 364, 35
Hawarden, T. G., van Woerden, H., Mebold, U., Goss, W. M., & Peterson, B. A. 1979, A&A, 76, 230
Hibbard, J. E., & Vacca, W. D. 1997, AJ, 114, 1741
Hibbard, J. E., & van Gorkom, J. H. 1996, AJ, 111, 655
Hibbard, J. E., & Yun, M. S. 1999a, ApJ, 522, L93
Hibbard, J. E., & Yun, M. S. 1999b, AJ, 118, 162
Hibbard, J. E., et al. 2002, in preparation
Hill, J. K. et al. 1992, ApJ, 395, L37 (Hl92)
Hubble, E. P., & Lundmark, K. 1923, PASP, 34, 292
Hunter, D. A., O'Connell, R. W., & Gallagher J. S. 1994, AJ, 108, 84
Israel, F., de Boer, K. S., & Bosma, A. 1986, A&A, 66, 117
Jansen, R. A., Knapen, J. H., Beckman, J. E., Peletier, R. F., & Hes, R. 1994, MNRAS, 270, 373
Keel, W. C. 1996, ApJS, 106, 27
Keel, W. C. 2000, BAAS197, Abstract 37.01
Keel, W. C., & Weedman, D. W. 1978, AJ, 83, 1
Keel, W. C., & Windhorst, R. A. 1993, AJ, 106, 455
Keel, W. C. 1996, AJ, 111, 696
Kent, S. M. 1985, ApJS, 59, 115
Khachikian, E. 1974, ApJ, 192, 581
Kinney, A. L., Bohlin, R. C., Calzetti, D., Panagia, N., & Wyse, R. F. G. 1993, ApJS, 86, 5
Kirhakos, S., Bahcall, J. N., Schneider, D. P., Kristian, J. 1999, ApJ, 520, 67
Knapen, J. H., & Beckman, J. E. 1996, MNRAS, 283 251
Knapen, J. H., Laine, S., Yates, J. A., Robinson, A., Richards, A. M., S., Doyon, R., & Nadeau, D. 1997, ApJ, 490, L29
Knapen, J. H., Shlosman, I., & Peletier, R. F. 2000, ApJ, 529, 93
Kobulnicky, H. A., Skillman, E. D. 1995, ApJ, 454, L121
Koo, D. C., & Kron, R. G. 1988, ApJ, 325, 92
Kregel, M., & Sancisi, R. 2001, A&A, 376, 59
Kuchinski, L. E., Terndrup, D. M., Gordon, K. D., & Witt, A. N. 1998, AJ, 115, 1438
Kuchinski, L. E. et al. 2000, ApJS, 131, 441
Kuchinski, L. E., Madore, B. F., Freedman, W. L., & Trewhella, M. 2001, AJ, 122, 729

Lauberts, A., & Valentijn, E. A. 1989, The Surface Photometry Catalogue of the ESO-Uppsala Galaxies (Garching-bei-München: European Southern Observatory)
Laurent-Muehleisen, S. A., Kollgaard, R. I., Ryan, P. J., Feigelson, E. D., Brinkmann, W., & Siebert, J. 1997, BAAS, 122, 235
Lilly, S. J., Schade, D., Ellis, R., Le Fevre, O., Brinchmann, J., Tresse, L., Abraham, R., Hammer, F., et al. 1998, ApJ, 500, 75
Magorrian, J., Tremaine, S., Richstone, D., et al. 1998, AJ, 115, 2285
Majewski, S. R., Hereld, M., Koo, D. C., Illingworth, G. D., & Heckman, T. M. 1993, ApJ, 402, 125
Maoz, D., Filippenko, A. V., Ho, L. C., Macchetto, F. D., Rix, H.-W., & Schneider, D. P. 1996, ApJS, 107, 215
Marcum, P. M., O'Connell, R. W., Fanelli, M. N., Cornett, R. H., Waller, W. H., Bohlin, R. C., Neff, S. G., Roberts, M. S., et al. 2001, ApJS, 132, 129
Marlowe, A. T., Heckman, T. M., Wyse, R. F. G., & Schommer, R. 1995, ApJ, 438, 563
Martin, C. L., & Kennicutt Jr., R. C. 1995, ApJ, 447, 171
Matthews, L. D. & Gallagher, J. S. 1997, AJ, 114, 1899
Matthews, L. D., Gallagher, J. S., Krist, J. E., Watson, A. M., & the WFPC2 IDT 1999, AJ, 118, 208
Meurer, G. R., Heckman, T. M., Leitherer, C., Kinney, A., Robert, C., & Garnett, D. R. 1995, AJ, 110, 2665
Moffat, A. F. J. 1969, A&A, 3, 455
Mulder, P. S., van Driel, W., & Braine, J. 1995, A&A, 300, 687
Mulder, P. S., & van Driel, W. 1996, A&A, 309, 403
Naab, T., & Burkert, A. 2001, ApJ, 444, 91
Neuschaefer, L. W., & Windhorst, R. A. 1995b, ApJS, 96, 371
Nordgren, T. E., Chengalur, J. N., Salpeter, E. E., & Terzian, Y. 1997, AJ, 114, 77
O'Connell, R. W., Bohlin, R. C., Collins, N. R., Cornett, R. H., Hill, J. K., Hill, R. S., Landsman, W. B., Roberts, M. S., Smith, A. M., & Stecher, T. P. 1992, ApJ, L45
O'Connell, R. W. 1999, ARA&A, 37, 603
Odewahn, S. C. 1995, PASP, 107, 770
Odewahn, S. C., Windhorst, R. A., Driver, S. P., & Keel, W. C. 1996, ApJ, 472, L013
Odewahn, S. C., Burstein, D., & Windhorst, R. A. 1997, AJ, 114, 2219
Odewahn, S. C., Cohen, S. H., Windhorst, R. A., & Phillip, S. 2002a, ApJ, 568, 001–019, in press (astro-ph/0110275)
Odewahn, S. C., Taylor, V. A., Windhorst, R. A., & Chiarenza, C. A. T. 2002b, AJ, in preparation
Osterbrock, D. 1977, ApJ, 215, 733
Pascarelle, S. M., Windhorst, R. A., Keel, W. C., & Odewahn, S.C. 1996b, Nature, 383, 45
Pascarelle, S. M., Windhorst, R. A., & Keel, W. C. 1998, AJ, 116, 2659 (astro-ph 9809181)
Payne-Gaposchkin, C. 1936, ApJ, 83, 173
Perlman, E. S., Padovani, P., Giommi, P., Sambruna, R., Jones, L.R., Tzioumis, A., & Reynolds, J. 1998, AJ, 115, 1253
Phookun, B., Mundy, L. G., Teuben, P., Wainscoat, R. J. 1992, ApJ, 400, 516
Quillen, A. C., McDonald, C., Alonso-Herrero, A., Lee, A., Shaked, S., Rieke, M. J., & Rieke, G. H. 2001, ApJ, 547, 129
Radecke, H. D. 1997, A&A, 319, 18
Ravindranath, S., Ho, L. C., Peng, C. Y., Filippenko, A. V., & Sargent, W. L. W. 2001, AJ 122, 653
Ruiz, J. R., Crenshaw, D. M., Kraemer, S. B., Bower, G. A., Gull, T. R., Hutchings, J. B., Kaiser, M. E., & Weistrop, D. 2001, AJ, 122, 2961
Sandage, A., Saha, A., Tammann, G. A., Labhardt, L., Schwengeler, H., Panagia, N., & Macchetto, F. D. 1994, ApJ, 423, L13
Sanders, D. B., Soifer, B. T., Elias, J. H., Madore, B. F., Matthews, K., Neugebauer, G., & Scoville, N. Z. 1988, ApJ, 325, 74
Schwarzkopf, U., & Dettmar, R.-J. 2000, A&A, 361, 451
Schweizer, F. 1996a, AJ, 111, 109
Schweizer, F., Miller, B. W., Whitmore, B. C., & Fall, S. M. 1996b, AJ, 112, 1839
Scoville, N.Z., Evans, A.S., Thompson, R., Rieke, M., Hines, D.C., Low, F.J., Dinshaw, N., Surace, J.A., & Armus, L. 2000, AJ, 119, 991
Sersic, J. L., Carranza, G., & Pastoriza, M. 1972, Ap&SS, 19, 469
Seyfert, C. K. 1943, ApJ, 97, 28S
Simard, L., Koo, D. C., Faber, S. M., Sarajedini, V. L., Vogt, N. P., Phillips, A. C., Gebhardt, K., Illingworth, G. D., & Wu, K. L. 1999, ApJ, 519, 563
Smith, D. A., Herter, T., Haynes, M. P., Beichman, C. A., & Gautier, T. N. 1996a, ApJS, 104, 217
Smith, D. A., Neff, S. G., Bothun, G. D., Fanelli, M. N., Offenberg, J. D., Waller, W. H., Bohlin, R. C., Robert W., Roberts, M. S., Smith, A. M., & Stecher, T. P. 1996b, ApJ, 473, L21
Smith, A. M., Collins, N. R., Waller, W. H., Roberts, M. S., Smith, D. A., Bohlin, R. C., Cheng, K.-P., Fanelli, M. N., Neff, S. G., O'Connell, R. W., Parise, R. A., Smith, E. P., & Stecher, T. P. 2001, ApJ, 546, 829
Stecher, T. P., Bohlin, R. C., Hill, J. K., & Jura, M. A. 1982, ApJ, 255, L99
Stecher, T. P., Cornett, R. H., Greason, M. R., Landsman, W. B., Hill, J. K., et al. 1997, PASP, 109, 584
Storchi-Bergmann, T., Kinney, A. L., & Challis, P. 1995, ApJS,98, 103
Strickland, D. K., & Stevens, I. R. 1999, MNRAS, 306, 43
Surace, J. A., Sanders, D. B., & Evans, A. S. 2000a, ApJ, 529, 170
Surace, J. A. & Sanders, D. B. 2000b, AJ, 120, 604
Taylor, G. B., Vermeulen, R. C., Readhead, A. C. S., Pearson, T.J., Henstock, D. R., & Wilkinson, P. N. 1996, ApJS, 107, 37
Taylor, V. A., Windhorst, R. A., Chiarenza, C. A. T., Odewahn, S. C., de Grijs, R., de Jong, R. S., & Frogel, J. A. 2002, AJ, in preparation
Toomre, A. 1977, in The Evolution of Galaxies and Stellar Populations, ed. B.M. Tinsley & R.B. Larson (Yale University Press, New Haven), 401
Turner, J. L., Beck, S. C., & Hurt, R. L. 1997, ApJ, 474, L11
Turner, J. L., Ho, P. T., & Beck, S. C. 1998, AJ, 116, 1212
Turner, J. L., Beck, S. C., & Ho, P. T. 2000, ApJ, 532, 109
Vogt, N. P., Phillips, A. C., Faber, S. M., Gallego, J., Gronwall, C., Guzman, R., Illingworth, G. D., Koo, D. C., & Lowenthal, J. D. 1997, ApJ, 479, L121
Wang, Z., Schweizer, F., & Scoville, N. Z. 1992, ApJ, 396, 510
White, R. L. & Becker, R. H. 1992, ApJS, 79, 331
Whitmore, B. C., Schweizer, F., Leitherer, C., Borne, K., & Robert, C. 1993, AJ, 106, 1354
Williams, R.E., Adorf, H.-M., Blacker, B., Dickinson, M., Dixon, W. V., Ferguson, H. C., Fruchter, A. S., Giavalisco, M., Gilliland, R., Heyer, I., Hook, R. N., Lucas, R. A., McElroy, D. B., Petro, L., & Postman, M. 1996, AJ, 112, 1335
Williams, R. E., Baum, S., Bergeron, L. E., et al. 2000, AJ, 120, 2735
Windhorst, R. A., Franklin, B. E., & Neuschaefer, L. W. 1994a, PASP, 106, 798
Windhorst, R. A., Gordon, J. M., Pascarelle, S. M., Schmidtke, P.C., Keel, W. C., Burkey, J. M., & Dunlop, J. S. 1994b, ApJ, 435, 577
Windhorst, R. A., et al. 1994c, AJ, 107, 930
Windhorst, R. A., et al. 1996, in Proceedings of the Max Planck Workshop on "Galaxies in the Young Universe", Springer Lecture Notes in Physics, Eds. H. Hippelein, K. Meisenheimer, & H. -J. Roeser (Berlin: Springer Verlag), Vol. 463, p. 265
Windhorst, R. A., Odewahn, S. C., Cohen, S. H., Burg, C. A., deJong, R. S., Driver, S. P., Marzke, R. O., Tyson, J. A., & Dell'Antonio, I. 1997, in "The Ultraviolet Universe at Low and High Redshift: Probing the Progress of Galaxy Evolution", ed. W. H. Waller, M. N. Fanelli, J. E. Hollis, & A. C. Danks (New York: AIP Press), Vol. 408, 242
Windhorst, R. A., Keel, W. C., & Pascarelle, S. M. 1998, ApJ, 494, L27
Windhorst, R., Pascarelle, S., Odewahn, S., Cohen, S., Burg, C., Keel, W., & Driver, S. 1998b, in Proceedings of the STScI Symposium on "The Hubble Deep Field", ed. M. Livio, S. M. Fall, & P. Madau (Cambridge University Press), 481
Windhorst, R. A., Odewahn, S. C., Burg, C., Cohen, S. H., &Waddington, I. 2000, in Proceedings of the New South Africa Conference, "Toward a New Millennium in Galaxy Morphology: from z=0 to the Lyman Break", ed. D. L. Block, I. Puerari, A. Stockton & D. Ferreira (Dordrecht: Kluwer), Astrophysics and Space Science, Volumes 269–270, 243
Windhorst, R. A., Conselice, C., & Petro, L. 2002, ApJ, in preparation
Witt, A. N., & Gordon, K. D. 1996, ApJ, 463, 681
Wright A. E., Griffith M. R., Hunt A. J., Troup E., Burke B. F., Ekers R. D. 1996, ApJS, 103, 145
Wu, K., Faber, S., & Lauer, T. 1997, in "The Hubble SpaceTelescope and the High Redshift Universe", ed. N. R. Tanvir, A. Aragon-Salamanca, & J. V. Wall (Singapore: World Scientific), 179
Yun, M. S., & Scoville, N. Z. 1995, ApJ, 451, L45
Yun, M. S., & Hibbard, J. E. 2001a, ApJ, 550, 104
Zeltwanger, T., Comins, N. F., & Lovelace, R. V. E. 2000, ApJ, 543, 669
Zepf, S. E., Ashman, K., English, J., Freeman, K.C., & Sharples, R.M. 1999, AJ, 118, 752

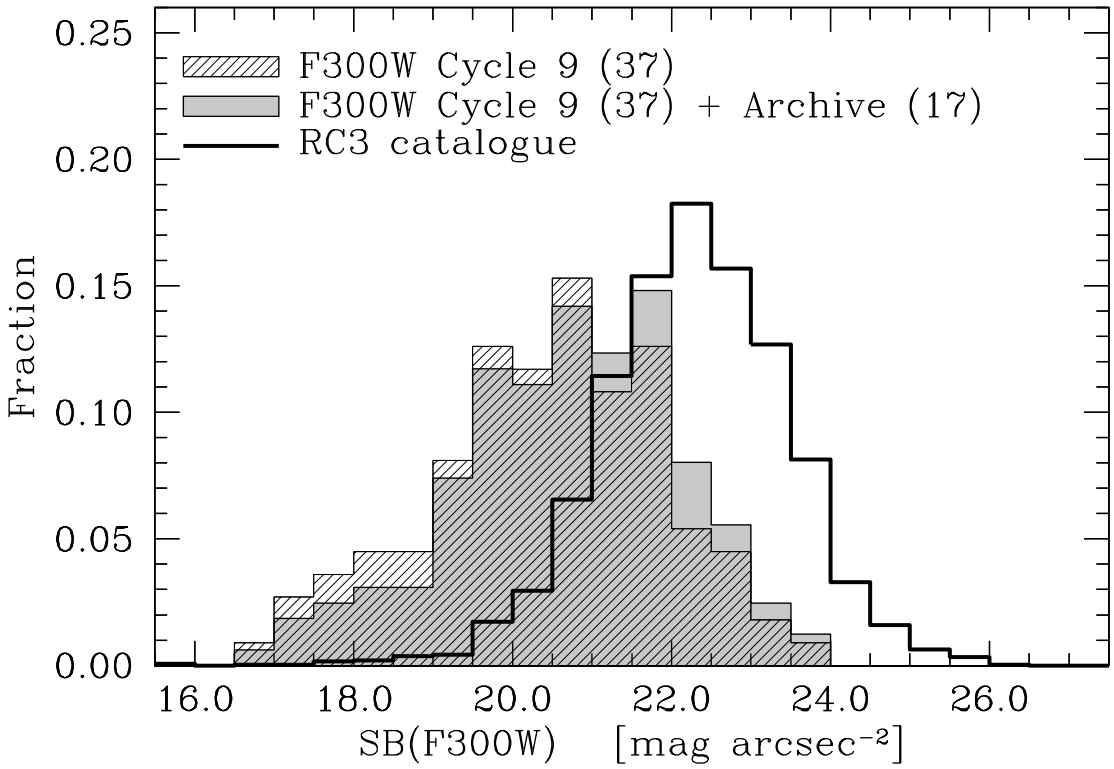

FIG. 1.— The normalized distribution of the predicted average mid-UV surface brightness (SB) out to r_e (see § 2.1.2) for the 37 galaxies observed during *HST* Cycle 9 (*hashed histogram*) and for the full galaxy sample (*solid histogram*), which includes 17 galaxies with mid-UV data taken prior to Cycle 9. For comparison, we also show the SB distribution for the 3009 galaxies in the RC3 with measured B_T, $(U-B)$ and r_e (*open histogram*). The galaxies were selected to have $\mu_{F300W} \lesssim 23$ mag arcsec^{-2}, allowing us to detect each object in F300W in no more than a single *HST* orbit. For our purpose of comparing nearby and distant galaxies this imposed SB-bias is justified, since the strong cosmological SB-dimming acts similarly in hiding lower SB objects at high redshifts from deep surveys.

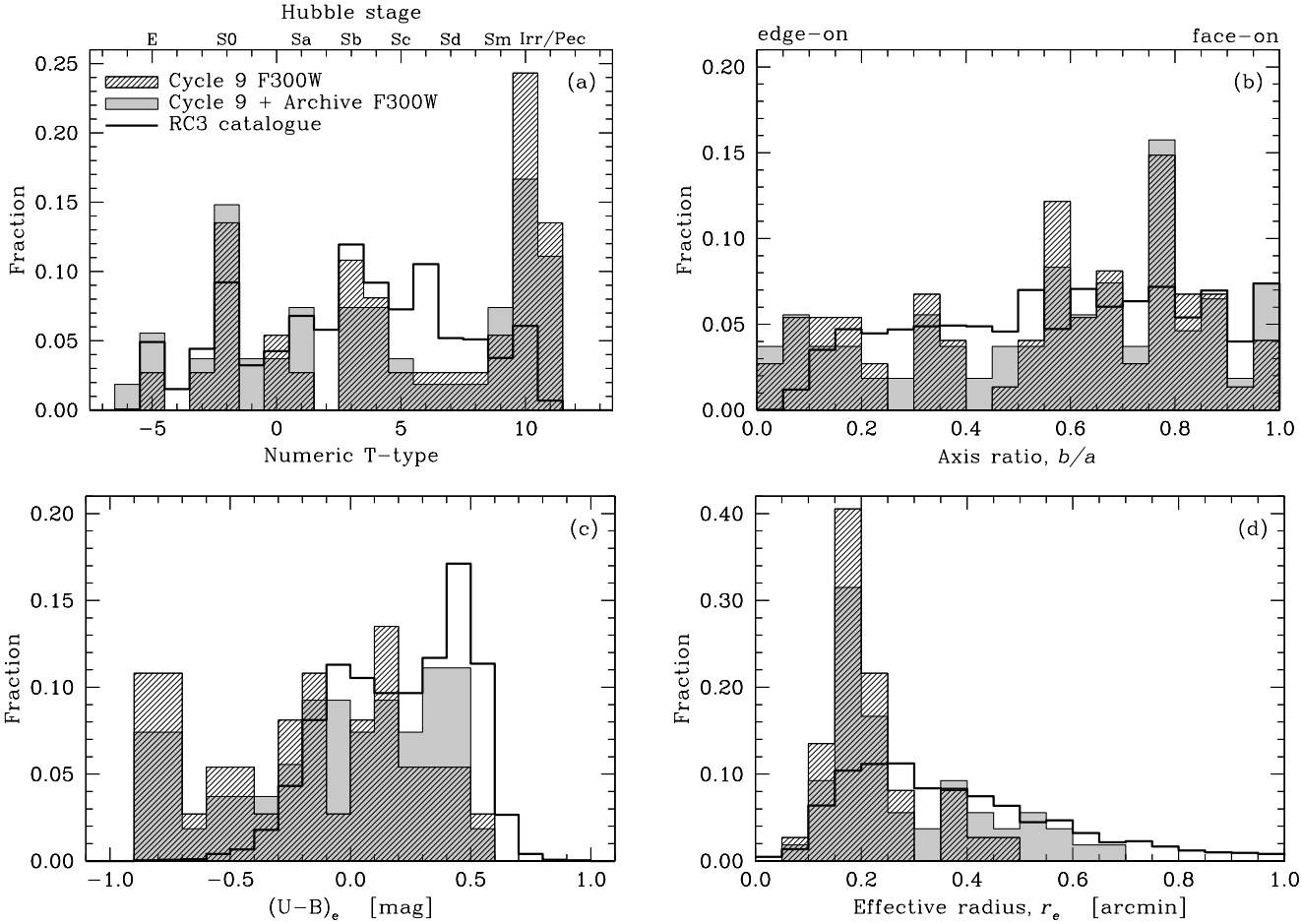

FIG. 2.— Other properties of the selected galaxy sample. As in Fig. 1, we present normalized distributions for the Cycle 9 galaxies (*hashed*), the full sample (*solid*), and the RC3 (*open*) of (*a*) morphological type; (*b*) apparent axis ratio, b/a; (*c*) average $(U-B)$ color out to r_e; and (*d*) effective radius r_e. Taking deviations due to small number statistics into account, our sample approximates the RC3 distribution, except that for the purpose of comparison with high redshift objects, we placed extra emphasis on the very latest types, bluest optical galaxy colors, and smallest angular sizes (to fit the FOV of the WFPC2). We also somewhat over-represent highly inclined systems.

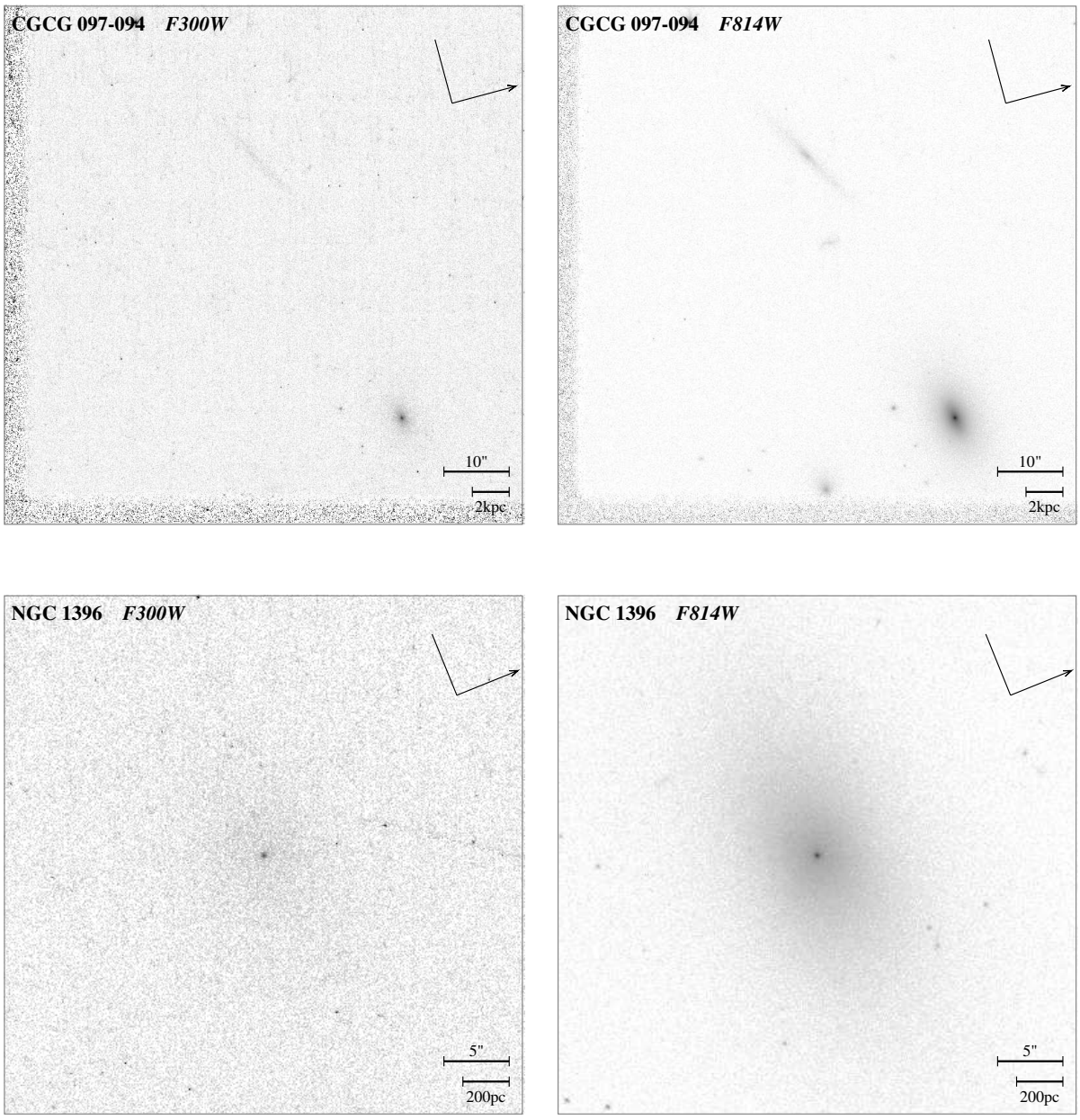

FIG. 3.— Atlas of *HST* WFPC2 observations of 37 nearby galaxies in the mid-UV F255W (only for the 11 galaxies in *HST*'s CVZ) and F300W filters, and in the optical *I*-band (F814W) filter. The galaxies are sorted in the atlas approximately according to their observed morphological type following the discussion of the individual objects in § 3. For the convenience of the reader, Table 2 cross-references the available galaxy data with the atlas page numbering. Each of the grey-scale renditions is displayed using a logarithmic stretch and the image scale and orientation on the sky are indicated. For some galaxies we will present images at two different image scales and stretches, in order to emphasize small-scale features discussed in the text (see § 3). We also present images for some serendipitously observed galaxies.

— MID-UV-FAINT ELLIPTICAL GALAXIES. **3.01 CGCG 097–094** (*top*): WFPC2 F300W and F814W. Serendipitous observation of an early-type galaxy. Also visible are an edge-on spiral galaxy and a face-on disk galaxy (both anonymous); **3.02 NGC 1396** (*bottom*): WFPC2 F300W and F814W.

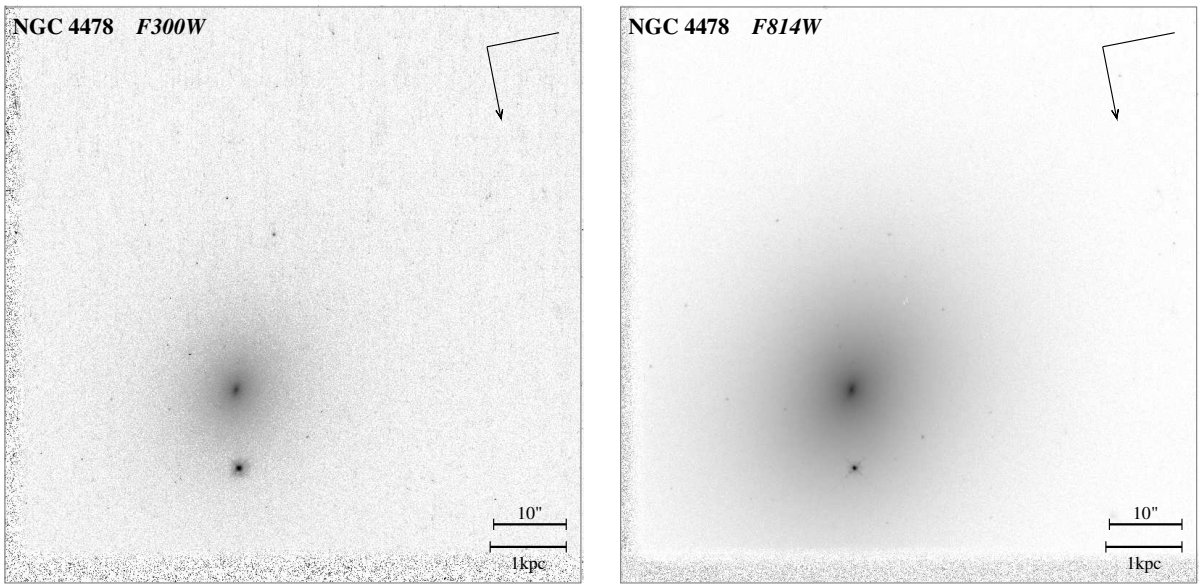

FIG. 3.— (CONT'D) **3.03 NGC 4478** WFPC2 F300W (*left*) and F814W (*right*).

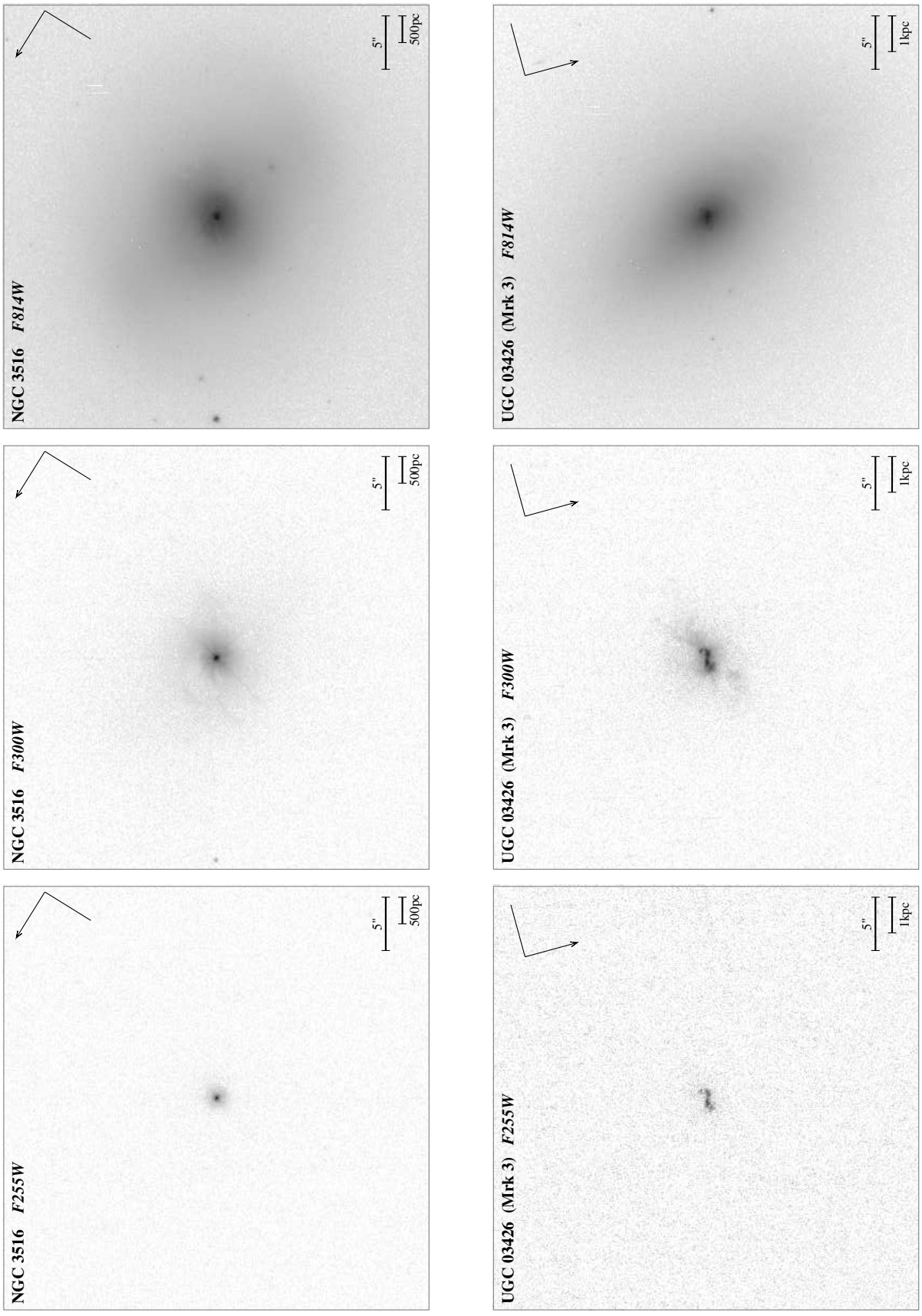

FIG. 3.— EARLY-TYPE GALAXIES WITH SIGNIFICANT AGN EMISSION IN THE MID-UV. **3.04 NGC 3516** (*top*): WFPC2 F255W, F300W and F814W; **3.05 UGC 03426** (*bottom*): WFPC2 F255W, F300W and F814W.

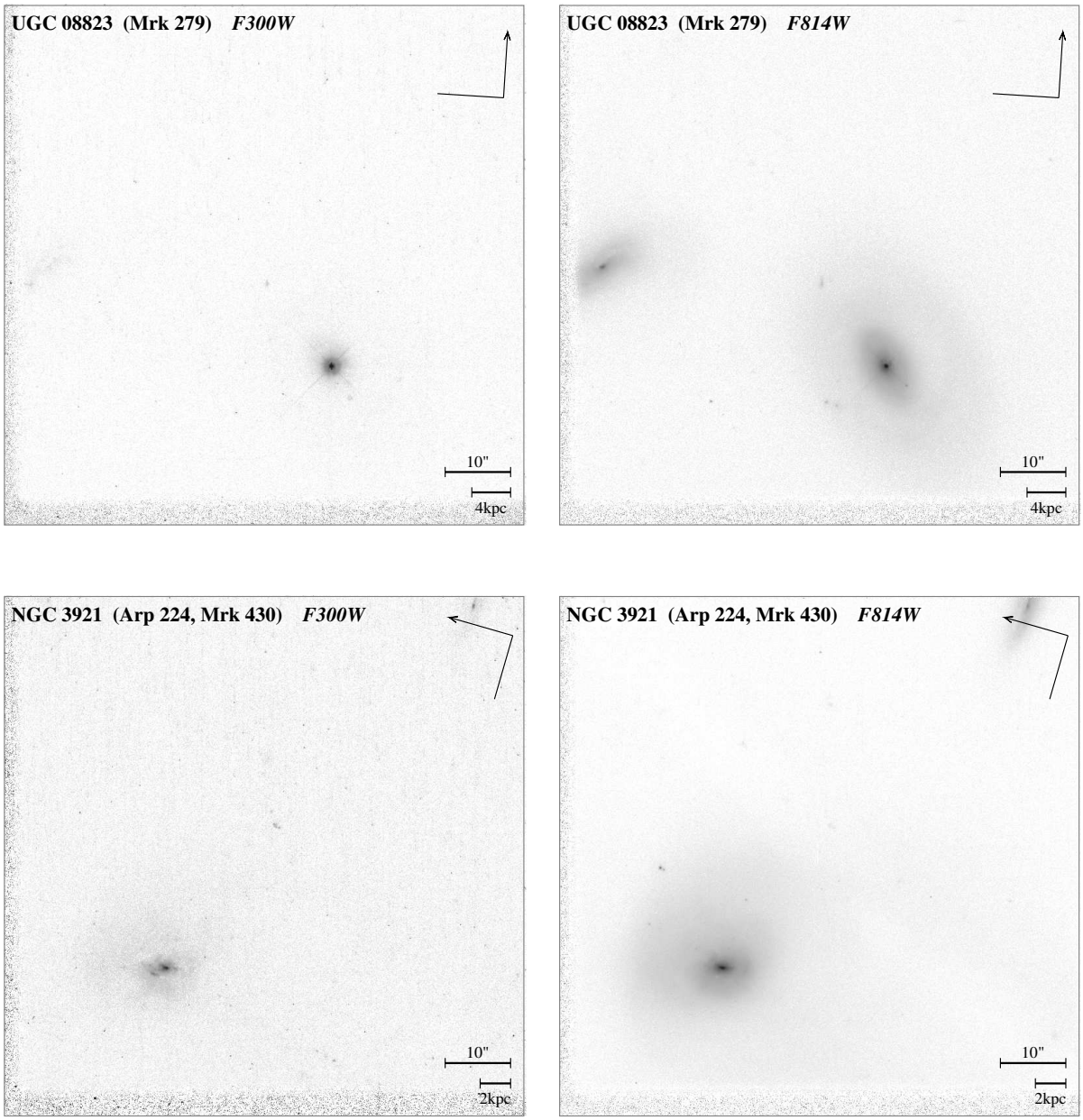

FIG. 3.— (CONT'D) **3.06 UGC 08823** (*top*): WFPC2 F300W and F814W.
EARLY-TYPE GALAXIES SHOWING EVIDENCE FOR RECENT MERGING OR STRONG INTERACTION. **3.07 NGC 3921** (*bottom*): WFPC2 F300W and F814W.

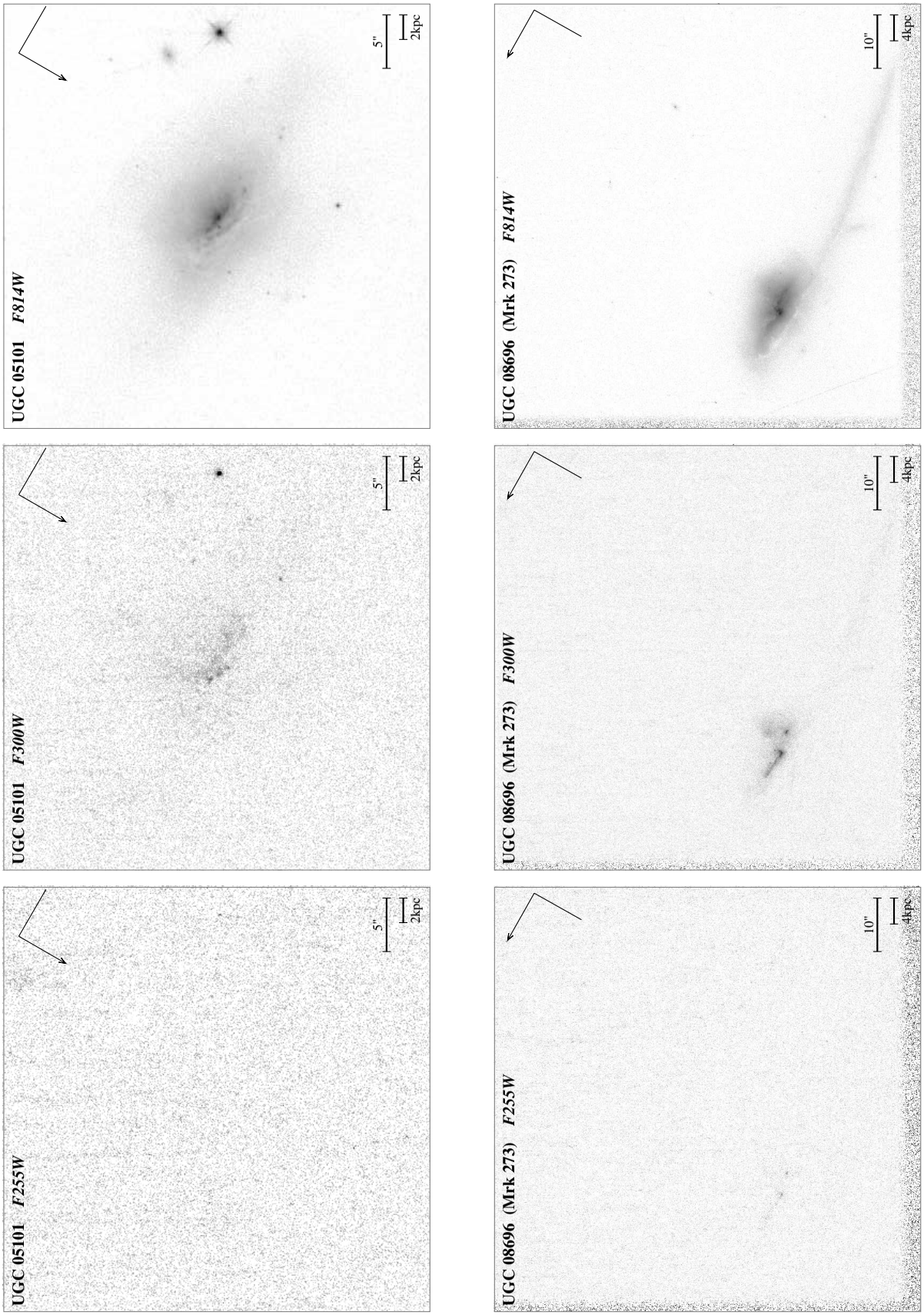

FIG. 3.— (CONT'D) **3.08 UGC 05101** (*top*): WFPC2 F255W, F300W and F814W; **3.09 UGC 08696** (*bottom*): WFPC2 F255W, F300W and F814W.

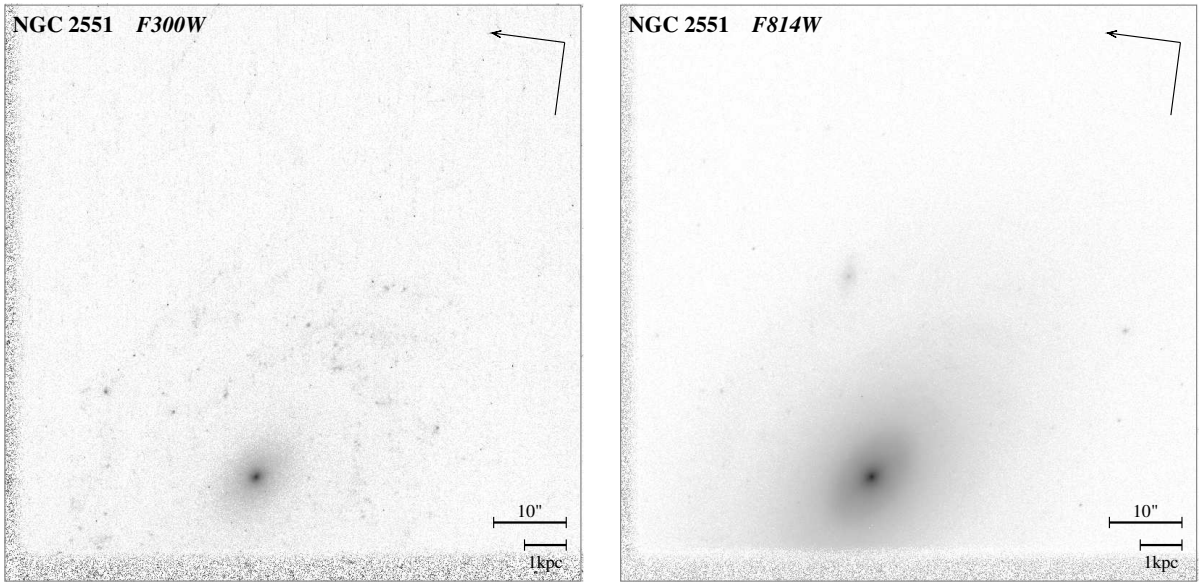

FIG. 3.— EARLY-TYPE GALAXIES DISPLAYING SPIRAL STRUCTURE IN THE MID-UV. **3.10 NGC 2551** WFPC2 F300W (*left*) and F814W (*right*).

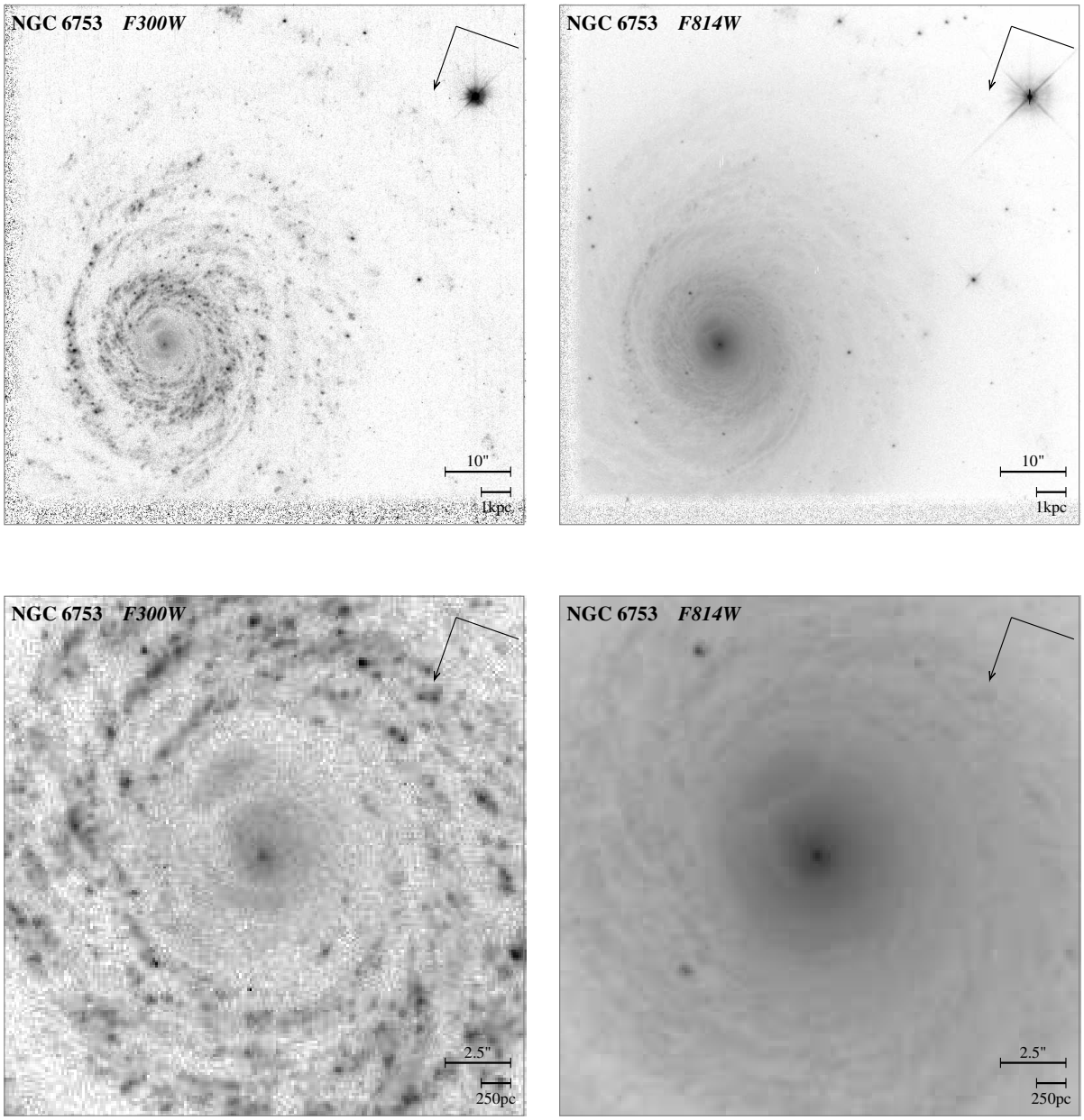

FIG. 3.— GRAND-DESIGN SPIRAL GALAXIES. **3.11a NGC 6753** (*top*): WFPC2 F300W and F814W; **3.11b NGC 6753** (*bottom*): Nuclear portion of NGC 6753, emphasizing the dust lane crossing the inner spiral arms discussed in the text.

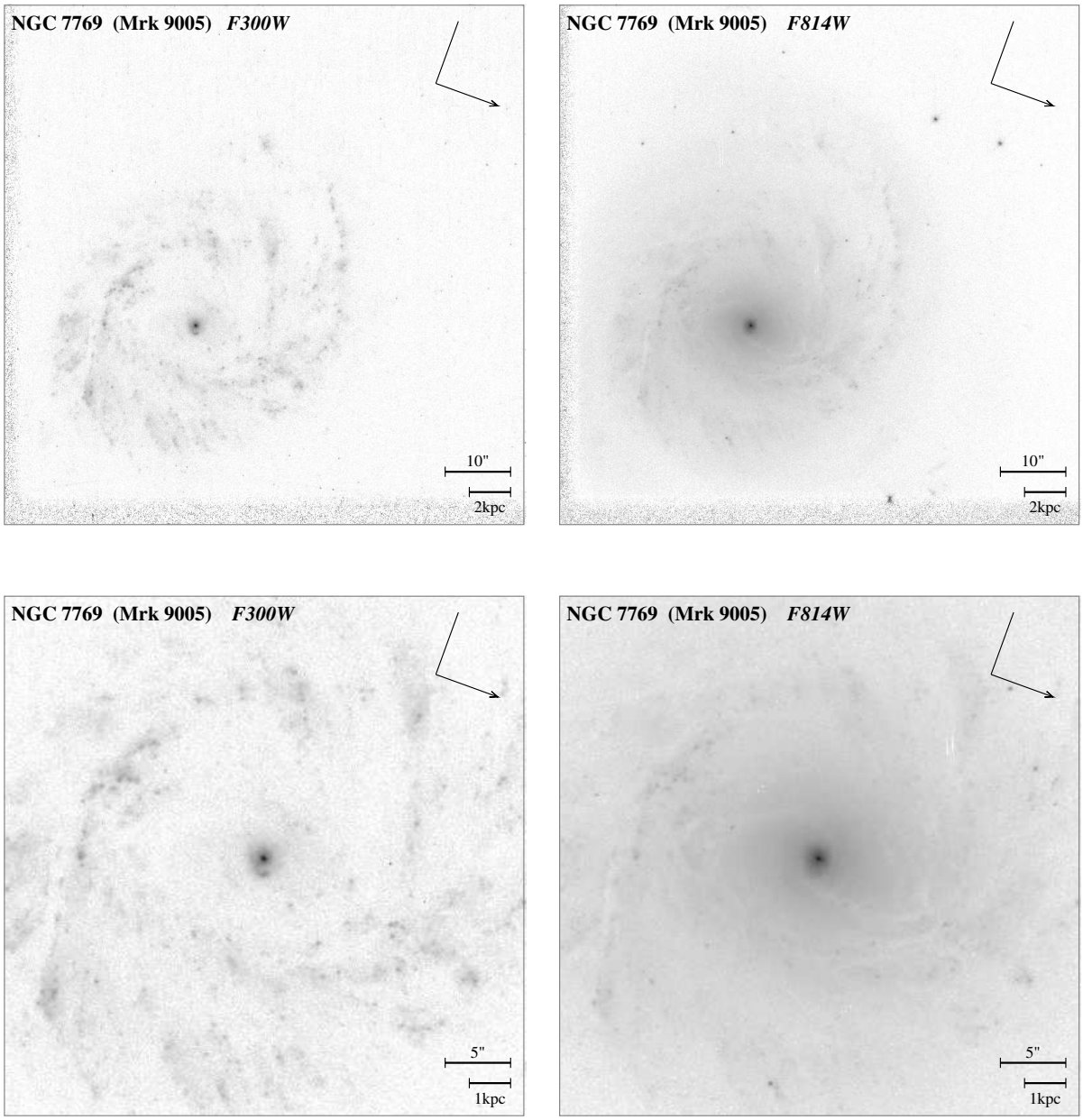

FIG. 3.— (CONT'D) **3.12a NGC 7769** (*top*): WFPC2 F300W and F814W; **3.12b NGC 7769** (*bottom*): Central portion of NGC 7769, emphasizing the dust lanes crossing the spiral arms and the dust lane crossing its small bulge.

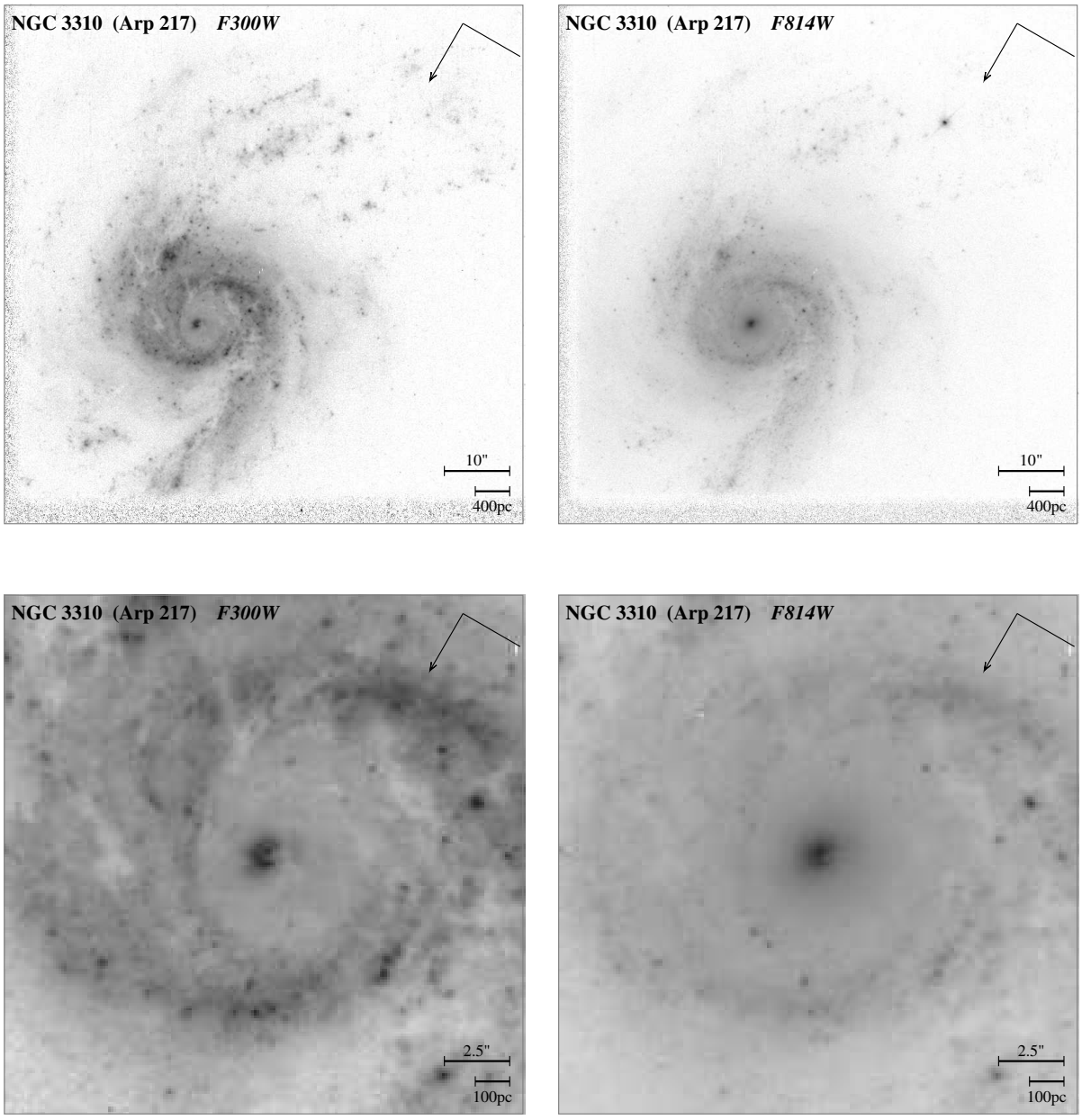

FIG. 3.— (CONT'D) **3.13a NGC 3310** (*top*): WFPC2 F300W and F814W; **3.13b NGC 3310** (*bottom*): Nuclear portion of NGC 3310, emphasizing the spiral arm and nucleus crossing dust lanes.

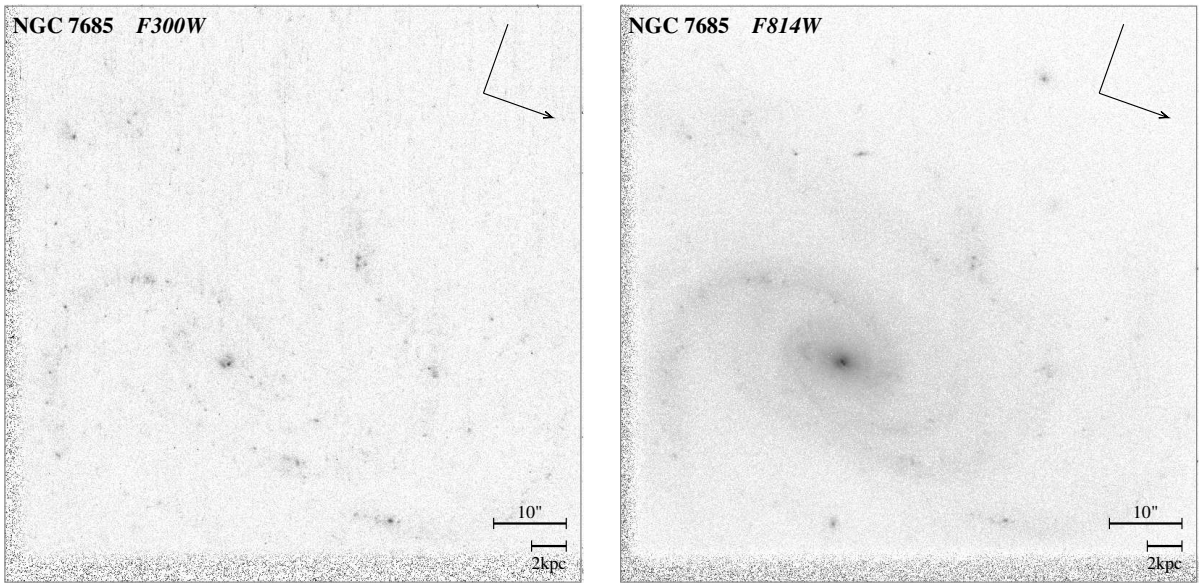

FIG. 3.— (CONT'D) **3.14 NGC 7685** WFPC2 F300W (*left*) and F814W (*right*).

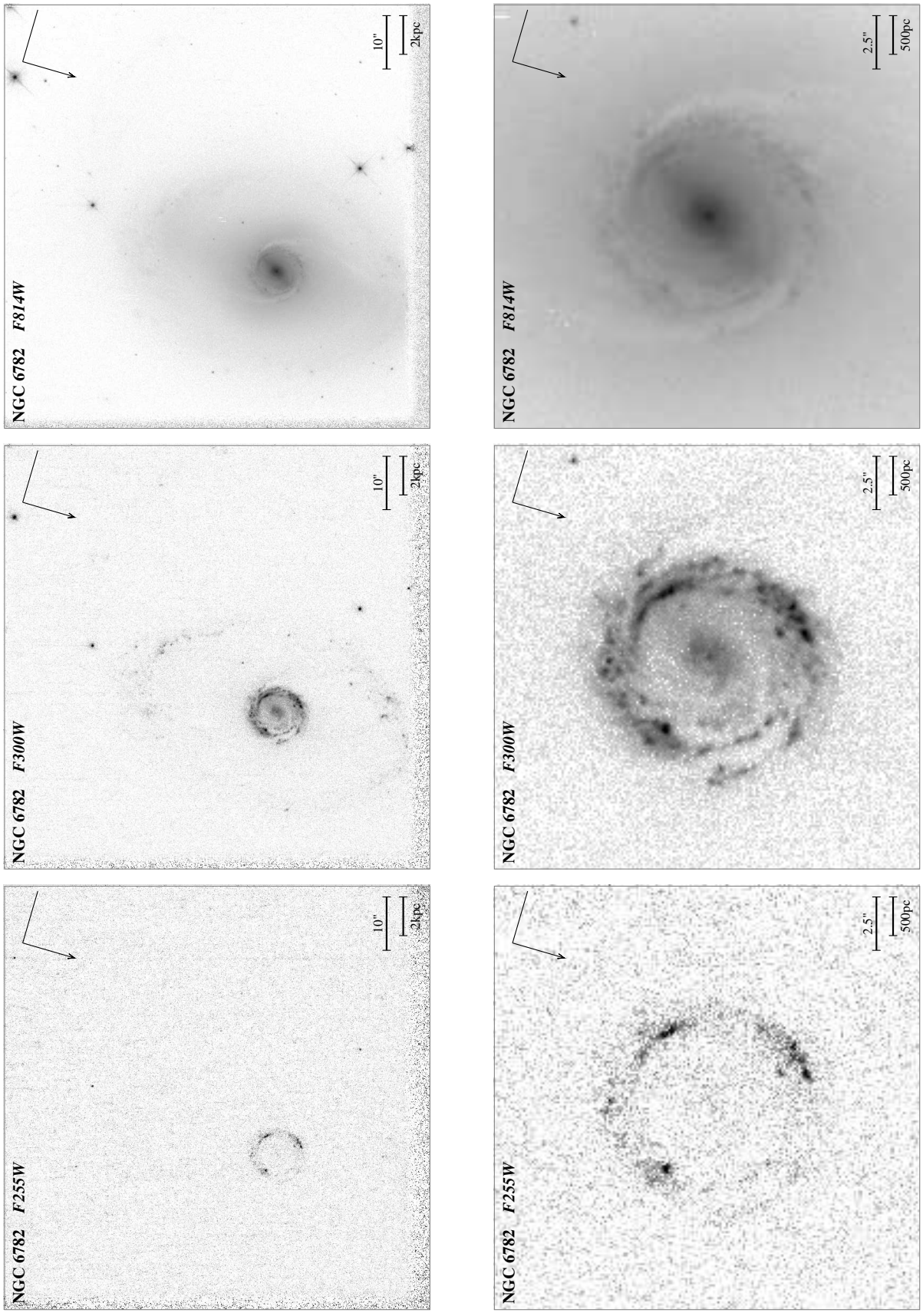

FIG. 3.— SPIRAL GALAXIES WITH INNER RINGS. **3.15a NGC 6782** (*top*): WFPC2 F255W, F300W and F814W; **3.15b NGC 6782** (*bottom*): Enlargement of the central portion of NGC 6782, emphasizing the spectacular ring of hot, young stars.

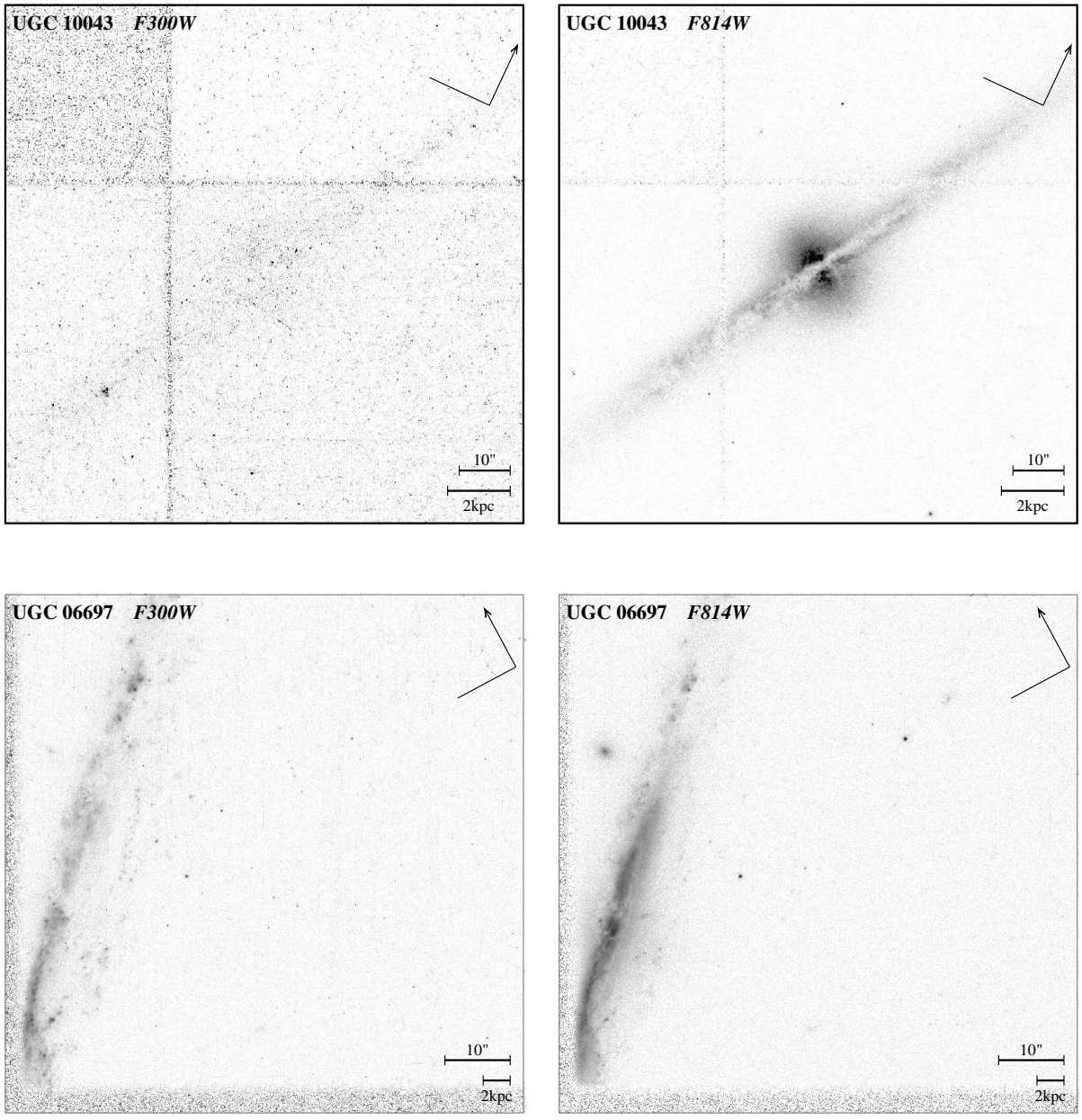

FIG. 3.— EDGE-ON SPIRAL GALAXIES. **3.16 UGC 10043** (*top*): WFPC2 F300W and F814W; **3.17 UGC 06697** (*bottom*): WFPC2 F300W and F814W.

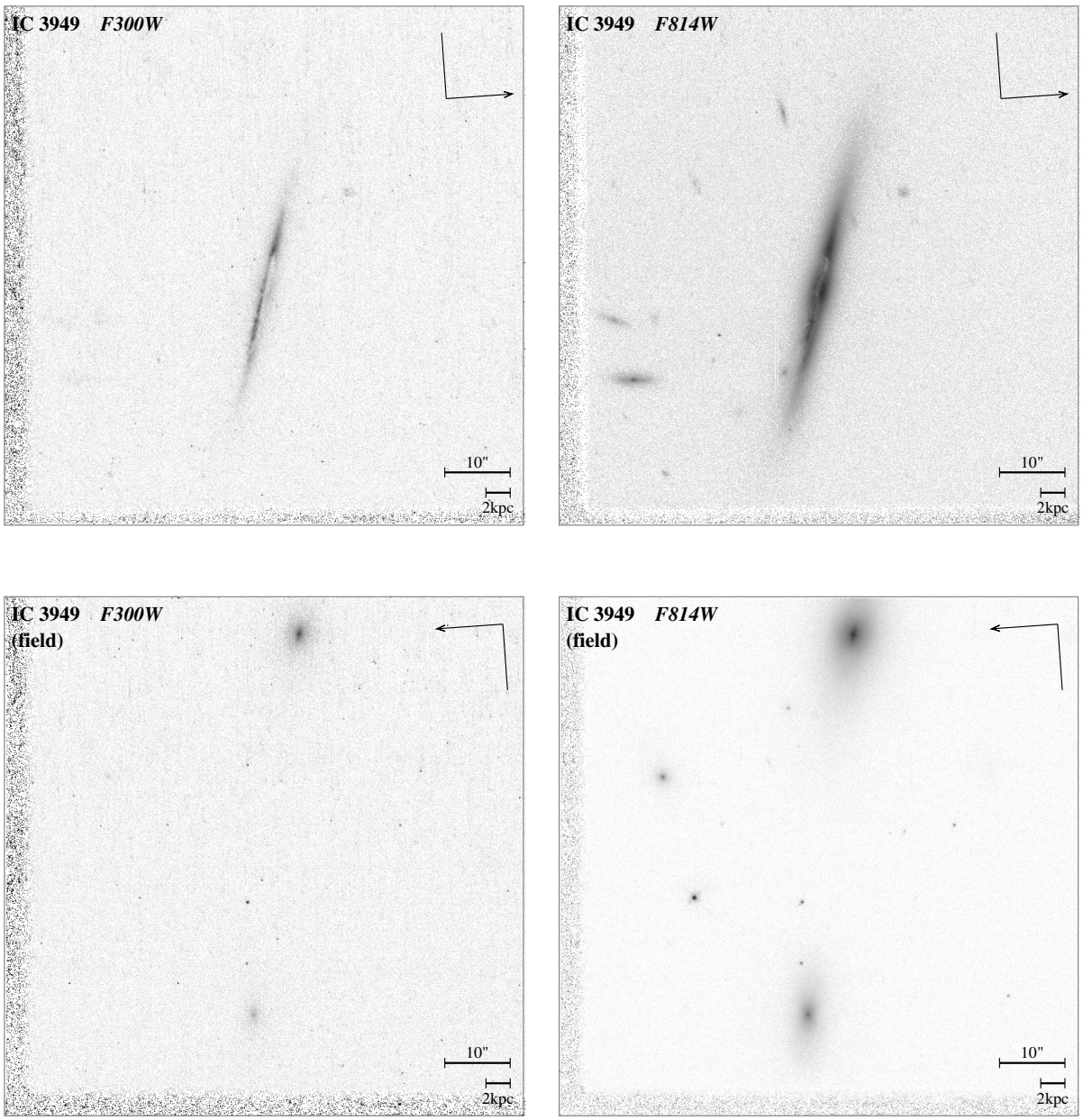

FIG. 3.— (CONT'D) **3.18a IC 3949** (*top*) WFPC2 F300W and F814W. Note the four highly inclined systems visible in F814W that have their major axes pointing toward IC 3949; **3.18b IC 3949 (field)** (*bottom*) Several serendipitously observed early-type galaxies.

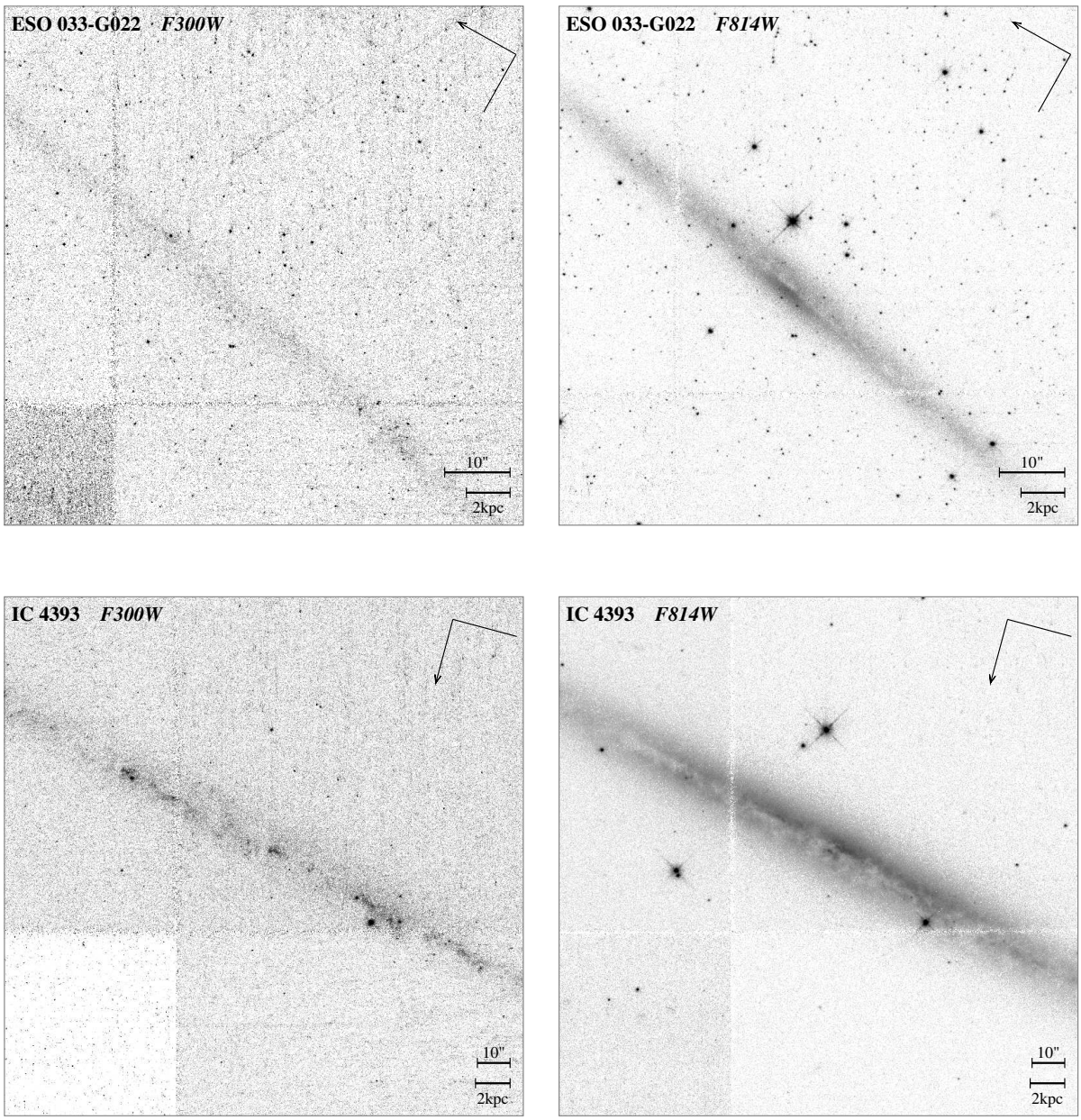

FIG. 3.— (CONT'D) **3.19 ESO 033–G022** (*top*): WFPC2 F300W and F814W; **3.20 IC 4393** (*bottom*): WFPC2 F300W and F814W.

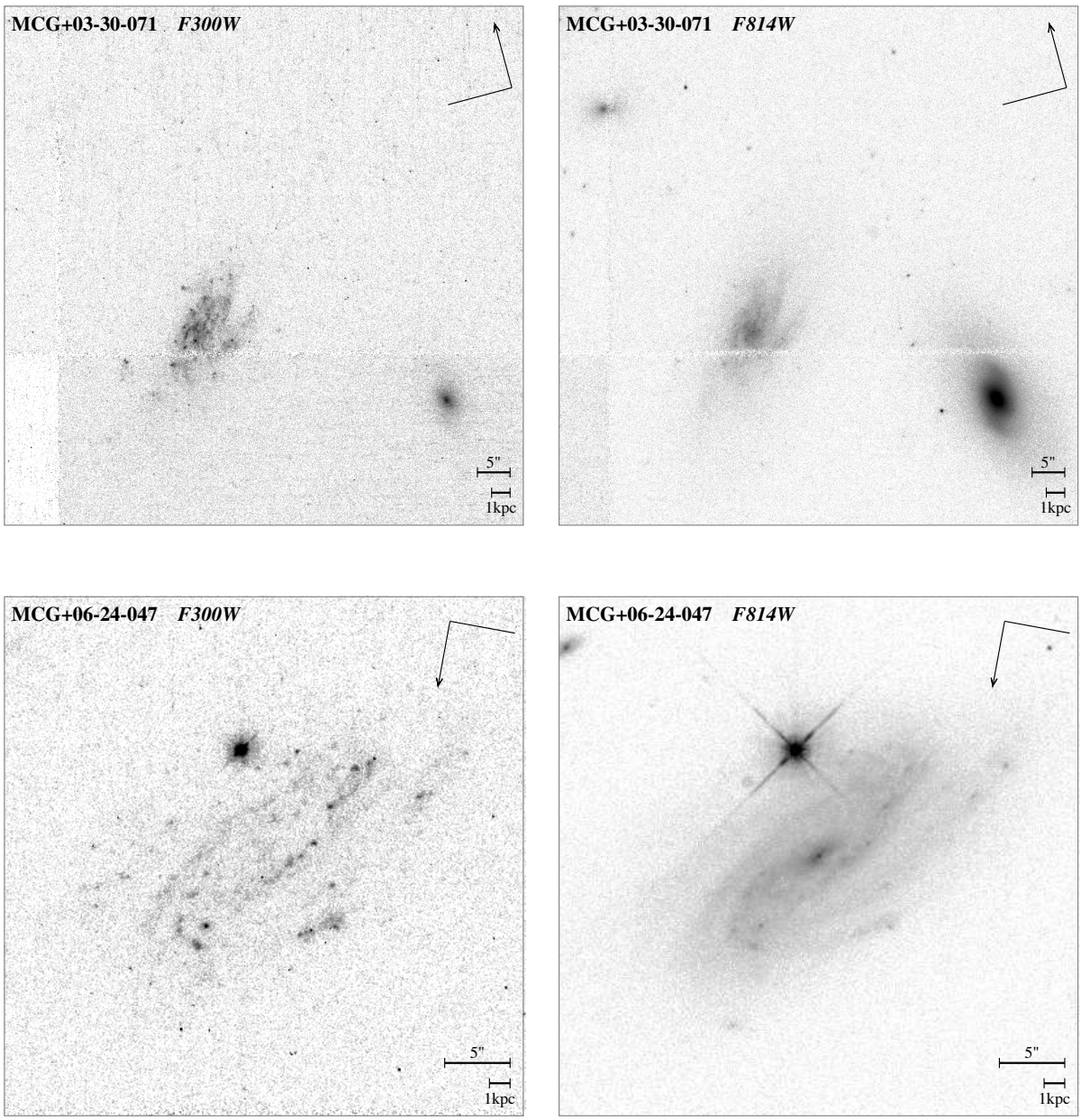

FIG. 3.— LATE-TYPE SPIRALS AND SMALLER SPIRALS. **3.21 MCG+03–30–071** (*top*): WFPC2 F300W and F814W. Also visible is neighboring early-type galaxy MCG+03–30–067. Comparison of the F300W and F814W images of these two galaxies gives the best example of the general trends seen in the present work; **3.22 MCG+06–24–047** (*bottom*): WFPC2 F300W and F814W. The bright point source is a galactic (fore-ground) star.

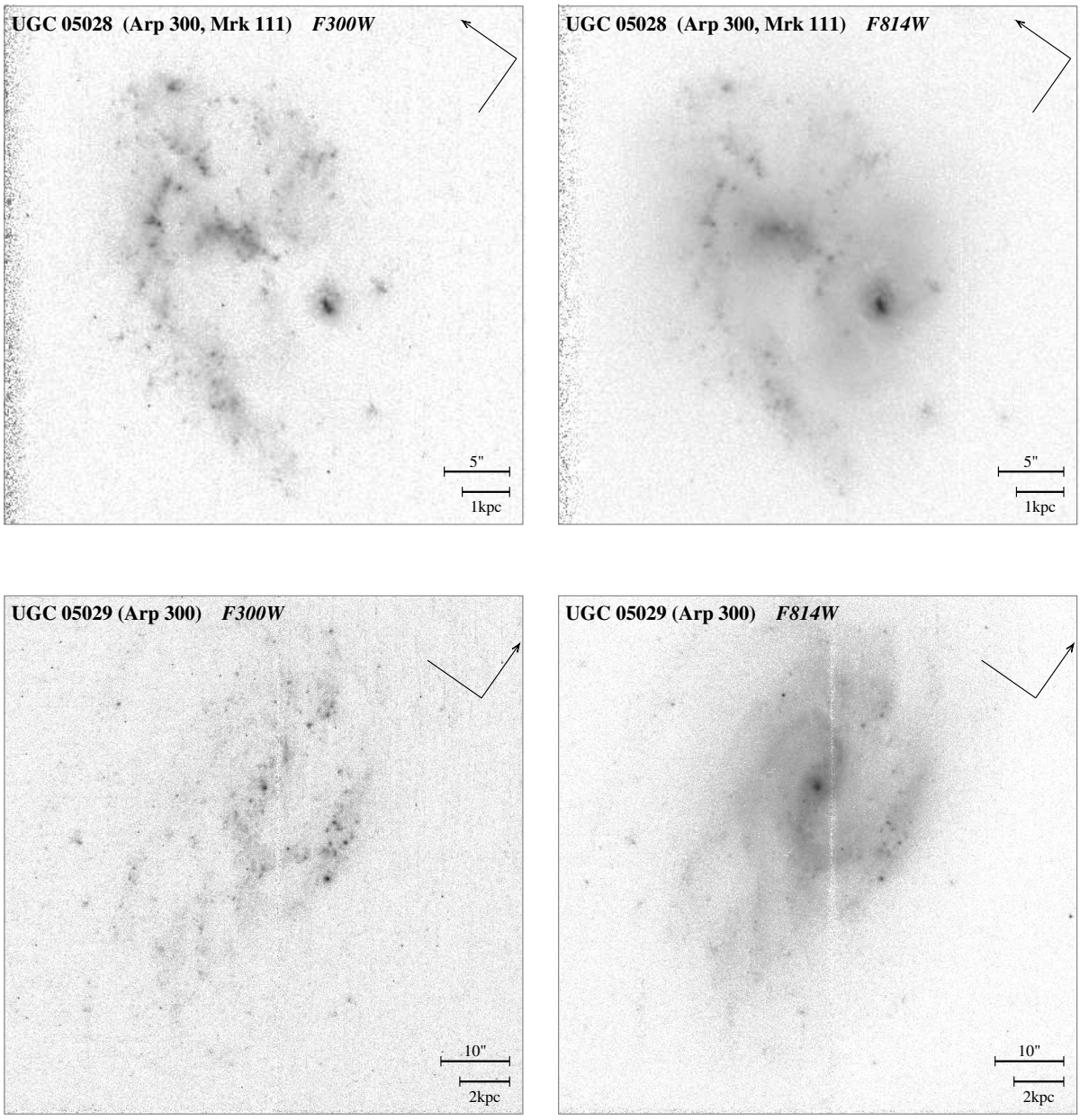

FIG. 3.— (CONT'D) **3.23a UGC 05028** (*top*): WFPC2 F300W and F814W; **3.23b UGC 05029** (*bottom*): WFPC2 F300W and F814W.

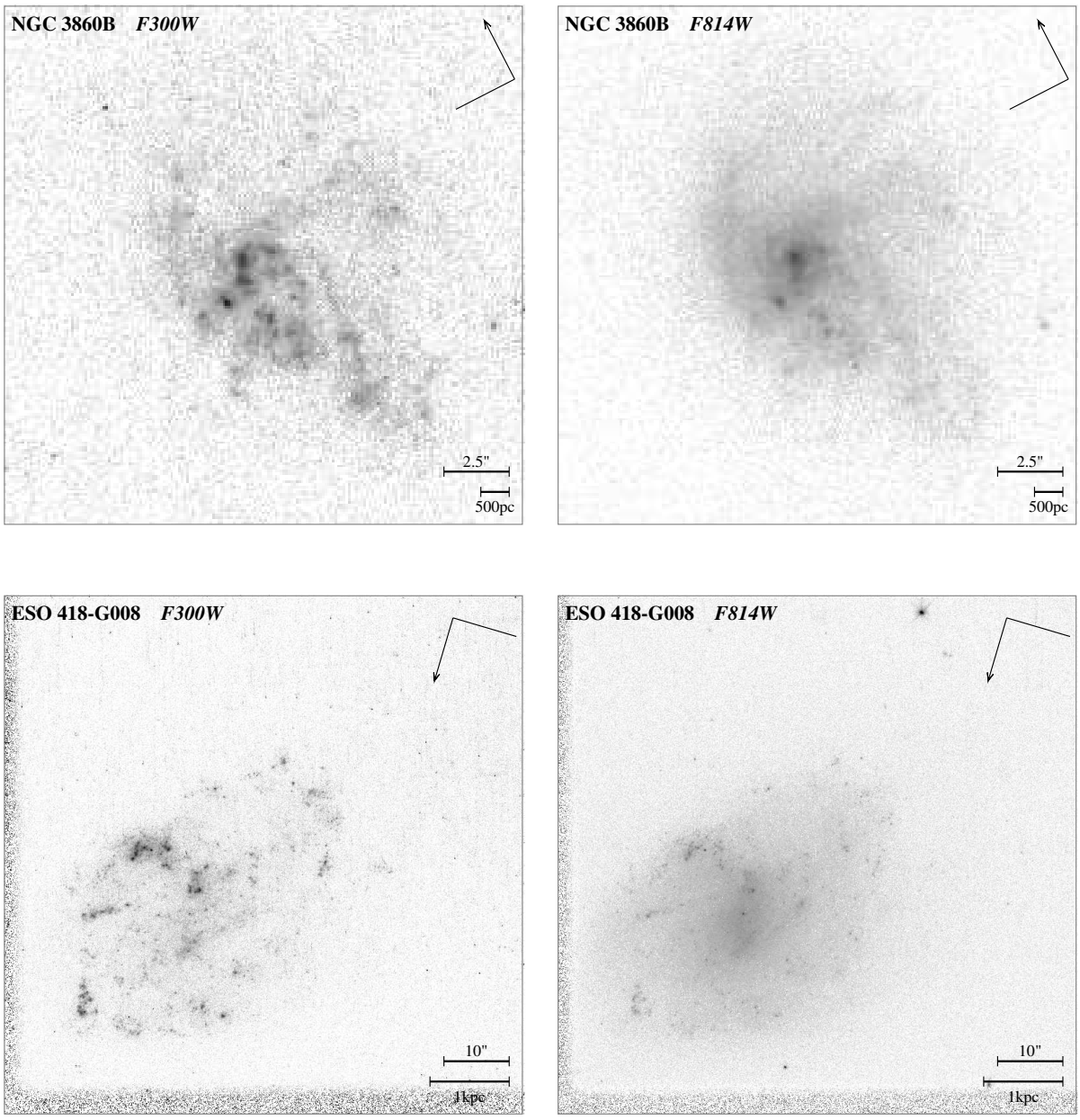

FIG. 3.— (CONT'D) **3.24 NGC 386B** (*top*): F300W and F814W; **3.25 ESO 418–G008** (*bottom*): WFPC2 F300W and F814W.

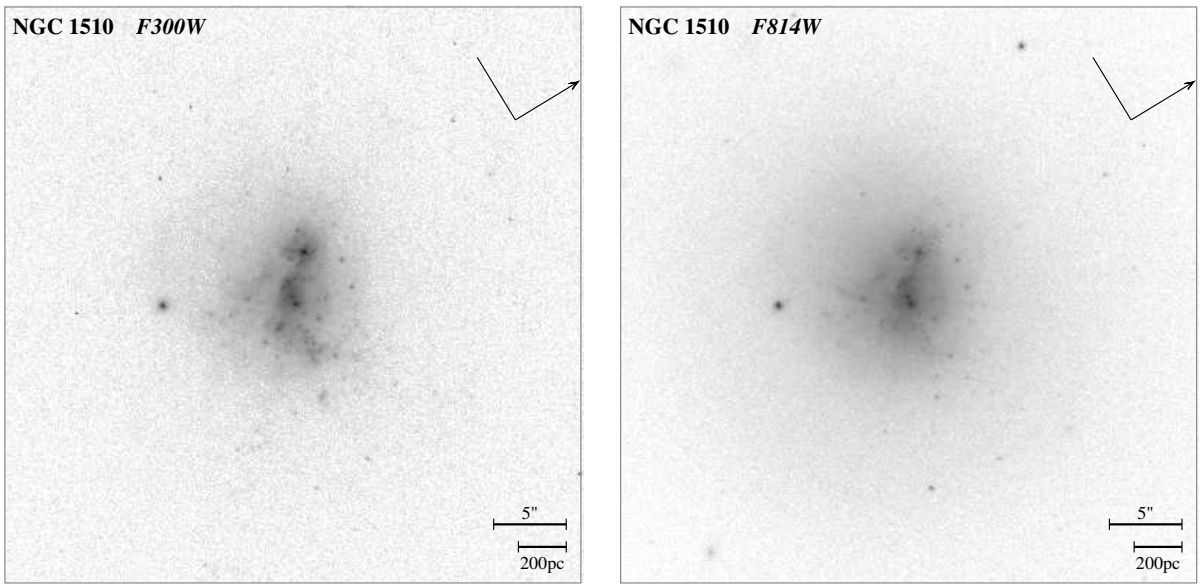

FIG. 3.— (CONT'D) **3.26 NGC 1510**: WFPC2 F300W (*left*) and F814W (*right*).

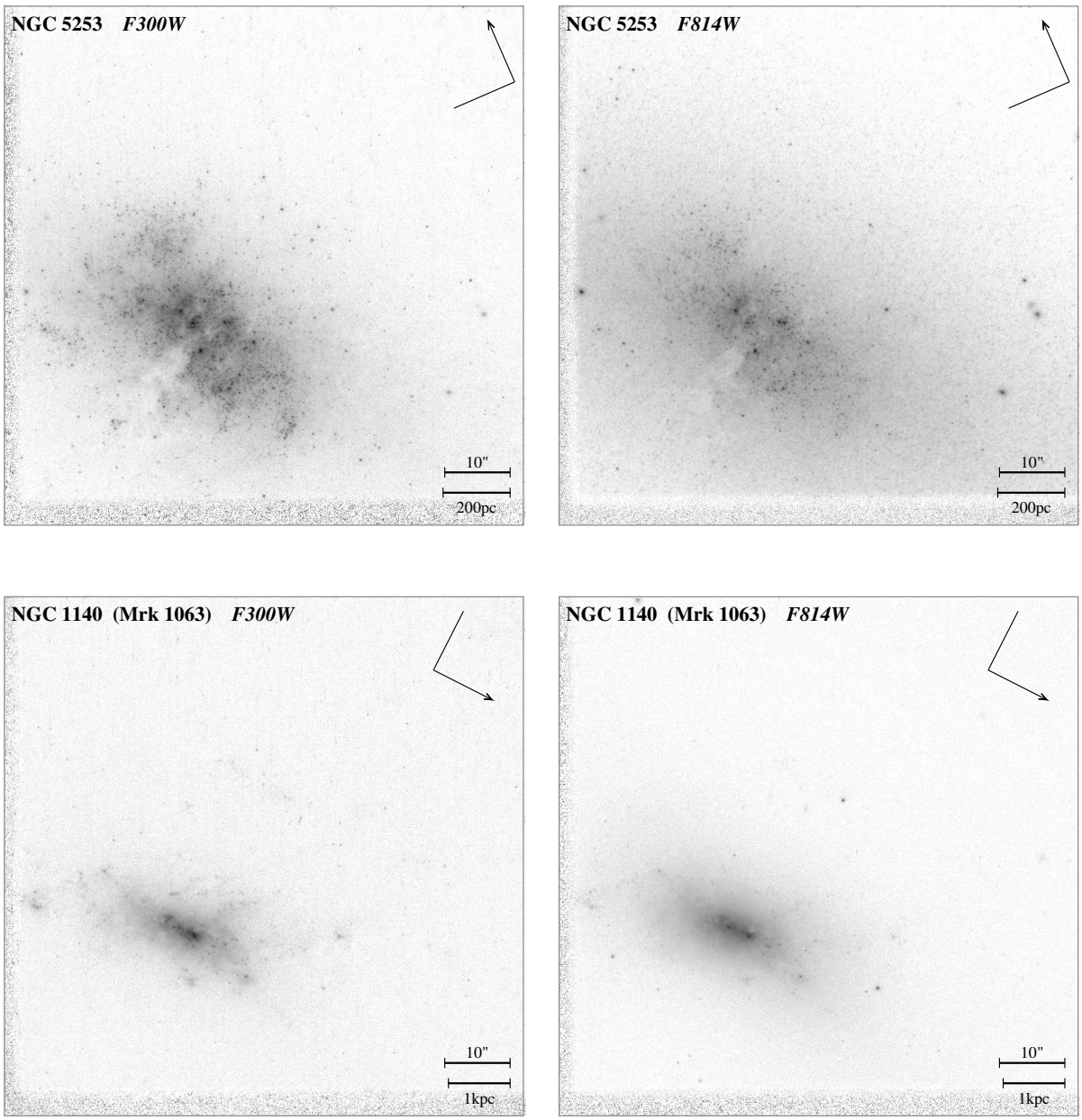

FIG. 3.— MAGELLANIC IRREGULAR GALAXIES. **3.27 NGC 5253** (*top*): WFPC2 F300W and F814W; **3.28 NGC 1140** (*bottom*): WFPC2 F300W and F814W.

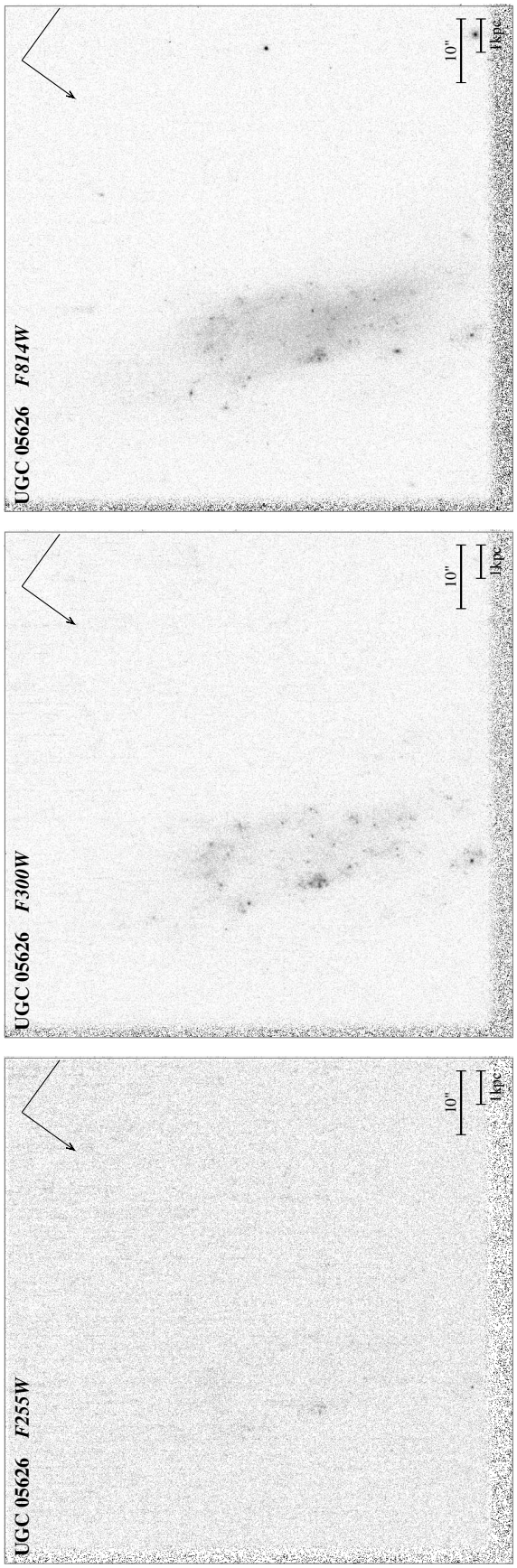

FIG. 3.— (CONT'D) **3.29 UGC 05626**; WFPC2 F255W (*left*), F300W (*middle*), and F814W (*right*).

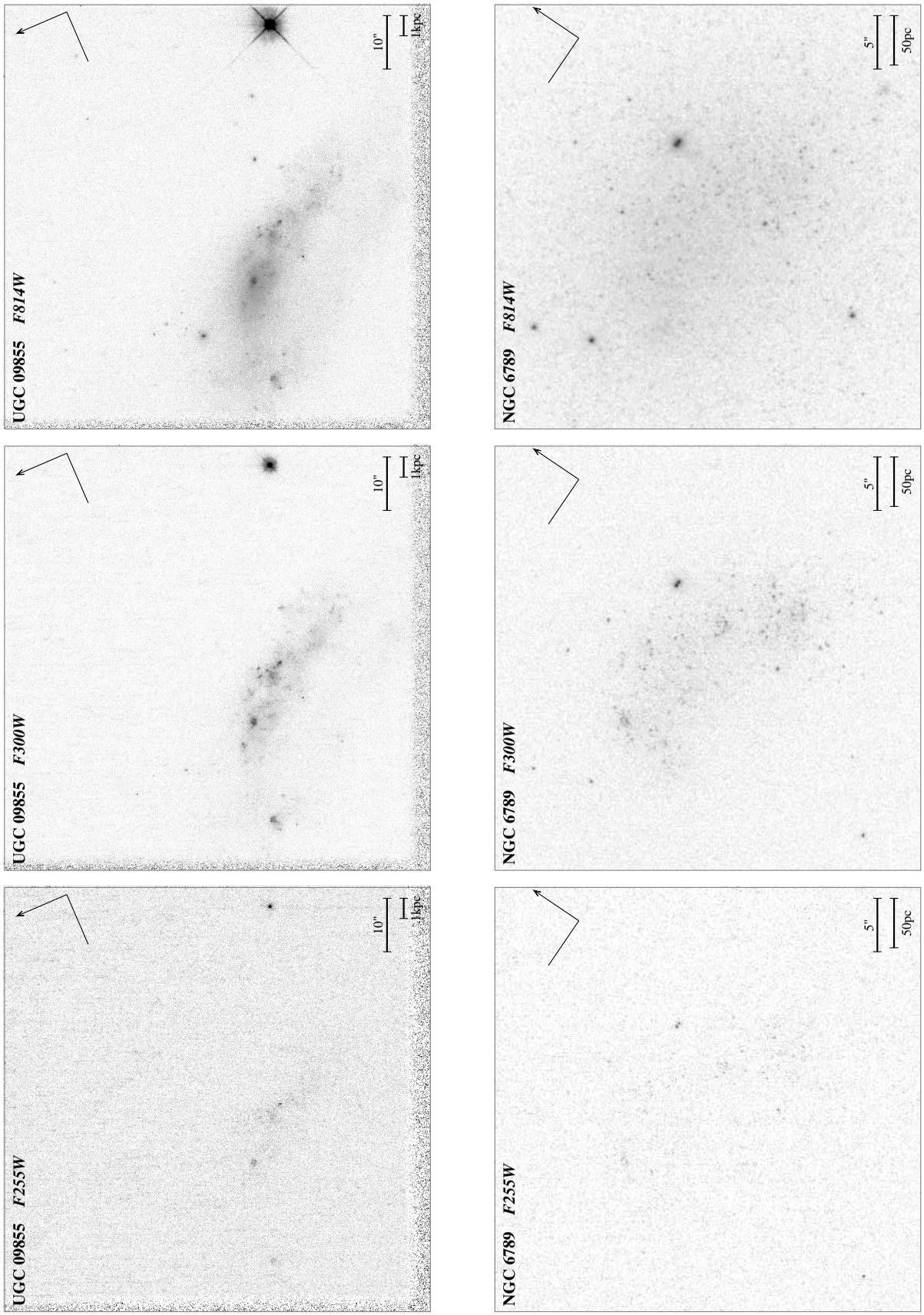

FIG. 3.— (CONT'D) **3.30 UGC 09855** (*top*): WFPC2 F255W, F300W and F814W; **3.31 NGC 6789** (*bottom*): WFPC2 F255W, F300W and F814W.

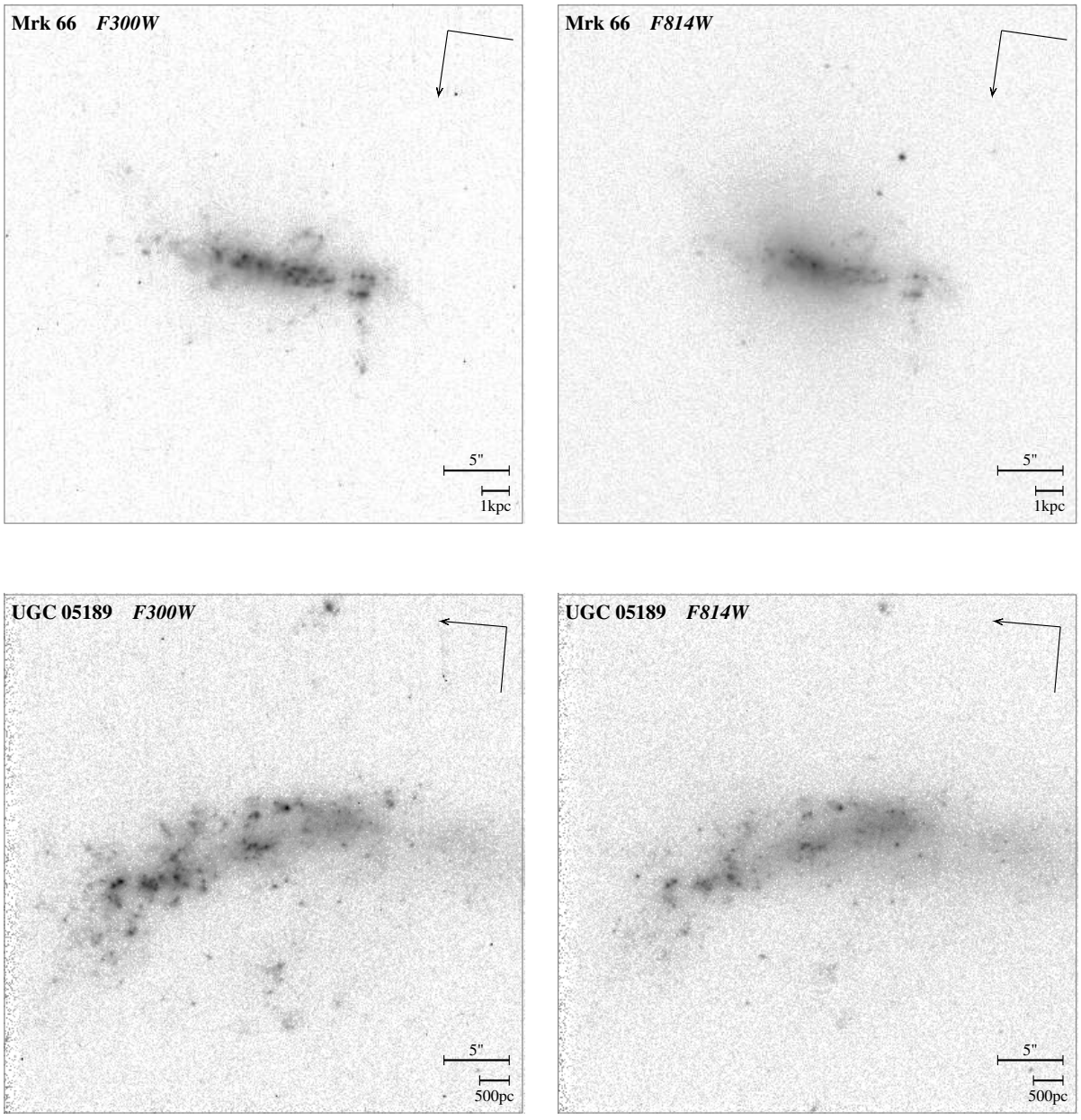

FIG. 3.— (CONT'D) **3.32 Mrk 66** (*top*): WFPC2 F300W and F814W; **3.33 UGC 05189** (*bottom*): WFPC2 F300W and F814W.

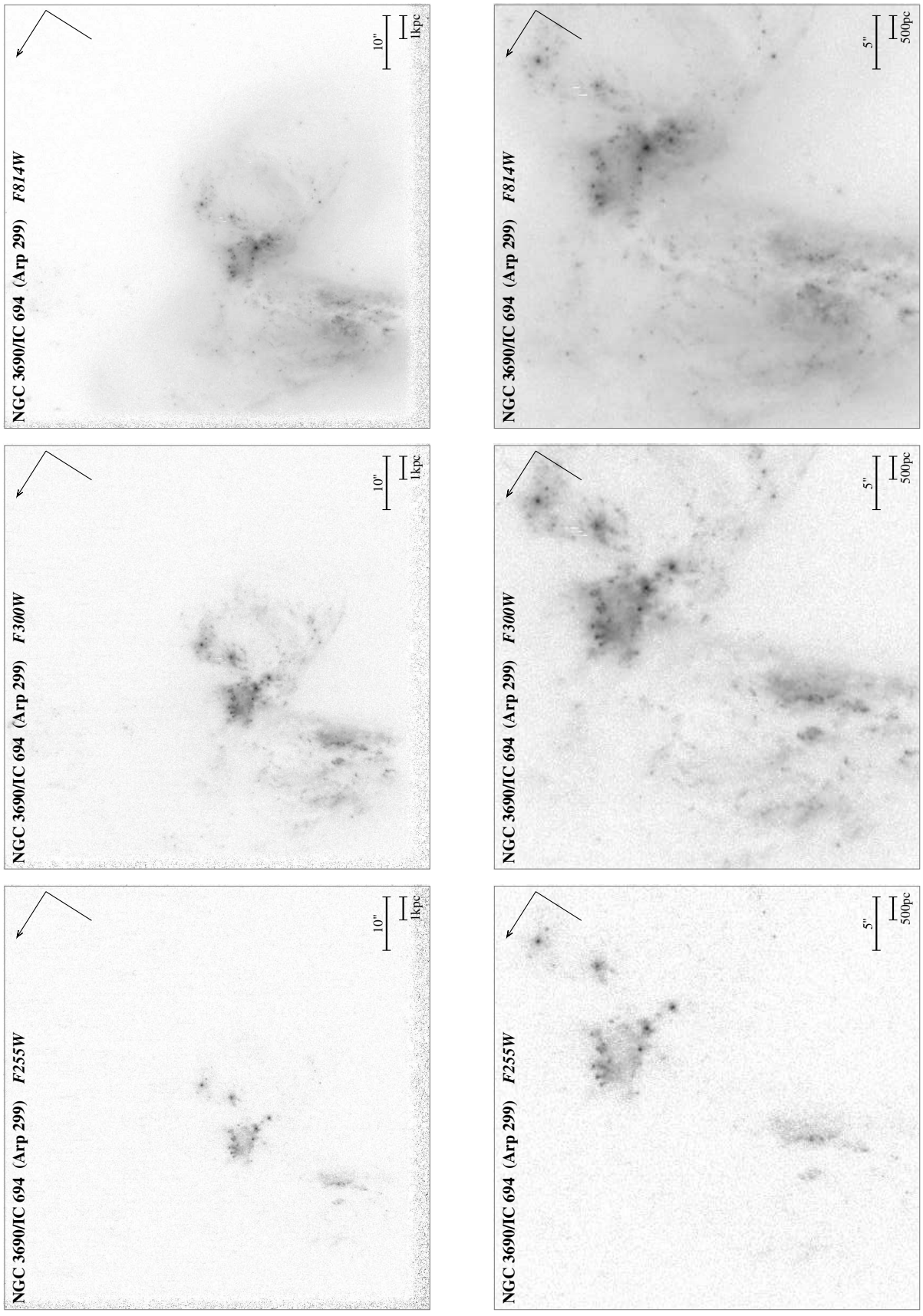

FIG. 3.— INTERACTING, PECULIAR, AND MERGING GALAXIES: **3.34a NGC 3690/IC 694** (*top*): WFPC2 F255W, F300W and F814W; **3.34b NGC 3690/IC 694** (*bottom*): Enlargement of the central portion of this merging galaxy pair, emphasizing the dusty patches and star forming knots.

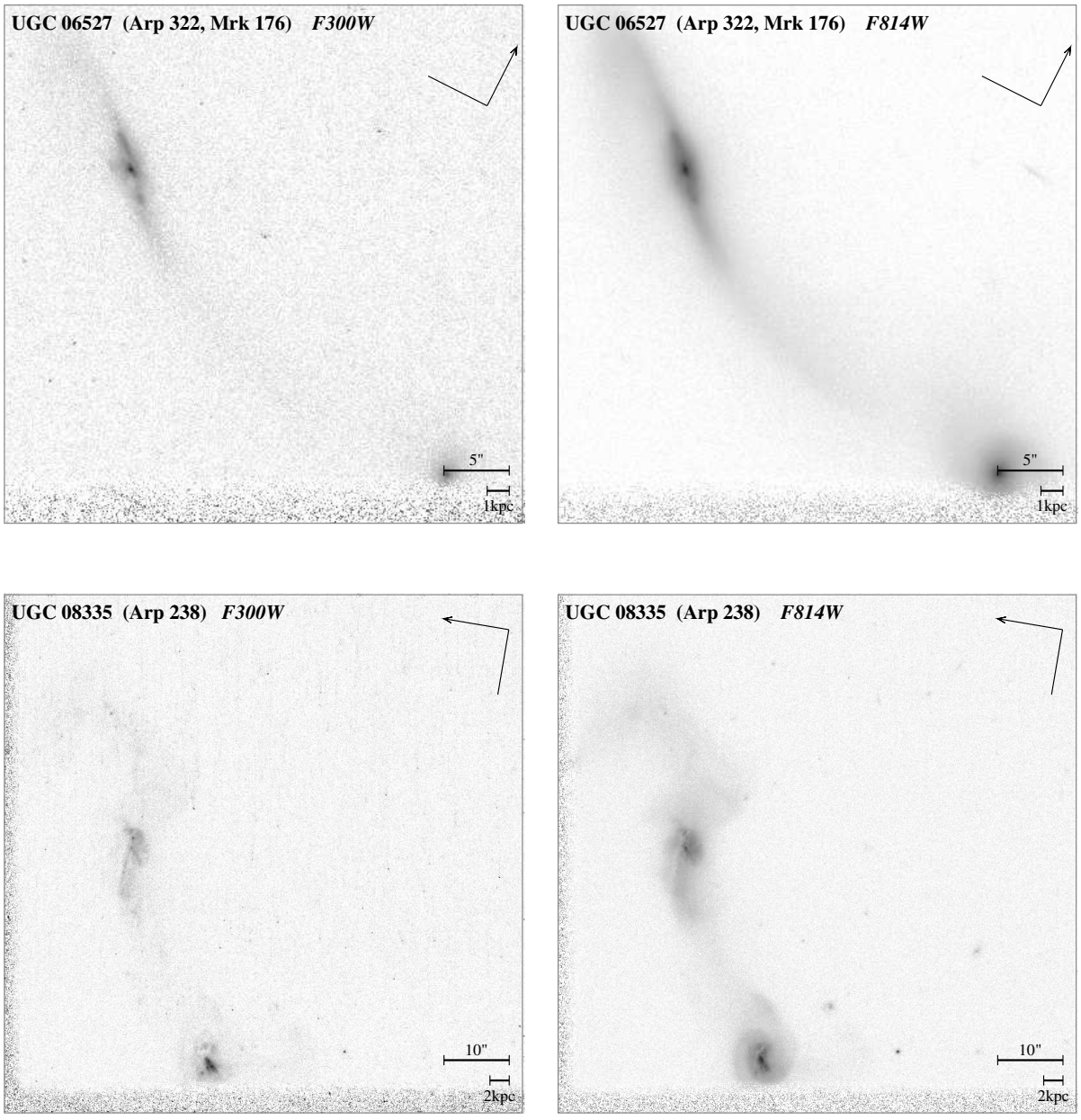

FIG. 3.— (CONT'D) **3.35 UGC 06527** (*top*): WFPC2 F300W and F814W; **3.36 UGC 08335** (*bottom*): WFPC2 F300W and F814W.

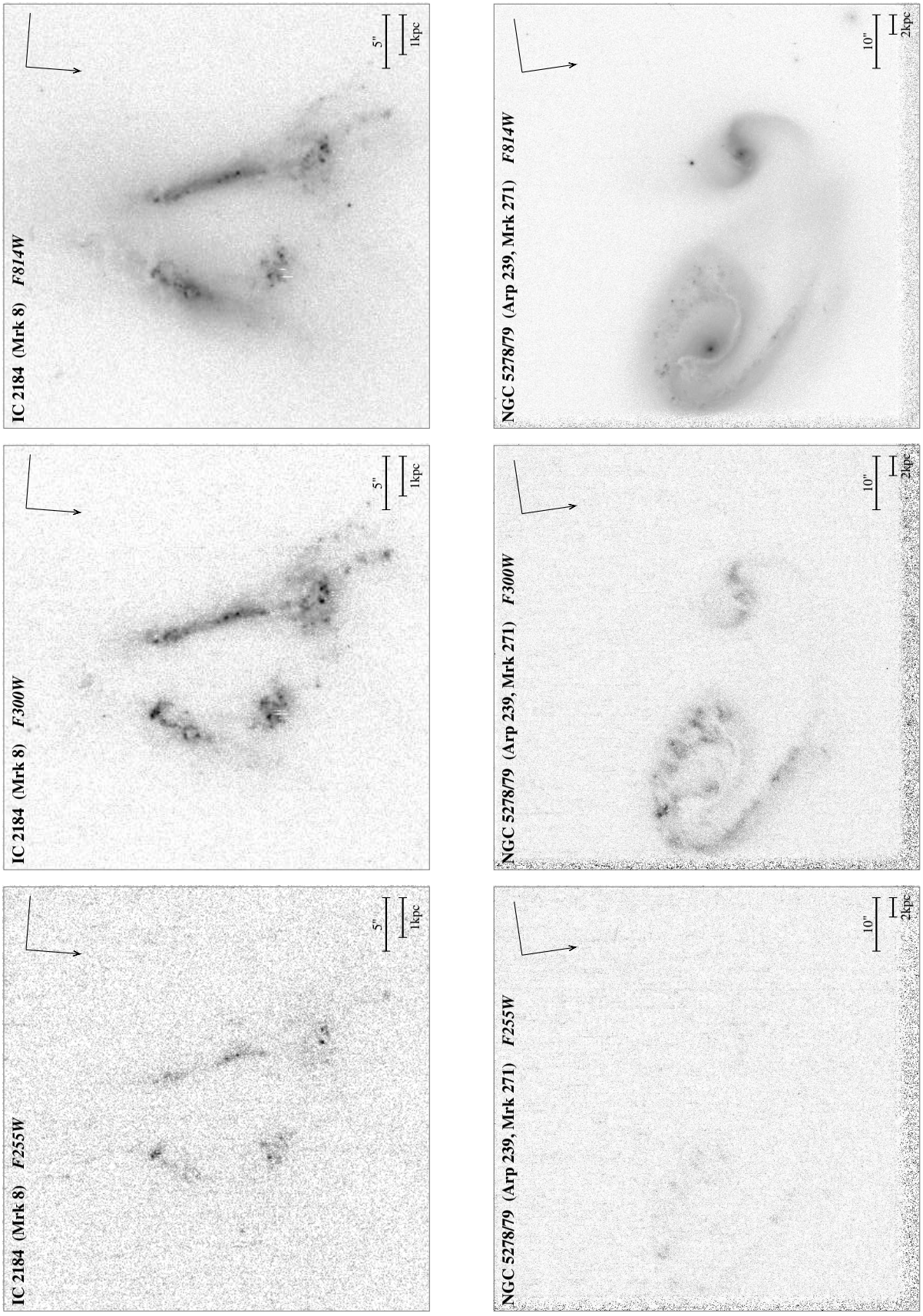

FIG. 3.— (CONT'D) **3.37 IC 2184** (*top*): WFPC2 F255W, F300W, and F814W; **3.38 NGC 5278/79** (*bottom*): WFPC2 F255W, F300W, and F814W.

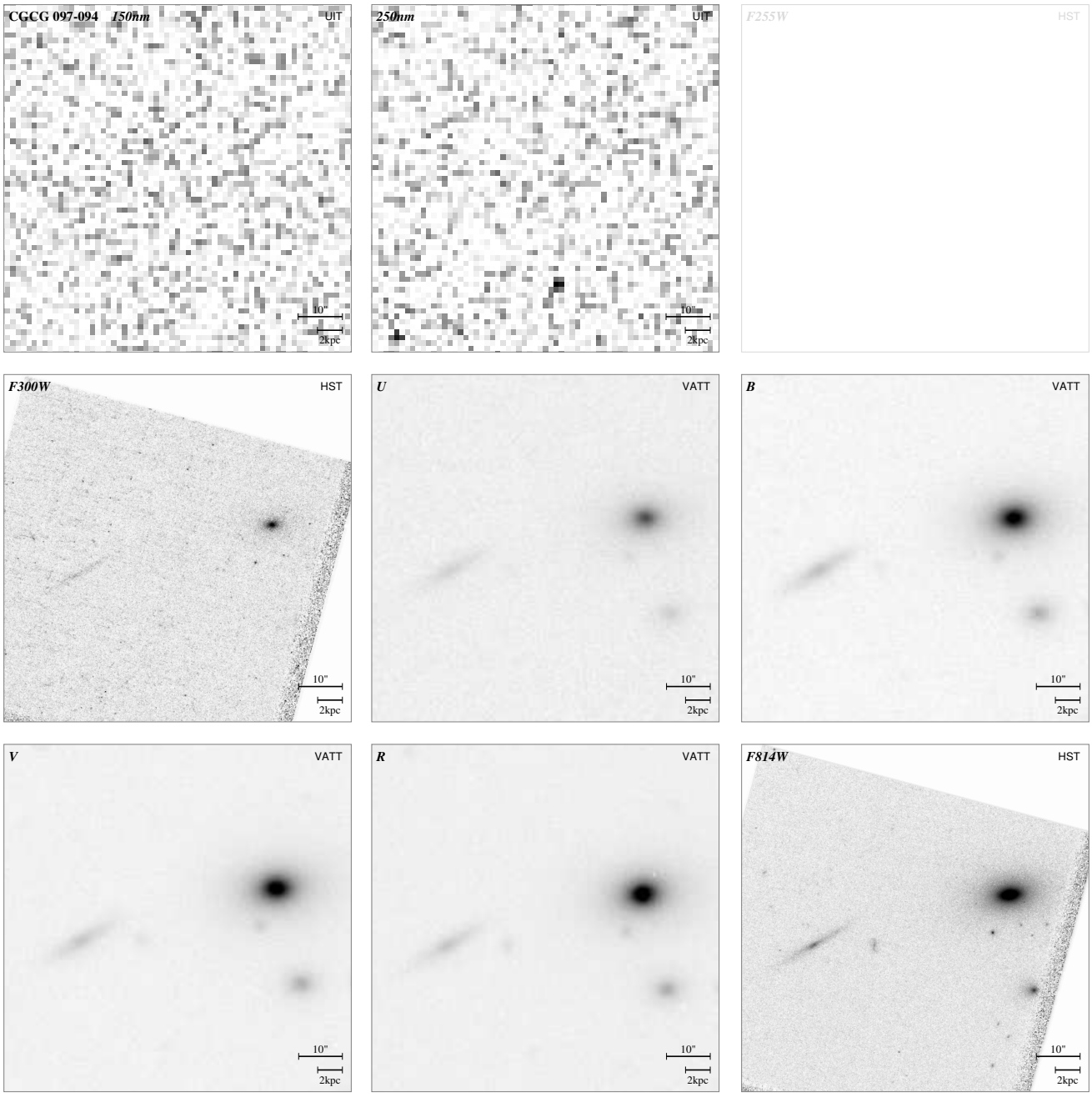

FIG. 4.— Pan-chromatic atlas of far- and mid-UV (*UIT*), mid-UV (*HST*/WFPC2), and ground-based optical *UBVR* and near-IR *JHK* (ground or *HST*/NICMOS) observations of the 37 nearby galaxies in the present sample. As in Fig. 3, the galaxies are sorted and numbered according to morphology, and each of the grey-scale renditions is displayed using a logarithmic stretch. Unlike Fig. 3, all images have been rotated to have North up and East to the left, and are presented on a common plate scale. The printed version contains only a few example pages; for the full atlas we refer the reader to the electronic version.
— MID-UV-FAINT ELLIPTICAL GALAXIES. **4.01 CGCG 097–094** (*top*): *UIT* 150nm and 250nm; (*middle*): *HST*/WFPC2 F300W, and ground-based *U* and *B*; (*bottom*): ground-based *V* and *R*, and *HST*/WFPC2 F814W.

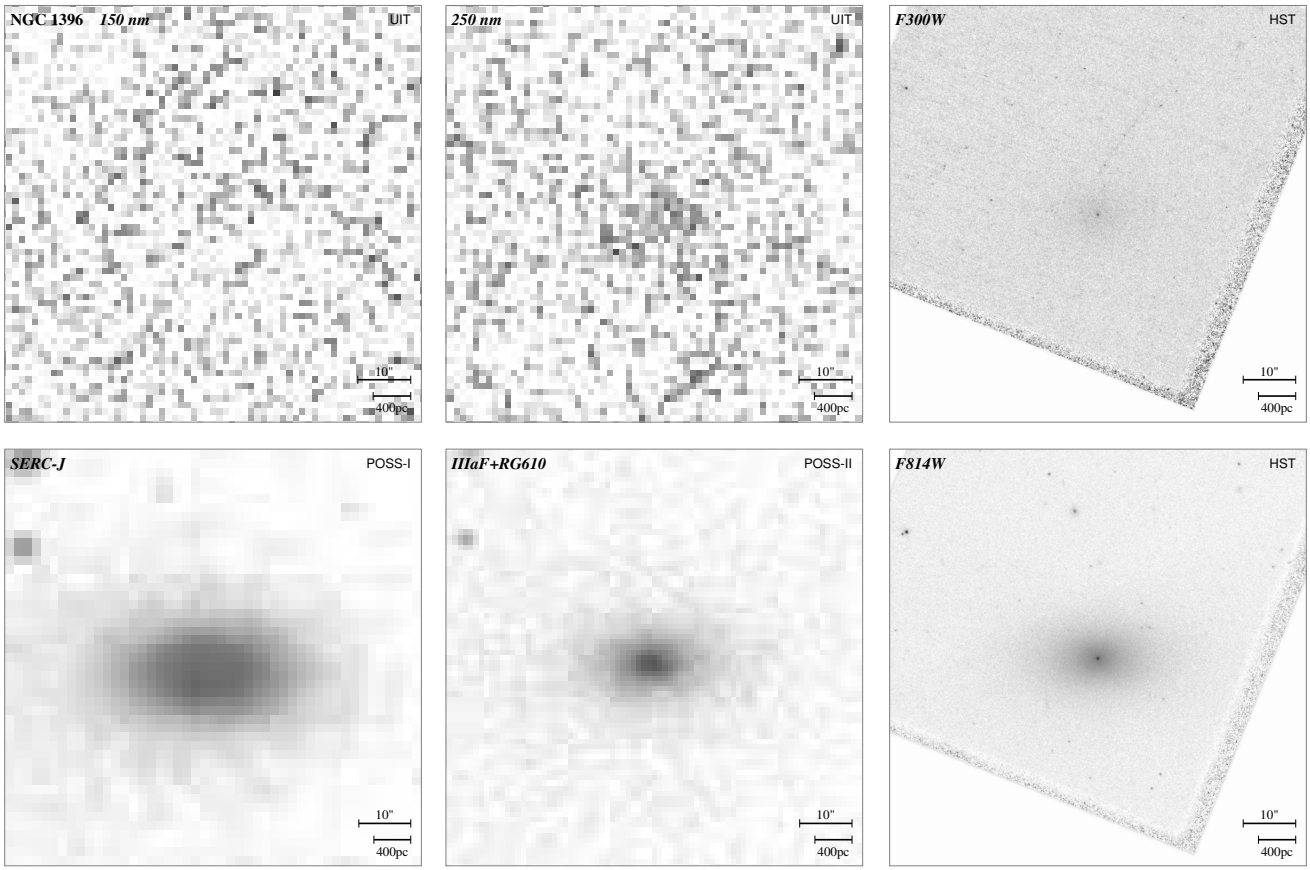

FIG. 4.— (CONT'D) **4.02 NGC 1396** (*top*): *UIT* 150nm and 250nm, and *HST*/WFPC2 F300W; (*bottom*): photographic *J* (blue) and IIIaF+RG610 (red), and *HST*/WFPC2 F814W.

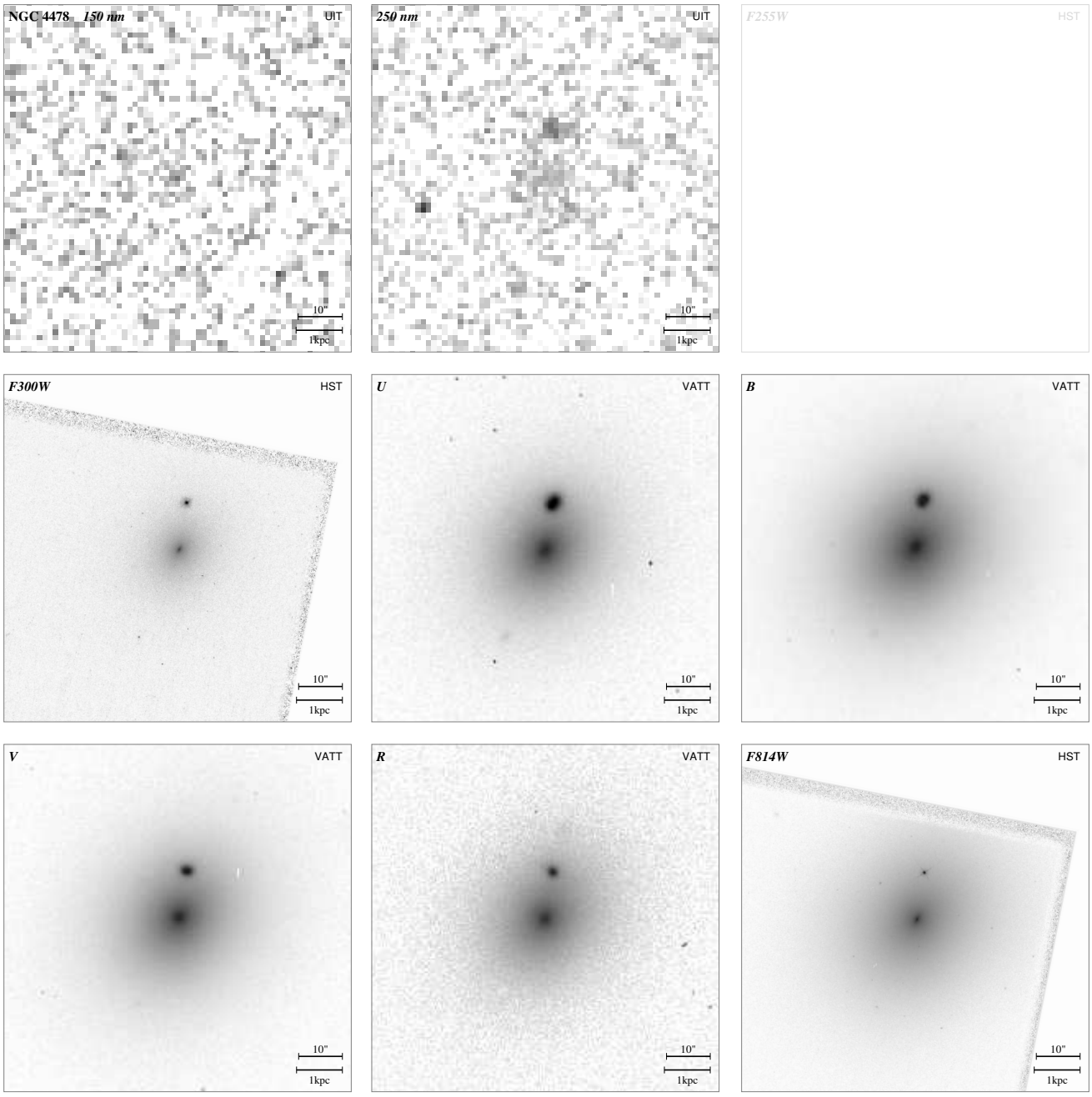

FIG. 4.— (CONT'D) **4.03 NGC 4478** (*top*): *UIT* 150nm and 250nm; (*middle*): WFPC2 F300W, and ground-based *U* and *B*; (*bottom*): ground-based *V* and *R*, and *HST*/WFPC2 F814W.

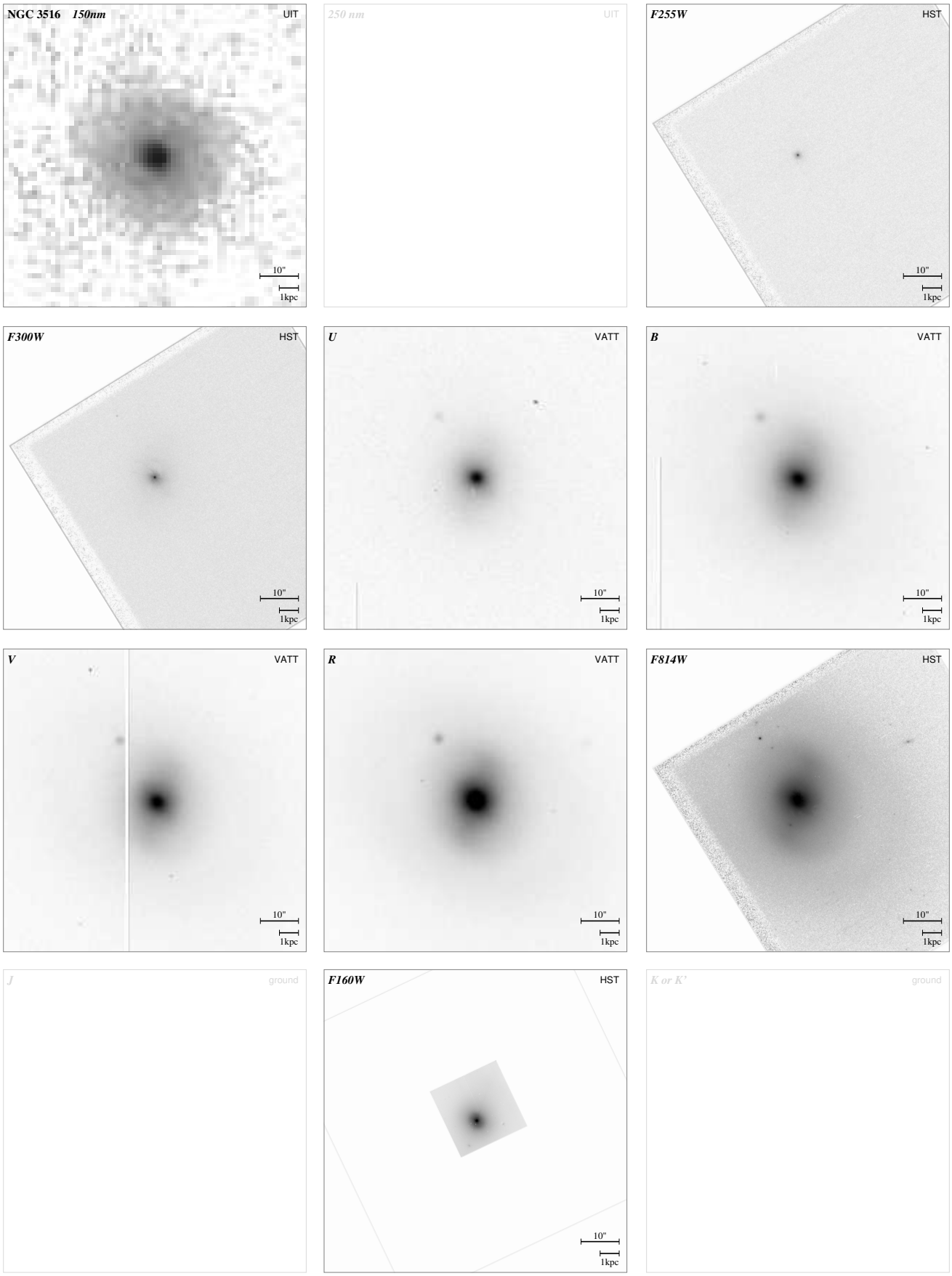

FIG. 4.— EARLY-TYPE GALAXIES WITH SIGNIFICANT AGN EMISSION IN THE MID-UV. **4.04 NGC 3516** (*top*): *UIT* 150nm, and *HST*/WFPC2 F255W; (2^{nd} *row*): *HST*/WFPC2 F300W, and ground-based *U* and *B*; (3^{rd} *row*): ground-based *V* and *R*, and *HST*/WFPC2 F814W; (*bottom*): *HST*/NICMOS F160W (*H*).

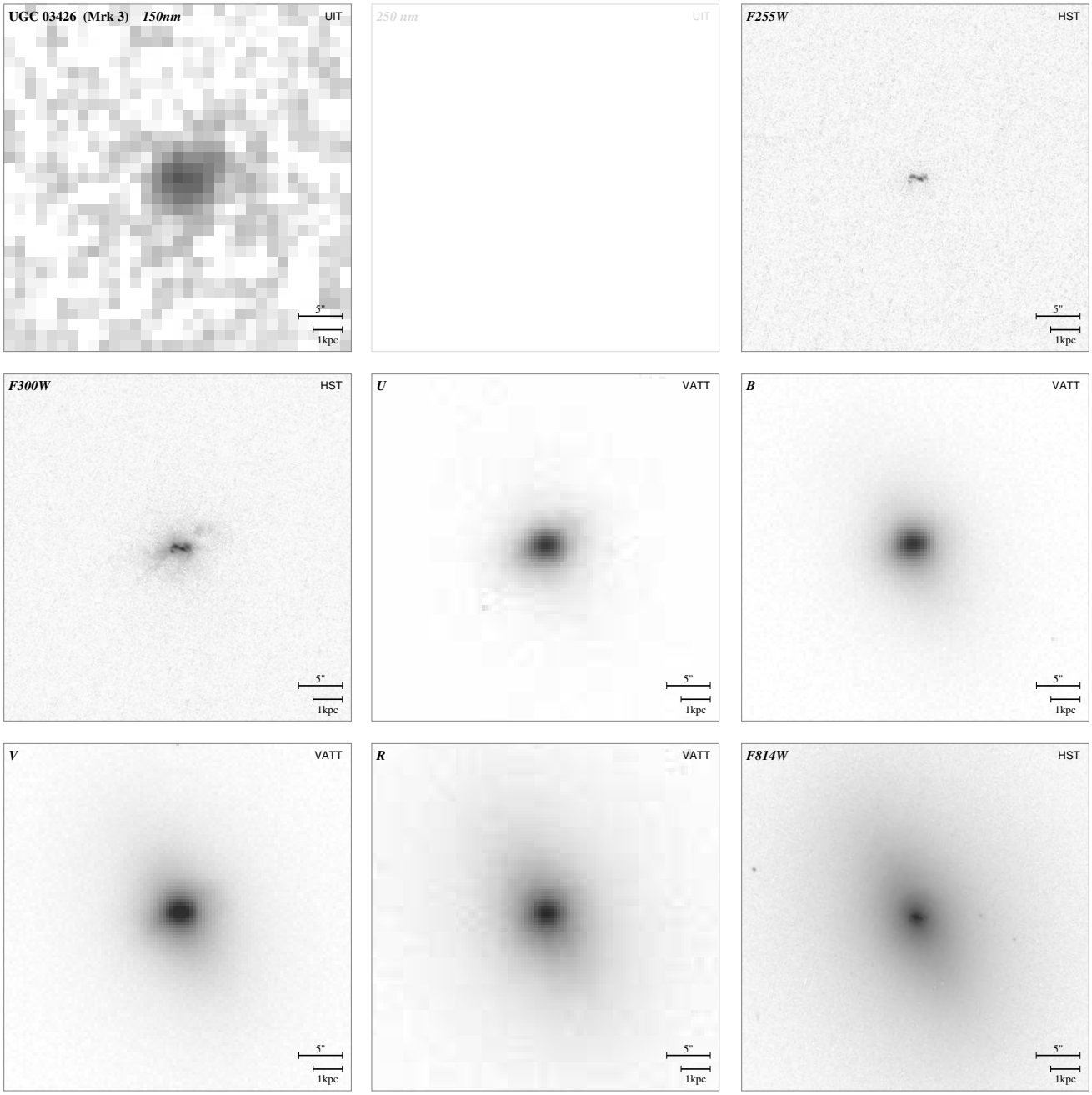

FIG. 4.— (CONT'D) **4.05 UGC 03426** (*top*): *UIT* 150nm and *HST*/WFPC2 F255W; (*middle*): *HST*/WFPC2 F300W, and ground-based *U* and *B*; (*bottom*): ground-based *V* and *R*, and *HST*/WFPC2 F814W.

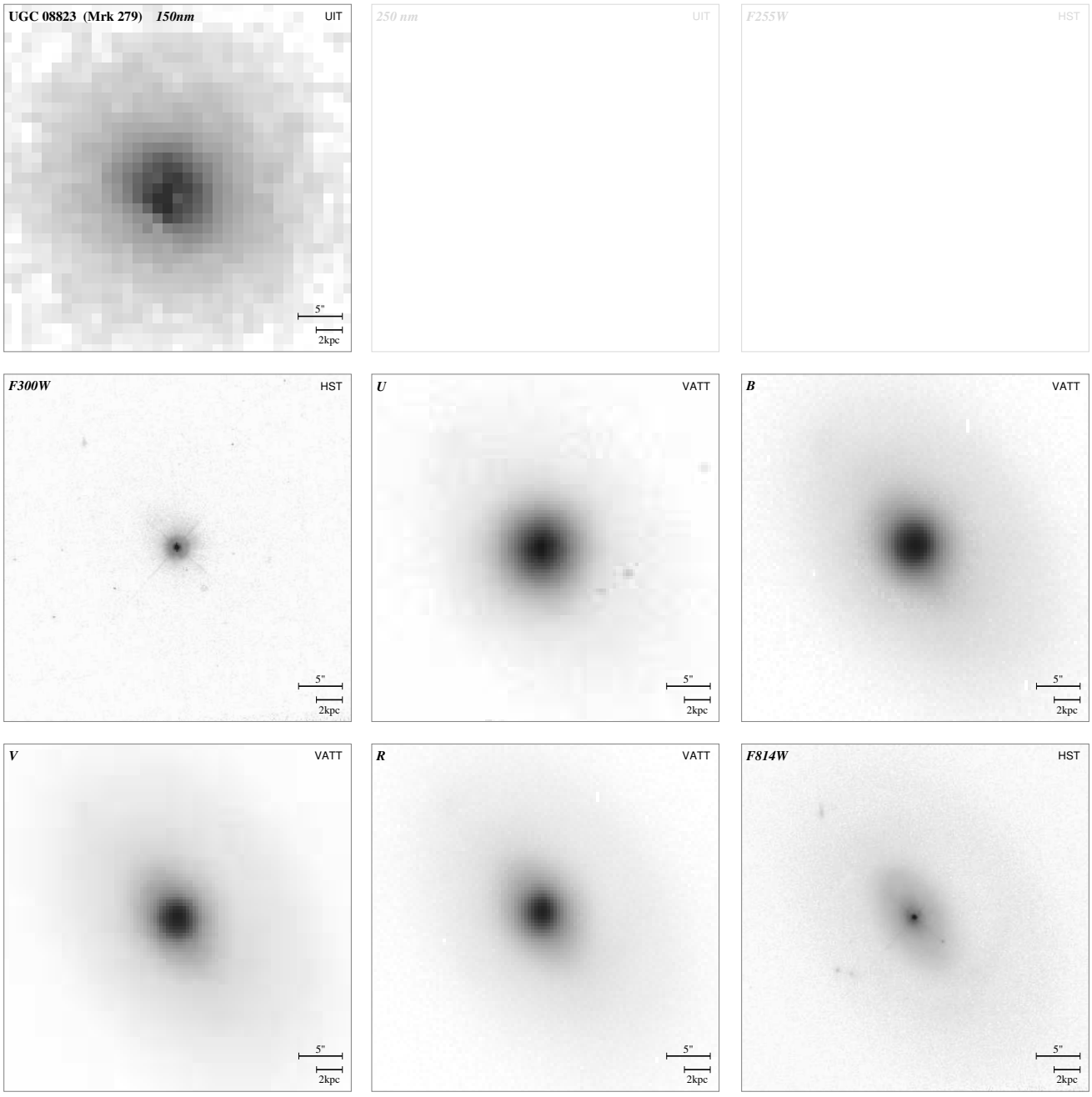

FIG. 4.— (CONT'D) **4.06 UGC 08823** (*top*): *UIT* 150nm; (*middle*): *HST*/WFPC2 F300W, and ground-based *U* and *B*; (*bottom*): ground-based *V* and *R*, and *HST*/WFPC2 F814W.

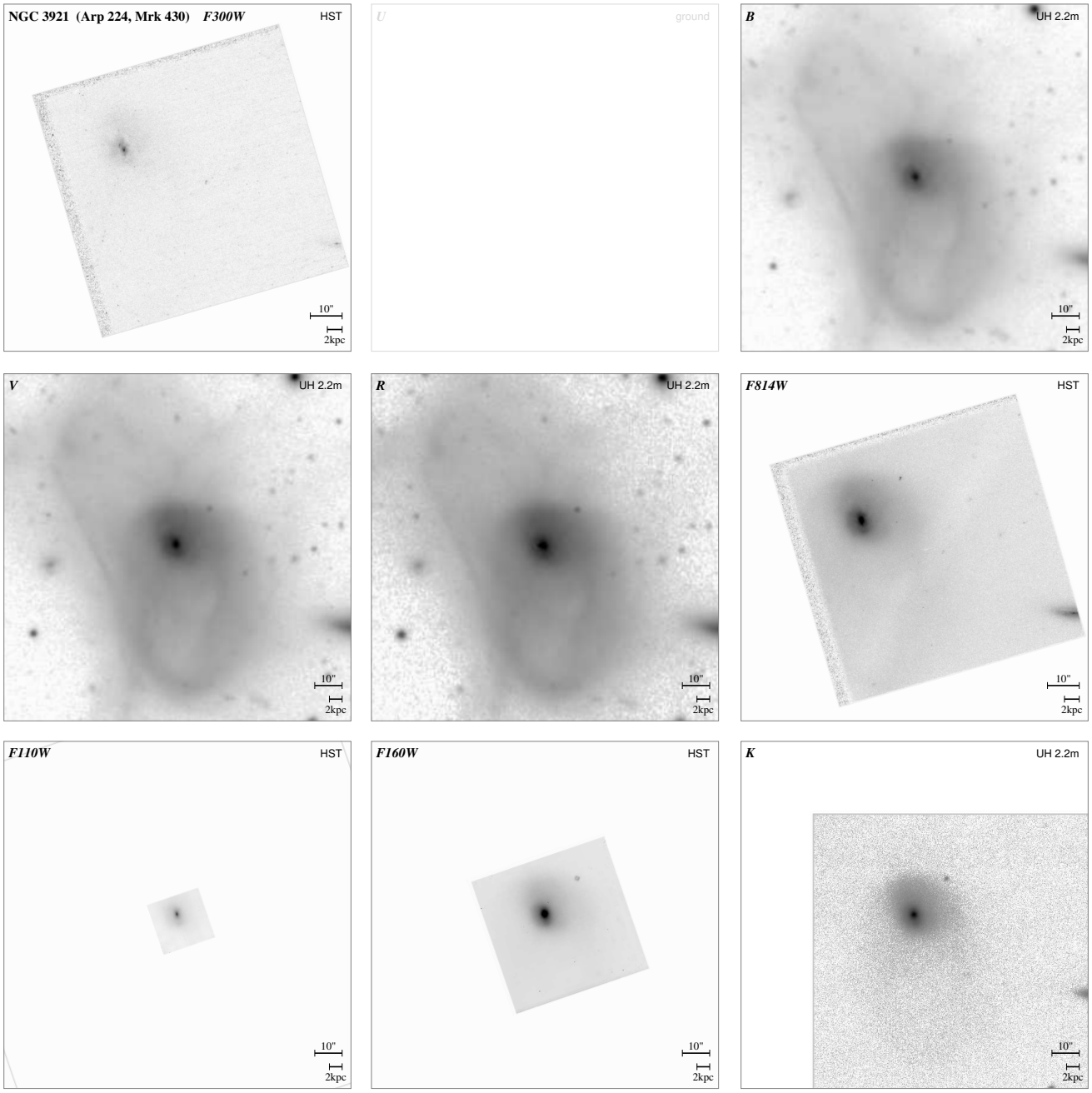

FIG. 4.— EARLY-TYPE GALAXIES SHOWING EVIDENCE FOR RECENT MERGING OR STRONG INTERACTION. **4.07 NGC 3921** (*top*): *HST*/WFPC2 F300W, and ground-based *B*; (*middle*): ground-based *V* and *R*, and *HST*/WFPC2 F814W; (*bottom*): *HST*/NICMOS F110W (*J*) and F160W (*H*), and ground-based *K*.

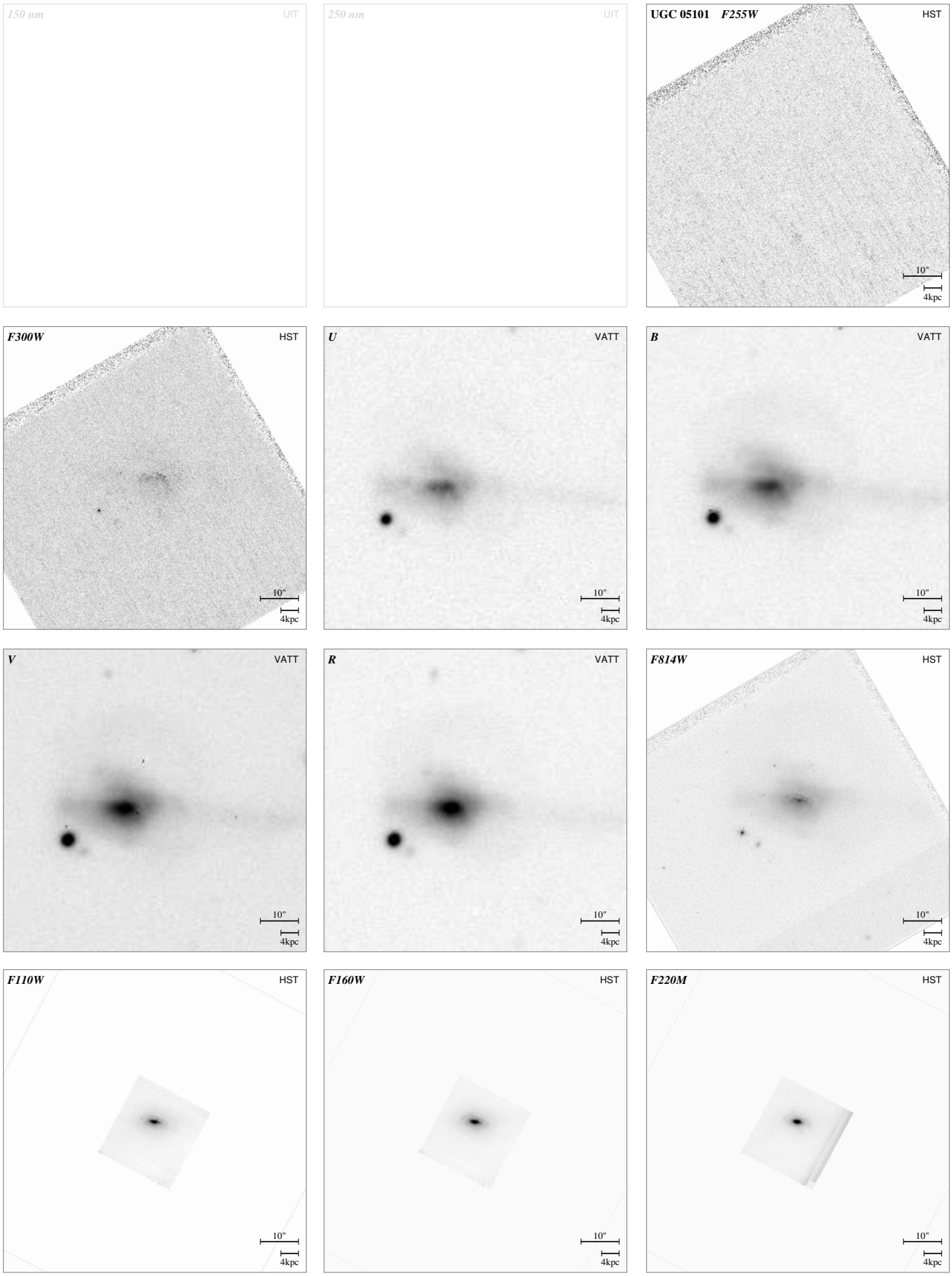

FIG. 4.— (CONT'D) **4.08 UGC 05101** (*top*): *HST*/WFPC2 F255W; (2^{nd} *row*): *HST*/WFPC2 F300W, and ground-based *U* and *B*; (3^{rd} *row*): ground-based *V* and *R*, and *HST*/WFPC2 F814W; (*bottom*): *HST*/NICMOS F110W (*J*), F160W (*H*), and F220M (*K*).

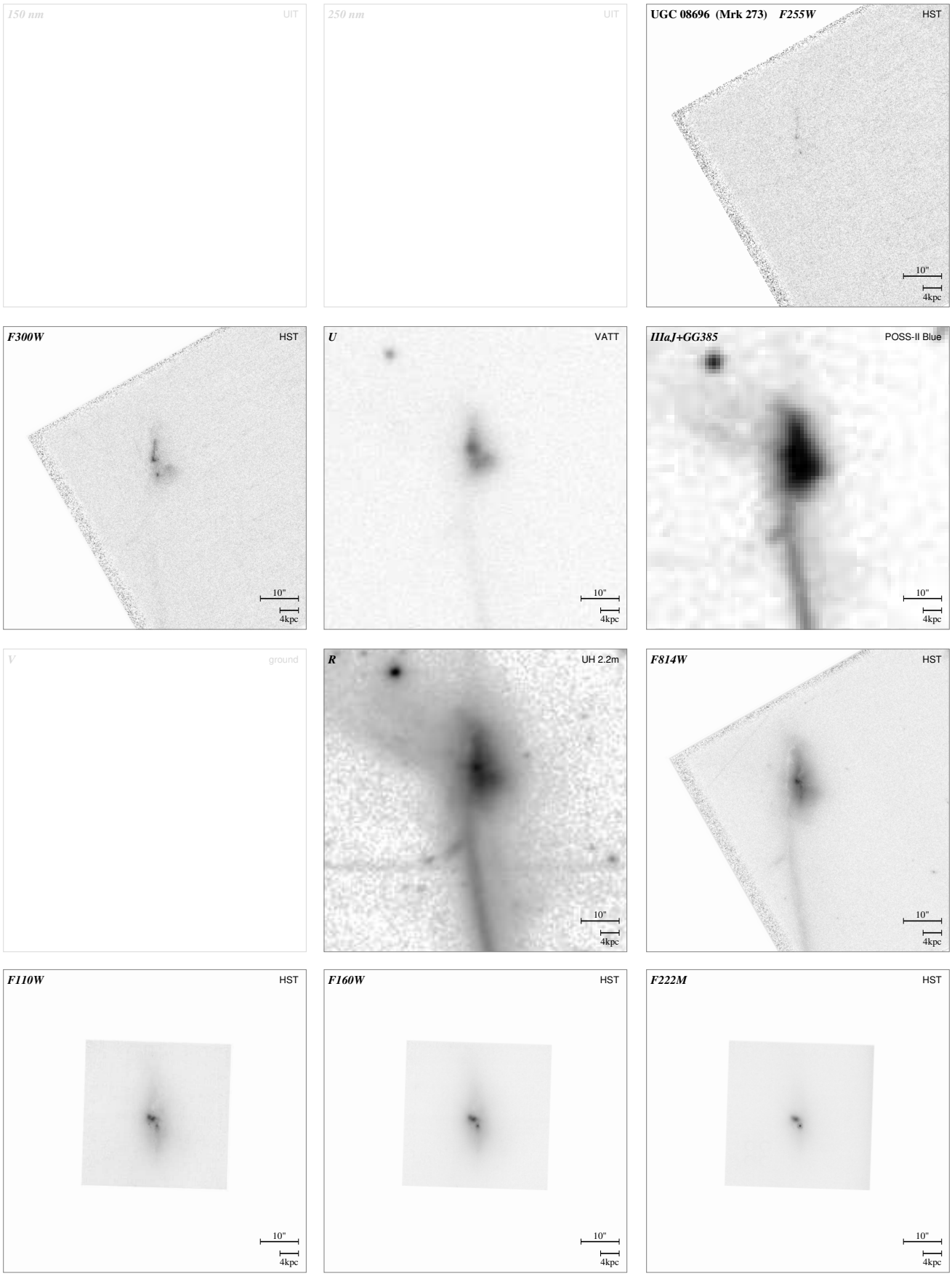

FIG. 4.— (CONT'D) **4.09 UGC 08696** (*top*): *HST*/WFPC2 F255W; (2^{nd} *row*): *HST*/WFPC2 F300W, and ground-based *U* and *IIIaJ* + *GG*385; (3^{rd} *row*): ground-based *R*, and *HST*/WFPC2 F814W; (*bottom*): *HST*/NICMOS F110W (*J*), F160W (*H*), and F222M (*K*).

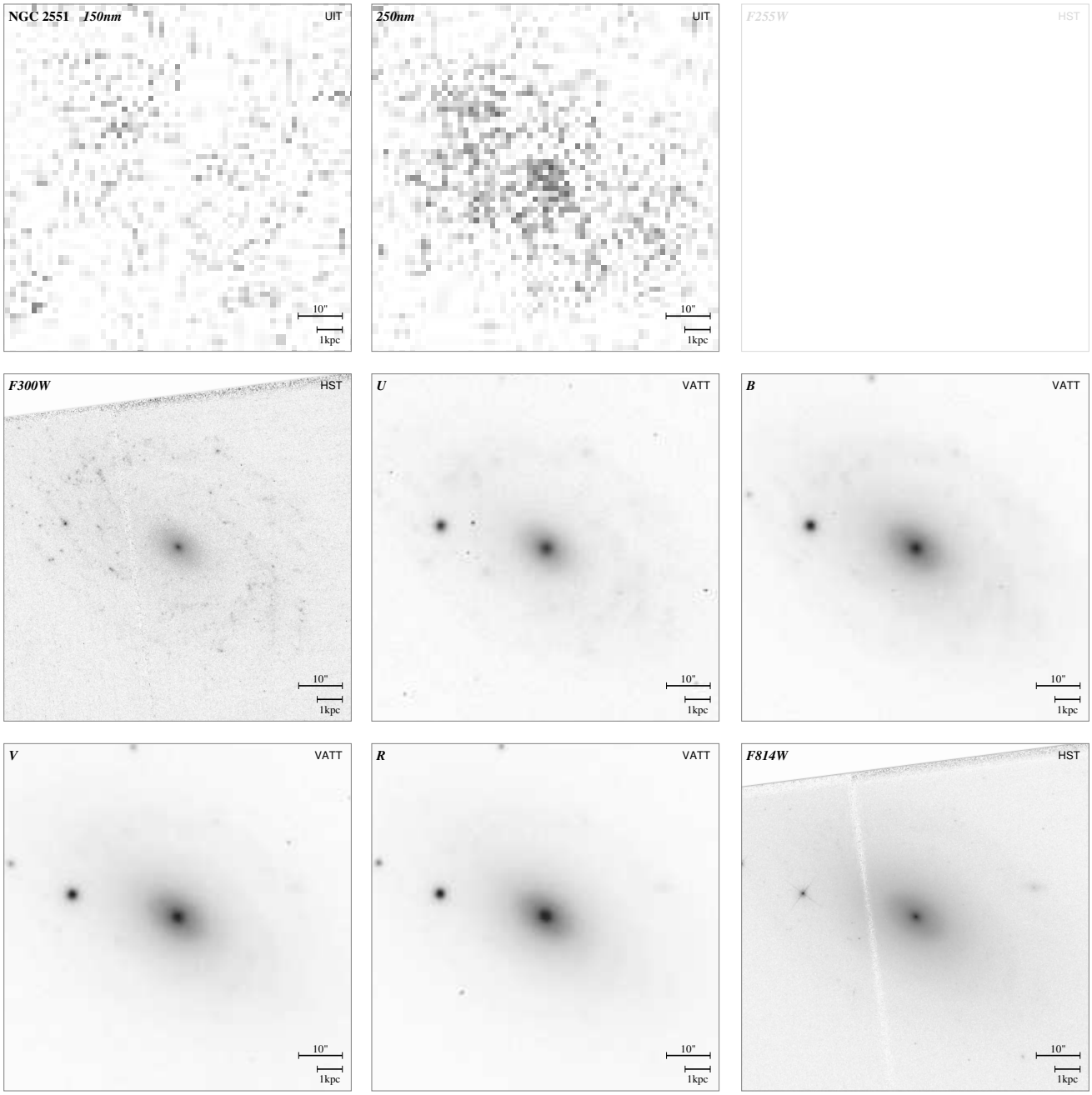

FIG. 4.— EARLY-TYPE GALAXIES DISPLAYING SPIRAL STRUCTURE IN THE MID-UV. **4.10 NGC 2551** (*top*): *UIT* 150nm and 250nm; (*middle*): *HST*/WFPC2 F300W, and ground-based *U* and *B*; (*bottom*): ground-based *V* and *R*, and *HST*/WFPC2 F814W.

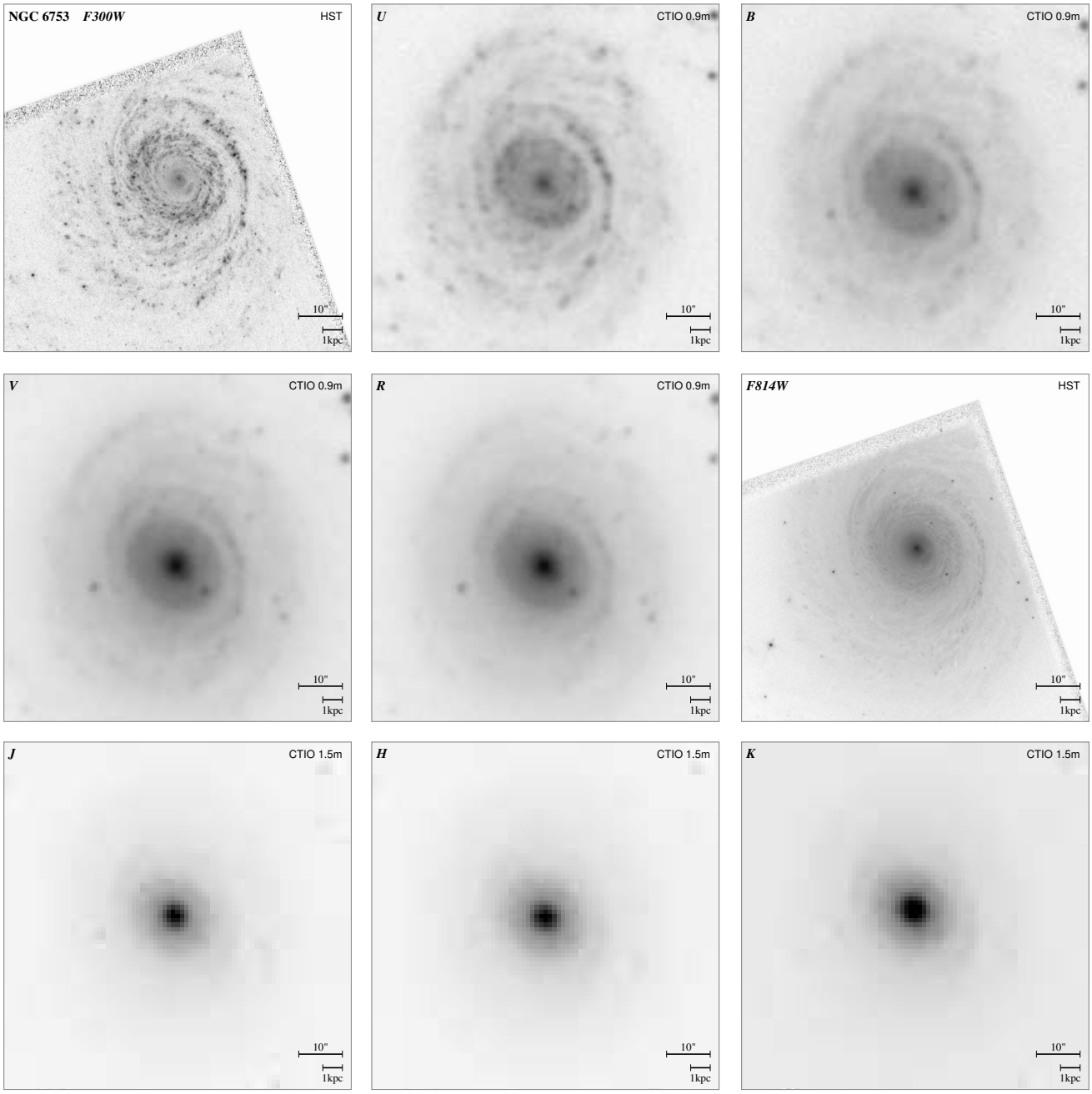

FIG. 4.— GRAND-DESIGN SPIRAL GALAXIES. **4.11 NGC 6753** (*top*): *HST*/WFPC2 F300W, and ground-based *U* and *B*; (*middle*): ground-based *V* and *R*, and *HST*/WFPC2 F814W; (*bottom*): ground-based *J*, *H*, and *K*.

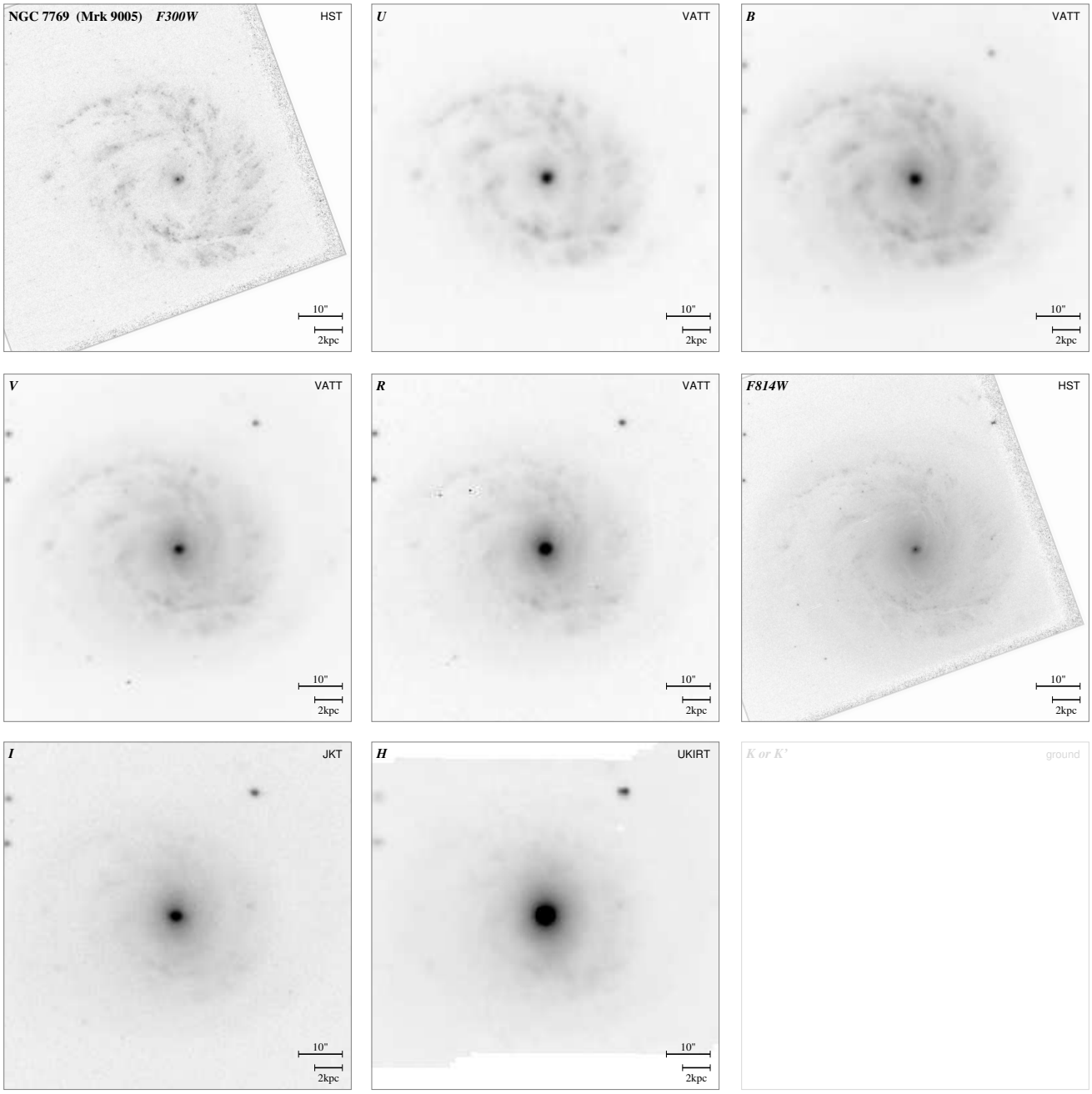

FIG. 4.— (CONT'D) **4.12 NGC 7769** (*top*): *HST*/WFPC2 F300W, and ground-based *U* and *B*; (*middle*): ground-based *V* and *R*, and *HST*/WFPC2 F814W; (*bottom*): ground-based *I* and *H*.

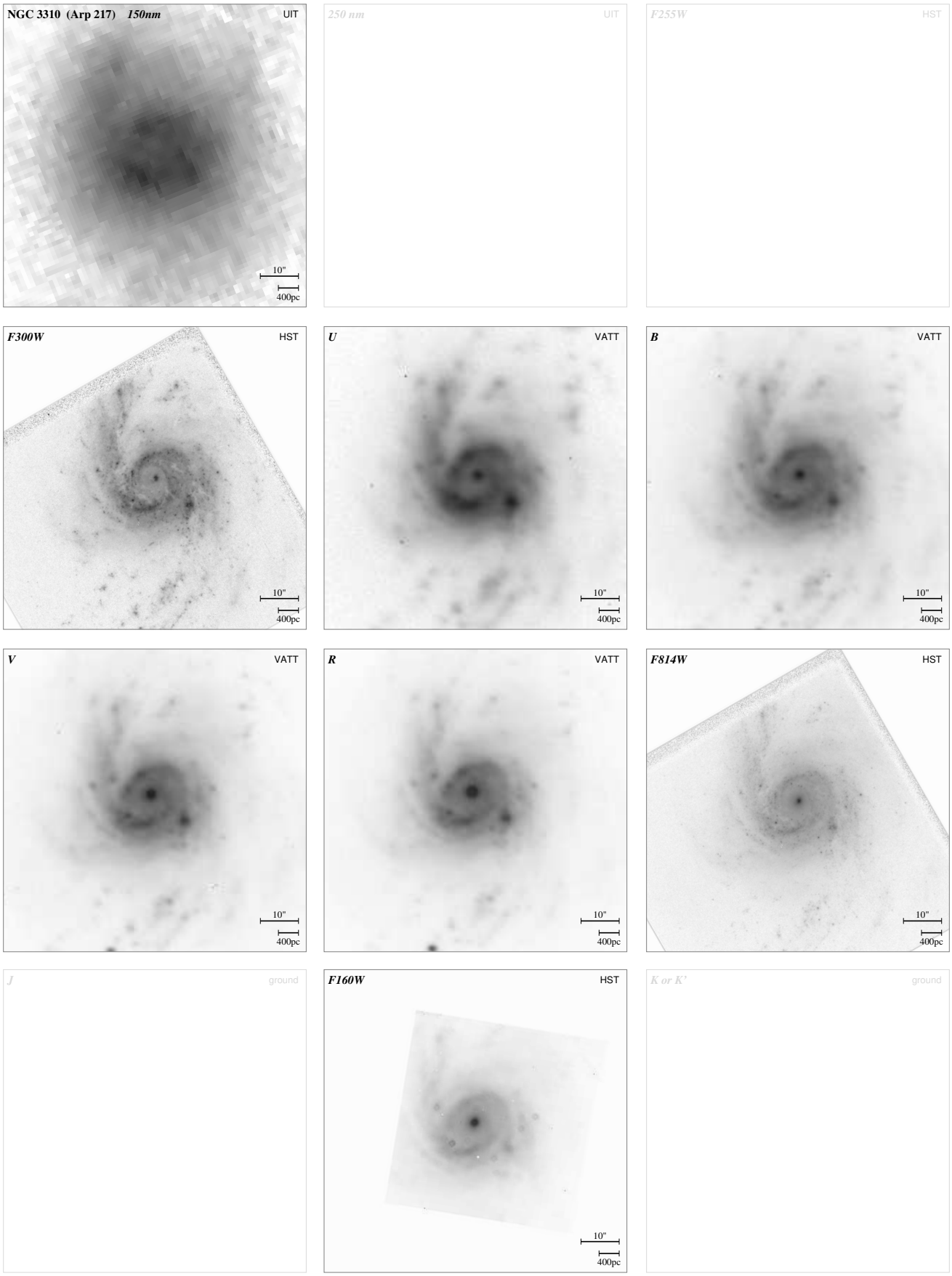

FIG. 4.— (CONT'D) **4.13 NGC 3310** (*top*): *UIT* 150nm; (2^{nd} *row*): *HST*/WFPC2 F300W, and ground-based *U* and *B*; (3^{rd} *row*): ground-based *V* and *R*, and *HST*/WFPC2 F814W; (*bottom*): *HST*/NICMOS F160W (*H*).

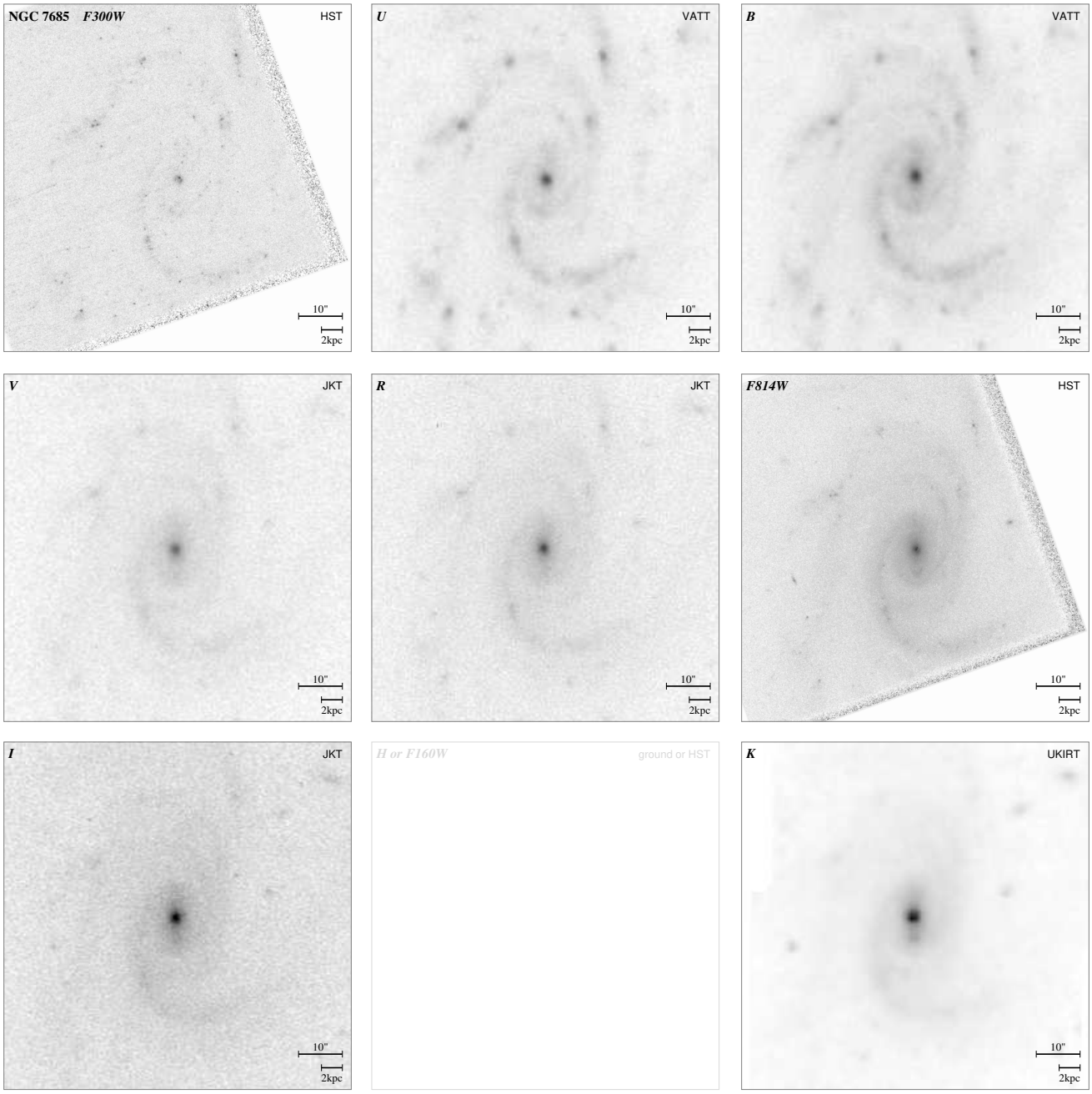

FIG. 4.— (CONT'D) **4.14 NGC 7685** (*top*): *HST*/WFPC2 F300W, and ground-based *U* and *B*; (*middle*): ground-based *V* and *R*, and *HST*/WFPC2 F814W; (*bottom*): ground-based *I* and *K*.

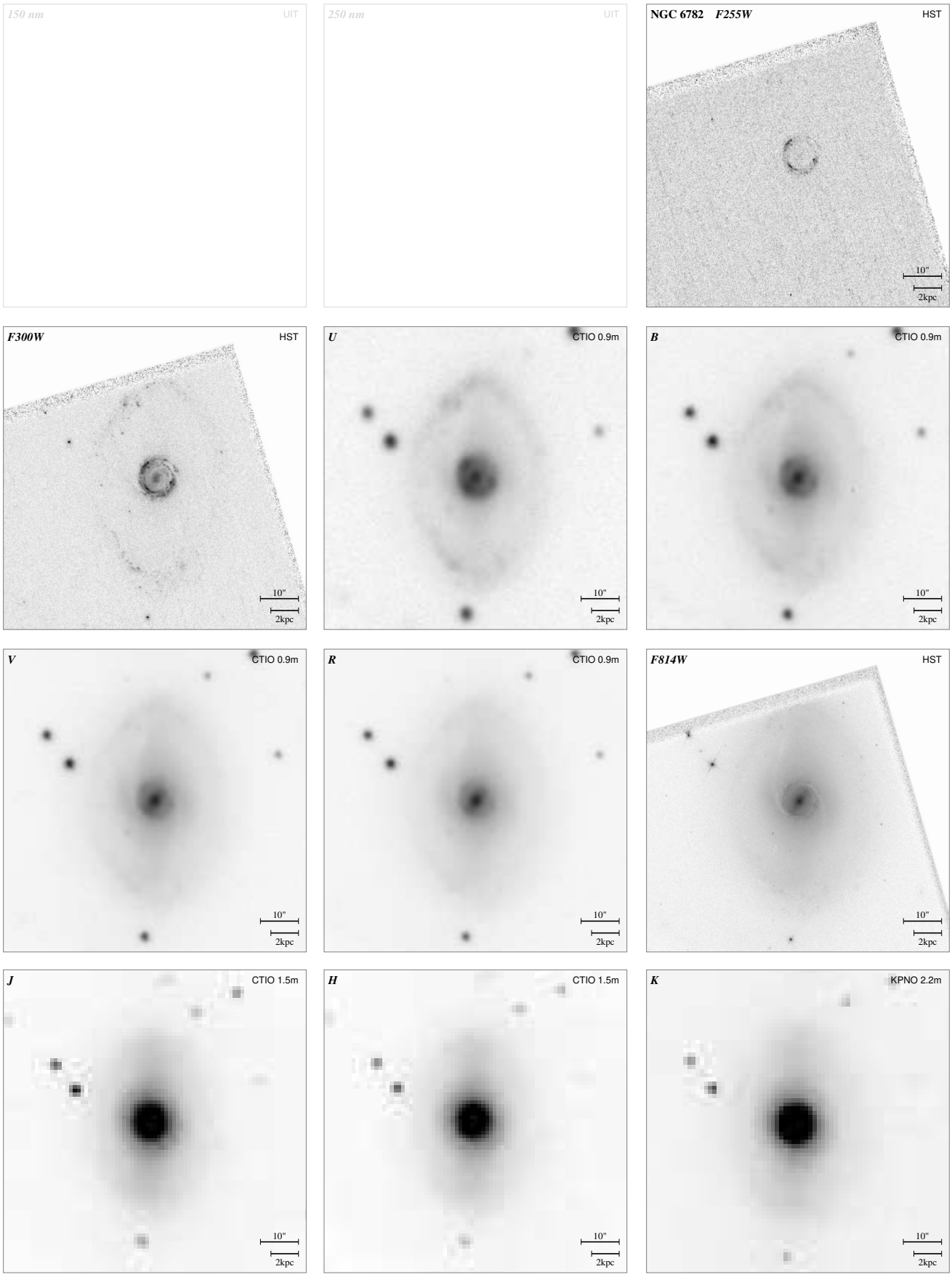

FIG. 4.— SPIRAL GALAXIES WITH INNER RINGS. **4.15 NGC 6782** (*top*): *HST*/WFPC2 F255W; (2^{nd} *row*): *HST*/WFPC2 F300W, and ground-based *U* and *B*; (3^{rd} *row*): ground-based *V* and *R*, and *HST*/WFPC2 F814W; (*bottom*): ground-based *J*, *H* and *K*.

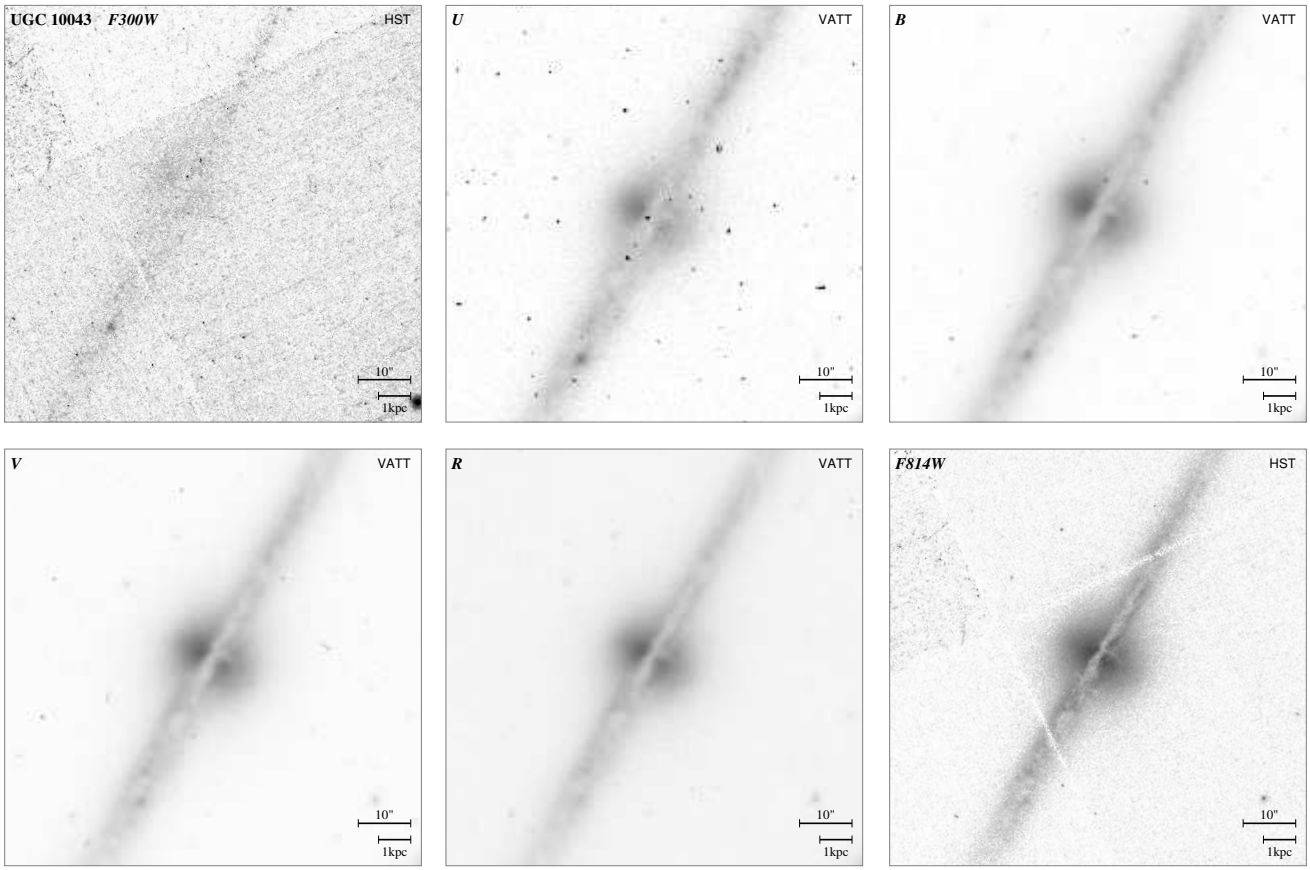

FIG. 4.— EDGE-ON SPIRAL GALAXIES. **4.16 UGC 10043** (*top*): *HST*/WFPC2 F300W, and ground-based *U* and *B*; (*bottom*): ground-based *V* and *R*, and *HST*/WFPC2 F814W.

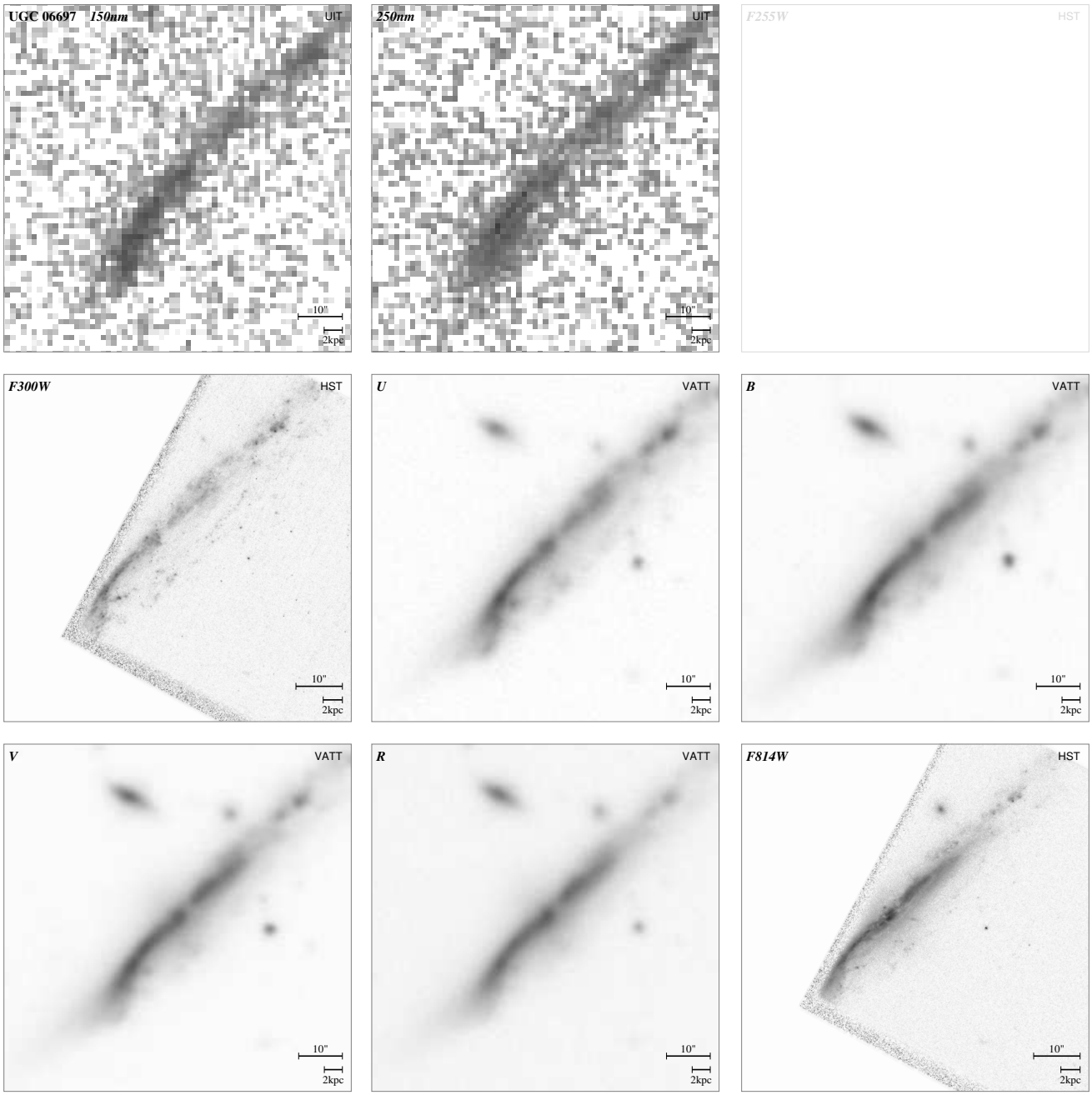

FIG. 4.— (CONT'D) **4.17 UGC 06697** (*top*): *UIT* 150nm and 250nm; (*middle*): *HST*/WFPC2 F300W, and ground-based *U* and *B*; (*bottom*): ground-based *V* and *R*, and *HST*/WFPC2 F814W.

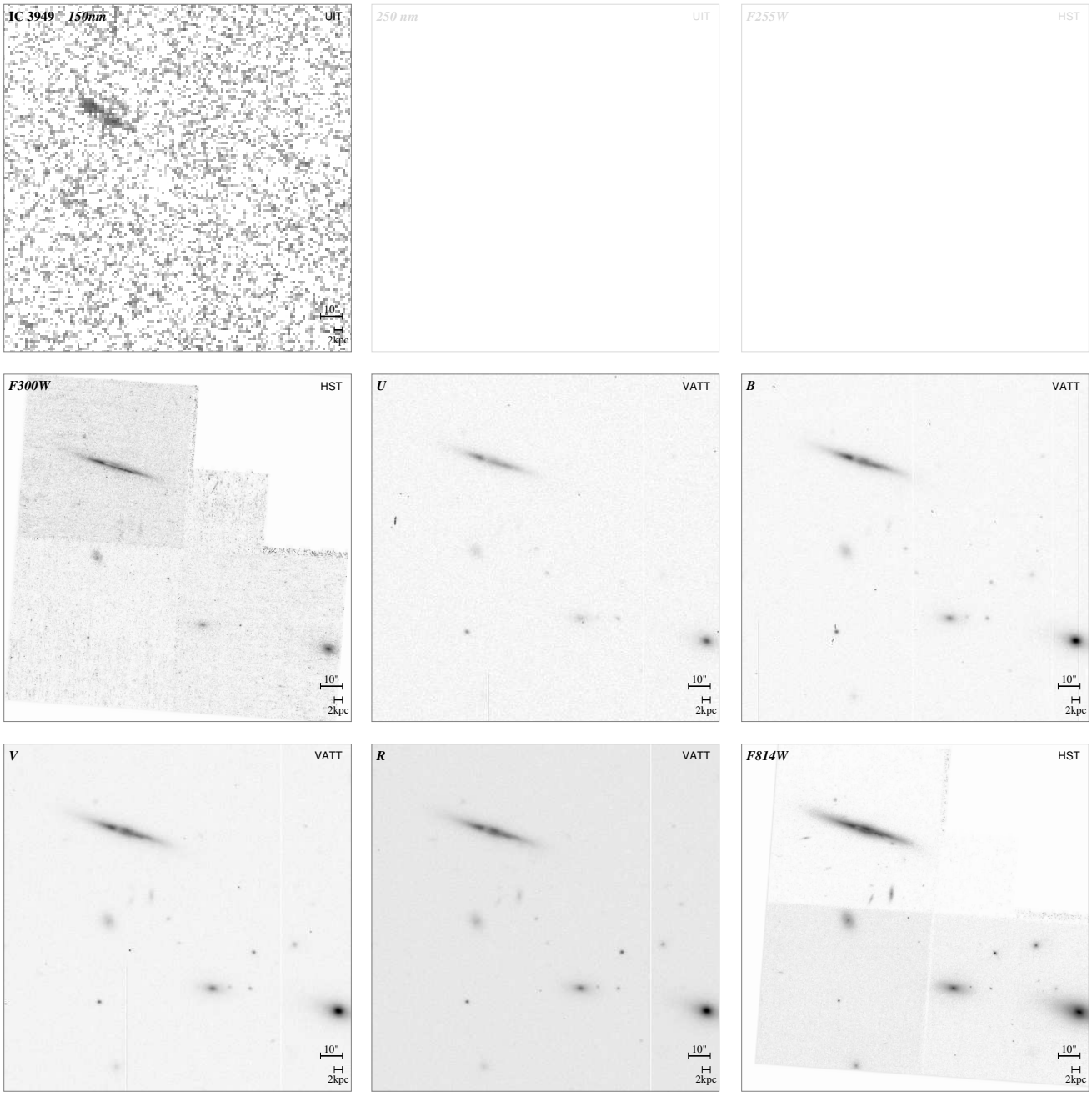

FIG. 4.— (CONT'D) **4.18 IC 3949** (*top*): *UIT* 150nm; (*middle*): *HST*/WFPC2 F300W, and ground-based *U* and *B*; (*bottom*): ground-based *V* and *R*, and *HST*/WFPC2 F814W.

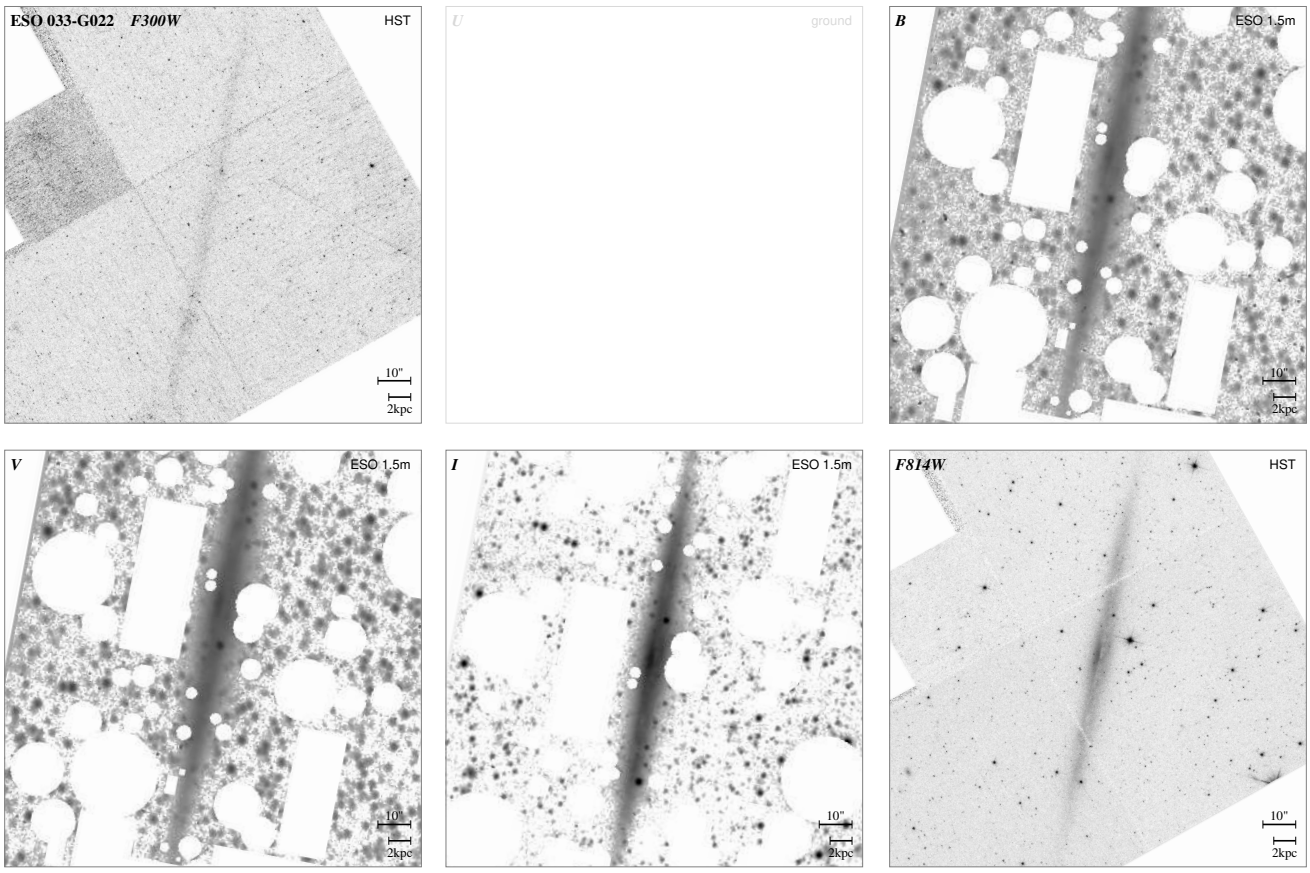

FIG. 4.— (CONT'D) **4.19 ESO 033–G022** (*top*): *HST*/WFPC2 F300W, and ground-based *B*; (*bottom*): ground-based *V* and *I*, and *HST*/WFPC2 F814W.

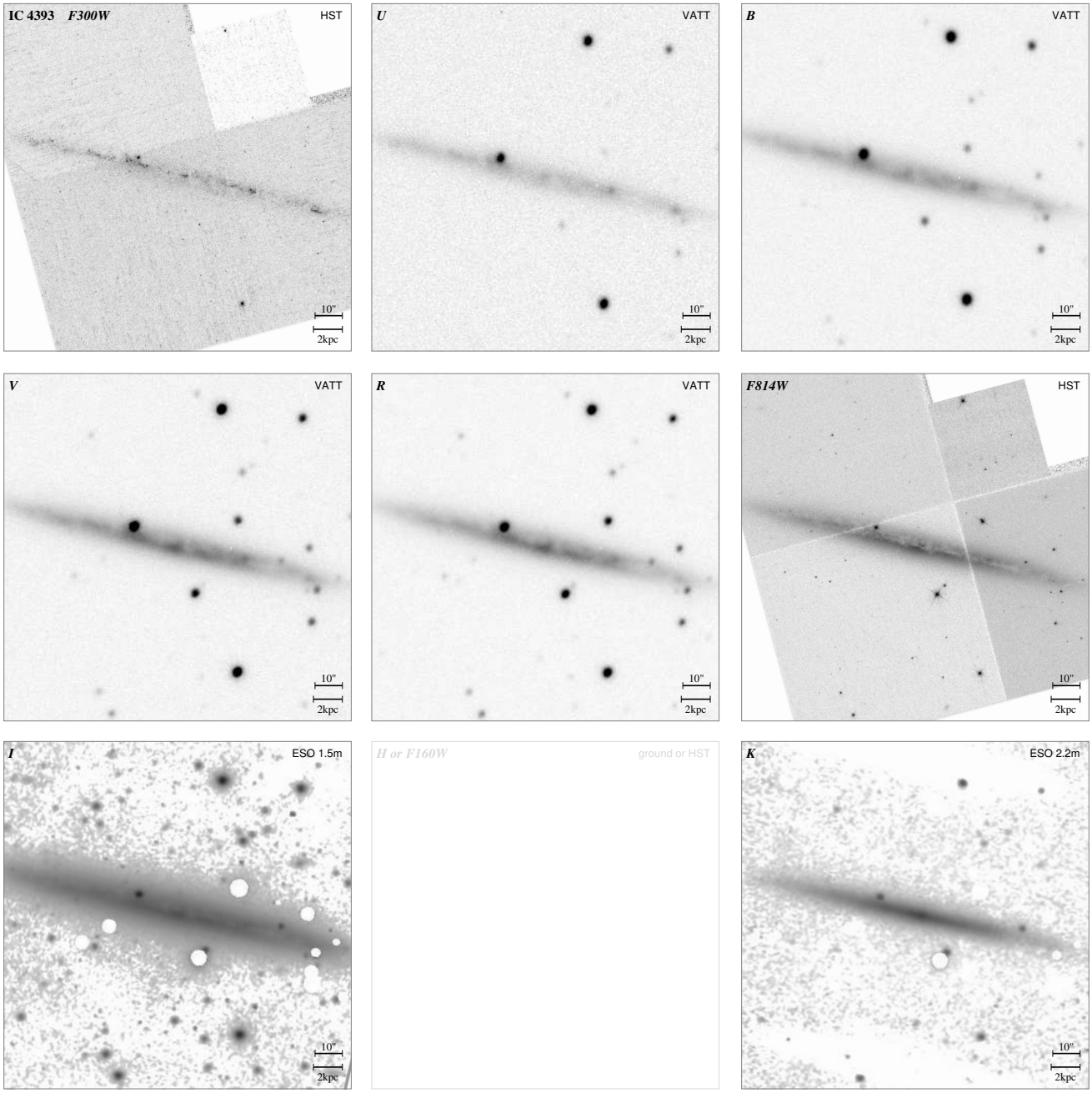

FIG. 4.— (CONT'D) **4.20 IC 4393** (*top*): *HST*/WFPC2 F300W, and ground-based *U* and *B*; (*middle*): ground-based *V* and *I*, and *HST*/WFPC2 F814W; (*bottom*): ground-based *I* and *K*.

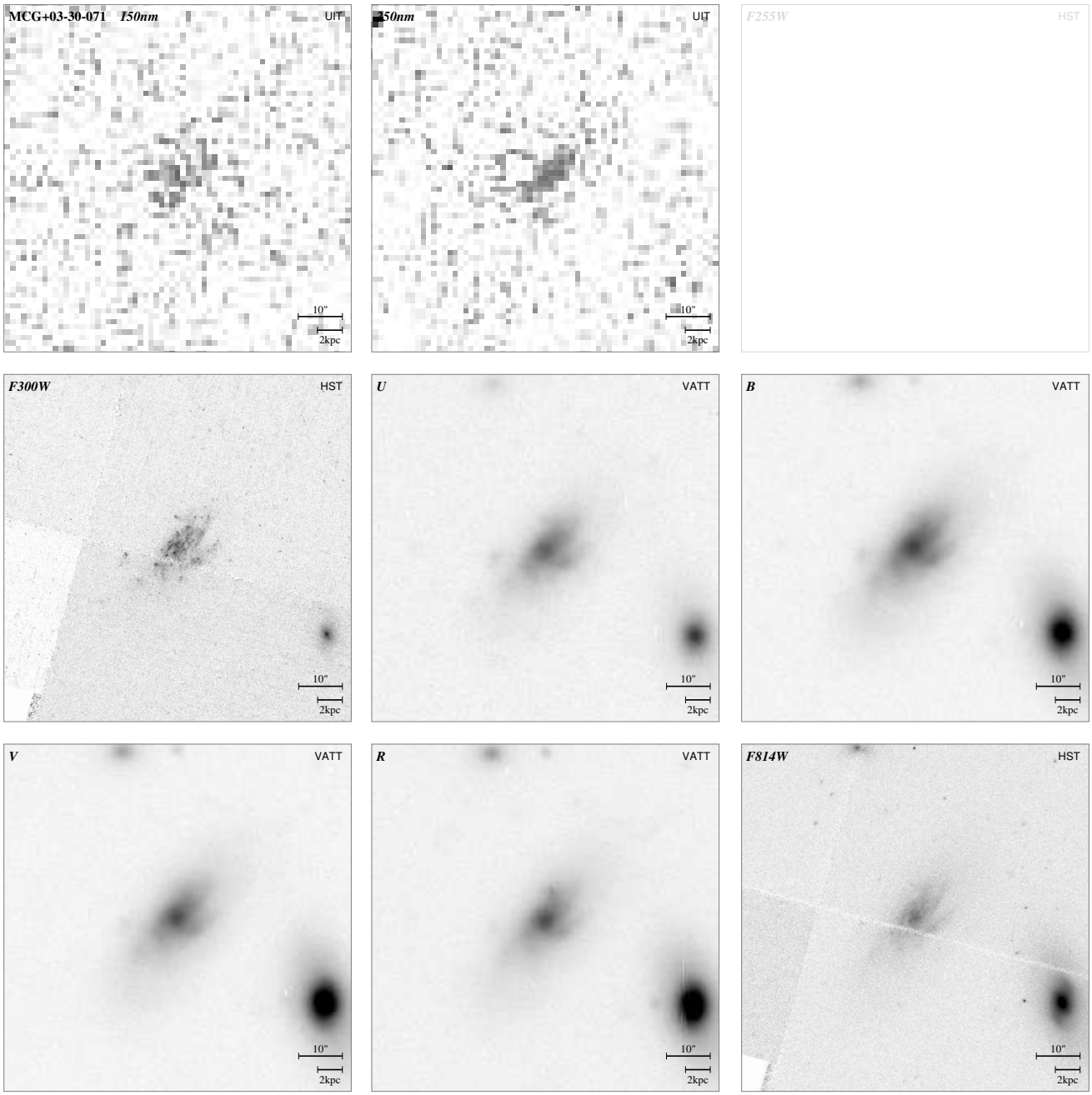

FIG. 4.— LATE-TYPE SPIRALS AND SMALLER SPIRAL GALAXIES. **4.21 MCG+03–30–071** (*top*): *UIT* 150nm and 250nm; (*middle*): *HST*/WFPC2 F300W, and ground-based *U* and *B*; (*bottom*): ground-based *V* and *I*, and *HST*/WFPC2 F814W.

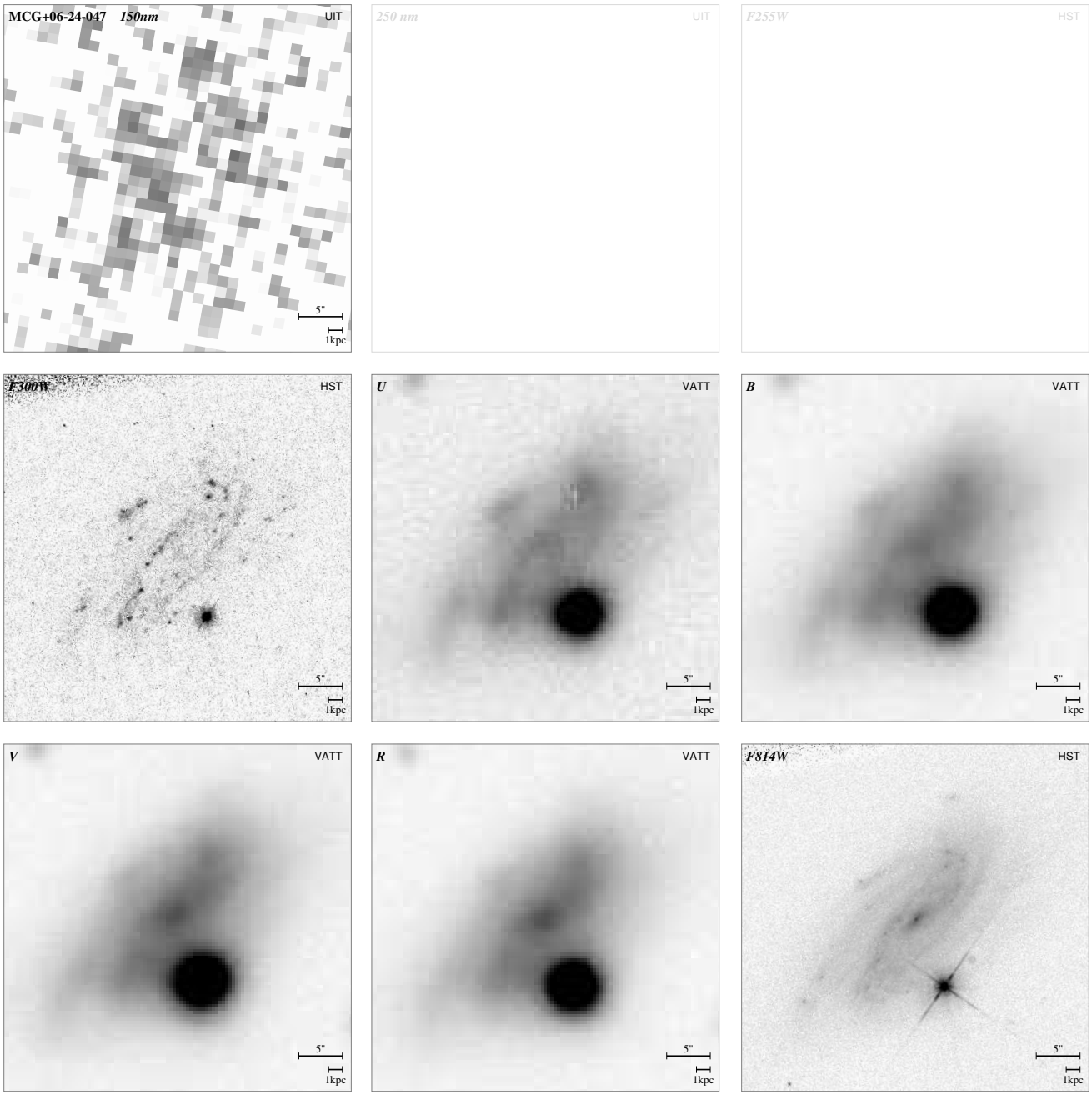

FIG. 4.— (CONT'D) **4.22 MCG+06–24–047** (*top*): *UIT* 150nm; (*middle*): *HST*/WFPC2 F300W, and ground-based *U* and *B*; (*bottom*): ground-based *V* and *I*, and *HST*/WFPC2 F814W.

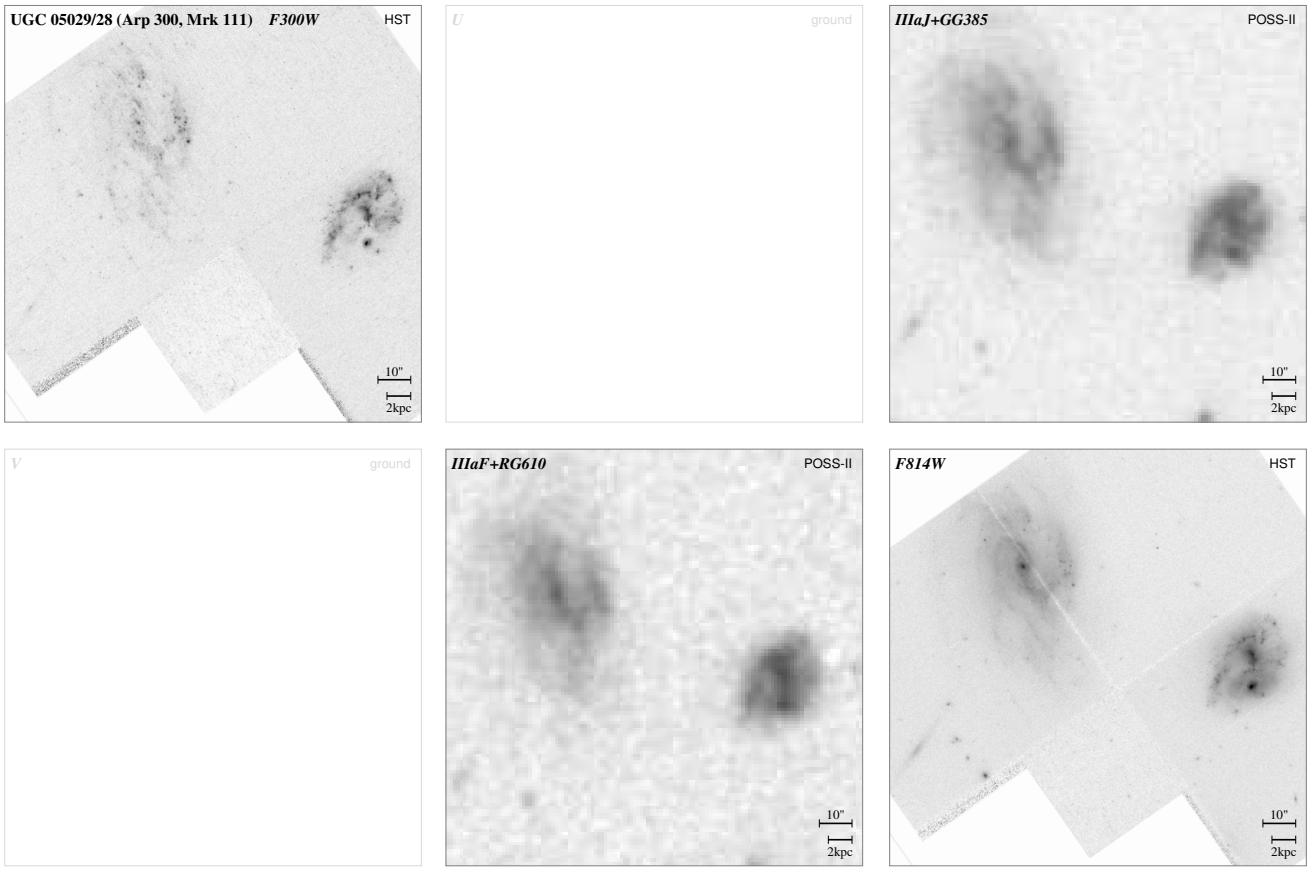

FIG. 4.— (CONT'D) **4.23 UGC 05028/29** (*top*): *HST*/WFPC2 F300W, and ground-based *IIIaJ*+*GG*385; (*bottom*): ground-based *IIIaF*+*RG*610, and *HST*/WFPC2 F814W.

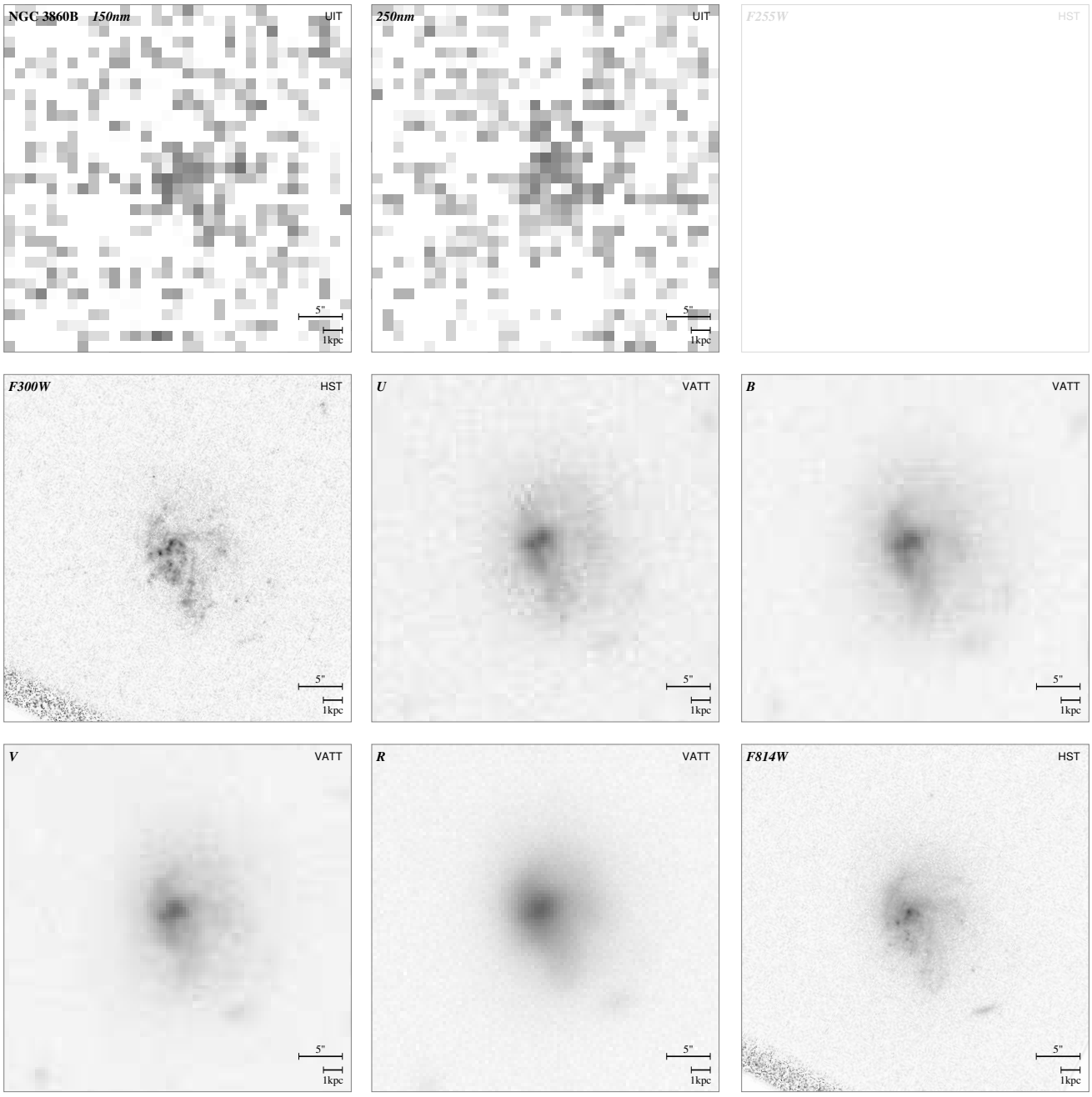

FIG. 4.— (CONT'D) **4.24 NGC 3860B** (*top*): *UIT* 150nm and 250nm; (*middle*): *HST*/WFPC2 F300W, and ground-based *U* and *B*; (*bottom*): ground-based *V* and *R*, and *HST*/WFPC2 F814W.

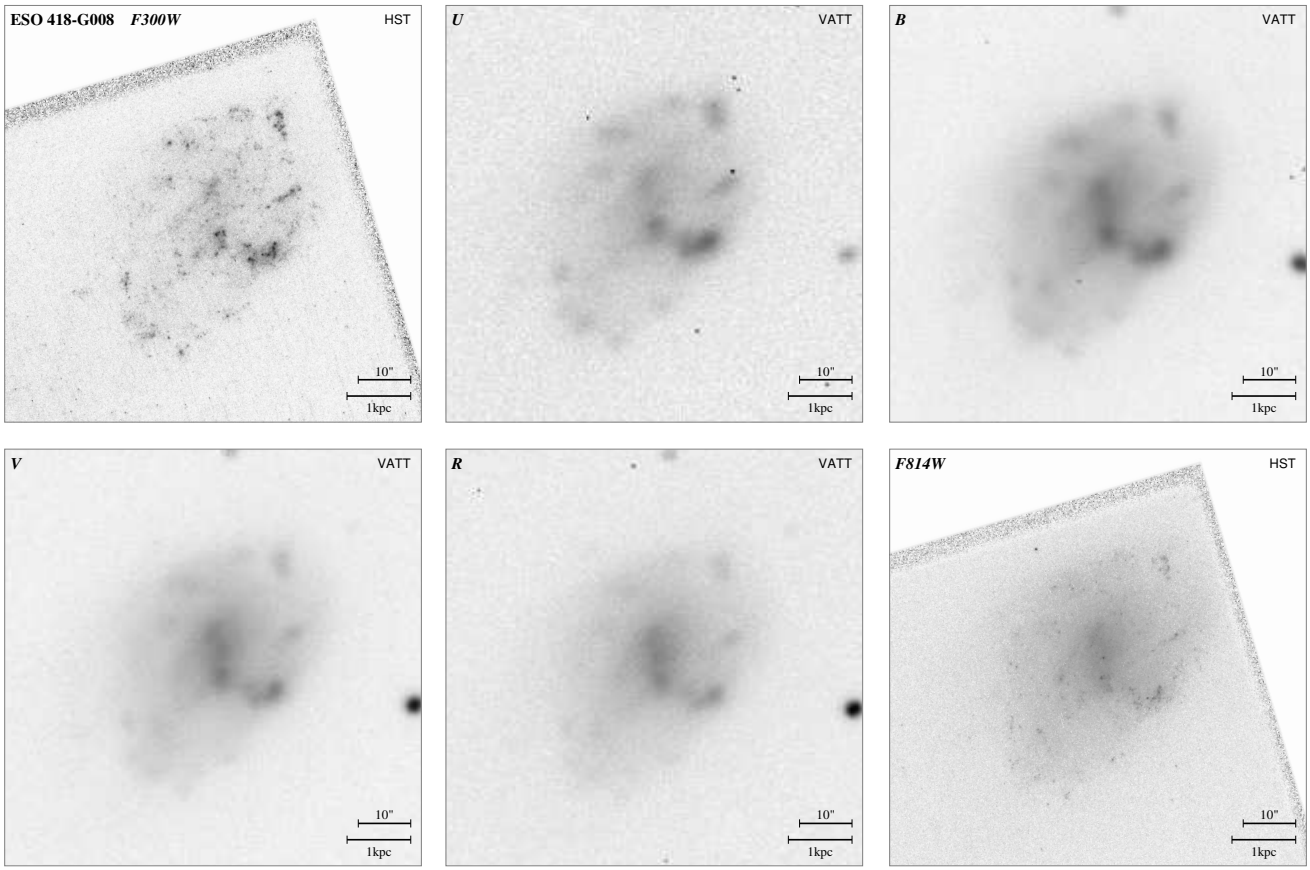

FIG. 4.— (CONT'D) **4.25 ESO 418–G008** (*top*): *HST*/WFPC2 F300W, and ground-based *U* and *B*; (*bottom*): ground-based *V* and *R*, and *HST*/WFPC2 F814W.

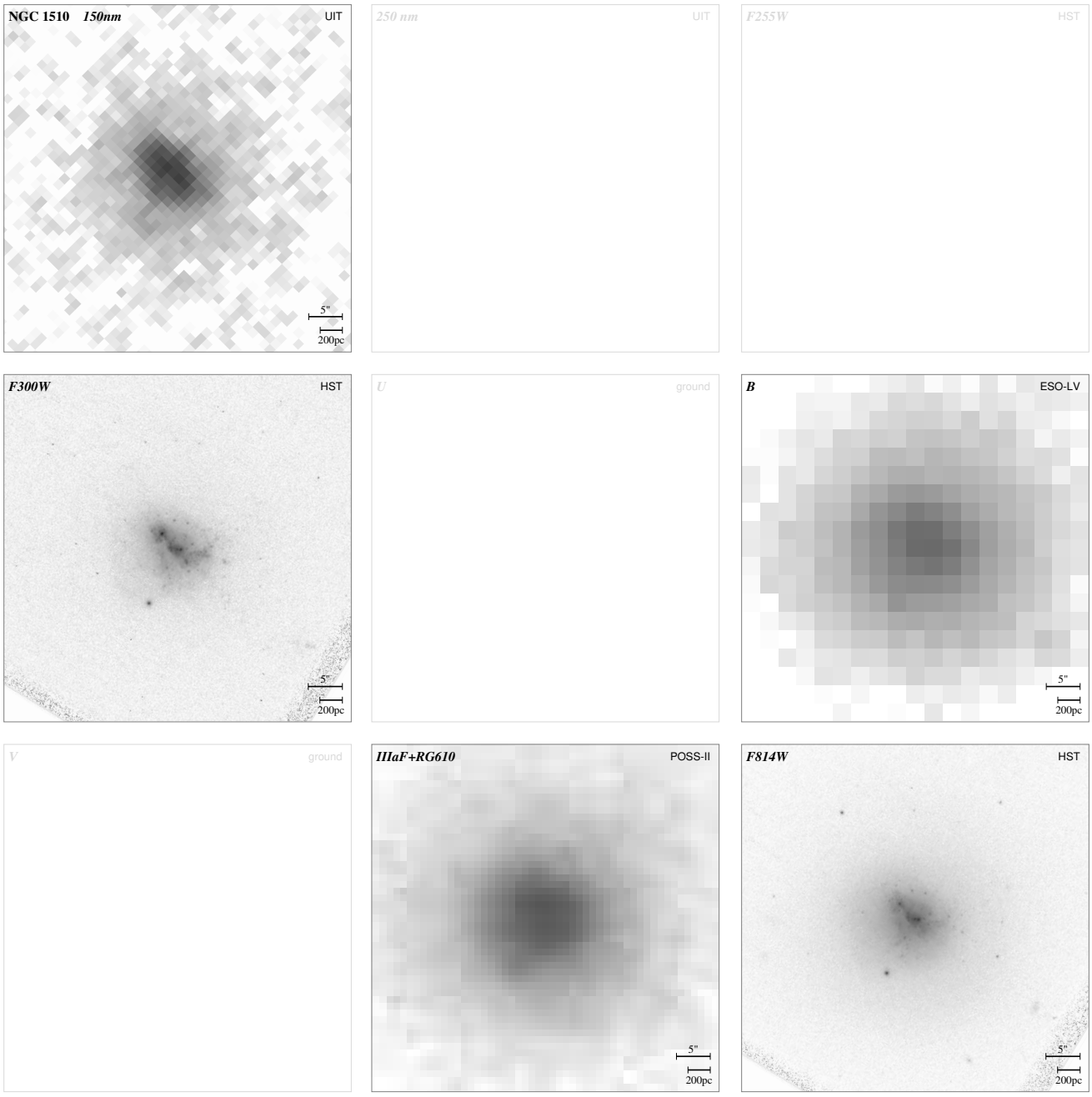

FIG. 4.— (CONT'D) **4.26 NGC 1510** (*top*): *UIT* 150nm; (*middle*): *HST*/WFPC2 F300W, and ground-based *B* (from Lauberts & Valentijn 1989, as obtained through NED); (*bottom*): ground-based *IIIaF* + *RG*610, and *HST*/WFPC2 F814W.

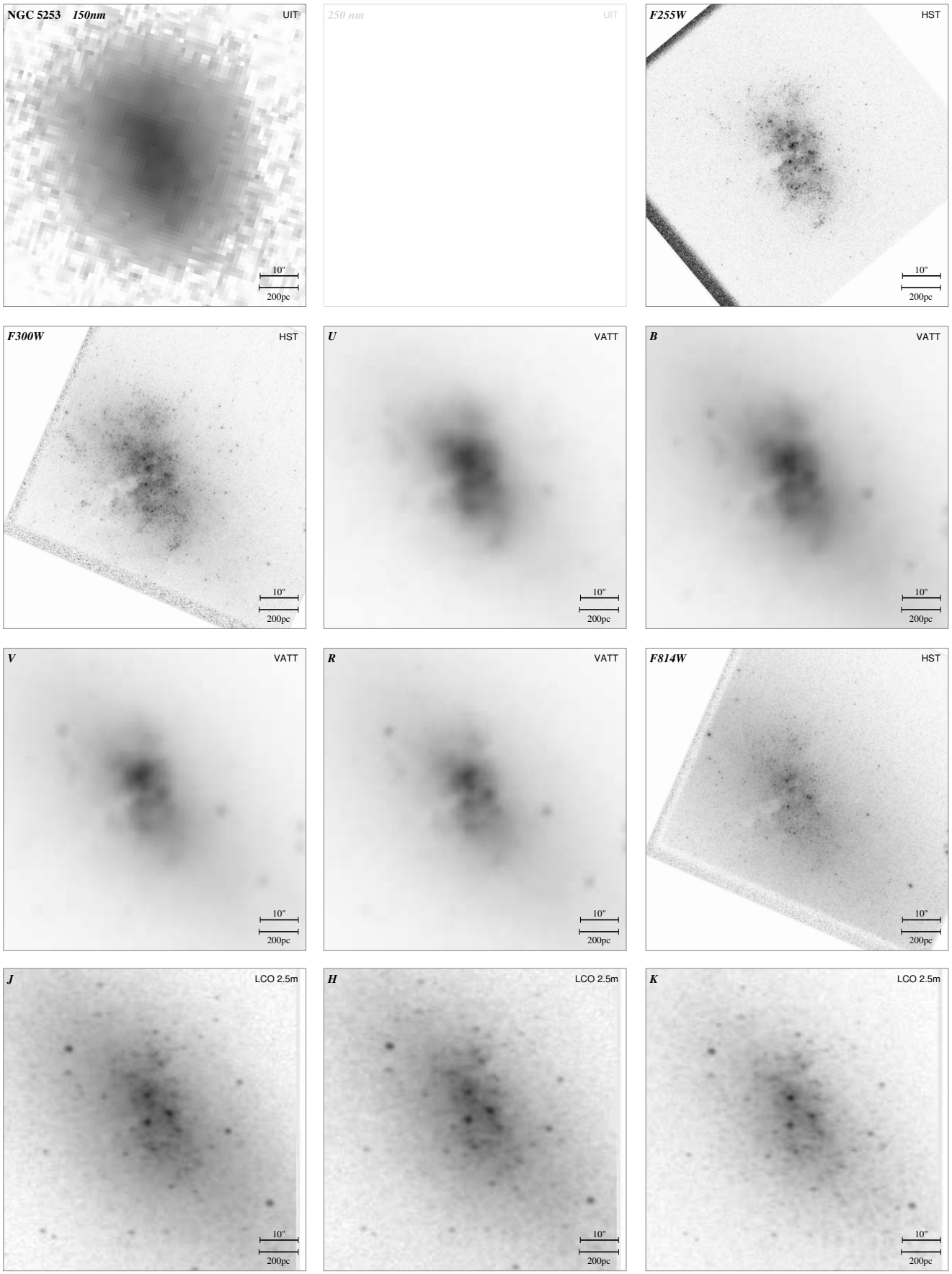

FIG. 4.— MAGELLANIC IRREGULAR GALAXIES. **4.27 NGC 5253** (*top*): *UIT* 150nm, and *HST*/WFPC2 F255W; (2^{nd} *row*): *HST*/WFPC2 F300W, and ground-based *U* and *B*; (3^{rd} *row*): ground-based *V* and *R*, and *HST*/WFPC2 F814W; (*bottom*): ground-based *J*, *H*, and *K*.

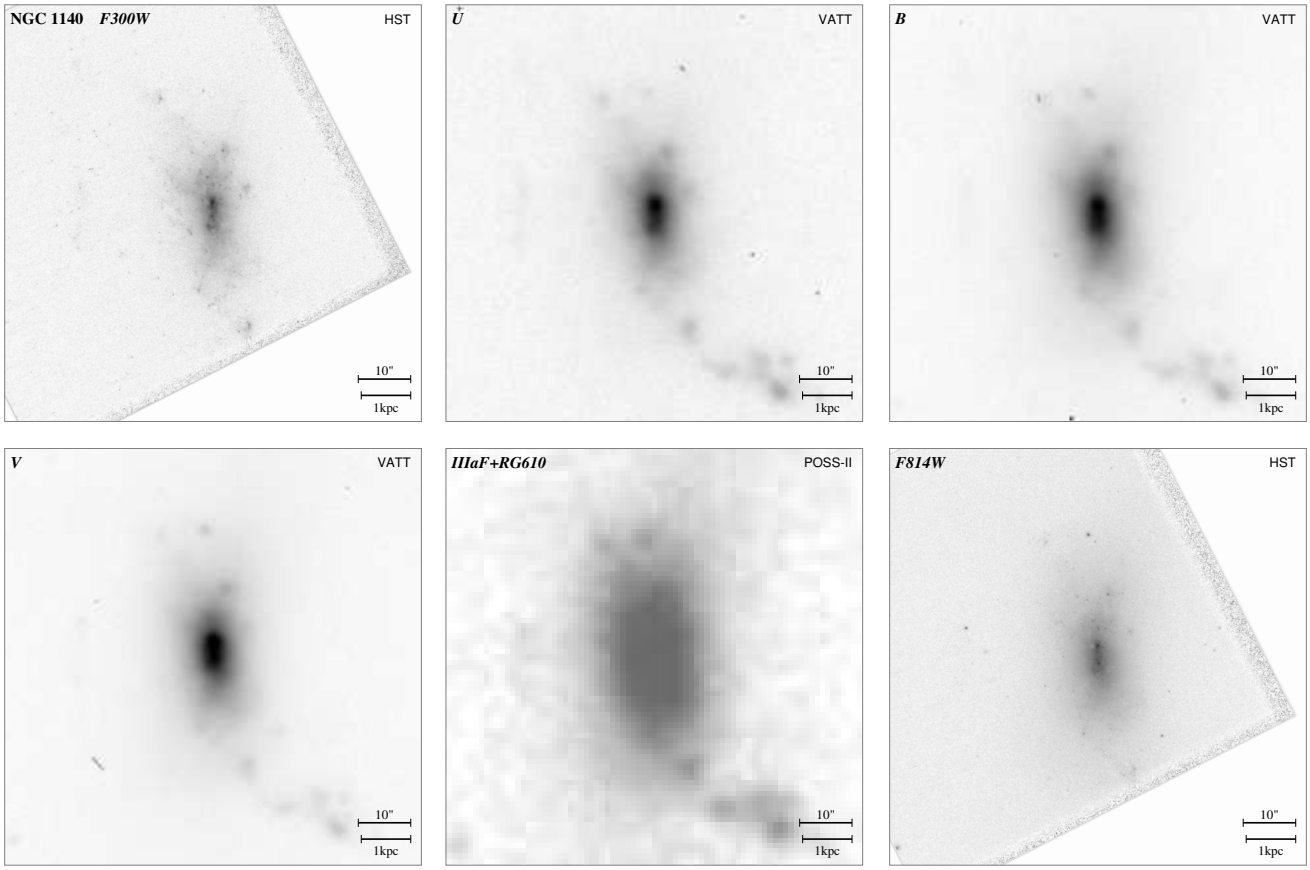

FIG. 4.— (CONT'D) **4.28 NGC 1140** (*top*): *HST*/WFPC2 F300W, and ground-based *U* and *B*; (*bottom*): ground-based *V* and *IIIaF* + *RG*610, and *HST*/WFPC2 F814W.

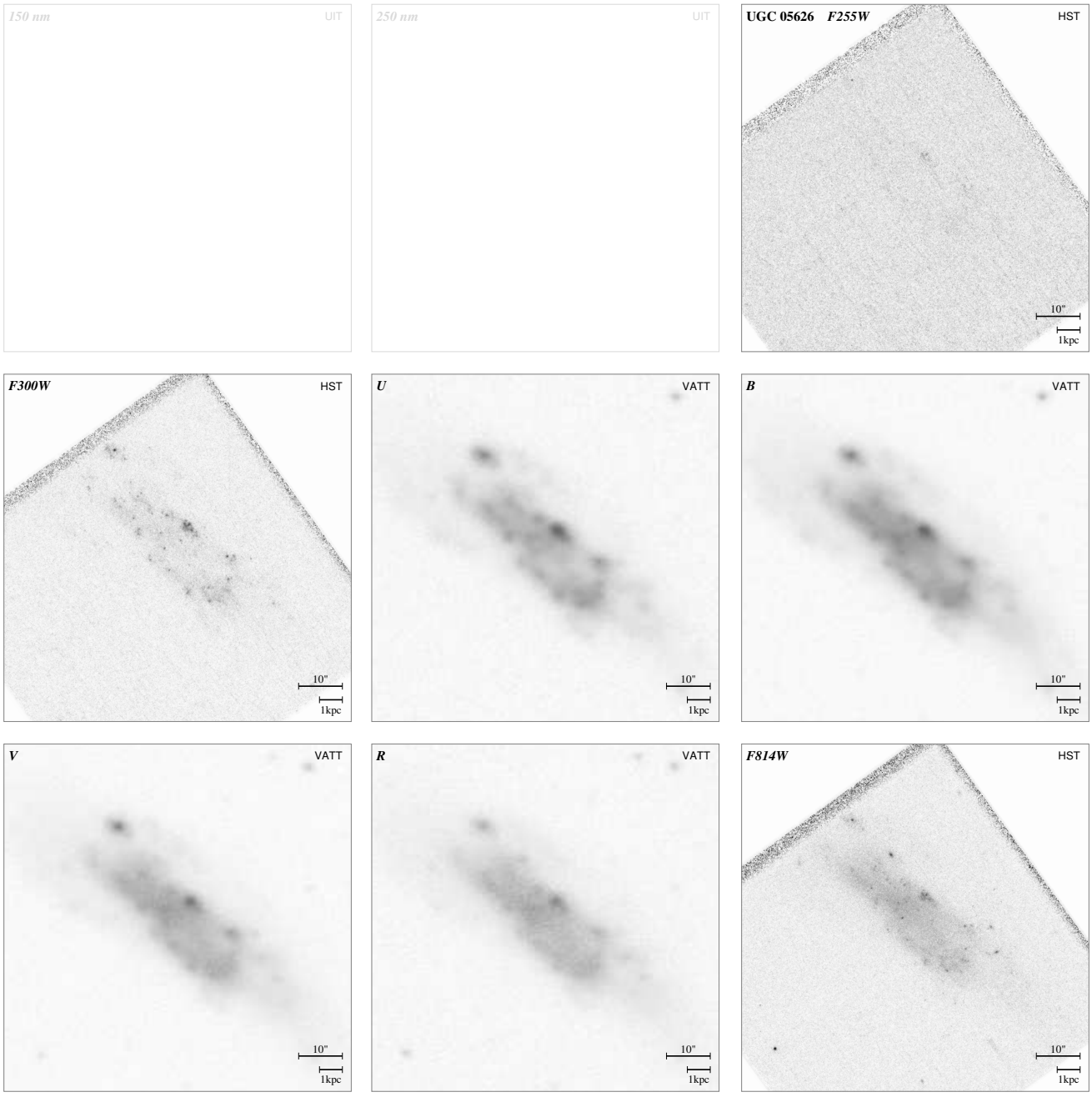

FIG. 4.— (CONT'D) **4.29 UGC 05626** (*top*): *HST*/WFPC2 F255W; (*middle*): *HST*/WFPC2 F300W, and ground-based *U* and *B*; (*bottom*): ground-based *V* and *R*, and *HST*/WFPC2 F814W.

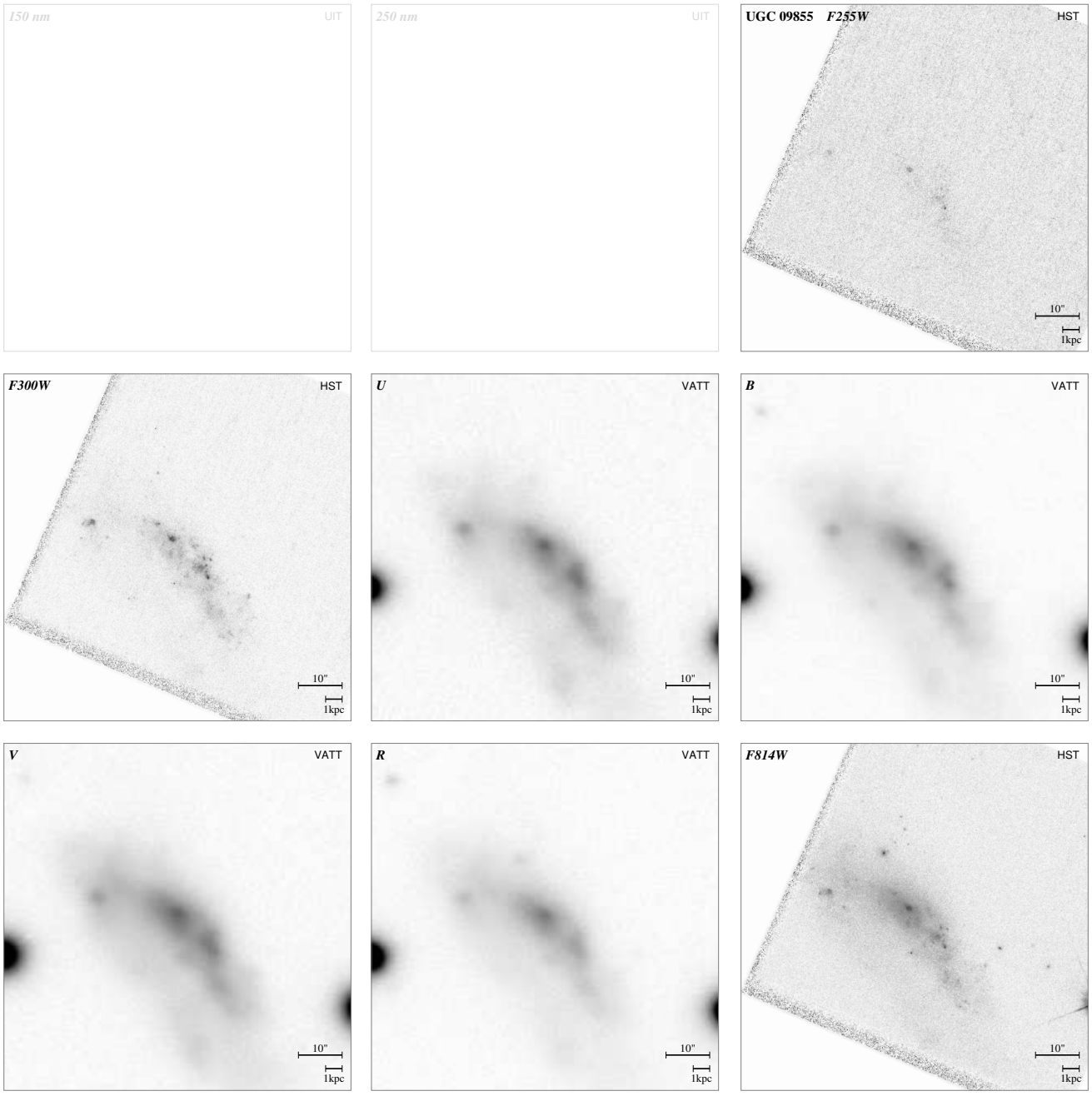

FIG. 4.— (CONT'D) **4.30 UGC 09855** (*top*): *HST*/WFPC2 F255W; (*middle*): *HST*/WFPC2 F300W, and ground-based *U* and *B*; (*bottom*): ground-based *V* and *R*, and *HST*/WFPC2 F814W.

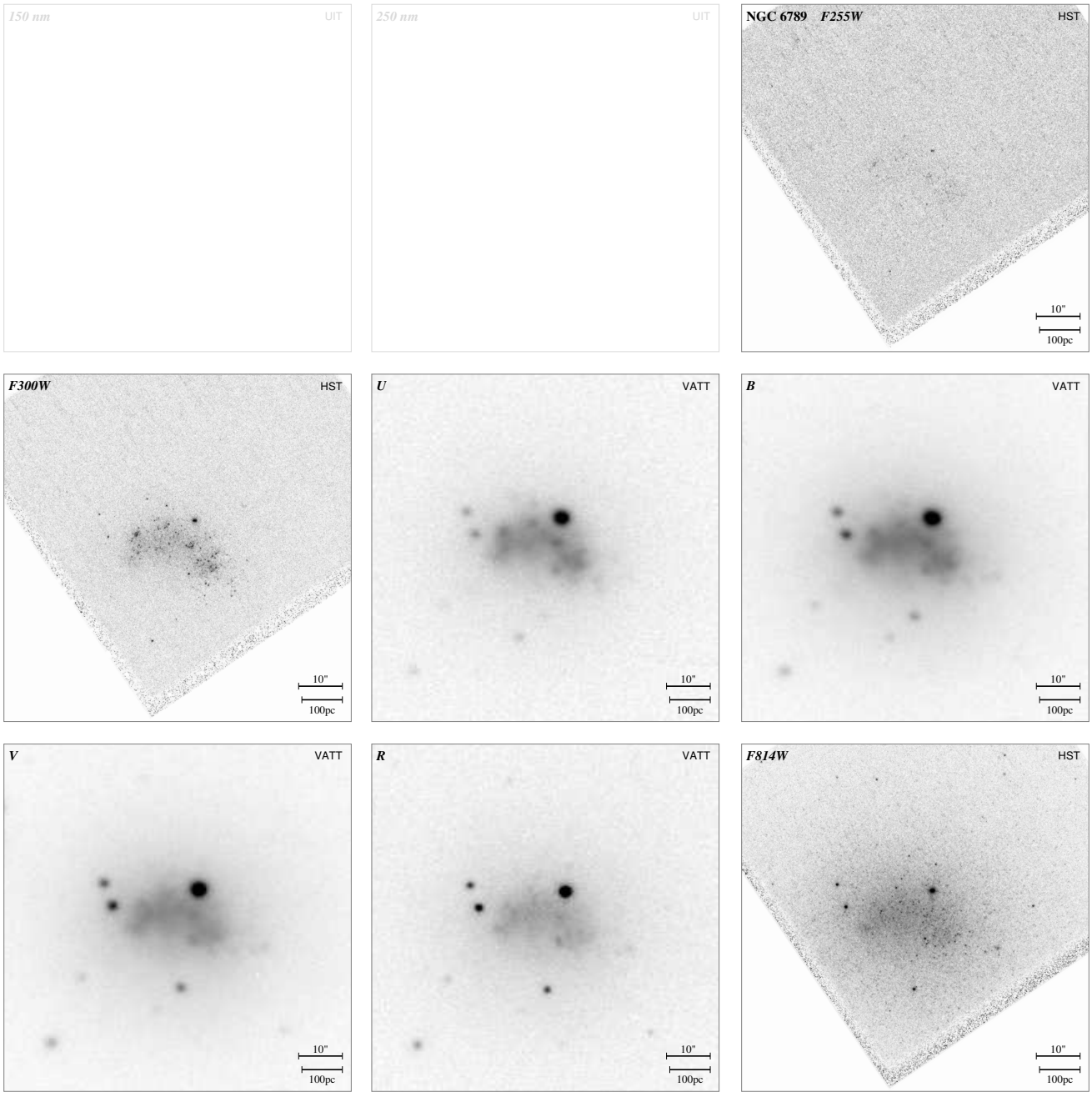

FIG. 4.— (CONT'D) **4.31 NGC 6789** (*top*): *HST*/WFPC2 F255W; (*middle*): *HST*/WFPC2 F300W, and ground-based *U* and *B*; (*bottom*): ground-based *V* and *R*, and *HST*/WFPC2 F814W.

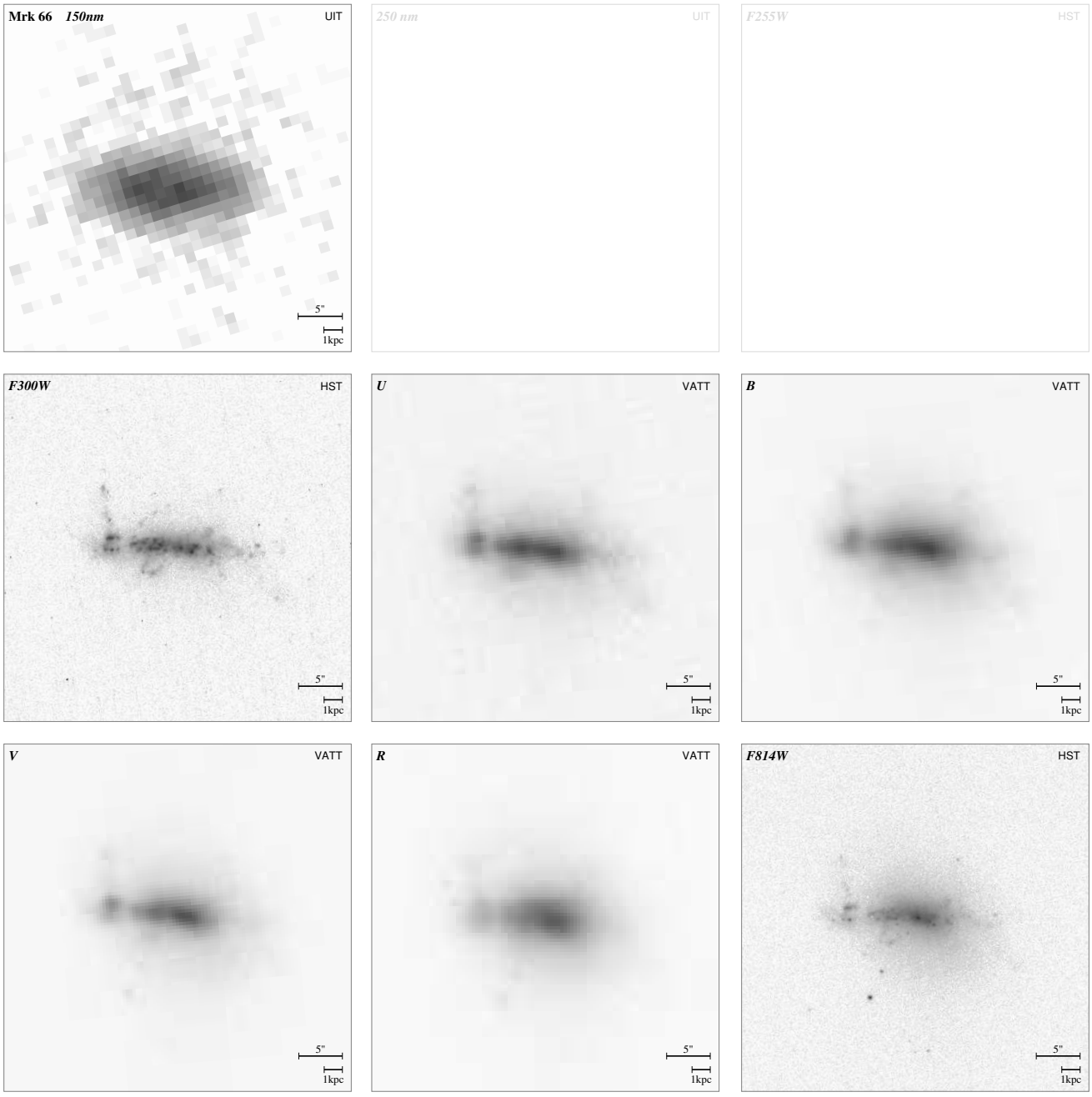

FIG. 4.— (CONT'D) **4.32 Mrk 66** (*top*): *UIT* 150nm; (*middle*): *HST*/WFPC2 F300W, and ground-based *U* and *B*; (*bottom*): ground-based *V* and *R*, and *HST*/WFPC2 F814W.

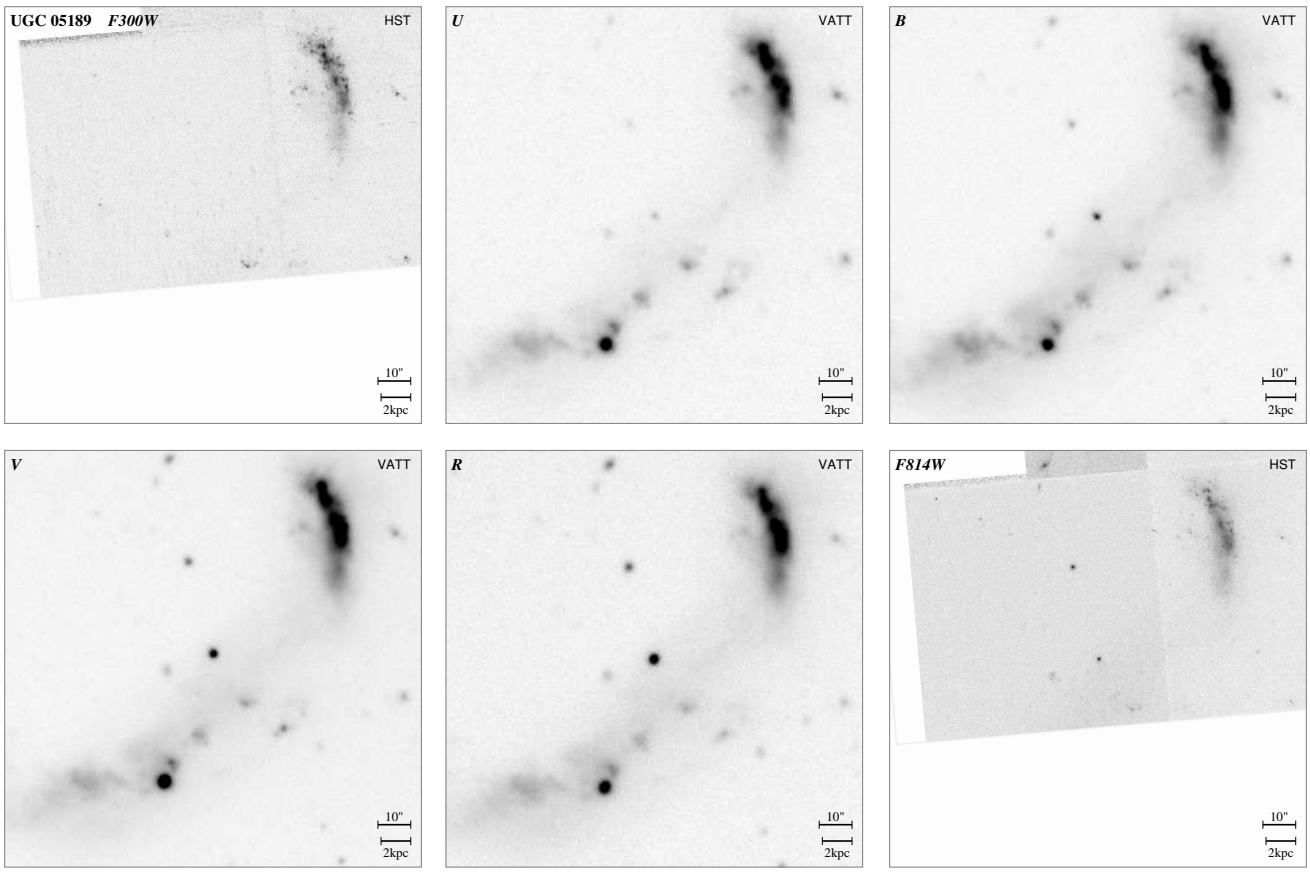

FIG. 4.— (CONT'D) **4.33 UGC 05189** (*top*): *HST*/WFPC2 F300W, and ground-based *U* and *B*; (*bottom*): ground-based *V* and *R*, and *HST*/WFPC2 F814W.

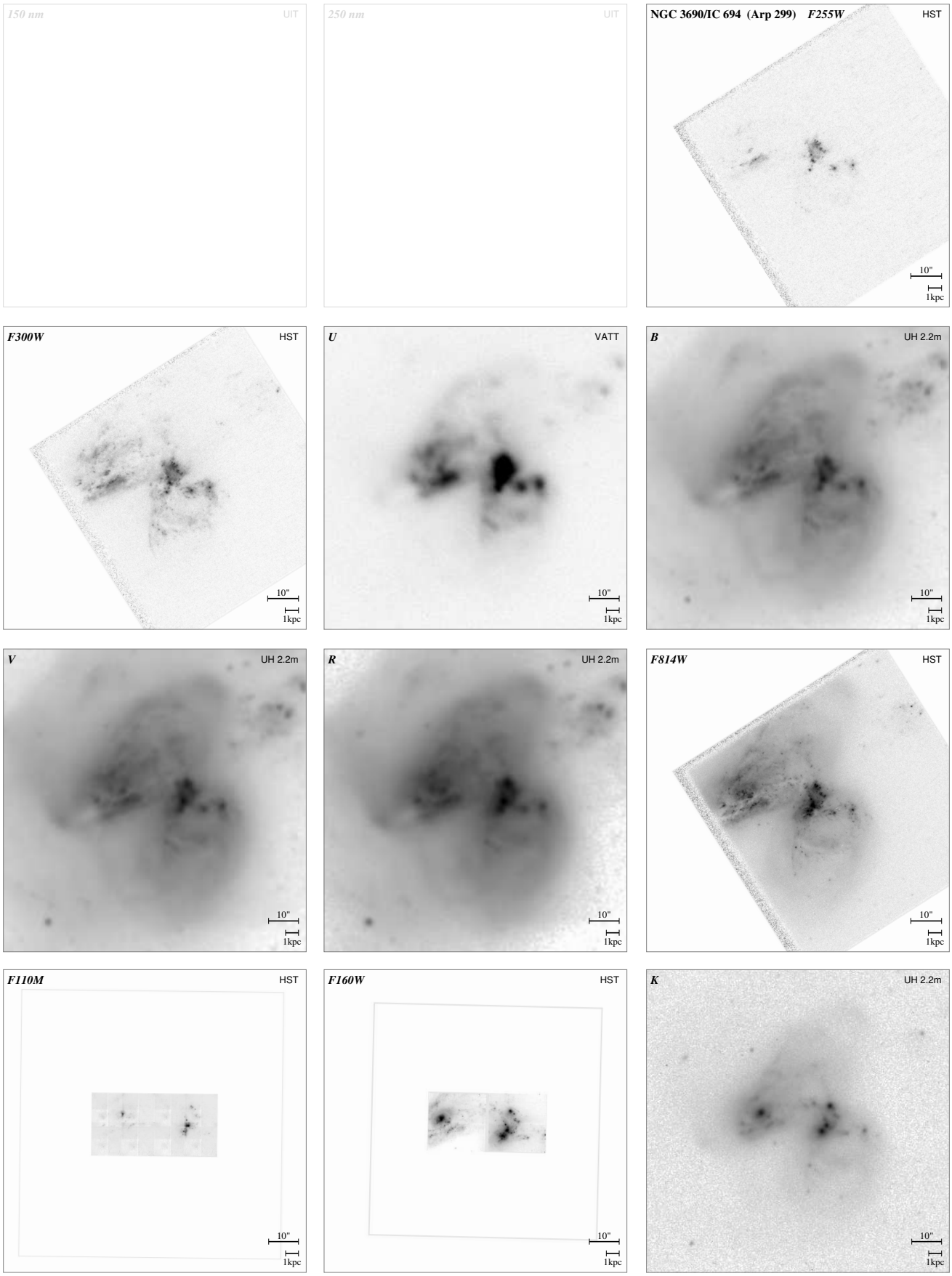

FIG. 4.— INTERACTING, PECULIAR, AND MERGING GALAXIES. **4.34 NGC 3690/IC 694** (*top*): *HST*/WFPC2 F255W; (2^{nd} *row*): *HST*/WFPC2 F300W, and ground-based *U* and *B*; (3^{rd} *row*): ground-based *V* and *R*, and *HST*/WFPC2 F814W; (*bottom*): *HST*/NICMOS F110M (*J*) and F160W (*H*), and ground-based *K*.

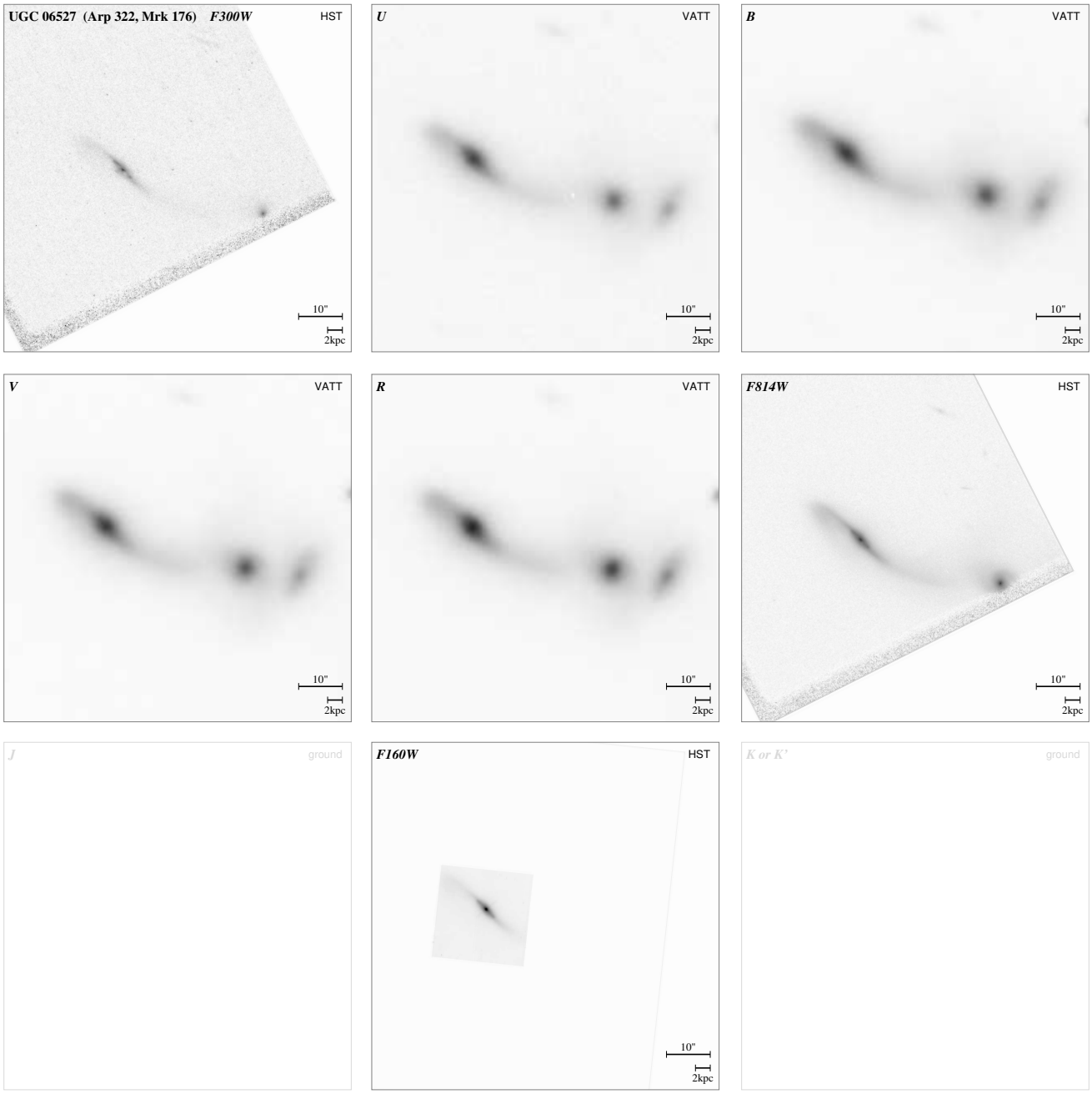

FIG. 4.— (CONT'D) **4.35 UGC 06527** (*top*): *HST*/WFPC2 F300W, and ground-based *U* and *B*; (*middle*): ground-based *V* and *R*, and *HST*/WFPC2 F814W; (*bottom*): *HST*/NICMOS F160W (*H*).

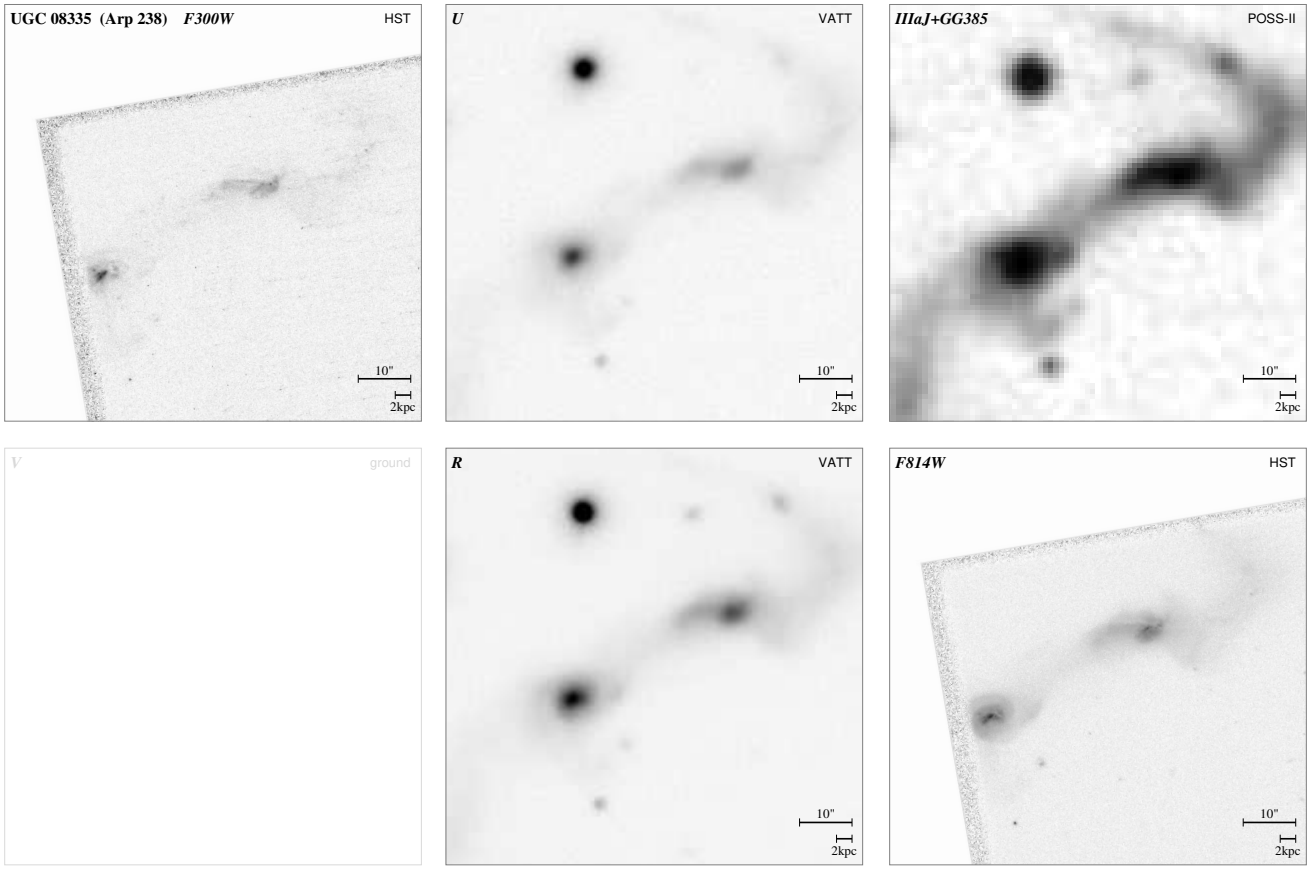

FIG. 4.— (CONT'D) **4.36 UGC 08335** (*top*): *HST*/WFPC2 F300W, and ground-based *U* and *IIIaJ*+*GG*385; (*bottom*): ground-based *R*, and *HST*/WFPC2 F814W.

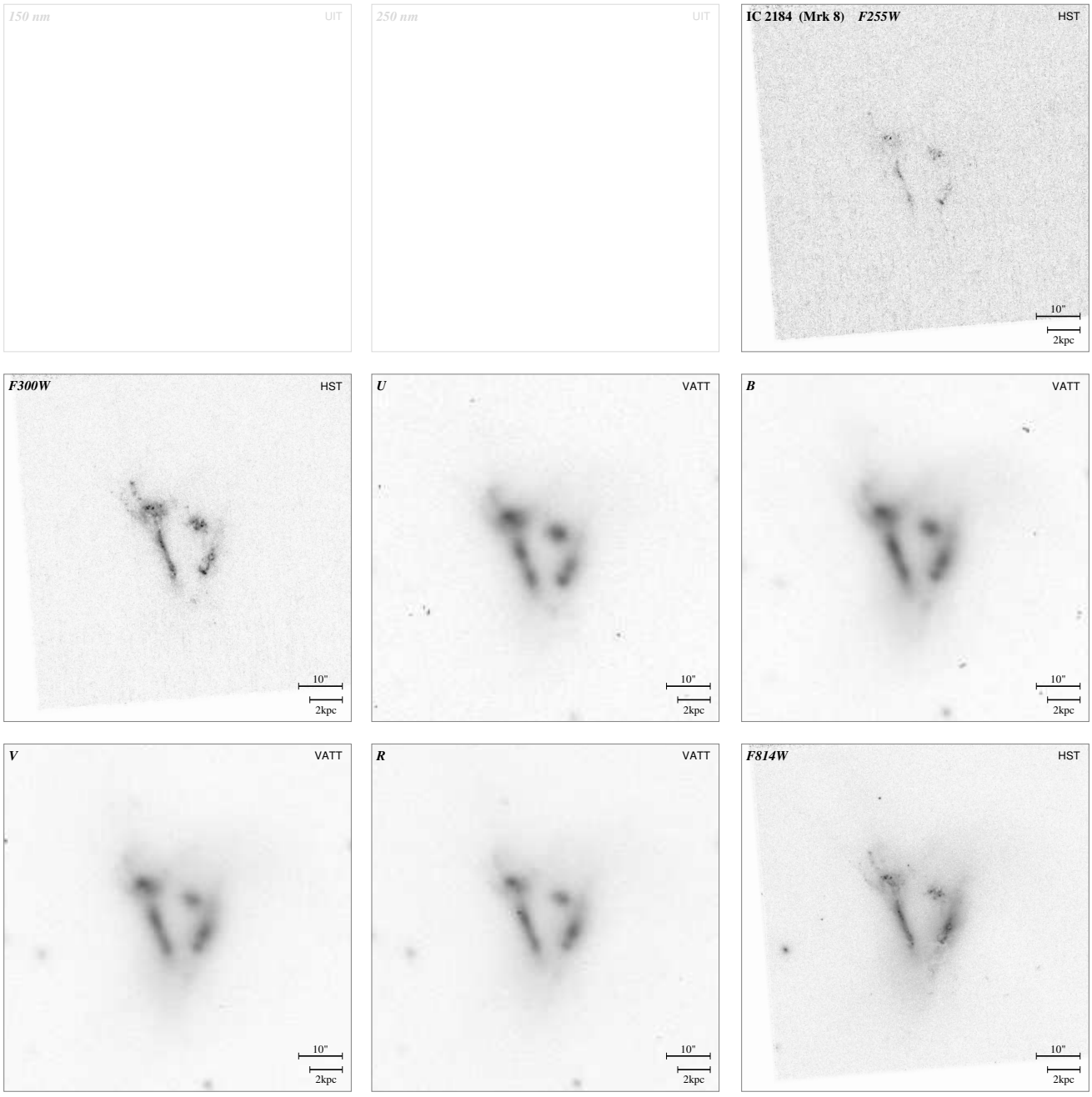

FIG. 4.— (CONT'D) **4.37 IC 2184** (*top*): *HST*/WFPC2 F255W; (*middle*): *HST*/WFPC2 F300W, and ground-based *U* and *B*; (*bottom*): ground-based *V* and *R*, and *HST*/WFPC2 F814W.

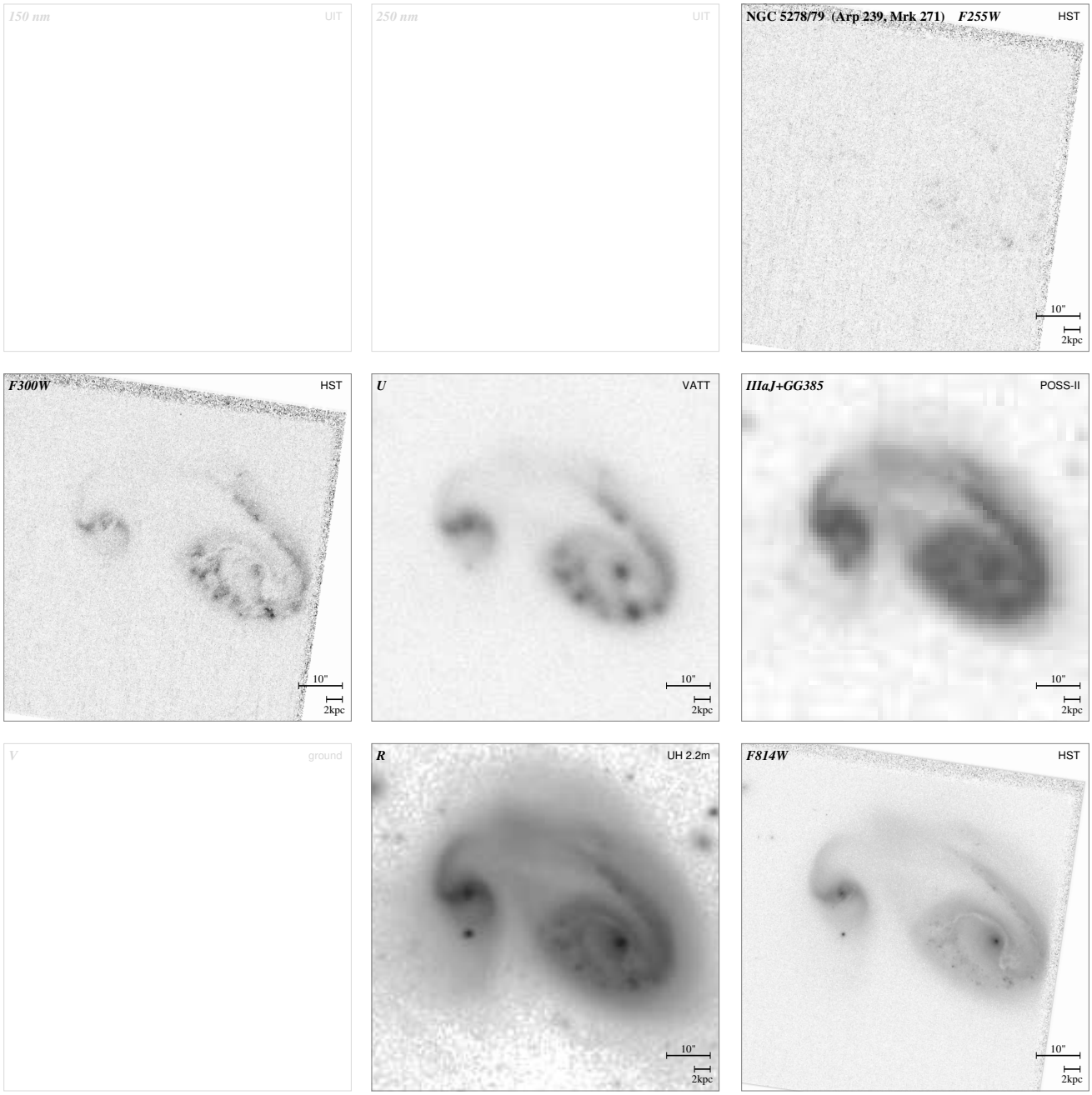

FIG. 4.— (CONT'D) **4.38 NGC 5278/79** (*top*): *HST*/WFPC2 F255W; (*middle*): *HST*/WFPC2 F300W, and ground-based *U* and *IIIaJ* + *GG*385; (*bottom*): ground-based *R*, and *HST*/WFPC2 F814W.

TABLE 1

NEARBY GALAXIES IMAGED WITH WFPC2 IN THE MID-UV IN CYCLE 9 [a]

Galaxy	RA (J2000)	DEC	b/a	r_e	r_{25}	SB_e^{U300}	SB_{r25}^{U300}	$U-B$	$B-V$	B	$U300$	T	z	Scale	kpc
				(′)	(′)	(mag/arcsec^2)		(mag)	(mag)	(mag)	(mag)			(pc/″)	/FOV
(1)	(2)	(3)	(4)	(5)	(6)	(7)	(8)	(9)	(10)	(11)	(12)	(13)	(14)	(15)	(16)
— CYCLE 9 WFPC2 MID-UV SAMPLE:															
NGC 1140	02:54:33.43	−10:01:42.4	0.55	0.144	0.830	18.29	21.34	−0.43	0.35	12.84	12.26	10.0	0.0049	106.	7.95
ESO 418–G008	03:31:30.58	−30:12:46.6	0.66	0.185	0.587	20.61	22.37	−0.23	0.41	13.92	13.84	8.0	0.0038	82.4	6.18
NGC 1396	03:38:06.63	−35:26:24.5	0.10	0.172	0.500	21.19	22.75	0.53	···	14.80	16.62	−3.0	0.0026	56.4	4.23
NGC 1510	04:03:32.55	−43:24:03.0	0.55	0.151	0.659	19.62	22.07	−0.19	0.45	13.47	13.49	−2.3	0.0028	60.7	4.55
ESO 033–G022	05:31:41.58	−73:45:04.2	0.06	0.248	1.021	19.92	22.24	−0.30	···	15.37	15.12	7.0	0.0138	299.	22.4
UGC 03426 (Mrk 3)	06:15:36.33	+71:02:13.8	0.87	0.085	0.910	20.36	24.76	0.18	1.06	14.03	14.98	−2.0	0.0138	299.	22.4
IC 2184 (Mrk 8)	07:29:25.31	+72:07:39.8	0.78	0.159	0.416	19.17	20.51	−0.58	···	13.50	12.55	9.0	0.0124	269.	20.2
NGC 2551	08:24:50.16	+73:24:43.0	0.68	0.220	0.830	21.75	23.88	0.39	0.99	13.10	14.57	0.2	0.0080	174.	13.1
UGC 05028/29 (Arp 300)	09:27:56.94	+68:24:56.9	0.58	0.150	0.354	21.32	22.44	0.14	···	14.30	15.15	4.0	0.0127	276.	20.7
UGC 05101	09:35:51.45	+61:21:10.5	0.59	0.183	0.574	20.10	21.83	−0.89	···	15.20	13.47	11.0	0.0401	870.	65.3
UGC 05189	09:42:55.27	+09:28:47.9	0.52	0.226	0.869	20.22	22.39	−0.73	···	14.60	13.27	10.0	0.0102	221.	16.6
UGC 05626	10:24:27.76	+57:23:31.1	0.37	0.215	0.792	20.04	22.12	−0.73	···	14.90	13.57	10.0	0.0088	191.	14.3
NGC 3310 (Arp 217)	10:38:45.99	+53:30:10.1	0.78	0.204	1.545	17.74	21.38	−0.43	0.35	11.15	10.57	4.0	0.0035	75.9	5.69
MCG+06–24–047	11:05:08.87	+38:04:08.7	0.07	0.143	0.301	17.45	18.31	−0.89	···	15.40	13.67	11.0	0.0292	633.	47.5
NGC 3516	11:06:47.48	+72:34:06.7	0.78	0.190	0.869	19.86	22.41	−0.06	0.81	12.50	12.85	−2.0	0.0092	200.	15.0
NGC 3690/IC 694 (Arp 299)	11:28:31.49	+58:33:45.9	0.83	0.185	0.587	17.87	19.62	−0.58	···	11.80	10.85	9.0	0.0107	232.	17.4
UGC 06527 (Arp 322)	11:32:42.24	+52:56:42.9	0.78	0.143	0.301	20.47	21.33	−0.89	···	15.80	14.07	11.0	0.0273	592.	44.4
UGC 06697	11:43:48.86	+19:58:06.1	0.17	0.288	0.931	20.04	21.83	−0.32	0.49	14.08	13.78	10.0	0.0223	484.	36.3
MCG+03–30–071	11:44:01.88	+19:47:23.7	0.34	0.162	0.435	21.42	22.82	−0.15	0.53	15.54	15.66	10.0	0.0163	354.	26.6
NGC 3860B	11:44:47.27	+19:46:05.3	1.00	0.134	0.245	22.02	22.58	−0.12	0.52	15.30	15.50	10.0	0.0212	460.	34.5
NGC 3921 (Arp 224)	11:51:06.78	+55:04:44.4	0.62	0.362	1.069	22.34	23.94	0.25	0.68	13.06	14.18	0.0	0.0198	430.	32.3
NGC 4478	12:30:17.33	+12:19:41.7	0.85	0.223	0.953	21.46	23.86	0.46	0.91	12.36	14.01	−5.0	0.0044	95.4	7.16
IC 3949	12:58:52.29	+27:49:21.6	0.19	0.174	0.512	21.41	23.00	0.21	0.84	15.10	16.12	−2.0	0.0249	540.	40.5
UGC 08335 (Arp 238)	13:15:32.91	+62:07:36.6	0.89	0.167	0.467	22.47	23.95	0.04	···	15.00	15.60	4.0	0.0312	677.	50.8
Mrk 66	13:25:53.68	+57:15:16.4	0.65	0.130	0.218	19.84	20.21	−0.66	0.02	15.00	13.85	11.0	0.0221	479.	35.9
NGC 5253	13:39:55.76	−31:38:38.5	0.39	0.379	2.506	18.52	21.88	−0.24	0.43	10.87	10.77	10.0	0.0009	19.5	1.46
NGC 5278/79 (Arp 239)	13:41:39.96	+55:40:12.4	0.71	0.197	0.674	21.43	23.35	0.14	···	13.60	14.45	3.0	0.0255	553.	41.5
UGC 08696 (Mrk 273)	13:44:42.29	+55:53:11.1	0.23	0.183	0.574	18.95	20.68	−0.89	···	15.07	13.34	11.0	0.0380	824.	61.8
UGC 08823 (Mrk 279)	13:53:03.55	+69:18:30.3	0.59	0.162	0.435	22.65	24.05	0.49	···	14.57	16.29	−2.0	0.0311	675.	50.6
IC 4393	14:17:49.07	−31:20:55.5	0.11	0.275	1.199	20.28	22.73	−0.18	···	14.55	14.60	6.0	0.0087	189.	14.2
UGC 09855	15:25:04.62	+66:15:15.8	0.33	0.210	0.757	19.77	21.80	−0.73	···	14.80	13.47	10.0	0.0122	265.	19.9
UGC 10043	15:48:41.22	+21:52:10.1	0.15	0.275	1.199	21.42	23.87	0.04	···	14.80	15.40	4.0	0.0075	163.	12.2
NGC 6753	19:11:23.75	−57:02:57.7	0.87	0.406	1.227	21.57	23.22	0.13	0.83	11.97	12.79	3.0	0.0103	223.	16.7
NGC 6789	19:16:41.93	+63:58:20.8	0.78	0.193	0.644	19.42	21.28	−0.73	···	13.70	12.37	10.0	0.0005	10.8	0.81
NGC 6782	19:23:57.96	−59:55:21.6	0.66	0.354	1.094	21.32	23.02	0.32	0.92	11.84	13.14	0.8	0.0127	276.	20.7
NGC 7685	23:30:33.35	+03:54:08.4	0.76	0.489	0.931	23.37	24.02	0.00	0.66	13.84	14.34	5.3	0.0193	419.	31.4
NGC 7769 (Mrk 9005)	23:51:03.96	+20:09:00.0	0.95	0.220	0.830	21.16	23.29	0.14	···	12.77	13.62	3.0	0.0146	317.	23.8
— ARCHIVAL WFPC2 MID-UV SAMPLE:															
NGC 0221	00:42:41.90	+40:51:55.0	0.76	0.601	4.355	20.21	23.76	0.48	0.95	9.03	10.73	−6.0	-0.0001	3.76	.282
NGC 1326	03:23:56.40	−36:27:50.0	0.65	0.416	1.945	21.12	23.72	0.28	0.87	11.41	12.61	−1.0	0.0041	88.9	6.67
NGC 1380	03:36:26.90	−34:58:33.0	0.66	0.659	2.393	22.02	24.07	0.45	0.94	10.87	12.49	−2.0	0.0057	124.	9.30
NGC 1507	04:04:27.30	−02:11:17.0	0.08	0.512	1.815	19.90	21.90	−0.07	0.57	12.89	13.21	9.0	0.0027	58.6	4.40
NGC 2798	09:17:22.90	+42:00:02.0	1.00	0.199	1.285	20.89	24.19	−0.01	0.72	13.04	13.51	1.0	0.0058	126.	9.45
NGC 3448	10:54:39.10	+54:18:24.0	0.76	0.388	2.812	21.03	24.59	−0.19	0.43	12.48	12.50	90.0	0.0047	102.	7.65
NGC 3516	11:06:47.30	+72:34:12.0	0.89	0.190	0.869	20.00	22.55	−0.06	0.81	12.50	12.85	−2.0	0.0092	200.	15.0
NGC 4278	12:20:07.20	+29:16:47.0	0.45	0.574	2.037	21.53	23.53	0.45	0.93	11.09	12.71	−5.0	0.0022	47.7	3.58
NGC 4425	12:27:13.40	+12:44:09.0	0.96	0.379	1.476	22.94	25.14	0.39	0.90	12.73	14.20	−1.0	0.0061	132.	9.90
NGC 4476	12:29:58.70	+12:20:53.0	0.50	0.301	0.849	21.71	23.21	0.27	0.82	13.01	14.18	−3.0	0.0062	134.	10.1
NGC 4564	12:36:27.00	+11:26:21.0	0.36	0.330	1.774	21.07	23.97	0.46	0.93	12.05	13.70	−5.0	0.0036	78.1	5.86
NGC 4639	12:42:52.60	+13:15:30.0	0.78	0.489	1.377	22.00	23.50	0.08	0.70	12.24	12.94	4.0	0.0032	69.4	5.21
NGC 4772	12:53:29.10	+02:10:11.0	0.45	0.397	1.694	21.29	23.70	0.33	0.92	11.96	13.28	1.0	0.0032	69.4	5.21
NGC 5273	13:42:08.40	+35:39:12.0	0.29	0.512	1.377	21.87	23.27	0.34	0.85	12.44	13.79	−2.0	0.0037	80.3	6.02
NGC 5377	13:56:16.80	+47:14:17.0	1.00	0.561	1.858	23.29	25.14	0.37	0.90	12.24	13.66	1.0	0.0063	137.	10.3
IC 4710	18:28:38.20	−66:58:54.0	0.79	0.632	1.815	22.38	23.92	−0.10	0.57	12.50	12.75	9.0	0.0021	45.6	3.42
NGC 7673	23:27:41.60	+23:35:24.0	0.91	0.155	0.644	19.58	21.92	−0.33	0.41	13.17	12.84	5.0	0.0119	258.	19.4

Note. — (a) Unless stated otherwise, all table entries are taken or derived from de RC3 catalogue (de Vaucouleurs et al. 1991).

NOTES ON TABLE COLUMNS — (1) galaxy name; (2) and (3) J2000 (RA, DEC) coordinates of the galaxy centers as measured on the Digital Sky Survey (DSS). In a few cases of complex galaxies, galaxy mergers, or galaxies in small groups, the listed coordinates refer to a "center of gravity position", allowing optimal centering inside the WFPC2 FOV; (4) ratio of the minor and major axis isophotal diameter at the SB(B) = 25.0 mag arcsec^{-2} isophote; (5) r_e denotes the half-light radius; (6) r_{25} denotes the radius at the SB(B) = 25.0 mag arcsec^{-2} isophote; (7) predicted average SB in F300W out to r_e (see section 2.2); (8) predicted average SB in F300W out to r_{25} (see §2.2); (9) measured Johnson ($U-B$) aperture color; (10) measured ($B-V$) aperture color; (11) total B-band magnitude; (12) predicted total F300W magnitude (see §2.2); (13) revised galaxy T-type (see also Fig. 2a); (14) Galactocentric galaxy redshift, as derived from the RC3; (15) number of parsec per arcsec at the distance of the galaxy, assuming a Hubble constant of 67 km s^{-1} Mpc^{-1}; (16) physical size in kpc corresponding to a single WFPC2 CCD of 75″ [Col. 16 = Col. 15 × 0.075).

TABLE 2

SUMMARY OF *HST*, *UIT* AND GROUND-BASED IMAGES OF OUR CYCLE 9 SAMPLE

Object	Telescope	Filter	Exposure time (sec)	Airmass	Orient (deg)	Zeropoint (mag)	Plate scale ($''$/pix)	FWHM ($''$)	Fig.nr.
(1)	(2)	(3)	(4)	(5)	(6)	(7)	(8)	(9)	(10)
NGC 1140 (Mrk 1063)	HST	F300W	2× 900.0	0	71.933	19.433	0.0996	0.04	3/4.28
	HST	F814W	2× 100.0	0	71.933	21.659	0.0996	0.08	3/4.28
	VATT	U	1× 300.0	1.364	0.0	—	0.3746	2.15	4.28
	VATT	B	1× 180.0	1.360	0.0	—	0.3746	2.59	4.28
	VATT	V	1× 180.0	1.358	0.0	—	0.3746	2.49	4.28
	POSS-II	IIIaF	1×3000.0	—	0.0	—	1.00	3.86	4.28
ESO 418-G008	HST	F300W	2× 900.0	0	151.410	19.433	0.0996	0.04	3/4.25
	HST	F814W	2× 130.0	0	151.410	21.659	0.0996	0.08	3/4.25
	VATT	U	1× 300.0	2.184	0.0	—	0.3746	2.80	4.25
	VATT	B	1× 360.0	2.186	0.0	—	0.3746	2.76	4.25
	VATT	V	1× 240.0	2.191	0.0	—	0.3746	2.50	4.25
	VATT	R	1× 120.0	2.197	0.0	—	0.3746	2.53	4.25
NGC 1396	UIT	150nm	1×1454.5	0	83.832	16.928	1.200	3.03	4.02
	UIT	250nm	1×1099.5	0	83.831	18.658	1.200	2.71	4.02
	HST	F300W	2× 900.0	0	22.975	19.433	0.0996	0.04	3/4.02
	HST	F814W	2× 130.0	0	22.975	21.659	0.0996	0.08	3/4.02
	POSS-I	IIIaJ	1×3600.0	—	0.0	—	1.70	5.0	4.02
	POSS-II	IIIaF	1×3600.0	—	0.0	—	1.00	3.56	4.02
NGC 1510	UIT	150nm	1× 948.5	0	0.020	16.806	1.137	3.03	4.26
	HST	F300W	2× 900.0	0	13.650	19.433	0.0996	0.04	3/4.26
	HST	F814W	2× 160.0	0	13.650	21.659	0.0996	0.08	3/4.26
	POSS-I	IIIaJ	1×4200.0	—	0.0	—	1.70	4.8	4.26
	POSS-II	IIIaF	1×3900.0	—	0.0	—	1.00	3.52	4.26
ESO 033-G022	HST	F300W	2×1000.0	0	254.257	19.433	0.0996	0.04	3/4.19
	HST	F814W	2× 130.0	0	254.257	21.659	0.0996	0.08	3/4.19
	ESO 1.5m	B	2×1500.0	—	0.28	22.331	0.36	1.7	4.19
	ESO 1.5m	V	1×2100.0	—	0.28	23.058	0.36	1.6	4.19
	ESO 1.5m	I	2× 900.0	—	0.28	22.351	0.36	0.9	4.19
UGC 03426 (Mrk 3)	UIT	150nm	2×1261.0	0	327.300	16.806	1.137	3.03	4.05
	HST	F255W	3× 466.7	0	119.723	17.037	0.0996	0.04	3/4.05
	HST	F300W	3× 500.0	0	119.723	19.433	0.0996	0.04	3/4.05
	HST	F814W	2× 130.0	0	119.723	21.659	0.0996	0.08	3/4.05
	VATT	U	1× 300.0	1.462	0.0	—	0.3746	1.96	4.05
	VATT	B	1× 180.0	1.502	0.0	—	0.3746	1.62	4.05
	VATT	V	1× 120.0	1.522	0.0	—	0.3746	1.52	4.05
	VATT	R	1× 30.0	1.553	0.0	—	0.3746	1.42	4.05
IC 2184 (Mrk 8)	HST	F255W	3× 466.7	0	139.416	17.037	0.0996	0.04	3/4.37
	HST	F300W	3× 500.0	0	139.416	19.433	0.0996	0.04	3/4.37
	HST	F814W	2× 130.0	0	139.416	21.659	0.0996	0.08	3/4.37
	VATT	U	1× 600.0	1.298	0.0	—	0.3746	2.12	4.37
	VATT	B	1× 300.0	1.298	0.0	—	0.3746	1.96	4.37
	VATT	V	1× 240.0	1.298	0.0	—	0.3746	2.00	4.37
	VATT	R	1× 180.0	1.302	0.0	—	0.3746	1.70	4.37
NGC 2551	UIT	150nm	1× 454.5	0	43.306	16.928	1.200	3.03	4.10
	UIT	250nm	1× 454.5	0	43.307	18.658	1.200	2.71	4.10
	HST	F300W	2×1000.0	0	232.495	19.433	0.0996	0.04	3/4.10
	HST	F814W	2× 130.0	0	232.495	21.659	0.0996	0.08	3/4.10
	VATT	U	1× 600.0	1.325	0.0	—	0.3746	1.60	4.10
	VATT	B	1× 180.0	1.325	0.0	—	0.3746	1.24	4.10
	VATT	V	1× 120.0	1.324	0.0	—	0.3746	1.15	4.10
	VATT	R	1× 120.0	1.324	0.0	—	0.3746	1.00	4.10
UGC 05028/29 (Arp 300)	HST	F300W	2× 950.0	0	350.000	19.433	0.0996	0.04	3/4.23
	HST	F814W	2× 160.0	0	350.000	21.659	0.0996	0.08	3/4.23
	POSS-II	IIIaJ	1×4800.0	—	0.0	—	1.00	3.48	4.23
	POSS-II	IIIaF	1×3000.0	—	0.0	—	1.00	3.40	4.23
UGC 05101	HST	F255W	3× 466.7	0	165.068	17.037	0.0996	0.04	3/4.08
	HST	F300W	3× 500.0	0	165.068	19.433	0.0996	0.04	3/4.08
	HST	F814W	2× 130.0	0	165.068	21.659	0.0996	0.08	3/4.08
	VATT	U	4× 300.0	1.223	0.0	25.000	0.3746	1.9	4.08
	VATT	B	1× 300.0	1.203	0.0	25.000	0.3746	2.0	4.08
	VATT	V	1× 240.0	1.197	0.0	25.000	0.3746	2.1	4.08
	VATT	R	1× 180.0	1.192	0.0	25.000	0.3746	2.1	4.08
	HST	F110W	1× 111.9	0	107.171	24.818	0.0758	0.11	4.08
	HST	F160W	1× 111.9	0	107.171	25.447	0.0758	0.16	4.08
	HST	F222M	1× 135.9	0	107.171	25.131	0.0758	0.22	4.08
UGC 05189	HST	F300W	2× 900.0	0	230.001	19.433	0.0996	0.04	3/4.33
	HST	F814W	2× 100.0	0	230.001	21.659	0.0996	0.08	3/4.33
	VATT	U	2×1200.0	1.1	0.0	25.000	0.3746	1.8	4.33
	VATT	B	2× 600.0	1.1	0.0	25.000	0.3746	1.6	4.33
	VATT	V	4× 480.0	1.1	0.0	25.000	0.3746	1.6	4.33
	VATT	R	2× 360.0	1.1	0.0	25.000	0.3746	1.5	4.33
UGC 05626	HST	F255W	3× 466.7	0	170.844	17.037	0.0996	0.04	3/4.29
	HST	F300W	3× 500.0	0	170.844	19.433	0.0996	0.04	3/4.29
	HST	F814W	2× 130.0	0	170.844	21.659	0.0996	0.08	3/4.29
	VATT	U	2×1200.0	1.417	0.0	25.000	0.3746	2.0	4.29
	VATT	B	2× 600.0	1.427	0.0	25.000	0.3746	1.9	4.29
	VATT	V	2× 480.0	1.436	0.0	25.000	0.3746	1.8	4.29
	VATT	R	2× 360.0	1.444	0.0	25.000	0.3746	1.8	4.29
NGC 3310 (Arp 217)	UIT	150nm	1×1130.5	0	112.049	16.806	1.1367	3.03	4.13

TABLE 2—*Continued*

Object	Telescope	Filter	Exposure time (sec)	Airmass	Orient (deg)	Zeropoint (mag)	Plate scale (″/pix)	FWHM (″)	Fig.nr.
(1)	(2)	(3)	(4)	(5)	(6)	(7)	(8)	(9)	(10)
	HST	F300W	2× 950.0	0	165.015	19.433	0.0996	0.04	3/4.13
	HST	F814W	2× 130.0	0	165.015	21.659	0.0996	0.08	3/4.13
	VATT	U	1× 300.0	1.225	0.0	—	0.3746	2.10	4.13
	VATT	B	1× 150.0	1.232	0.0	—	0.3746	1.62	4.13
	VATT	V	1× 150.0	1.242	0.0	—	0.3746	2.21	4.13
	VATT	R	1× 150.0	1.251	0.0	—	0.3746	1.37	4.13
	HST	F160W	1× 256.0	0	80.830	21.100	0.2000	0.20	4.13
MCG+06-24-047	UIT	150nm	1×1430.5	0	127.736	16.806	1.1367	3.03	4.22
	HST	F300W	2× 900.0	0	145.410	19.433	0.0996	0.04	3/4.22
	HST	F814W	2× 130.0	0	145.410	21.659	0.0996	0.08	3/4.22
	VATT	U	2× 600.0	1.032	0.0	25.000	0.3746	2.5	4.22
	VATT	B	2× 300.0	1.030	0.0	25.000	0.3746	2.8	4.22
	VATT	V	2× 240.0	1.029	0.0	25.000	0.3746	2.5	4.22
	VATT	R	2× 180.0	1.186	0.0	25.000	0.3746	2.5	4.22
NGC 3516	UIT	150nm	1×1480.5	0	299.210	16.806	1.1367	3.03	4.04
	HST	F255W	3× 466.7	0	256.848	17.037	0.0996	0.04	3/4.04
	HST	F300W	3× 500.0	0	256.848	19.433	0.0996	0.04	3/4.04
	HST	F814W	2× 130.0	0	256.848	21.659	0.0996	0.08	3/4.04
	VATT	U	1× 300.0	1.636	0.0	—	0.3746	1.85	4.04
	VATT	B	1× 150.0	1.655	0.0	—	0.3746	1.80	4.04
	VATT	V	1× 100.0	1.662	0.0	—	0.3746	1.66	4.04
	VATT	R	1× 180.0	1.711	0.0	—	0.3746	2.00	4.04
NGC 3690/IC 0694 (Arp 299, Mrk 171)	HST	F255W	3× 466.7	0	257.350	17.037	0.0996	0.04	3/4.34
	HST	F300W	3× 500.0	0	257.350	19.433	0.0996	0.04	3/4.34
	HST	F814W	2× 130.0	0	257.350	21.659	0.0996	0.08	3/4.34
	VATT	U	2× 600.0	1.120	0.0	—	0.3746	2.84	4.34
	UH 2.2m	B	1× 600.0	1.283	359.910	—	0.4400	1.4	4.34
	UH 2.2m	V	1× 900.0	1.284	359.910	—	0.4400	1.5	4.34
	UH 2.2m	R	1× 600.0	1.283	359.910	—	0.4400	1.5	4.34
	UH 2.2m	K	5× 120.0	1.286	0.006	—	0.2200	1.1	4.34
UGC 06527 (Arp 322, Mrk 176)	HST	F300W	2× 950.0	0	251.824	19.433	0.0996	0.04	3/4.35
	HST	F814W	2× 130.0	0	251.824	21.659	0.0996	0.08	3/4.35
	VATT	U	2×1200.0	1.083	0.0	25.000	0.3746	2.3	4.35
	VATT	B	2× 600.0	1.078	0.0	25.000	0.3746	2.6	4.35
	VATT	V	2× 480.0	1.077	0.0	25.000	0.3746	2.4	4.35
	VATT	R	2× 360.0	1.212	0.0	25.000	0.3746	2.5	4.35
	HST	F160W	1× 256.0	0	-6.017	21.100	0.2000	0.20	4.35
UGC 06697	UIT	150nm	1× 529.5	0	84.124	16.928	1.200	3.03	4.17
	UIT	250nm	1× 105.5	0	84.125	18.658	1.200	2.71	4.17
	HST	F300W	2× 900.0	0	286.763	19.433	0.0996	0.04	3/4.17
	HST	F814W	2× 100.0	0	286.763	21.659	0.0996	0.08	3/4.17
	VATT	U	2× 600.0	1.035	0.0	25.000	0.3746	2.3	4.17
	VATT	B	2× 300.0	1.032	0.0	25.000	0.3746	2.4	4.17
	VATT	V	3× 240.0	1.043	0.0	25.000	0.3746	2.2	4.17
	VATT	R	2× 180.0	1.162	0.0	25.000	0.3746	2.6	4.17
CGCG 097-094 (observed in the field of MCG+03-30-071)	UIT	150nm	1× 529.5	0	84.124	16.928	1.200	3.03	4.01
	UIT	250nm	1× 105.5	0	84.125	18.658	1.200	2.71	4.01
	HST	F300W	2× 900.0	0	300.002	19.433	0.0996	0.04	3/4.01
	HST	F814W	2× 100.0	0	300.002	21.659	0.0996	0.08	3/4.01
	VATT	U	2× 600.0	1.045	0.0	25.000	0.3746	2.4	4.01
	VATT	B	2× 300.0	1.043	0.0	25.000	0.3746	2.4	4.01
	VATT	V	2× 240.0	1.042	0.0	25.000	0.3746	2.3	4.01
	VATT	R	2× 180.0	1.120	0.0	25.000	0.3746	2.2	4.01
MCG+03-30-071	UIT	150nm	1× 529.5	0	84.124	16.928	1.200	3.03	4.21
	UIT	250nm	1× 105.5	0	84.125	18.658	1.200	2.71	4.21
	HST	F300W	2× 900.0	0	300.002	19.433	0.0996	0.04	3/4.21
	HST	F814W	2× 100.0	0	300.002	21.659	0.0996	0.08	3/4.21
	VATT	U	2× 600.0	1.045	0.0	25.000	0.3746	2.4	4.21
	VATT	B	2× 300.0	1.043	0.0	25.000	0.3746	2.4	4.21
	VATT	V	2× 240.0	1.042	0.0	25.000	0.3746	2.3	4.21
	VATT	R	2× 180.0	1.120	0.0	25.000	0.3746	2.2	4.21
NGC 3860B	UIT	150nm	1× 529.5	0	84.124	16.928	1.200	3.03	4.24
	UIT	250nm	1× 105.5	0	84.125	18.658	1.200	2.71	4.24
	HST	F300W	2× 900.0	0	287.781	19.433	0.0996	0.04	3/4.24
	HST	F814W	2× 100.0	0	287.781	21.659	0.0996	0.08	3/4.24
	VATT	U	2× 600.0	1.036	0.0	25.000	0.3746	1.5	4.24
	VATT	B	2× 300.0	1.035	0.0	25.000	0.3746	1.6	4.24
	VATT	V	2× 240.0	1.034	0.0	25.000	0.3746	1.7	4.24
	VATT	R	2× 180.0	1.166	0.0	25.000	0.3746	2.4	4.24
NGC 3921 (Arp 224, Mrk 430)	HST	F300W	2× 950.0	0	241.061	19.433	0.0996	0.04	3/4.07
	HST	F814W	2× 130.0	0	241.061	21.659	0.0996	0.08	3/4.07
	UH 2.2m	B	2× 600.0	1.237	359.869	—	0.4400	?	4.07
	UH 2.2m	V	1× 900.0	1.250	359.869	—	0.4400	?	4.07
	UH 2.2m	R	1× 600.0	1.231	359.869	—	0.4400	?	4.07
	HST	F110W	1× 160.0	0	18.507	21.100	0.0758	0.11	4.07
	HST	F160W	1× 256.0	0	18.839	21.100	0.2000	0.20	4.07
	UH 2.2m	K′	3× 120.0	1.231	0.006	—	0.1850	?	4.07
NGC 4478	UIT	150nm	1× 352.5	0	303.985	16.928	1.200	3.03	4.03
	UIT	250nm	1× 70.5	0	303.985	18.658	1.200	2.71	4.03

TABLE 2—*Continued*

Object	Telescope	Filter	Exposure time (sec)	Airmass	Orient (deg)	Zeropoint (mag)	Plate scale (″/pix)	FWHM (″)	Fig.nr.
(1)	(2)	(3)	(4)	(5)	(6)	(7)	(8)	(9)	(10)
	HST	F300W	2× 900.0	0	123.922	19.433	0.0996	0.04	3/4.03
	HST	F814W	2× 100.0	0	123.922	21.659	0.0996	0.08	3/4.03
	VATT	U	1× 300.0	1.072	0.0	—	0.3746	2.31	4.03
	VATT	B	1× 300.0	1.070	0.0	—	0.3746	2.10	4.03
	VATT	V	1× 200.0	1.066	0.0	—	0.3746	1.62	4.03
	VATT	R	1× 120.0	1.068	0.0	—	0.3746	1.70	4.03
IC 3949	UIT	150nm	1×1900.5	0	211.560	16.806	1.1367	3.03	4.18
	HST	F300W	2× 900.0	0	130.973	19.433	0.0996	0.04	3/4.18
	HST	F814W	2× 100.0	0	130.973	21.659	0.0996	0.08	3/4.18
	VATT	U	1× 300.0	1.392	0.0	—	0.3746	2.25	4.18
	VATT	B	1× 180.0	1.487	0.0	—	0.3746	1.77	4.18
	VATT	V	1× 120.0	1.539	0.0	—	0.3746	1.77	4.18
	VATT	R	1× 60.0	1.585	0.0	—	0.3746	1.21	4.18
UGC 08335 (Arp 238)	HST	F300W	2× 900.0	0	234.614	19.433	0.0996	0.04	3/4.36
	HST	F814W	2× 130.0	0	234.614	21.659	0.0996	0.08	3/4.36
	VATT	U	2× 600.3	1.399	0.0	—	0.3746	1.99	4.36
	POSS-II	IIIaJ	1×4500.0	—	0.0	—	1.00	3.15	4.36
	VATT	R	2× 180.1	1.388	0.0	—	0.3746	1.87	4.36
Mrk 66	UIT	150nm	1× 775.5	0	27.310	16.806	1.1367	3.03	4.32
	HST	F300W	2× 900.0	0	143.091	19.433	0.0996	0.04	3/4.32
	HST	F814W	2× 130.0	0	143.091	21.659	0.0996	0.08	3/4.32
	VATT	U	2× 600.1	1.143	0.0	—	0.3746	1.66	4.32
	VATT	B	2× 300.0	1.133	0.0	—	0.3746	1.75	4.32
	VATT	V	2× 240.8	1.128	0.0	—	0.3746	1.66	4.32
	VATT	R	2× 180.0	1.426	0.0	—	0.3746	2.27	4.32
NGC 5253	UIT	150nm	2× 726.1	0	163.350	16.806	1.1367	3.03	4.27
	HST	F255W	9× 766.7	0	264.709	17.037	0.0996	0.04	4.27
	HST	F300W	2× 900.0	0	291.500	19.433	0.0996	0.04	3/4.27
	HST	F814W	2× 130.0	0	291.500	21.659	0.0996	0.08	3/4.27
	VATT	U	5× 300.0	2.307	0.0	25.000	0.3746	3.3	4.27
	VATT	B	2× 300.0	2.304	0.0	25.000	0.3746	2.6	4.27
	VATT	V	2× 240.0	2.308	0.0	25.000	0.3746	2.5	4.27
	VATT	R	2× 180.0	2.314	0.0	25.000	0.3746	2.3	4.27
	LCO 2.5m	J	5× 50.0	0.500	0.0	22.20	0.3500	1.94	4.27
	LCO 2.5m	H	5× 30.0	0.500	0.0	21.96	0.3500	1.91	4.27
	LCO 2.5m	K	9× 20.0	0.500	0.0	21.62	0.3500	0.98	4.27
NGC 5278/79 (Arp 239, Mrk 271)	HST	F255W	3× 466.7	0	126.600	17.037	0.0996	0.04	3/4.38
	HST	F300W	3× 500.0	0	126.600	19.433	0.0996	0.04	3/4.38
	HST	F814W	2× 130.0	0	126.600	21.659	0.0996	0.08	3/4.38
	VATT	U	4× 300.7	1.496	0.0	—	0.3746	2.49	4.38
	POSS-II	IIIaJ	1×3900.0	—	0.0	—	1.00	3.4	4.38
	UH 2.2m	R	1× 600.0	1.352	359.684	—	0.4400	—	4.38
UGC 08696 (Mrk 273)	HST	F255W	3× 466.7	0	254.413	17.037	0.0996	0.04	3/4.09
	HST	F300W	3× 500.0	0	254.413	19.433	0.0996	0.04	3/4.09
	HST	F814W	2× 130.0	0	254.413	21.659	0.0996	0.08	3/4.09
	VATT	U	2× 303.8	1.645	0.0	—	0.3746	2.47	4.09
	UH 2.2m	R	1× 600.0	1.377	359.684	—	0.4400	—	4.09
	HST	F110W	4× 63.9	0	88.267	24.818	0.0758	0.11	4.09
	HST	F160W	4× 63.9	0	88.267	25.447	0.0758	0.16	4.09
	HST	F222M	4× 79.9	0	88.267	25.131	0.0758	0.22	4.09
UGC 08823 (Mrk 279)	UIT	150nm	2× 777.5	0	39.999	16.806	1.1367	3.03	4.06
	HST	F300W	2× 950.0	0	318.595	19.433	0.0996	0.04	3/4.06
	HST	F814W	2× 160.0	0	318.595	21.659	0.0996	0.08	3/4.06
	VATT	U	4× 300.0	1.333	0.0	25.000	0.3746	3.2	4.06
	VATT	B	2× 300.0	1.316	0.0	25.000	0.3746	3.1	4.06
	VATT	V	2× 240.0	1.317	0.0	25.000	0.3746	2.7	4.06
	VATT	R	2× 180.0	1.317	0.0	25.000	0.3746	2.6	4.06
IC 4393	HST	F300W	2× 900.0	0	150.001	19.433	0.0996	0.04	3/4.20
	HST	F814W	2× 130.0	0	150.001	21.659	0.0996	0.08	3/4.20
	VATT	U	2× 600.0	2.286	0.0	25.000	0.3746	2.4	4.20
	VATT	B	2× 300.0	2.291	0.0	25.000	0.3746	2.3	4.20
	VATT	V	2× 240.0	2.297	0.0	25.000	0.3746	2.2	4.20
	VATT	R	2× 180.0	2.304	0.0	25.000	0.3746	2.1	4.20
	ESO 1.5m	I	2×1200.0	—	1.46	20.928	0.36	1.2	4.20
	ESO 2.2m	K	24× 10.0	—	0.11	20.772	0.491	1.4	4.20
UGC 09855	HST	F255W	3× 466.7	0	291.667	17.037	0.0996	0.04	3/4.30
	HST	F300W	3× 500.0	0	291.667	19.433	0.0996	0.04	3/4.30
	HST	F814W	2× 130.0	0	291.667	21.659	0.0996	0.08	3/4.30
	VATT	U	2× 600.0	1.234	0.0	25.000	0.3746	2.7	4.30
	VATT	B	2× 240.0	1.255	0.0	25.000	0.3746	2.9	4.30
	VATT	V	2× 300.0	1.234	0.0	25.000	0.3746	2.5	4.30
	VATT	R	2× 180.0	1.264	0.0	25.000	0.3746	2.7	4.30
UGC 10043	HST	F300W	2× 900.0	0	250.001	19.433	0.0996	0.04	3/4.16
	HST	F814W	2× 100.0	0	250.001	21.659	0.0996	0.08	3/4.16
	VATT	U	2×1800.0	1.048	0.0	25.000	0.3746	1.5	4.16
	VATT	B	2×1200.0	1.158	0.0	25.000	0.3746	1.3	4.16
	VATT	V	2× 900.0	1.167	0.0	25.000	0.3746	1.1	4.16
	VATT	R	2× 600.0	1.331	0.0	25.000	0.3746	1.2	4.16
NGC 6753	HST	F300W	2× 950.0	0	154.222	19.433	0.0996	0.04	3/4.11

TABLE 2—*Continued*

Object	Telescope	Filter	Exposure time (sec)	Airmass	Orient (deg)	Zeropoint (mag)	Plate scale ($''$/pix)	FWHM ($''$)	Fig.nr.
(1)	(2)	(3)	(4)	(5)	(6)	(7)	(8)	(9)	(10)
	HST	F814W	2× 160.0	0	154.222	21.659	0.0996	0.08	3/4.11
	CTIO 0.9m	U	1×1200.0	1.125	0.0	—	0.396	1.45	4.11
	CTIO 0.9m	B	4× 300.0	1.382	0.0	—	0.396	1.68	4.11
	CTIO 0.9m	V	3× 300.0	1.453	0.0	—	0.396	1.76	4.11
	CTIO 0.9m	R	3× 200.0	1.514	0.0	—	0.396	1.90	4.11
	CTIO 1.5m	J	···	—	0.0	—	0.645	1.11	4.11
	CTIO 1.5m	H	···	—	0.0	—	0.645	1.25	4.11
	CTIO 1.5m	K	···	—	0.0	—	0.645	1.10	4.11
NGC 6789	HST	F255W	3× 466.7	0	349.145	17.037	0.0996	0.04	3/4.31
	HST	F300W	3× 500.0	0	349.145	19.433	0.0996	0.04	3/4.31
	HST	F814W	2× 130.0	0	349.145	21.659	0.0996	0.08	3/4.31
	VATT	U	2× 600.0	1.674	0.0	25.000	0.3746	2.1	4.31
	VATT	B	2× 300.0	1.676	0.0	25.000	0.3746	2.0	4.31
	VATT	V	2× 240.0	1.586	0.0	25.000	0.3746	1.8	4.31
	VATT	R	2× 180.0	1.657	0.0	25.000	0.3746	1.5	4.31
NGC 6782	HST	F255W	3× 466.7	0	151.206	17.037	0.0996	0.04	3/4.15
	HST	F300W	3× 500.0	0	151.206	19.433	0.0996	0.04	3/4.15
	HST	F814W	2× 130.0	0	151.206	21.659	0.0996	0.08	3/4.15
	CTIO 0.9m	U	2×2400.0	1.154	0.0	—	0.396	2.09	4.15
	CTIO 0.9m	B	4× 450.0	1.321	0.0	—	0.396	1.59	4.15
	CTIO 0.9m	V	3× 300.0	1.399	0.0	—	0.396	1.37	4.15
	CTIO 0.9m	R	3× 200.0	1.448	0.0	—	0.396	1.38	4.15
	CTIO 1.5m	J	2× 20.0	—	0.0	—	0.645	1.33	4.15
	CTIO 1.5m	H	2× 10.0	—	0.0	—	0.645	1.31	4.15
	KPNO 2.2m	K	···	—	0.0	—	1.09	1.72	4.15
NGC 7685	HST	F300W	2× 900.0	0	64.488	19.433	0.0996	0.04	3/4.14
	HST	F814W	2× 100.0	0	64.488	21.659	0.0996	0.08	3/4.14
	VATT	U	2× 600.0	1.261	0.0	—	0.3746	1.59	4.14
	VATT	B	1× 300.0	1.286	0.0	—	0.3746	1.39	4.14
	JKT	V	1× 346.8	1.102	0.0	22.322	0.30	1.39	4.14
	JKT	R	1× 289.0	1.106	0.0	22.558	0.30	1.63	4.14
	JKT	I	1× 289.0	1.114	0.0	21.833	0.30	1.21	4.14
	UKIRT	K	8× 75.0	1.057	0.0	20.018	0.30	1.55	4.14
NGC 7769 (Mrk 9005)	HST	F300W	2× 900.0	0	64.927	19.433	0.0996	0.04	3/4.12
	HST	F814W	2× 100.0	0	64.927	21.659	0.0996	0.08	3/4.12
	VATT	U	2× 600.0	1.025	0.0	—	0.3746	1.42	4.12
	VATT	B	2× 300.0	1.026	0.0	—	0.3746	1.34	4.12
	VATT	V	1× 300.0	1.086	0.0	—	0.3746	0.97	4.12
	VATT	R	1× 300.0	1.059	0.0	—	0.3746	1.10	4.12
	JKT	I	1× 404.6	1.035	0.0	21.709	0.30	1.36	4.12
	UKIRT	H	5× 60.0	1.000	0.0	20.500	0.30	1.41	4.12

NOTES ON TABLE COLUMNS: (1) galaxy name; (2) telescope that produced the listed images; (3) filter: *HST*/WFPC2 (see Biretta et al. 2000), *UIT* (see Stecher et al. 1997; 150nm denotes both B1 and B2, 250nm both A1 and A5 filters), or ground-based Johnson *UBV* and Kron-Cousins *RIJHK*; (4) total exposure time, given as the number of independent integrations times the single image exposure time (as listed in the FITS headers and corresponding to the zero-points listed in Col. 7). For unequal length exposures, the listed single-exposure time is the mean of the actual exposure times; (5) average airmass of the image stack (0 for space-based observations); (6) image orientation. For *HST*, this is angle `PA_V3` (measured from North through East) of the V3 axis (i.e., the X=Y diagonal of the WFC3 CCD + 180°). For *UIT* and ground based images, the P.A. of the Y-axis of the CCD image is given (i.e., P.A. = 0 means that North is up and East is to the left); (7) photometric zero-point ZP derived for the ground-based images using: Vega-mag = ZP $-2.5\log_{10}(\mathrm{DN}/t)$, with DN the total object flux, and t in sec (see Col. 4). For *HST*/WFPC2, these are the Holtzman et al. (1995) Vega zero-points, and for *UIT*, $\mathrm{ZP_{ST}} = -2.5\log_{10}C - 21.1$, with C the calibration constants C_{NUV} and C_{FUV} listed in Stecher et al. (1997). We only list available and confirmed zero-points, but will update the FITS headers in the public data base as ground-based calibrations become available (see Taylor et al. 2002); (8) image pixel scale; (9) estimated FWHM of the relevant image PSF in arcsec. For HST images, these are not to be confused with the $0.0996''$ WFC pixel scale, and are derived as $\mathrm{FWHM} = 206265'' \times 1.22 \times \lambda_{cent}/\mathrm{D}$, with the central wavelength of the filter (see text) in m and primary aperture D = 2.4 m. Note that especially the WFPC2 UV images are badly under-sampled. Micro-roughness of the HST mirror limits the mid-UV PSF to $\sim 0.04''$ FWHM. For ground-based images, the FWHM values were measured using unsaturated stellar objects in each image as identified using `SExtractor`; (10) number of the figure(s) displaying each image.

TABLE 3

OTHER IMAGING DATA IN THE *HST* ARCHIVE ON OUR CYCLE 9 GALAXY SAMPLE.

Object	Filter	λ_c (Å)	$\Delta\lambda$ (Å)	Exposure time (sec)	Orient (deg)	Proposal ID	PI	Note
(1)	(2)	(3)	(4)	(5)	(6)	(7)	(8)	(9)
— WFPC2 IMAGES:								
ESO 418-G008	F606W	5957	1508	2×80	227.216	SNAP 5446	G. Illingworth	center in PC1
	F814W	7940	1531	2×600	16.701	SNAP 8599	T. Boeker	PC1
NGC 1510	F170W	1730	500	2×400	303.570	GO 6716	T. Stecher	
	F336W	3344	381	2×260	303.570	""	""	
	F555W	5407	1236	1×200	303.570	""	""	
	F814W	7940	1531	1×200	303.570	""	""	
UGC 03426	F606W	5957	1508	1×500	73.315	SNAP 5479	M. Malkan	PC1
IC 2184	F555W	5407	1236	1×700+1×400	94.381	GTO 6870	J. Trauger	
	F814W	7940	1531	2×600	94.381	""	""	
UGC 05101	F814W	7940	1531	2×400	321.786	SNAP 6346	K. Borne	
NGC 3310	F606W	5957	1508	1×500	280.821	SNAP 5479	M. Malkan	PC1
	F336W	3344	381	2×500	350.875	GO 6639	G. Meurer	PC1
	F439W	4300	475	2×300	350.875	""	""	
	F814W	7940	1531	1×160+1×180	350.875	""	""	
MCG+06-24-047	F814W	7940	1531	2×700	53.898	GO 5370	R. Griffiths	WF4 and PC1
NGC 3516	F606W	5957	1508	1×500	218.572	SNAP 5479	M. Malkan	PC1; core saturated
	F300W	2911	745	2×400	344.525	SNAP 6355	M. Giavalisco	PC1
	F547M	5479	486	2×70	28.496	GO 6419	A. Wilson	PC1
	F791W	7829	1218	2×70	28.465	""	""	
	F450W	4520	958	1×900+1×1400	12.393	GO 6633	C. Carollo	PC1
	F555W	5407	1236	1×300+1×700	12.393	""	""	
	F814W	7940	1531	1×230+1×500	12.393	""	""	
NGC 3690/IC 694	F606W	5957	1508	1×500	177.915	SNAP 5479	M. Malkan	PC1
	F336W	3344	381	4×400	142.669	GO 6639	G. Meurer	PC1
	F439W	4300	475	2×200+2×260	142.669	""	""	
	F814W	7940	1531	2×40+160+260	142.669	""	""	
	F555W	5407	1236	2×350	306.258	SNAP 8602	A. Filippenko	PC1
	F814W	7940	1531	2×350	356.266	""	""	
	F814W	7940	1531	2×350	293.276	""	""	
UGC 06527	F606W	5957	1508	1×500	157.556	SNAP 5479	M. Malkan	PC1
NGC 3921	F336W	3344	381	2×600	172.058	GO 5416	B. Whitmore	PC1
	F555W	5407	1236	1×30+2×1200	172.058	""	""	
	F814W	7940	1531	1×30+2×900	172.058	""	""	
	F555W	5407	1236	2×400+2×500	321.026	GO 7466	J. Charlton	targets tidal tails
	F814W	7940	1531	2×400+2×400	321.026	""	""	
NGC 4478	F814W	7940	1531	1×1200+1×2400	299.972	GO 5369	R. Griffiths	
	F606W	5957	1508	6×2800	299.972	GTO 6252	E. Groth	saturated center and star
	F814W	7940	1531	5×2800+1×2500	299.972	""	""	""
	F300W	2911	745	1×100	293.598	GO 6253	J. MacKenty	
	F606W	5957	1508	3×2800	291.727	GTO 6254	E. Groth	saturated center and star
	F814W	7940	1531	2×1700	291.727	""	""	""
	F702W	6895	1389	1×300+1×700	325.004	SNAP 6357	W. Jaffe	PC1
	F555W	5407	1236	4×400	291.943	GO 6587	D. Richstone	PC1
	F814W	7940	1531	2×800	291.943	""	""	
NGC 5253	F606W	5957	1508	1×500	131.324	SNAP 5479	M. Malkan	PC1
	F255W	2553	393	3×800+3×800+3×700	264.709	GO 6124	R. Fesen	
	F547M	5479	486	2×200+2×600	264.460	GO 6524	D. Calzetti	
	F656N	6563	21	2×500+1100+1500	264.460	""	""	
	F814W	7940	1531	2×180+2×400	264.460	""	""	
	F487N	4866	26	3×1300+1×1200	264.460	""	""	
	F170W	1730	500	2×400	280.005	GO 6716	T. Stecher	PC1
	F336W	3344	381	2×260	280.005	""	""	
	F555W	5407	1236	1×200	280.005	""	""	
	F814W	7940	1531	1×200	280.005	""	""	
	F502N	5013	27	200+260+600+800	259.612	GO 9144	D. Calzetti	
	F673N	6732	47	2×600+1×1200	259.612	""	""	
UGC 08696	F814W	7940	1531	2×400	343.721	SNAP 6346	K. Borne	PC1
	F814W	7940	1531	2×400	20.558	""	""	WF3
UGC 08823	F606W	5957	1508	1×500	182.130	SNAP 5479	M. Malkan	PC1; core saturated
NGC 6789	F336W	3344	381	2×1400	303.896	GO 8122	R. Schulte-Ladbeck	PC1
	F555W	5407	1236	2×1300+4×1400	303.896	""	""	
	F656N	6563	21	2×1400	303.896	""	""	
	F814W	7940	1531	2×1300+4×1400	303.896	""	""	
NGC 6782	F450W	4520	958	3×300	151.212	GO/DD 8550	K. Noll	
	F606W	5957	1508	2×160	151.212	""	""	
	F814W	7940	1531	2×160	151.212	""	""	
— NICMOS IMAGES:								
UGC 05101	F110W	11285	1632	1×112	107.171	GTO 7219	N. Scoville	NIC2
	F160W	16060	1177	1×112	107.171	""	""	""
	F220M	22182	512	1×136	107.171	""	""	""
NGC 3310	F110W	11292	1654	1×128	125.84	GO 7268	R. van der Marel	NIC1
	F110W	11285	1632	1×160	125.84	""	""	NIC2
	F160W	16071	1170	2×256	125.84	""	""	NIC1
	F160W	16060	1177	1×128+1×192	125.84	""	""	NIC2
	F160W	16078	1172	1×128+1×256	125.84	""	""	NIC3
	F205W	20714	1832	1×256	125.84	""	""	NIC2
NGC 3516	F160W	16060	1177	1×704	251.013	SNAP 7330	J. Mulchaey	NIC2
NGC 3690/IC 694	F110M	11026	590	8×128	133.864	GTO 7218	M. Rieke	NIC1; mosaic of 8 pointings

TABLE 3—*Continued*

Object	Filter	λ_c (Å)	$\Delta\lambda$ (Å)	Exposure time (sec)	Orient (deg)	Proposal ID	PI	Note
(1)	(2)	(3)	(4)	(5)	(6)	(7)	(8)	(9)
	F160W	16060	1177	2×104	133.851	""	""	NIC2; 2 pointings
	F166N	16583	59	1×256	133.901	""	""	NIC3
	F187N	18748	67	4×640	133.851	""	""	NIC1; mosaic of 4 pointings
	F187N	18740	68	2×160	133.851	""	""	NIC2; 2 pointings
	F190N	18986	73	4×640	133.842	""	""	NIC1; mosaic of 4 pointings
	F190N	19003	63	2×160	133.851	""	""	NIC2; 2 pointings
	F212N	21213	89	1×1280+1×1408	133.851	""	""	""; 2 pointings
	F237M	23696	473	2×288	133.851	""	""	""; 2 pointings
	F215N	21487	80	1×1408+1×1408	133.842	""	""	""; 2 pointings
	F222M	22182	512	2×176	133.842	""	""	""; 2 pointings
UGC 06527	F160W	16060	1177	1×256	39.150	SNAP 7328	M. Malkan	NIC2
NGC 3921	F110W	11285	1632	1×160	63.944	GO 7268	R. van der Marel	NIC2
	F110W	11292	1654	1×128	63.948	""	""	NIC1
	F160W	16060	1177	1×192+1×128	63.944	""	""	NIC2; 2 pointings
	F160W	16078	1172	2×256+2×128+192	63.944	""	""	NIC3; mosaic of 4 pointings
	F205W	20714	1832	3×256	63.944	""	""	NIC2; 3 pointings
NGC 5253	F110W	11285	1632	1×24	105.339	GTO 7219	N. Scoville	NIC2
	F187N	18740	68	1×64	105.339	""	""	""
	F160W	16060	1177	1×24	105.339	""	""	""
	F190N	19003	63	1×64	105.339	""	""	""
	F222M	22182	512	1×80	105.339	""	""	""
	F160W	16071	1170	3×384+2×640	296.776	GO 7849	W. Freedman	NIC1
	F160W	16060	1177	3×384+2×640	296.776	""	""	NIC2
UGC 08696	F110W	11285	1632	1×64	133.577	GTO 7219	N. Scoville	NIC2
	F160W	16060	1177	1×64	133.577	""	""	""
	F222M	22182	512	1×80	133.577	""	""	""
— FOC IMAGES:								
UGC 03426	F210M	2156	214	1×596	274.030	GTO 5140	F. Macchetto	
	F320W	3360	844	1×596	274.030	""	""	
	F342W	3410	702	1×597	277.678	""	""	
	F372M	3710	406	1×896	274.030	""	""	
	F502M	4940	530	1×750	274.030	""	""	
	F550M	5460	188	1×1196	274.030	""	""	
	F502M	4940	530	3×5262	289.829	GO 5918	D. Axon	imaging polarimetry
	F275W	2770	594	3×5187	20.342	GO 6702	L. Kay	imaging polarimetry
	F342W	3410	702	3×1697	20.342	""	""	
IC 2184	F220W	2280	480	1×996	120.036	GO 4800	P. Conti	pre-refurbishment
NGC 3310	F220W	2280	480	1×197	13.102	GO 3591	T. Heckman	pre-refurbishment
NGC 3690/IC 694	F220W	2280	480	1×897	333.653	GO 3591	T. Heckman	pre-refurbishment
	F220W	2280	480	2×896+2×896	269.868	GO 3792	S. Neff	""; 2 pointings
NGC 5253	F220W	2280	480	1×497	122.891	GO 3591	T. Heckman	pre-refurbishment